Generation and Action Spectroscopy of Gaseous DNA Cation Radicals

Yue Liu

A dissertation
submitted in partial fulfillment of the
requirements for the degree of

Doctor of Philosophy

University of Washington

2022

Reading Committee:
František Tureček, Chair
Matthew F. Bush
Robert E. Synovec
Bo Zhang

Program Authorized to Offer Degree:
Department of Chemistry

University of Washington

Abstract

Generation and Action Spectroscopy of Gaseous DNA Cation Radicals

Yue Liu

Chair of the Supervisory Committee:
František Tureček
Department of Chemistry

Reactions between genetic material and secondary low-energy electrons emitted from high energy radiation can cause various DNA lesions such as base modifications and cleavage, single strand breaks and double strand breaks. The mechanism of DNA lesions has been well studied by many research groups for the past two decades. However, little is known about the electronic structure of DNA radicals which are the immediate precursors in the early-stage of DNA damage. Due to the multistage capacity of the ion trap and great progress of photodissociation action spectroscopy, we are able to generate biomolecule cation radicals in a control manner in the gas phase, purify them and their precursors by mass selection, store the reactive species in an inert environment of low-pressure helium, and investigate the ion structures and electronic excitations via various molecular dissociation processes and quantum chemistry calculations. Here, I focus on novel mass spectroscopic studies and theoretical investigations that range from gaseous DNA nucleoside to oligonucleotide cation radicals. The DNA radical generation relies on a fine-tuned electron transfer from fluoranthene anion to either charge tagged nucleoside cations or hydrogen-rich oligonucleotide multi-cations. As the charge tag, I used the 6-(trimethylammonium)hexane-1-aminocarbonyl group that was attached to O5' of the ribose moiety. This tag was found to have negligible effect on the electronic transitions of nucleobase radicals. The charge-tagged adenosine, cytidine and guanosine radicals were further characterized by action spectra as N-7-H adenosine, N-7-H guanosine and N-3-H cy-

tidine radical tautomers. All three radicals were found to undergo spontaneous dissociations by loss of the nucleobase and a hydrogen atom. Hydrogen deuterium exchange experiments showed a negligible isotope effect on the unimolecular dissociation of adenosine and cytidine radicals, while the guanosine radical displayed an unusual inverse isotope effect. This might arise from the dynamics of post-transition-state complexes preceding the product separation. The investigation of the three nucleoside radicals provided us a chance to elucidate the structure, energetics and electronic states of the fundamental DNA constituent, and the spectra provided a reference for the electronic properties of larger DNA cation-radical oligomers. The last chapter describes intramolecular interactions of hydrogen-rich DNA tetranucleotide cation radicals $GATT^{+\bullet}$ and $AGTT^{+\bullet}$. These radicals were generated in the gas phase by one-electron reduction of the respective dications. The spectroscopic study indicated the formation of the 7,8-H-dihydroguanine cation radical isomer via a hydrogen atom migration from adenine N-1-H to the C-8 position in N-7-protonated guanine. This isomerization occurred spontaneously in hot cation radicals produced by electron transfer and was facilitated by low transition state energies as indicated by Rice–Ramsperger–Kassel–Marcus (RRKM) and transition state theory kinetic analysis.

TABLE OF CONTENTS

LIST OF FIGURES

LIST OF TABLES

ACKNOWLEDGMENTS

I would like to thank Prof. František Tureček for the 5-year support and guidance. Thank you so much for creating such a productive and creative work environment where I can rapidly grow from a research novice with language barrier to a researcher with so many accomplishments! It's your breath of knowledge and enthusiasm for research that gives me the confidence to complete every project. Having you around during my presentation can always calm me down and make me confidently and proudly present my research. It's my honor to have you as my research and life advisor. Hope I will be as passionate about work and curious about nature as you are! Thank you!

I would like to thank my undergraduate advisor, Prof. Shuji Ye for guiding me to the research field. Thank you for giving me the chance to work on an independent project! Thank you for your patience and trust so that I can have my first publication! Thank you for your suggestions and help with my graduate application! You started my research journey. Thank you!

I would like to thank the amazing UW fellows. Thank you, Martin Sadilek, for your suggestions on instruments and organization of PacMass meetings! Thank you, Andy Dang, for your patient training about the instrument and experiment! Thank you, Yang Liu, for your guidance about the experiment and computation, your suggestions about my career, and your accompany during the ASMS conference! Thank you, Shu R. Huang! You are always reliable to help me out when I get in trouble! Thank you, Congcong Ma, Hongyi Zhu, Jiahao Wan and Václav Zima! It's a pleasure to know all of you during my last year staying here. You all bring me tons of joy!

I would like to thank my committee members, Prof. Matthew F. Bush, Prof. Robert E.

Synovec and Prof. Bo Zhang, and my GSR, Prof. James Bruce. Thank you for your time and suggestions on my research! I would like to thank National Science Foundation Funding for support our research projects!

I would like to thank my friend, Dr. Shan Lin for exploring popular restaurants and hiking with me to escape from the stress of research. I would like to thank my undergraduate roommates, Jie Huang, Dr. Zhaohan Zhang, and Dr. Xi Chen! Thank you for the 4-year accompany! Even though we went to different universities after graduation, having old friends in a foreign country makes me feel not alone. Good luck to your own defense, Jie!

Lastly, I would like to thank my family for consistent love and unconditional support for my decisions. I would like to thank my fiancé, Dr. Hengji Wang for your love, encouragement, and tolerance for the past 10 years! Thank you for planning for our mutual future, pushing me forward and growing with me together!

Chapter 1

INTRODUCTION

1.1 The DNA Damage Pathway

Genetic information is encoded in the deoxyribonucleic acid (DNA) and any damage to DNA can cause genetic mutations, malfunctioning or cell death.[1] The mechanism of DNA damage has been well studied by many research groups for the past two decades.[2] As shown in Figure 1.1, the two pathways of DNA damage caused by radiolysis are the direct pathway corresponding to a direct energy deposition into DNA and the indirect pathway arising from the energetic particles released by ionization of the surrounding medium.[3]

Direct absorption of the ionization energy of DNA, DNA $\rightarrow$ $DNA^{+\bullet}$ + DNA^{*} + e^{-}, gives rise to a DNA cation radical ($DNA^{+\bullet}$), an electronically excited DNA (DNA^{*}) and an electron.[3] $DNA^{+\bullet}$ is the primary product in this direct action and it may undergo rapid hole transfer to other base moieties. The direct deposit of the secondary low energy (0-20 eV) electron (LEE) generated by high energy radiation can also lead to substantial strand breaks even though the energy is below the ionization threshold.[4, 5] The transient anion radicals formed by the addition of the LEE are responsible for strand breaks via a dissociative electron attachment process and a decay into dissociating electronically excited states.[6, 7]

The indirect pathway is considered to be more efficient at inducing DNA lesions than the direct one.[8] For example, ionization of water, $H_2O \rightarrow H_2O^{+\bullet}$ + $SE(e^{-})$, leads to the formation of the strong acid $H_2O^{+\bullet}$ and a secondary electron.[3] These two species can induce DNA electron and hole transfer in the form of $SE(e^{-})$ + DNA $\rightarrow$ $DNA^{-\bullet}$ and $H_2O^{+\bullet}$ + DNA $\rightarrow$ $DNA^{+\bullet}$ +H_2O. The produced $DNA^{+\bullet}$ is a strong base that is readily protonated by the surrounding molecules of solvent. $H_2O^{+\bullet}$ can also react with water to form hydroxyl

radical ($HO^{\bullet}$),[9] which induces oxidative DNA damage mostly by addition to the base moiety, forming OH-adduct radicals or by hydrogen atom abstraction from the sugar or base moiety forming neutral radicals.[10] The formation of $HO^{\bullet}$ increases the yield of DNA strand breaks compared to the effect of direct deposition of LEE.[3] Even though the hydrated electrons generated during the ionization of water are not efficient at inducing biomolecule damage, its precursor electrons (the prehydrated electron) are found to be about twice as efficient at inducing strand breaks than $HO^{\bullet}$.[11, 12] Electron transfer from the prehydrated electron to the guanosine nucleobase, forming an intermediate anion radical, triggers dissociation within several picoseconds.[11]

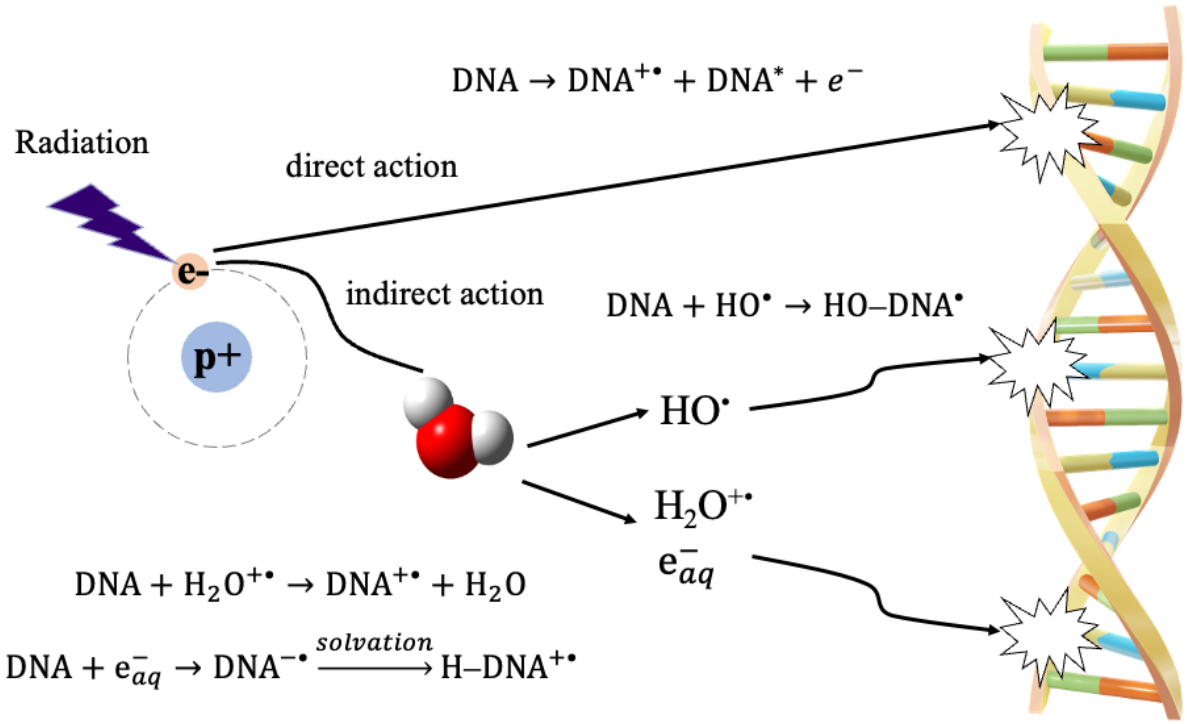

Figure 1.1: Direct and indirect radiation damage to the DNA. Direct energy deposition can cause DNA damage. Hydroxyl radicals, acidic water cation radical and secondary electrons released from the ionization of water also lead to DNA damage in different chemical reactions.

1.2 Generation of DNA Cation Radicals in the Gas Phase

Free radicals on the DNA deoxyribose moiety are intermediate precursors that are responsible for DNA base cleavage and strand breaks.[3, 13] However, the electronic structure and excited states of DNA radicals have not been investigated in detail. This is due to the fact that transient reactive species undergo rapid dissociation, hole or electron transfer, and other competitive reactions. Environmental factors, such as pH, solvent and other reactive species that are present in the condense phase may complicate the study and structure elucidation of DNA radicals. Thanks to novel mass spectrometry and action spectroscopy techniques developed by our group, we can now generate, purify, and store DNA-related radicals in the ion trap for further investigation![14, 15]

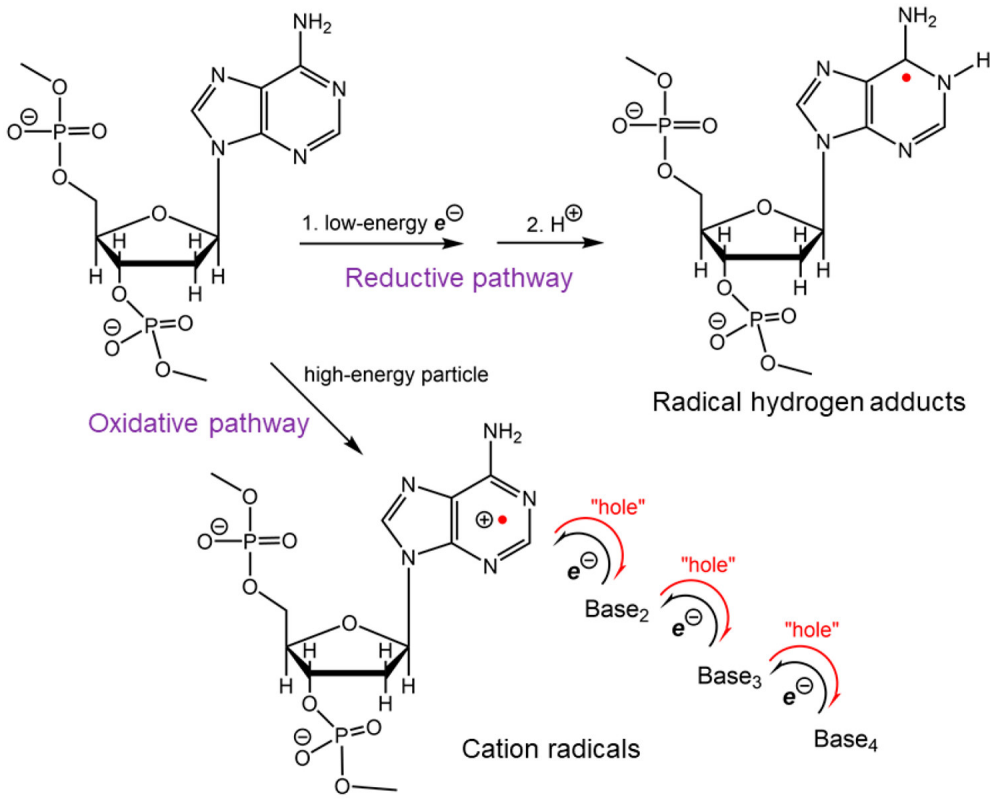

Figure 1.2: Reductive and oxidative pathways to DNA radicals, reproduced from [15].

In my thesis, I focus on the generation of the DNA cation radicals, which can represent intermediates of the direct DNA damage and protonated intermediates of the capture of low energy electron.[15] The primary product of the direct absorption of ionization energy, $DNA^{+\bullet}$, is generated in the oxidative pathway (Figure 1.2). The reductive pathway of Figure 1.2 pictures the formation of hydrogen-adduct DNA cation radicals, which are called hydrogen-rich cation radicals. The transient anion radicals, formed by attaching a low energy electron, undergo a rapid protonation by solvent and lead to the formation of the hydrogen-rich DNA cation radicals.

The Tureček group has already developed techniques (Figure 1.3) and successfully generated various DNA cation radicals in the gas phase. The technique using ternary transition metal developed by O'Hair and coworkers[16] has been applied to generate cation radicals of standard or modified adenine[17], guanine[18], cytosine[19, 20] and thymine[21]. This relies on the collision induced dissociation (CID) of the transition metal complexes, typically ternary Cu(II) complexes, containing terpyridine and neutral nucleobase (Figure 1.3eq1, Figure 1.4). In this way, the nucleobase cation radical is generated using oxidation by Cu(II). However, in generating nucleoside cation radicals, this method is limited to the generation of most readily oxidized 2'-deoxyguanosine and guanosine. [16, 22]

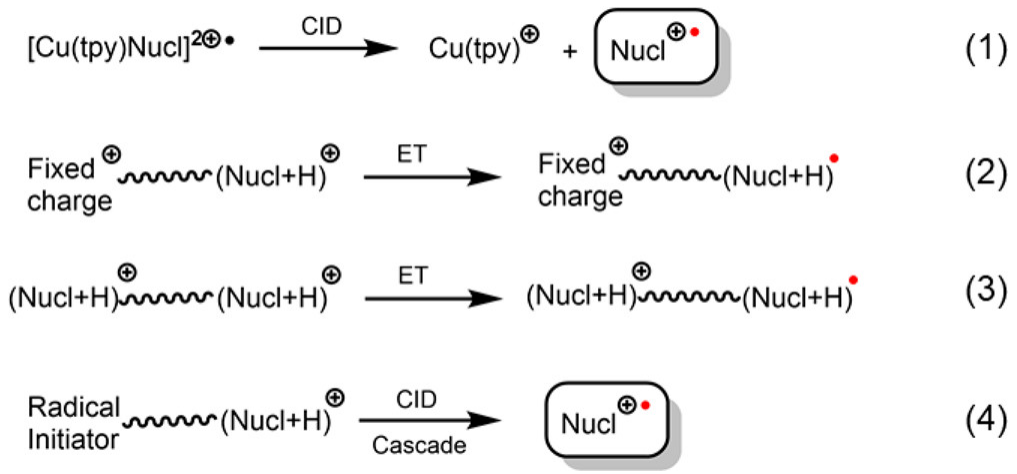

Figure 1.3: Formation of nucleobase, nucleoside, and nucleotide cation radicals in the gas phase, reproduced from [23].

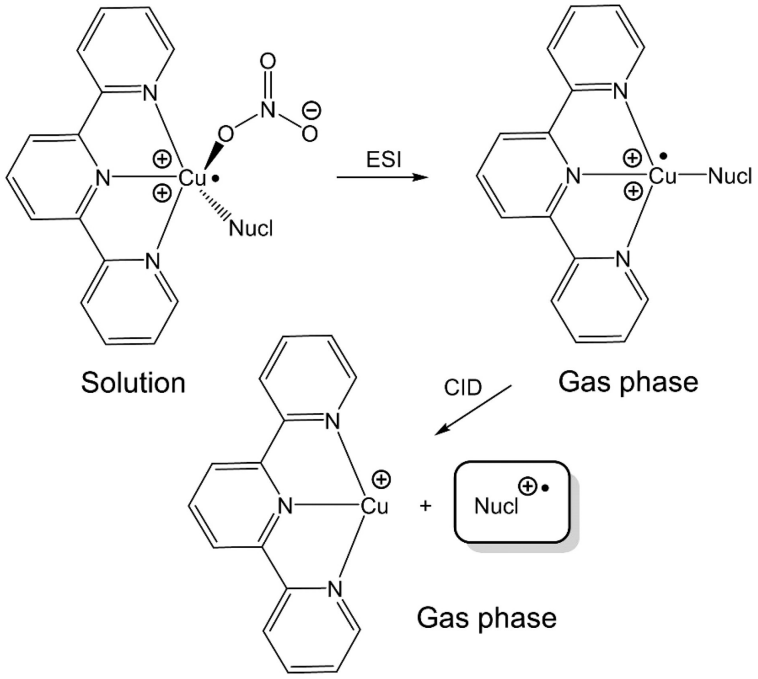

Figure 1.4: Formation of gas-phase nucleobase cation radicals from Cu (II) complexes, reproduced from [22].

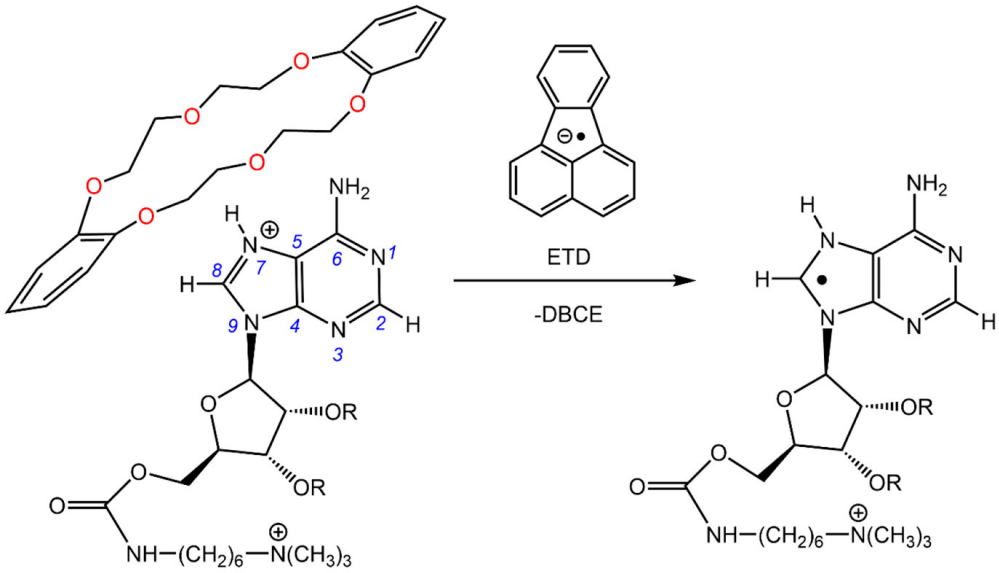

Figure 1.5: Reductive pathway for the formation of adenine radical conjugates, reproduced from [15].

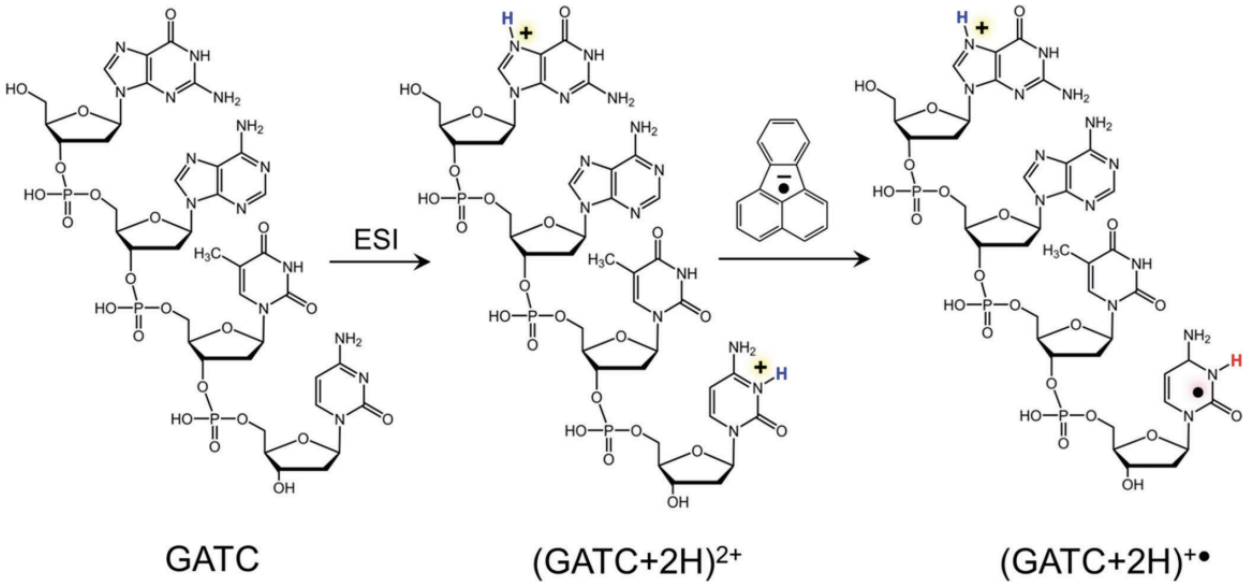

Figure 1.6: Reduction of $(GATC+2H)^{2+}$ dication to cation radical, reproduced from [24].

Besides the oxidation pathway, I have developed a reductive pathway that utilizes electron transfer (ET) from fluoranthene anion radicals to either charge-tagged complexes (Figure 1.3eq2, Figure 1.5) or multiply charged oligonucleotide ions (Figure 1.3eq3, Figure 1.6). The charge tag was designed as a 6-(trimethylammonium)hexane-1-aminocarbonyl group that was attached to O5' of the ribose moiety. These conjugates have been used for the first time to successfully generate adenosine[25], guanosine[26], and cytidine[27] neutral radicals. The fixed charge tag makes the neutral nucleobase radicals visible for the mass spectrometer and has been shown to have little effect on the excited states of the base moiety.[25–27] Even though in my experiments the site of the electron attachment is not controlled and can occur in either charged moiety, the formed hypervalent trimethylammonium radicals undergo fast dissociation, guaranteeing that the surviving radicals reside in the nucleobase.[28] Oligonucleotide, possessing multiple basic sites, can acquire multiple charges when electro-sprayed from an acidic solvent. Upon an ion-ion reaction with the anion, the oligonucleotide dication is converted to an oligonucleotide cation radical, as illustrated for dinucleotides[29, 30] and tetranucleotides[31]. Extending this method to multi-cations, such as tri-cations, induces the

formation of dication radicals and cation diradicals in addition to mono-cation radicals[32, 33], giving this method more flexibility.

Other parallel efforts in the Tureček group have been aimed at generating novel isomers of nucleobase cation radicals using the new non-redox approach (Figure 1.3eq4, Figure 1.7) leading to the formation of novel adenine and guanine cation radical isomers.[23] This approach required the uncoupled generation of the charged nucleobase and radical carrying moieties. The charge was produced by electrospray ionization of the protonated nucleobase conjugates. The radical was generated by CID of a radical initiator moiety, for example, the standard 4,4'-azobis(4-cyanovaleric acid) (ABCV) group.[34] A second step of the selective CID upon the nucleobase conjugate cation radical resulted in the loss of the sugar moiety and formation of novel nucleobase cation radicals. This cascade CID approach has been used to generate novel nucleobase radicals that are not accessible by the first three approaches.

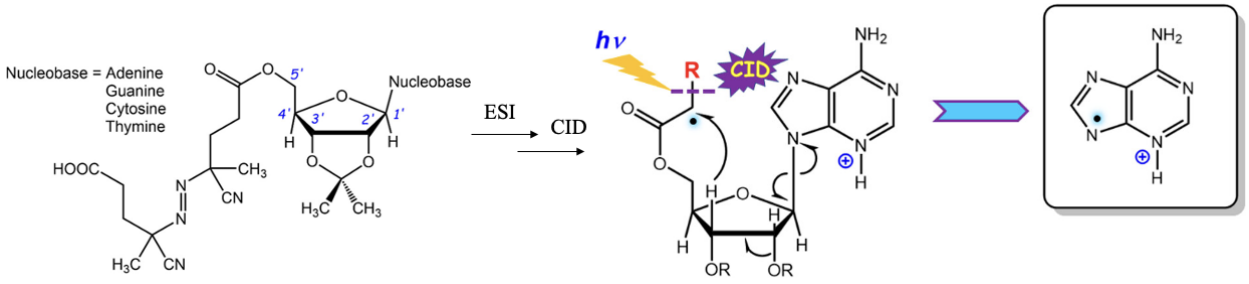

Figure 1.7: The formation of novel adenosine cation radicals using nonredox cascade CID approach upon adenosine-ABCV conjugates, adapted from [23].

1.3 Novel Mass Spectrometry

Mass spectrometry is an analytical technique used to measure mass to charge ratios of ions in the mass spectrometer. The mass spectrometer contains at least three basic components: (1) the ionization source used to convert samples to gas-phase ions; (2) the mass analyzer used to sort and separate the ions based on their mass-to-charge (m/z) ratio; and (3) the ion detection system to generate the mass spectrum, which is a plot of the relative ion abun-

dance as a function of m/z values (Figure 1.8 top panel). From the mass spectrum, we can identify unknown samples through the correlation with the known masses and a characteristic fragmentation pattern. For example, the presence of two singly charged ions that differ by 15 m/z might indicate loss of methyl group from the larger ion.[35] However, distinction by mass spectrometry of isomers that share the same atom composition and similar structures can be difficult to accomplish. Specifically, mass spectrometry alone cannot be used to confirm the existence and characterize the electronic properties of different nucleobase radical isomers in my study. In contrast to mass spectrometry, spectroscopic methods are sensitive to distinct chromophores. The characteristic interaction of the matter with the radiation at different frequencies can be assigned to particular functional groups. Thus, the coupling of spectroscopy to mass spectrometry provides another dimension of information, namely structure elucidation (Figure 1.9). Now, let's dive into the details of the novel mass spectrometer used in our group!

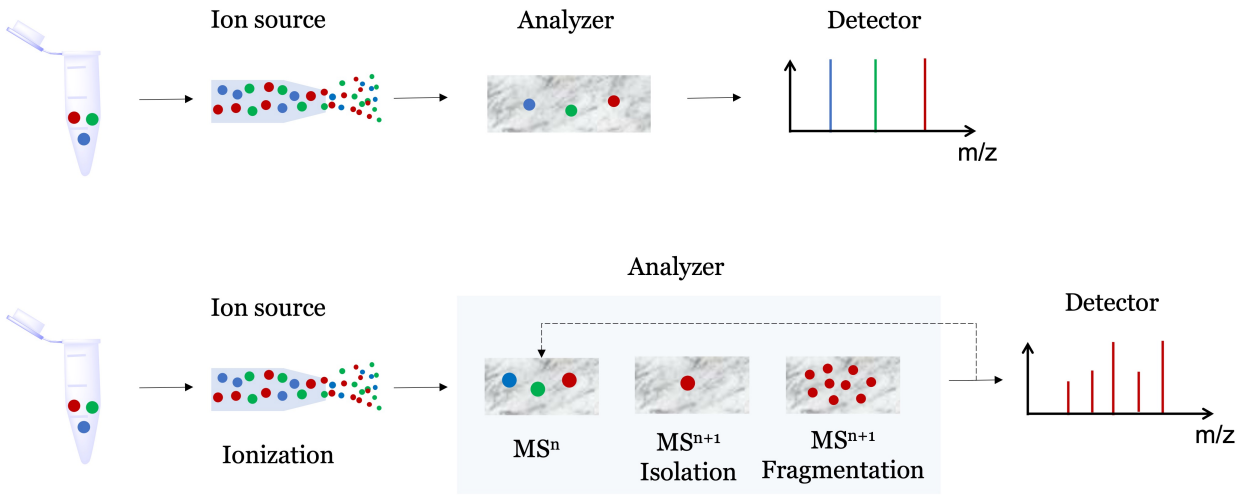

Figure 1.8: Schematic of mass spectrometry and tandem mass spectrometry.

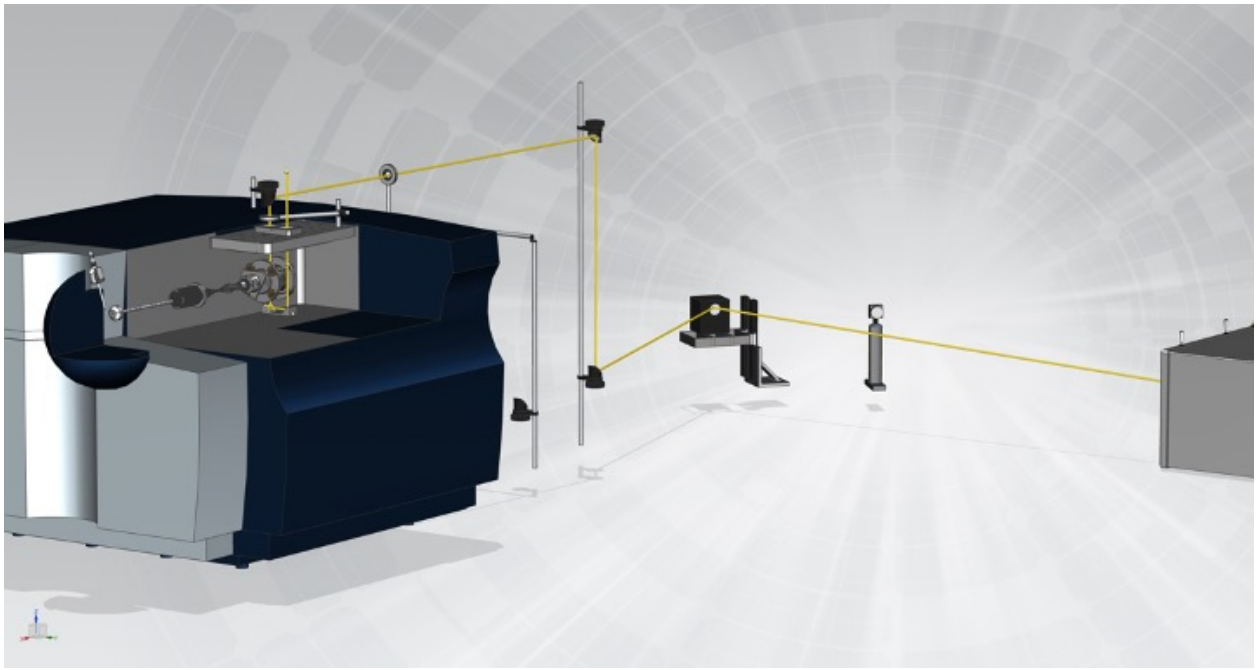

Figure 1.9: Optical setup and modifications of Bruker amaZon mass spectrometer for MS^n-UVPD and automated action spectroscopy with tunable wavelength from 210-700 nm, reproduced from [18].

1.3.1 Electrospray Ionization

Why do we use electrospray ionization (ESI) to transfer ions from solution phase to gaseous phase? The answer is given by Professor Fenn in his Nobel lecture: "A few years ago the idea of making proteins or polymers "fly" by electrospray ionization (ESI) seemed as improbable as a flying elephant, but today it is a standard part of modern mass spectrometers".[36] ESI is the jet technology that makes the elephant fly! Before ESI-mass spectrometry (ESI-MS), the ionization methods such as electron ionization and chemical ionization easily lead to the fragmentation of the analyte. ESI, a soft ionization technique, can solve this problem because little residual energy is retained by the analyte. It also enjoys another two advantages: the analyte might be able to carry multiple charges;[37] and the noncovalent interactions can be preserved in the gas phase.[38] So the development of ESI-MS has opened a new era for large molecules such as proteins and nucleic acids.

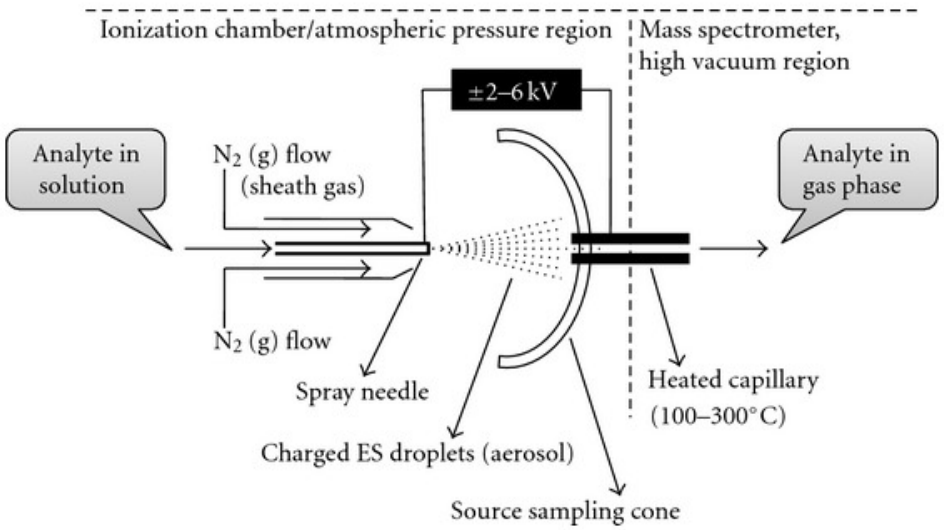

Figure 1.10: A schematic representation of ESI-ion source, reproduced from [39].

How does ESI work? Generally, a dilute solution of the analyte (under 1 mM) is injected into a nebulizer by a syringe pump through a very thin needle at a low flow rate (1 – 20 μL/min). The needle is mounted inside of a tube that transports sheath gas (dry N_2) for steady nebulization. The charged droplets generated by the nebulizer diminish in size via solvent evaporation which is aided by heated drying N_2 gas and is accelerated by the strong electric field between the nebulizer (ground potential) and the tip of the negatively charged capillary in the case of positively charged droplets. The electric field strength within the diminishing charged droplet finally reaches a limit and the charged analyte, releasing from the droplet, can pass through the heated capillary into the mass analyzer (Figure 1.10).[39]

1.3.2 Ion Trap Tandem Mass Spectrometer

How do we obtain structural information while ESI reserves the whole structure of the analyte by avoiding the analyte fragmentation? Using post-source fragmentation in the tandem mass spectrometry (MS/MS) is the key to solve the problem.

Three fragmentation techniques discussed in this study are collision induced dissociation

(CID), electron transfer dissociation (ETD) and UV-vis photodissociation (UVPD). CID is a process of converting ion kinetic energy into its internal energy. The selected ion is accelerated and collides with neutral gas atoms or molecule which results in bond break and fragmentation. Electron transfer (ET) refers to an ion-ion reaction in which an electron is transferred from an anion radical to the selected multi-cation. Such exothermic ion-ion reaction can lead to a rapid dissociation of the formed cation radical. As for UVPD, the energy gained by the selected ion from resonant absorption of a photon can result in photodissociation.

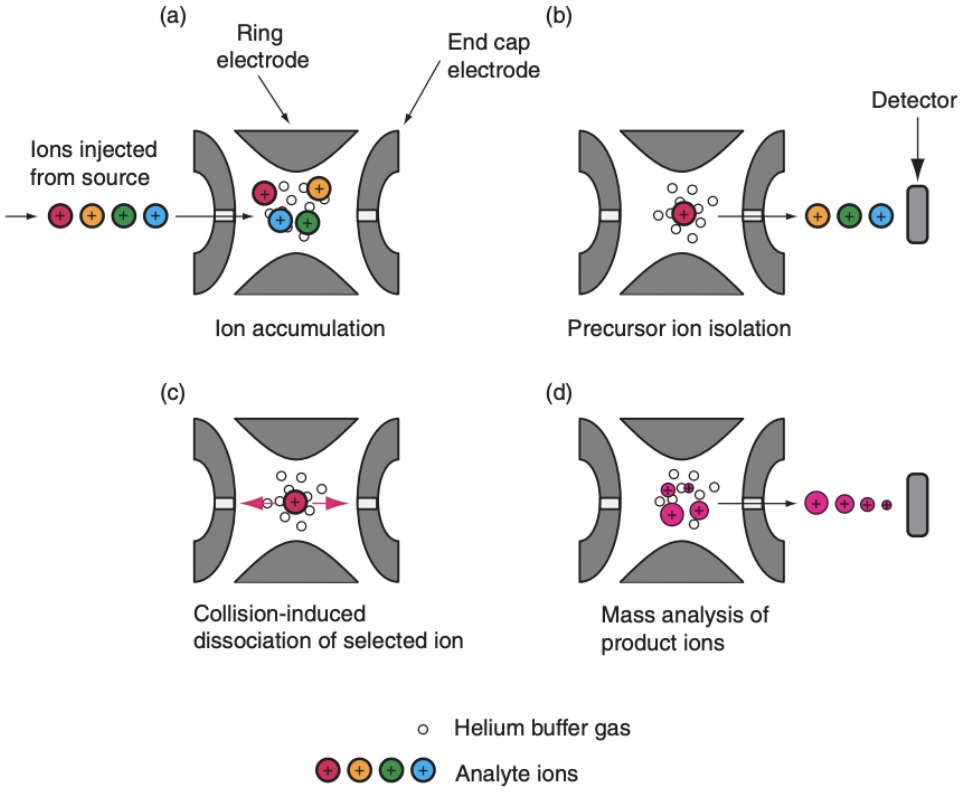

Figure 1.11: Schematic of MS^2-CID in the quadrupole ion trap, reproduced from [40].

Tandem mass spectrometry (Figure 1.8 bottom panel) can be achieved in space by coupling a series of mass analyzers and collision chambers[41] or in time through multiple steps of fragmentation and separation taking place over time in the same mass analyzer[42]. In

our lab, we utilize an ion trap mass analyzer since it can be used to perform multiple stage mass spectrometry (MS^n) without the limitation of the number of mass analyzers. The ion trap is composed of a ring electrode between two end cap electrodes (Figure 1.11), forming a 3-dimensional hyperbolic space for creating an ideal quadrupole filed to trap the ion. The ion can pass through the ion trap through holes at the center of the cap electrodes. The confinement of the ion is achieved by applying a high radiofrequency (RF) potential to the ring electrode while cap electrodes are grounded. Concurrently, the damping gas (He) in the ion trap extracts kinetic energy from the ion cloud to cool it down. Besides the primary RF potential fed to the ring electrode, an auxiliary RF potential is applied on the exit end cap or the both end cap electrodes for ion isolation, fragmentation and mass analysis. By applying a RF potential to the ring electrode, the ion trap can achieve the function of ion accumulation (Figure 1.11a), selective mass ion isolation (Figure 1.11b), excitation for CID/ETD/UVPD (Figure 1.11c) and sequential mass ejection to produce a mass spectrum (Figure 1.11d).

To be specific, Figure 1.12 pictures how the potential of the gate lens and the RF potential of the electrode change during a round of MS^n scan. A round of MS^n scans starts with dropping the blocking potential of the gate lens to let the ions enter the ion trap. Ions are accumulated and stored in the trap using a low quadrupolar amplitude for a given time. To isolate the desired ion for the next-step characterization, the electronics system of the instrument creates a broadband frequency spectrum containing resonant frequencies for all ions except the selected one. In the excitation phase, CID for example, the isolated ions are accelerated by a dipole field to collide with the background helium gas. All these fragment ions created by CID are ejected out of the trap with increasing m/z values by increasing the quadrupolar and dipolar fields progressively. These ions are detected by a Daly detector where ions are accelerated by an electric field onto a phosphor screen forming photons and detected by a photomultiplier.[43] Finally, dropping primary RF potential to zero, aiming to remove the remaining ions in the trap, marks the end of one MS^n scan. Alternatively, additional stages of fragmentation can be performed for the selected product ion. That's why the ion trap mass spectrometry can be extended to obtain mass spectra of MS^n stage

as long as signal-to-noise ratio is sufficient to carry out the measurement.

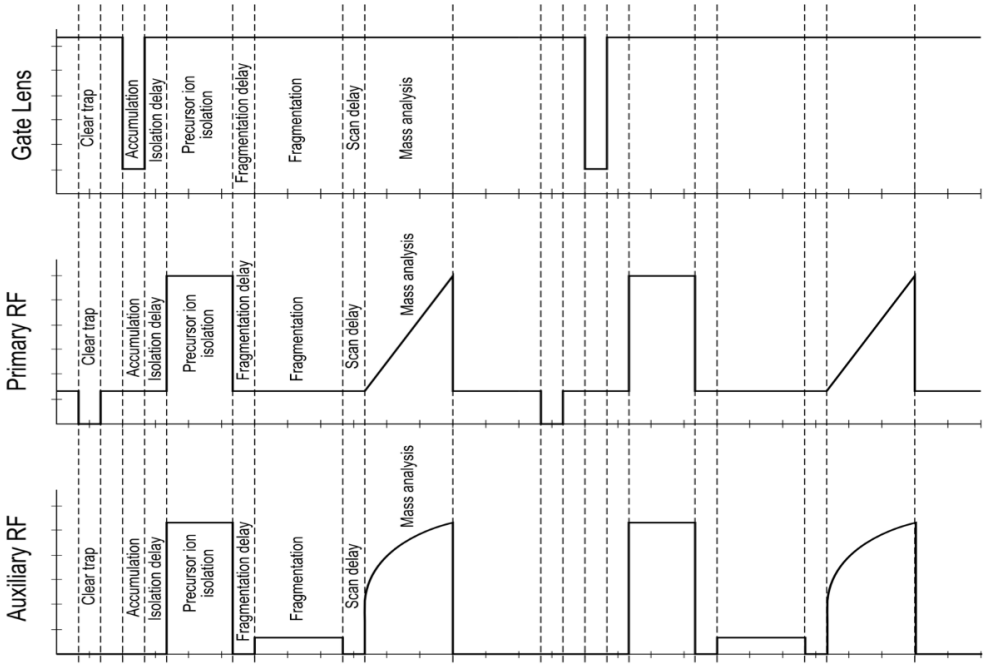

Figure 1.12: The important scan segments for an MS^n scan, reproduced from Figure 3-12 of "amaZon Series User Manual", *Bruker Daltonik GmbH*, **2016**.

To implement ETD, an auxiliary chemical ionization (CI) source is mounted perpendicularly to the ion path before the ion trap module. During the ETD stage, the anion radicals generated by CI of fluoranthene are released to the ion trap to react with the isolated precursor ions. Electron transfer is related to the charge state of the precursor ions, and it is usually used to study multiply charged ions.

Similar to the modification for infrared multiphoton action spectroscopy (IRMPD) measurements (Figure 1.13),[44] we have adapted our Bruker amaZon speed ion trap for optical access (Figure 1.9).[18] The ring electrode of the modified ion trap has two 1-mm holes, one at the top center and the other at the bottom center, to allow the laser beam to pass perpendicular to the ion beam. An optical breadboard with two sealed UV windows is mounted above the ion trap, replacing the previous vacuum housing lid. Two mirrors are installed

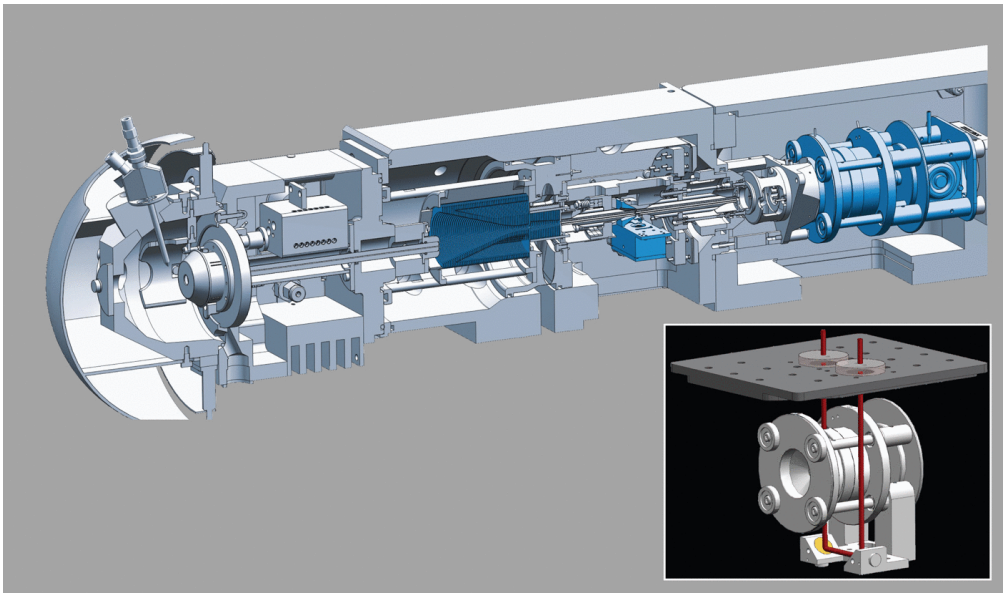

Figure 1.13: The schematic of the quadrupole ion trap mass spectrometer and electrospray ionization source, with modifications for optical access to the trapped ions highlighted in the inset, reproduced from [44].

below the ion trap to guide the laser beam back out through the exit UV window. The outgoing laser beam can be used to confirm the laser path is tuned properly.

1.3.3 UV-Vis Photodissociation Action Spectroscopy

Considering the limited ion number densities in the ion trap, how could we obtain an absorption spectrum of the ion of interest for a better structure elucidation? This is achieved by action spectroscopy, which is also called consequence spectroscopy! Instead of measuring photon absorption via absorbance, action spectroscopy measures the consequence of photon absorption resulting in dissociation.[45]

The energy gained by absorption of a single photon in the UV region usually is sufficient to induce dissociation that can proceed in different ways. Three most common pathways are discussed here (Figure 1.14). If the photon energy is above the dissociation threshold, it can promote a transition from the electronic ground state (S_0) to vibrationally excited electronic excited state (S_0), which means it can induce the dissociation directly (Figure 1.14 left

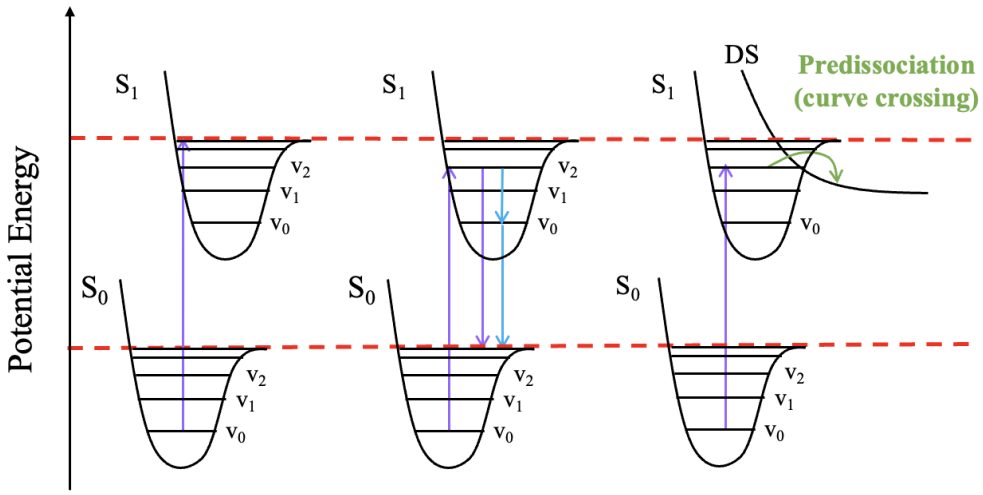

Figure 1.14: Three potential dissociation mechanisms upon absorption of a UV photon. Dissociation thresholds are indicated via red, dashed lines. Adapted from [45].

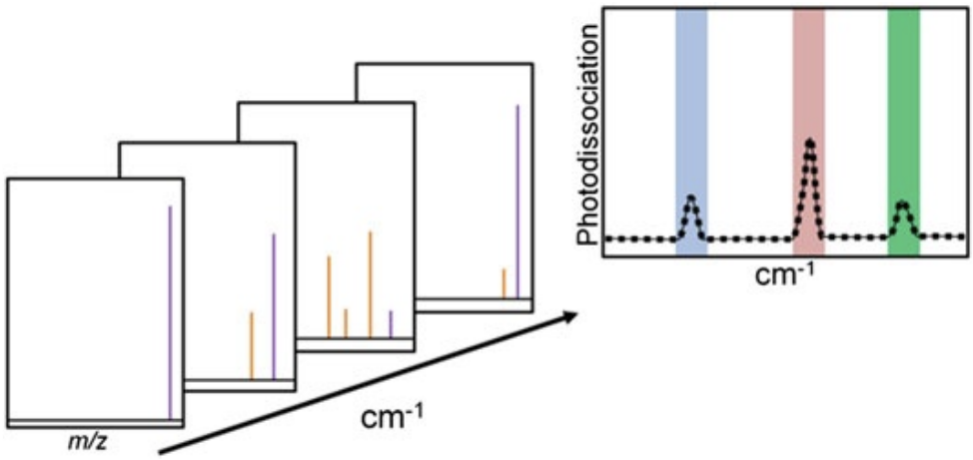

Figure 1.15: Methodology of a photodissociation consequence spectroscopy measurement. Precursor ions (purple) photodissociate to fragments (orange) upon resonant photon absorption. Absorption bands are highlighted for illustrative purposes. Reproduced from [45].

panel). Otherwise, the excited state may undergo an internal conversion to a highly excited vibrational state of S_0., which is above the dissociation threshold of S_0. Or it decays to S_1 v_0 and then relaxes to the unbounded vibrational state of S_0 (Figure 1.14 middle panel). Another potential pathway is through energy crossing to a dissociative state, which has

no or shallow potential energy minimum and causes dissociation below normal dissociation threshold (Figure 1.14 right panel). Overall, photons with different energy can open different dissociation channels. By monitoring the dissociation fragments and measuring the fragment ion intensity as a function of photon frequency, we can obtain the consequence of photon absorption by the precursor ion (Figure 1.15). In this way, we can obtain an action spectrum that reflects the same electron excitation as the absorption spectrum to gain information of the energy needed to activate different dissociation channels.

1.3.4 Quantum Chemistry Methods

The characteristic absorption pattern can be used to identify distinct nucleobase radical isomers. How can we know which isomer contributes to the measured action spectrum? To solve this issue, we compare the theoretical absorption spectra of the isomer candidates with the action spectrum collected in the experiment (Figure 1.16). Moreover, we can gain the information of the electronic structure and excited states from the quantum chemistry calculations.

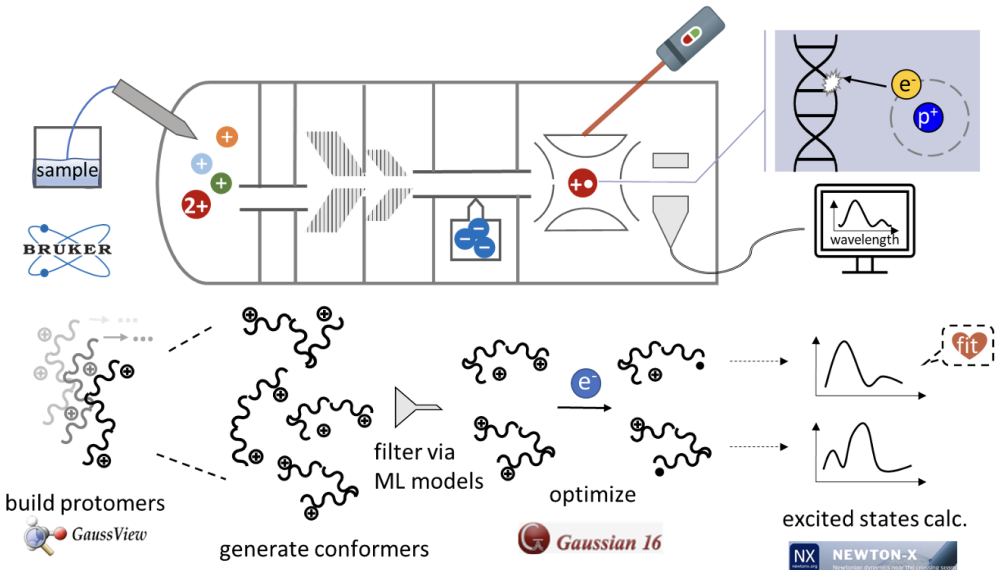

Figure 1.16: The schematic of quantum chemistry calculations used for interpretation of photodissociation action spectra.

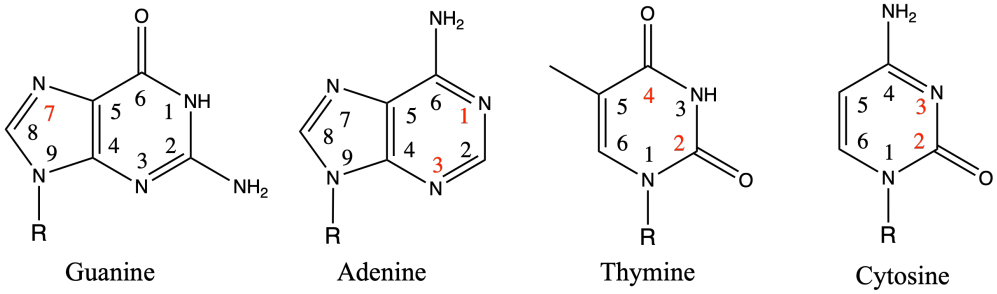

Figure 1.17: The numbering system of the DNA nucleobase ring. The most basic positions are highlight in red color.

The calculation starts with building several initial structures. For the DNA study, we mimic the DNA radical generation process, so we first build structures of the DNA cations and then add an electron to the optimized structure to get the DNA radical. The possible positions of proton attachment are highlighted in red in Figure 1.17. After generating the initial structures, we can choose to optimize the structures with density functional theory (DFT) calculations. The optimized structures are searched in the direction of minimizing the potential energy and are converged to the local energy minimum where the first derivatives of potential energy with respective to the nuclei coordinates are close to zero and the second derivatives are not negative. It is obvious that the local energy minimum may not represent the global minimum. To approximate the real structure, Born-Oppenheimer Molecular Dynamics (BOMD) calculations run by MOPAC under Cuby4 platform[46] are performed to generate a trajectory of distinct conformers so as to provide several thousand (typically 20,000) candidates. All conformers from the trajectory are divided into several clusters based on the structure similarity using machine learning (ML) model. We only pick one conformer from each cluster to save the resources for the further optimization. Combining the DFT energy from the optimization with entropy and enthalpy values derived from the harmonic frequency calculations of the optimized structures, we can obtain relative Gibbs energies of all the optimized protomers and conformers. From these, we pick a set of low-energy structures and add an electron to convert the DNA cation to a radical. With the same

structure optimization method, we then get the stable electronic structure of DNA radicals. To confirm which electronic structure has the absorption pattern comparable to the one collected in the experiment, Time-dependent density functional theory (TD-DFT)[47] is performed to calculate the excitation energies and oscillator strength. The generated theoretical absorption bands correspond to the excitation transition at 0 K, while the experiment refers to thermal ions, so the actual bands may be broadened and red-shifted by 10-30 nm. To evaluate the thermal effect, 300 Boltzmann-ranked vibrational configurations at the experiment temperature are generated for TD-DFT calculations by Newton-X program[48]. The Newton-X method is 300 times more expensive than a single-run TD-DFT, so depending on the size of the molecular system we may compute fewer excited states to cover the regions of interest.

1.4 Bibliography

[1] JF Ward. Complexity of damage produced by ionizing radiation. In *Cold Spring Harbor Symposia on Quantitative Biology*, volume 65, pages 377–382. Cold Spring Harbor Laboratory Press, 2000.

[2] Harry B Gray. *Charge transfer in DNA: from mechanism to application*. John Wiley & Sons, 2006.

[3] Clemens von Sonntag. *Free-radical-induced DNA damage and its repair*. Springer, 2006.

[4] Badia Boudaıffa, Pierre Cloutier, Darel Hunting, Michael A Huels, and Léon Sanche. Resonant formation of dna strand breaks by low-energy (3 to 20 ev) electrons. *Science*, 287(5458):1658–1660, 2000.

[5] Barry D Michael and Peter O'Neill. A sting in the tail of electron tracks. *Science*, 287(5458):1603–1604, 2000.

[6] Leon Sanche. Low energy electron-driven damage in biomolecules. *The European Physical Journal D-Atomic, Molecular, Optical and Plasma Physics*, 35(2):367–390, 2005.

[7] Elahe Alizadeh, Thomas M Orlando, and Léon Sanche. Biomolecular damage induced by ionizing radiation: the direct and indirect effects of low-energy electrons on dna. *Annual review of physical chemistry*, 66:379–398, 2015.

[8] John F Ward. Dna damage produced by ionizing radiation in mammalian cells: identities, mechanisms of formation, and reparability. *Progress in nucleic acid research and molecular biology*, 35:95–125, 1988.

[9] Elahe Alizadeh, Ana G Sanz, Gustavo Garcia, and Leon Sanche. Radiation damage to dna: The indirect effect of low-energy electrons. *The journal of physical chemistry letters*, 4(5):820–825, 2013.

[10] Amitava Adhikary, Anil Kumar, David Becker, and Michael D Sevilla. Understanding dna radicals employing theory and electron spin resonance spectroscopy. *Encyclopedia of Radicals in Chemistry, Biology and Materials*, 2012.

[11] Chun-Rong Wang, Jenny Nguyen, and Qing-Bin Lu. Bond breaks of nucleotides by dissociative electron transfer of nonequilibrium prehydrated electrons: a new molecular mechanism for reductive dna damage. *Journal of the American Chemical Society*, 131(32):11320–11322, 2009.

[12] Jenny Nguyen, Yuhan Ma, Ting Luo, Robert G Bristow, David A Jaffray, and Qing-Bin Lu. Direct observation of ultrafast-electron-transfer reactions unravels high effectiveness of reductive dna damage. *Proceedings of the National Academy of Sciences*, 108(29):11778–11783, 2011.

[13] Miral Dizdaroglu and Pawel Jaruga. Mechanisms of free radical-induced damage to dna. *Free radical research*, 46(4):382–419, 2012.

[14] František Tureček. Uv-vis spectroscopy of gas-phase ions. *Mass Spectrometry Reviews*, 2021.

[15] František Tureček. Flying dna cation radicals in the gas phase: generation and action spectroscopy of canonical and noncanonical nucleobase forms. *The Journal of Physical Chemistry B*, 125(26):7090–7100, 2021.

[16] Sheena Wee, Richard AJ O'Hair, and W David McFadyen. Can radical cations of the constituents of nucleic acids be formed in the gas phase using ternary transition metal complexes? *Rapid Communications in Mass Spectrometry: An International Journal Devoted to the Rapid Dissemination of Up-to-the-Minute Research in Mass Spectrometry*, 19(13):1797–1805, 2005.

[17] Shu R Huang, Andy Dang, and František Tureček. Ground and excited states of gas-phase dna nucleobase cation-radicals. a uv–vis photodisociation action spectroscopy and computational study of adenine and 9-methyladenine. *Journal of the American Society for Mass Spectrometry*, 31(6):1271–1281, 2020.

[18] Andy Dang, Joseph A Korn, James Gladden, Brandon Mozzone, and František Tureček. Uv–vis photodissociation action spectroscopy on thermo ltq-xl etd and bruker amazon ion trap mass spectrometers: a practical guide. *Journal of The American Society for Mass Spectrometry*, 30(9):1558–1564, 2019.

[19] Michael Lesslie, John T Lawler, Andy Dang, Joseph A Korn, Daniel Bím, Vincent Steinmetz, Philippe Maître, František Tureček, and Victor Ryzhov. Cytosine radical cations: A gas-phase study combining irmpd spectroscopy, uvpd spectroscopy, ion–molecule reactions, and theoretical calculations. *ChemPhysChem*, 18(10):1293–1301, 2017.

[20] Shu R Huang and František Tureček. Cation radicals of hachimoji nucleobases. canonical purine and noncanonical pyrimidine forms generated in the gas phase and characterized by uv–vis photodissociation action spectroscopy. *The Journal of Physical Chemistry A*, 124(35):7101–7112, 2020.

[21] Andy Dang, Huong TH Nguyen, Heather Ruiz, Elettra Piacentino, Victor Ryzhov, and František Tureček. Experimental evidence for noncanonical thymine cation radicals in the gas phase. *The Journal of Physical Chemistry B*, 122(1):86–97, 2018.

[22] Andy Dang, Yue Liu, and František Tureček. Uv–vis action spectroscopy of guanine, 9-methylguanine, and guanosine cation radicals in the gas phase. *The Journal of Physical Chemistry A*, 123(15):3272–3284, 2019.

[23] Václav Zima, Yue Liu, and František Tureček. Radical cascade dissociation pathways to unusual nucleobase cation radicals. *Journal of the American Society for Mass Spectrometry*, 2022.

[24] Shu R Huang, Yue Liu, and František Tureček. Uv–vis photodissociation action spectroscopy reveals cytosine–guanine hydrogen transfer in dna tetranucleotide cation radicals upon one-electron reduction. *The Journal of Physical Chemistry B*, 124(17):3505–3517, 2020.

[25] Yue Liu, Andy Dang, Jan Urban, and František Tureček. Charge-tagged dna radicals in the gas phase characterized by uv/vis photodissociation action spectroscopy. *Angewandte Chemie International Edition*, 132(20):7846–7851, 2020.

[26] Yue Liu, Congcong Ma, Calvin J. A. Leonen, Champak Chatterjee, Gabriela Nováková, Aleš Marek, and František Tureček. Tackling a curious case: Generation of charge-tagged guanosine radicals by gas-phase electron transfer and their characterization by uv–vis photodissociation action spectroscopy and theory. *Journal of the American Society for Mass Spectrometry*, 32(3):772–785, 2021.

[27] Yue Liu, Congcong Ma, Gabriela Nováková, Ales Marek, and František Tureček. Charge-tagged nucleosides in the gas phase: Uv–vis action spectroscopy and structures of cytidine cations, dications, and cation radicals. *The Journal of Physical Chemistry A*, 125(28):6096–6108, 2021.

[28] Scott A Shaffer and František Tureček. Hydrogentrimethylammonium: A marginally stable hypervalent radical. *Journal of the American Chemical Society*, 116(19):8647–8653, 1994.

[29] Yang Liu, Joseph A Korn, Andy Dang, and František Tureček. Hydrogen-rich cation radicals of dna dinucleotides: Generation and structure elucidation by uv–vis action spectroscopy. *The Journal of Physical Chemistry B*, 122(42):9665–9680, 2018.

[30] Yang Liu, Joseph A Korn, and František Tureček. Uv-vis action spectroscopy and structures of hydrogen-rich 2'-deoxycytidine dinucleotide cation radicals. a difficult case. *International Journal of Mass Spectrometry*, 443:22–31, 2019.

[31] Yue Liu, Shu R Huang, and František Tureček. Guanine–adenine interactions in dna tetranucleotide cation radicals revealed by uv/vis photodissociation action spectroscopy and theory. *Physical Chemistry Chemical Physics*, 22(29):16831–16842, 2020.

[32] Yue Liu, Shu R. Huang, Břetislav Brož, Aleš Marek, and František Tureček. Tandem mass spectrometry and uv-vis action spectroscopy reveals the nucleobase stability toward radical-driven dissociations in dna codons. Number 305935, 2021.

[33] Jiahao Wan, Yue Liu, Břetislav Brož, Aleš Marek, and František Tureček. Tandem mass spectrometry and uv-vis action spectroscopy of dna codons: From cations to cation radicals. Number 309238, 2022.

[34] Robert Hodyss, Heather A Cox, and JL Beauchamp. Bioconjugates for tunable peptide fragmentation: free radical initiated peptide sequencing (frips). *Journal of the American Chemical Society*, 127(36):12436–12437, 2005.

[35] FW McLafferty and F Tureček. Interpretation of mass spectra. university science books. *Mill Valley, California*, 1993.

[36] John B Fenn. Electrospray wings for molecular elephants (nobel lecture). *Angewandte Chemie International Edition*, 42(33):3871–3894, 2003.

[37] John B Fenn, Matthias Mann, Chin Kai Meng, Shek Fu Wong, and Craig M Whitehouse. Electrospray ionization for mass spectrometry of large biomolecules. *Science*, 246(4926):64–71, 1989.

[38] Michael Przybylski and Michael O Glocker. Electrospray mass spectrometry of biomacromolecular complexes with noncovalent interactions—new analytical perspectives for supramolecular chemistry and molecular recognition processes. *Angewandte Chemie International Edition*, 35(8):806–826, 1996.

[39] Shibdas Banerjee and Shyamalava Mazumdar. Electrospray ionization mass spectrometry: a technique to access the information beyond the molecular weight of the analyte. *International journal of analytical chemistry*, 2012, 2012.

[40] Charles H Hocart. 9.10 mass spectrometry: An essential tool for trace identification and quantification. *Comprehensive Natural Products II*, pages 327–388, 2010.

[41] Fred W McLafferty. Tandem mass spectrometry. *Science*, 214(4518):280–287, 1981.

[42] Raymond E March. An introduction to quadrupole ion trap mass spectrometry. *Journal of mass spectrometry*, 32(4):351–369, 1997.

[43] NR Daly. Scintillation type mass spectrometer ion detector. *Review of Scientific Instruments*, 31(3):264–267, 1960.

[44] Jonathan Martens, Giel Berden, Christoph R Gebhardt, and Jos Oomens. Infrared ion spectroscopy in a modified quadrupole ion trap mass spectrometer at the felix free electron laser laboratory. *Review of Scientific Instruments*, 87(10):103108, 2016.

[45] Corey N Stedwell and Nicolas C Polfer. Spectroscopy and the electromagnetic spectrum. In *Laser Photodissociation and Spectroscopy of Mass-separated Biomolecular Ions*, pages 1–20. Springer, 2013.

[46] Jan Řezáč. Cuby: An integrative framework for computational chemistry, 2016.

[47] Filipp Furche and Reinhart Ahlrichs. Erratum:"time-dependent density functional methods for excited state properties"[j. chem. phys. 117, 7433 (2002)]. *The Journal of Chemical Physics*, 121(24):12772–12773, 2004.

[48] Mario Barbatti, Matthias Ruckenbauer, Felix Plasser, Jiri Pittner, Giovanni Granucci, Maurizio Persico, and Hans Lischka. Newton-x: a surface-hopping program for nonadiabatic molecular dynamics. *Wiley Interdisciplinary Reviews: Computational Molecular Science*, 4(1):26–33, 2014.

Chapter 2

CHARGE-TAGGED ADENOSINE RADICALS

Reproduced in part with permission from Yue Liu, Andy Dang, Jan Urban, and František Tureček. Charge-tagged dna radicals in the gas phase characterized by uv/vis photodissociation action spectroscopy. *Angewandte Chemie International Edition*, 59(20):7772-7777, 2020.

Abstract *Adenosine radicals tagged with a fixed-charge group were generated in the gas phase and structurally characterized by tandem mass spectrometry, deuterium labeling, and UV/Vis action spectroscopy. Experimental results in combination with Born–Oppenheimer molecular dynamics, ab initio, and excited-state calculations led to unambiguous assignment of adenosine radicals as N-7 hydrogen atom adducts. The charge-tagged radicals were found to be electronically equivalent to natural DNA nucleoside radicals.*

2.1 Introduction

Capture of secondary low-energy electrons by DNA is one of the major ionization processes leading to radical intermediates and triggering DNA damage. Previous studies using pulse radiolysis have revealed that electron adducts to nucleobases, nucleosides, and nucleotides underwent fast protonation by the solvent, forming neutral radicals as hydrogen atom adducts.[1–5] The sites of hydrogen atom addition have been investigated by electron paramagnetic resonance spectroscopy, which revealed that the reaction products strongly depend on the environment conditions, such as pH and the concentration of metal ions. In particular, radical intermediates from pulse radiolysis of adenine, adenosine, and adenosine monophosphate have been studied by fast UV/Vis absorption spectroscopy and found

to undergo consecutive reactions in solution and frozen glasses that complicated structure analysis.[6–8]

An alternative approach to hydrogen atom adducts to nucleobases relies on a process that is a reversal of the radiolysis sequence in the condensed phase while largely avoiding consecutive and side reactions. Gas-phase or electrospray protonation of the nucleobase is first used to produce a cation in which the protonation site is determined by the topical gas-phase or solution basicity of the nucleobase, and can be controlled by the ionization conditions. In the next step, the cations are discharged by collisions with a gaseous electron donor, forming radicals that are analyzed by tandem mass spectrometry.[9, 10] While this approach worked well for nucleobases, the more complex oligonucleotide cation radicals formed by electron transfer underwent fast isomerizations by proton or hydrogen atom migrations between the nucleobases.[11] To generate and characterize nucleoside radicals, which are the primary intermediates of relevance for the early stages of DNA damage, a different approach was needed.

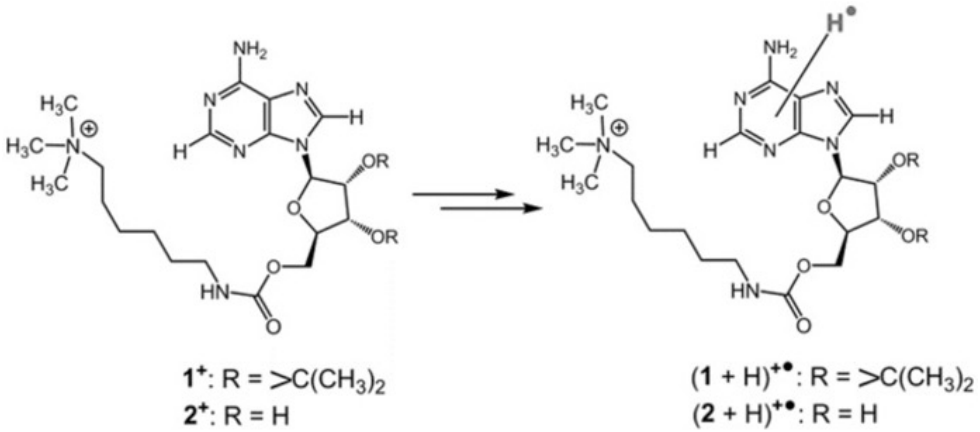

Figure 2.1: The schematic of quantum chemistry calculations used for interpretation of photodissociation action spectra.

We now report a new general approach to nucleoside radicals, as illustrated with adenosine, that circumvents the above-mentioned difficulties and allows spectroscopic investigations to be carried out. The nucleoside is furnished with a permanent-charge group forming a

charged conjugate (Figure 2.1). The conjugate is further charged by electrospray ionization, the doubly charged ion is selected by its m/z ratio and stored in a quadrupole ion trap. An ion-ion reaction with fluoranthene anion radical delivers the electron, reducing the dication into a cation radical which is again selected by its m/z and stored in the ion trap.

The cation radical is interrogated by UV/Vis photodissociation action spectroscopy,[12] which probes transitions in the valence-electron excitation region of 210–700 nm. By combining efficient ion preparation, selection, and manipulation in the ion trap with wavelength-resolved laser photodissociation, we achieve the first spectroscopic characterization of well-defined adenosine radicals. We also show that the charge-tagged radicals are electronically equivalent to natural DNA radicals, making this method suitable for generating and studying a variety of transient DNA intermediates.

2.2 Experimental Section

2.2.1 Synthetic Procedures of Adenosine Conjugates

Adenosine conjugates (6-Trimethylammoniumhexane-1-aminocarbonyl)-2',3'-isopropylidene-adenosine ion ($\mathbf{1}^+$) and 5'-(6-Trimethylammoniumhexane-1-aminocarbonyl)adenosine ion ($\mathbf{2}^+$) were synthesized as shown in Figure 2.2. 2',3'-Isopropylideneadenosine (26.5 mg, 0.086 mmol) was suspended in THF (1 mL) containing diisopropylethyl amine (33.4 mg, 0.258 mmol). To the solution was added p-nitrophenyl chloroformate (16.9 mg, 0.084 mmol) and the mixture was stirred for 6 h at room temperature. To the reaction mixture was added solid 6-aminohexyltrimethylammonium trifluoroacetate (27mg, 0.1 mmol) and the mixture was kept at r.t. for 4 days. The solvent was evaporated, the residue was reconstituted in acetonitrile-water and purified by liquid chromatography on a C18 column, using gradient elution with 5-90% CH_3CN-water mixture. Fractions containing **1** were combined and the product was characterized by electrospray ionization high resolution tandem mass spectrometry (Table 2.1) showing doubly charged (m/z 246.6524) and singly charged ions (m/z 492.2964) corresponding to the expected formula of $C_{23}H_{38}N_7O_5$.

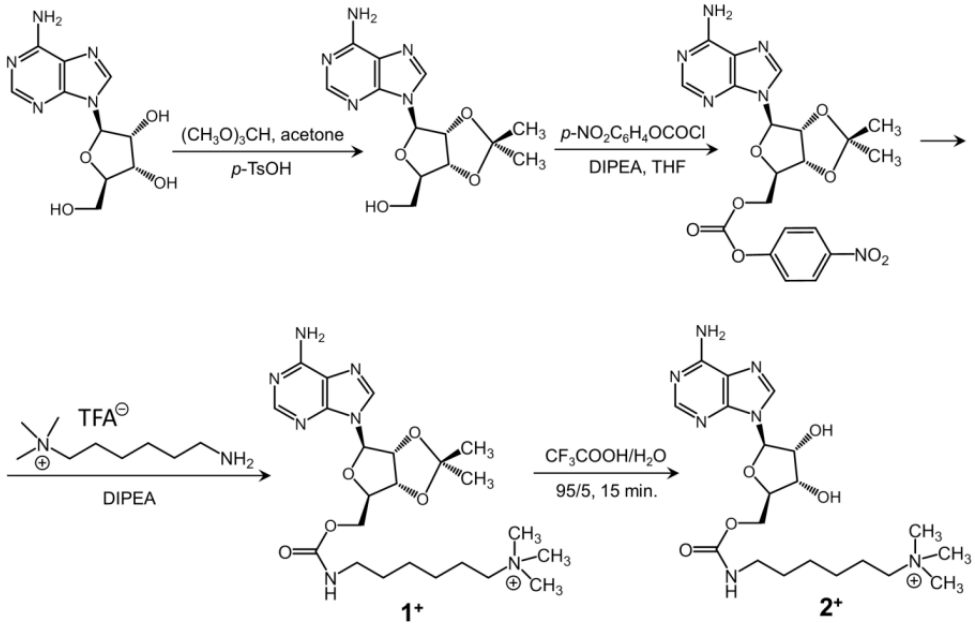

Figure 2.2: Synthetic route to adenosine conjugates.

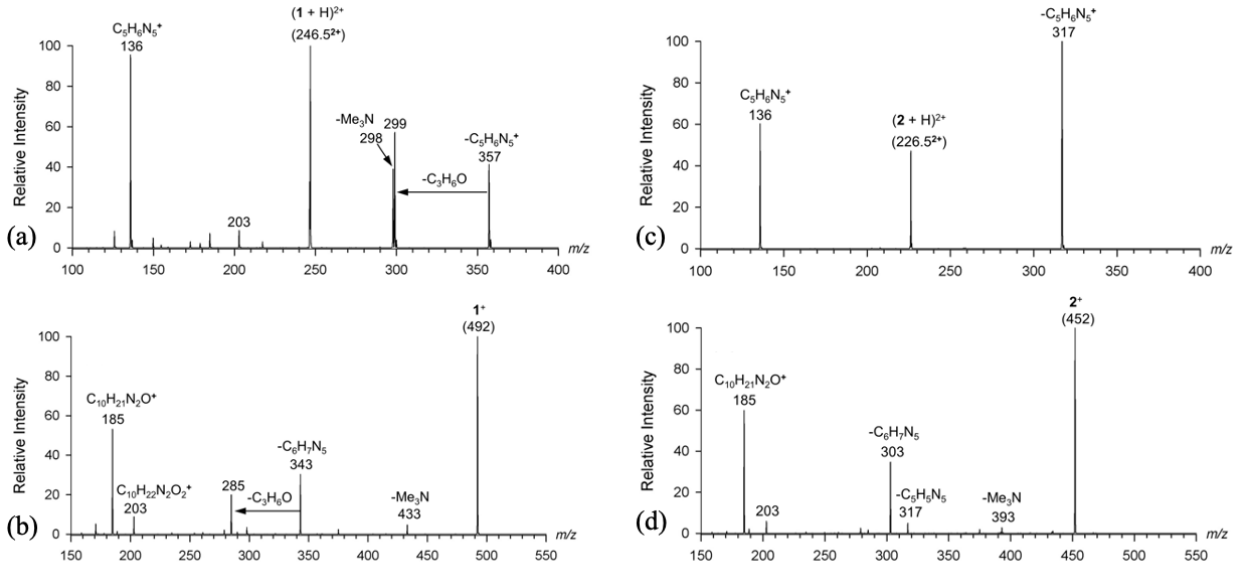

Figure 2.3: CID mass spectra of (a) doubly charged $(\mathbf{1}+\mathrm{H})^{2+}$ ion at m/z 246.5, (b) $\mathbf{1}^{+}$ at m/z 492. (c) doubly charged $(\mathbf{2}+\mathrm{H})^{2+}$ ion at m/z 226.5, (d) $\mathbf{2}^{+}$ at m/z 452.

Table 2.1: Accurate mass measurements of adenosine conjugates.

Ion m/z	Formula	Error (mmu)[a]	Neutral or ion fragment	Error(mmu)[a]
ESI of 2',3'-isopropylidene conjugate (**1**)				
492.2964	$C_{23}H_{38}N_7O_5$	4.6		
246.6524	$C_{23}H_{39}N_7O_5(2+)$	3.5		
357.2417	$C_{18}H_{33}N_2O_5$	3.3	$C_5H_6N_5^+$	1.3
136.0628	$C_5H_6N_5$	1.0		
CID of isopropylidene conjugate $\mathbf{1}^+$, m/z 492				
492.2964	$C_{23}H_{38}N_7O_5$	4.6		
343.2262	$C_{17}H_{31}N_2O_5$	3.5	$C_6H_7N_5$	1.1
285.1837	$C_{14}H_{25}N_2O_4$	2.8	C_3H_6O	0.6
203.1773	$C_{10}H_{23}N_2O_2$	1.9	$C_{13}H_{15}N_5O_3$	1.7
185.1666	$C_{10}H_{21}N_2O$	1.8	$C_{13}H_{17}N_5O_4$	1.7
ESI-CID of free adenosine conjugate (**2**)				
452.2651	$C_{20}H_{34}N_7O_5$	3.5		
226.6366	$C_{20}H_{35}N_7O_5(2+)$	4.3		
317.2101	$C_{15}H_{29}N_2O_5$	3.0	$C_5H_6N_5^+$	1.3
136.0628	$C_5H_6N_5$	1.0		
CID of free adenosine conjugate $\mathbf{2}^+$, m/z 452				
452.2655	$C_{20}H_{34}N_7O_5$	3.9		
303.1942	$C_{14}H_{27}N_2O_5$	2.7	$C_6H_7N_5$	1.1
185.1664	$C_{10}H_{21}N_2O$	1.6	$C_{10}H_{13}N_5O_4$	2.3

[a] Difference in millimass units from the theoretical value.

Adenosine conjugate **1** was characterized by high-resolution and collision-induced dissociation tandem mass spectrometry, CID-MS^2. The collision-induced dissociation (CID) spectrum of the doubly charged (m/z 246.65) $(\mathbf{1}+H)^{2+}$ ion showed the complementary $C_5H_6N_5^+$ and $C_{18}H_{33}N_2O_5$ fragments at m/z 136.0628 and 357.2417, respectively, the latter undergoing eliminations of acetone from the 2',3'-isopropylidene group and trimethylamine from the charged tag (Figure 2.3a).

These dissociations indicated that the fixed charged group was attached to the ribose 5'-position and not to the adenine group. Interestingly, the CID mass spectrum of the singly charged ion $\mathbf{1}^+$ (Figure 2.3b) showed a fragment ion at m/z 343 that according to accurate

mass measurements (Table 2.1) corresponded to a loss of a neutral $C_6H_7N_5$ molecule. This unexpected dissociation indicated an intramolecular methyl transfer from the trimethylammonium group onto the adenine ring. Note that this dissociation is much less represented (m/z 150) in the spectrum of the $(\mathbf{1}+H)^{2+}$ ion, probably because of Coulomb repulsion of the charged moieties.

A 1-mL aliquot of CH_3CN solution of 1 from the HPLC separation was evaporated to dryness and the residue was reconstituted in 1 mL of 95/5 CF_3COOH/water. After vortexing for 15 min at room temperature the solvents were evaporated, the residue was dissolved in 50/50/1 acetonitrile/water/acetic acid and analyzed by electrospray ionization high resolution tandem mass spectrometry (Table 2.1). The collision-induced dissociation (CID) spectrum of the doubly charged (m/z 226.5) ion showed the complementary $C_5H_6N_5^+$ and $C_{15}H_{29}N_2O_5$ fragments at m/z 136.0628 and 317.2101, respectively (Figure 2.3c). The CID spectrum of the singly charged ion $\mathbf{2}^+$ (Figure 2.3d) again showed a loss of $C_6H_7N_5$ (m/z 303) that was accompanied by loss of $C_5H_5N_5$ (m/z 317) and formation of the trimethylammoniumhexaneisocyanate fragment ion from the charge tag (m/z 185).

2.2.2 Methods

Action spectroscopy measurements were performed on a modified Bruker amaZon (Bruker Daltonik, Bremen, Germany) ion trap mass spectrometer equipped with an auxiliary ion source for electron transfer dissociation (ETD) and coupled to a Nd-YAG laser/OPO laser system.[13] The adenosine conjugates and 2,3:11,12-dibenzo-18-crown-6-ether (DBCE) in a 1:1 molar ratio were dissolved in 50:50:1 acetonitrile-water acetic acid at 10-20 micromolar concentrations and electrosprayed into the ion trap. The doubly charged ions, $(\mathbf{1}+H+DBCE)^{2+}$ or $(\mathbf{2}+H+DBCE)^{2+}$ were selected by mass, m/z 426.5 and m/z 406.5, respectively, and subjected to one-electron reduction by ion-ion reactions with fluoranthene anion radicals at 150 ms reaction time. The resulting cation radicals, m/z 493 and m/z 453 for $(\mathbf{1}+H)^{+\bullet}$ and $(\mathbf{2}+H)^{+\bullet}$, respectively, were again selected by mass in the ion trap and probed by laser photodissociation. The laser beam was provided by an EKSPLA NL301G Nd-YAG laser (Altos

Photonics, Bozeman, MT, USA) working at 20 Hz frequency and 3- to 6-ns pulse width. The photon pulses were treated by a PG142C unit (AltosPhotonics, Bozeman, MT, USA) which incorporated a third harmonic generator and optical parametric oscillator coupled with an optional second harmonic generator to enable wavelength tuning in the range of 210-700 nm. The laser beam (6-mm diameter) exiting the PG142C unit was aligned and focused into the ion trap. The laser pulse energies were S14 measured at each experimental wavelength using an EnergyMax-USB J-10MB energy sensor (Coherent Inc., Santa Clara, CA, USA) to calibrate the action spectra. The measured photofragment ion intensities were normalized to the number of photons per pulse.

2.2.3 Calculations

Calculations were performed according to the multistep protocol that had been previously developed for peptide and DNA conformational and structure analysis[14]. Briefly, in the first step, 6-10 conformers were constructed for each cation-radical protomer where the additional hydrogen atom was placed at the adenine N-1, C-2, N-3, N-7, C-8, and the NH_2 group. Conformation search of the cation-radical structures was performed by Born-Oppenheimer molecular dynamics calculations (BOMD) using the Berendsen thermostat algorithm[15] at 310 K. BOMD trajectories were run for 20 ps with 1 fs steps using the all-valence-electron semiempririal PM6-D3H4 method[16] that includes corrections for hydrogen bond and dispersion energies. These calculations were run by MOPAC[17] under the Cuby4 platform.[18] This generated 20000 snapshots from each trajectory from which 200 $\times$ n (n = number of trajectories) structures were selected at regular intervals and gradient-optimized with PM6-D3H4. The optimized structures for each protomer were ranked by energy and the sets were compacted by removing duplicates. The structures were then grouped according to their secondary and supersecondary structural similarities using a home-written code[14].

Gradient optimization of this second selection structures was carried out with the B3LYP hybrid density functional[19] in the spin-unrestricted format and the 6-31+G(d,p) basis set. This provided several structures for each protomer that were characterized by harmonic

frequency calculations as local energy minima. B3LYP structures within 40 kJ mol^{-1} of each protomer group energy minimum were then reoptimized with ωB97X-D[20] and M06-2X[21] methods using the 6-31+G(d, p) basis set including harmonic vibrational analysis. These standard density functional theory (DFT) calculations were run with the Gaussian 16 program suite (Revision A01)[22].

We selected the B3LYP/6-31+G(d,p) harmonic frequencies, scaled by 0.975, to evaluate the zero-point energies and vibrational enthalpy and entropy terms. This was guided by the known reliability of scaled B3LYP/6-31+G(d,p) harmonic frequencies to provide a good match with frequencies measured in infrared action spectra in the gas phase[23]. Additionally, Gaussian frequency calculations with B3LYP were found on average 2.3 times faster than those with M06-2X, and so B3LYP was more economical for handling large numbers of isomers. The B3LYP and M06-2X frequency sets, when expressed by zero-point vibrational energies (ZPVE) for 23 cation-radicals and transition states, closely correlated, ZPVE(M06-2X) = 1.013476 $\times$ ZPVE(B3LYP), with a correlation coefficient $r^2 = 0.999999$ and standard error of slope at 0.000234.

For single-point energy calculations we used the M06-2X/6-31+G(d,p) optimized geometries. This is natural for M06-2X/6-311++G(2d, p) single-point energy calculations, where triple-zeta quality basis sets improve accuracy and were used by Zhao and Truhlar to benchmark the density functional[21]. We also used the M06-2X/6-31+G(d,p) geometries for CCSD(T) single-point calculations. This was based on benchmarking CCSD(T)/aug-cc-pVDZ single-point energies for geometries of adenine cation radicals obtained with CCSD, MP2(FULL), and M06-2X optimizations, all with the 6-31+G(d,p) basis set. The CCSD(T)/aug-cc-pVDZ//M06-2X/6-31+G(d,p) energies showed the best match (+1.5 millihartree) with the CCSD(T)/aug-cc-pVDZ//CCSD/6-31+G(d,p) energies, and so we used M06-2X geometries for calculations of the adenosine radicals (33 atoms) and adenosine conjugate cation radicals (67 atoms) where CCSD optimizations were prohibitively expensive. Optimized geometries were also obtained with Møller-Plesset calculations,[24] MP2(FULL)/6-31+G(d,p). The DFT and MP2 geometry optimizations gave very similar structures for the

individual tautomers and similar rankings of relative energies.

For energy benchmarking, single point energies were obtained with coupled - clusters calculations[25] with single, double, and disconnected triple excitations, CCSD(T)[26] with the aug-cc-pVDZ basis set. Basis set extension relied on MP2 calculations with the aug-cc-pVTZ and aug-cc-pVQZ correlation-consistent basis sets.[27] Hartree-Fock (HF) and MP2 single-point energies were used to estimate the complete basis set limits of correlation energy by fitting with a least squares the formula, $E_{corr}(HF) = a + be^{-cX}$, where where X = 2-4 is the ζ split in the aug-cc-pVXZ basis set.[28] This fit was used because it was found to be tighter than the usual X^{-3} dependence[28]. Coefficients a, b, and c are given in Table 2.2. Energies extrapolated to the complete basis set (CBS) limit were calculated according to the formula: E[CCSD(T)/CBS] = E[HF/aug-cc-pVQZ] + E_{corr}(HF, X$\rightarrow \infty$) + E[CCSD(T)/aug-cc-pVDZ] – E[MP2/aug-cc-pVDZ]. Spin projection[29, 30] was used to annihilate higher spin states in UHF and UMP2 calculations (PMP2).

Table 2.2: Correlation energy fits for adenosine radicals.

Radical[a]	a(UHF)[b,c]	a(RHF)[b,c]	b(UHF)[c]	b(RHF)[c]	c(UHF)[c]	c(RHF)[c]
3a$^\bullet$	–3.93959	–3.93769	7.81908	7.81847	1.06869	1.06868
3b$^\bullet$	–3.90291	–3.89903	7.84269	7.84209	1.07109	1.07108
3c$^\bullet$	–3.92413	–3.92126	7.83007	7.82948	1.06978	1.06977
3d$^\bullet$	–3.94124	–3.94006	7.82806	7.82400	1.06904	1.06900
3e$^\bullet$	–3.91039	–3.90732	7.83821	7.83842	1.07041	1.07044
TS(3a)	–3.94084	–3.93883	7.81778	7.81814	1.06964	1.06971
TS(3c)	–3.93634	–3.93402	7.79011	7.79062	1.06798	1.06805
TS(3d)	–3.93977	–3.93791	7.78027	7.80223	1.06847	1.06847

[a] For optimized adenosine radical structures see Figure 2.13. [b] MP2 correlation energies in hartrees extrapolated to the complete basis set limit via aug-cc-pVXZ basis sets, X = 3-5. [c] Least-squares fits to the equation: $E_{corrr} = a + be^{-cX}$, where X is the ζ split level in the aug-cc-pVXZ basis set.

Based on previous benchmarks,[31] we selected UM06-2X/6-31+G(d,p) TD-DFT for calculations of an extensive set of vertical and vibronic transitions in the cation radicals. Ver-

tical excitations were calculated for 45-50 excited states to probe transitions within the experimentally studied region of 210-700 nm. To calculate vibronic excitations, we used 300 Boltzmann-ranked ground-state configurations that were generated by the Newton X program[32] from the B3LYP/6-31+G(d,p) calculated harmonic normal modes of each cation radical at 310 K and submitted for TD-DFT calculations. The number of excited states in these vibronic TD-DFT calculations (18-23) was chosen to include excitations with wavelengths down to below 250 nm, covering a large part of the experimental wavelength range of 210-700 nm.

Transition states for hydrogen loss were located by stepwise B3LYP, M06-2X and ωB97X-D calculations to map the potential energy surface along the reaction coordinate. The TS were characterized by harmonic frequency analysis as having one imaginary frequency and further corroborated by intrinsic reaction coordinate calculations[33]. Transition-state theory calculations of unimolecular rate constants used the standard formulas with M06-2X/6-311++G(2d,p) TS energies and partition functions from B3LYP frequency analysis.

2.3 Results and Discussion

2.3.1 Cation Radical Formation

Adenosine conjugates $\mathbf{1}^+$ and $\mathbf{2}^+$ were synthesized and characterized as described in subsection 2.2.1. We found that electron transfer to doubly charged $(\mathbf{2}+\mathrm{H})^{2+}$ (m/z 226.5) resulted in a near complete dissociation (Figure 2.4a) by loss of a H atom from the reduced adenine ring (m/z 452) and loss of a CH_3 group (m/z 438) and trimethylamine (m/z 394) from the reduced side-chain. To generate a stable cation radical $(\mathbf{2}+\mathrm{H})^{+\bullet}$ for action spectroscopy, we resorted to a previously developed technique11 that relies on electron-transfer dissociation (ETD)[34] of non-covalent complexes with crown ethers, such as 2,3:11,12-dibenzo-18-crown-6-ether (DBCE). The doubly charged complex, $(\mathbf{2}+\mathrm{H}+\mathrm{DBCE})^{2+}$, m/z 406.5, was formed readily by electrospray ionization and furnished abundant cation radicals $(\mathbf{2}+\mathrm{H})^{+\bullet}$ (m/z 453) by reduction and loss of DBCE upon ETD (Figure 2.4b). The minor fragment ions

by loss of CH_3 from $(\mathbf{2}+H)^{+\bullet}$ (m/z 438) and loss of $(CH_3)_3N$ from the DBCE complex (m/z 754) were representative of reduction of the fixed charged trimethylammonium group followed by fast dissociation of the hypervalent trimethylammonium radicals.[35] Thus, the surviving $(\mathbf{2}+H)^{+\bullet}$ cation radical can be unequivocally assigned to an adenine radical in the form of a hydrogen atom adduct. Quite analogous results were obtained for $(\mathbf{1}+H)^{+\bullet}$ (m/z 493, Figure 2.4c,d), illustrating the similarity of radicals formed by electron transfer to both dications.

The cation-radicals were characterized by CID-MS^3 (Figure 2.5). Upon mild excitation in the ion trap, $(\mathbf{2}+H)^{+\bullet}$ underwent a loss of an H atom as the sole fragmentation. Upon increasing the excitation amplitude, the $(\mathbf{2}+H)^{+\bullet}$ ion underwent further dissociation, forming fragment ions that were identical to those in the CID spectrum of $\mathbf{2}^+$ (Figure 2.5a, Figure 2.3d).The dissociations of $\mathbf{2}^+$ and $(\mathbf{2}+H)^{+\bullet}$ were further investigated by deuterium labeling of the six exchangeable protons in $(\mathbf{2}\text{-}D_5+D+DBCE)^{2+}$ (m/z 409.5, Figure 2.6 a). The CID-MS^3 spectrum of $(\mathbf{2}\text{-}D_5+D)^{+\bullet}$ (m/z 459, Figure 2.5 b) revealed >99 % selective loss of D. The absence of loss of a light H atom indicated that the OD, ND_2, and ND protons in $(\mathbf{2}\text{-}D_5+D)^{+\bullet}$ did not mix with the other adenosine hydrogen atoms, namely, with the ring C-2-H and C-8-H. The results for $(\mathbf{1}\text{-}D_3+D)^{+\bullet}$ were quite analogous, showing an exclusive loss of D from the N-D tagged positions upon CID of the cation radical (Figure 2.6c,d).

2.3.2 Action Spectra and Dissociation Kinetics

Photodissociation of $(\mathbf{1}+H)^{+\bullet}$ and $(\mathbf{2}+H)^{+\bullet}$ across the 210–700 nm wavelength region resulted in the loss of H as a major channel (Figure 2.7).

This presented a complication, because loss of H also occurred spontaneously upon storing the cation radicals in the ion trap. Time-dependent measurements, using $(\mathbf{1}+H)^{+\bullet}$ and $(\mathbf{2}+H)^{+\bullet}$ that were thermalized in the ion trap for 150 ms, provided a single-exponential decay curves (Figure 2.8), from which we obtained the respective unimolecular rate constants for the spontaneous, thermally driven, loss of H as k_{H-diss} =0.61 and 0.56 s^{-1}. Although we did not directly measure the stored ion temperature, previous studies estimated the tem-

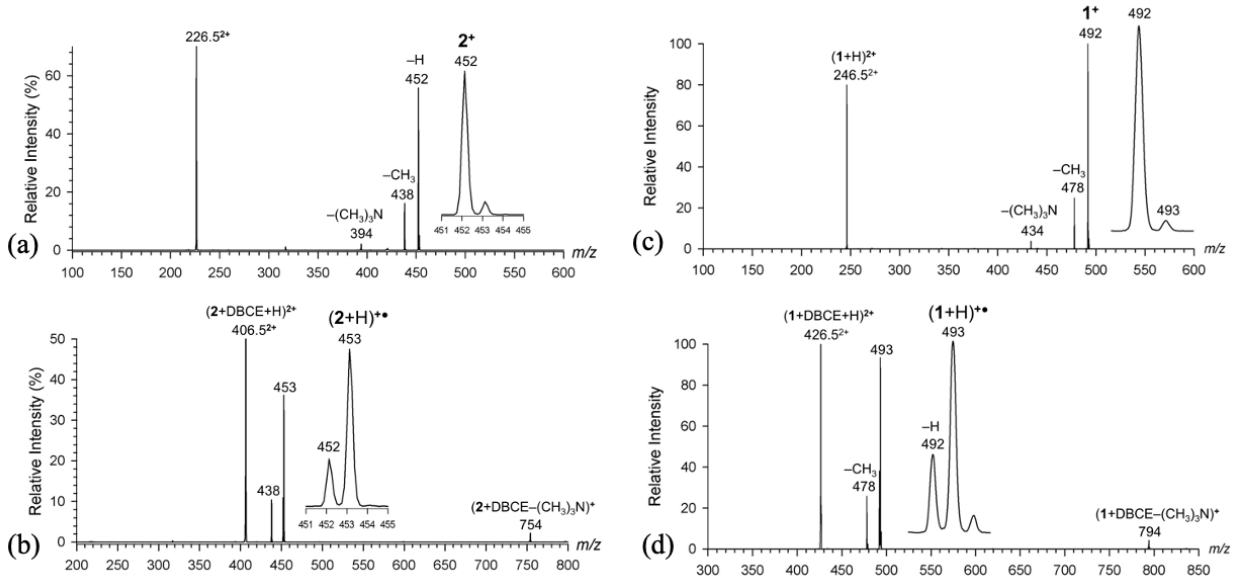

Figure 2.4: Electron-transfer dissociation mass spectra of (a) $(\mathbf{2}+\mathrm{H})^{2+}$ (m/z 226.5), (b) $(\mathbf{2}+\mathrm{H}+\mathrm{DBCE})^{2+}$ (m/z 406.5), (c) $(\mathbf{1}+\mathrm{H})^{2+}$ (m/z 246.5), and (d) $(\mathbf{1}+\mathrm{H}+\mathrm{DBCE})^{2+}$ (m/z 426.5).

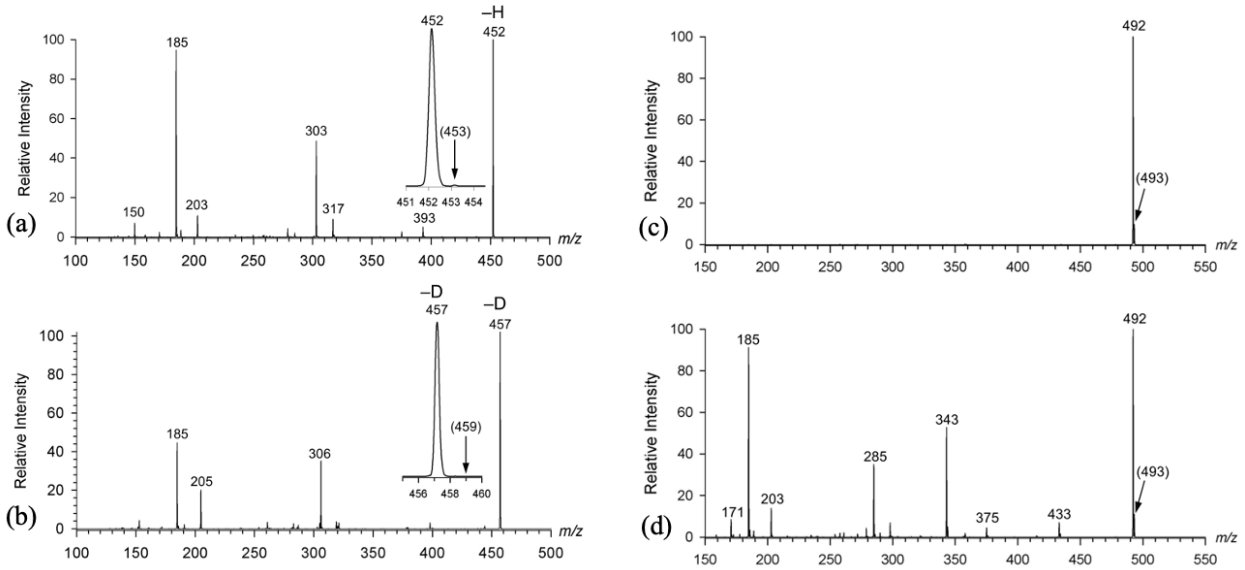

Figure 2.5: CID-MS^3 spectra of (a) $(\mathbf{2}+\mathrm{H})^{+\bullet}$ (m/z 453), (b) $(\mathbf{2}\text{-}\mathrm{D}_5+\mathrm{D})^{+\bullet}$ (m/z 459), (c) $(\mathbf{1}+\mathrm{H})^{+\bullet}$ (m/z 493) low excitation, (d) $(\mathbf{1}+\mathrm{H})^{+\bullet}$ (m/z 493) high excitation.

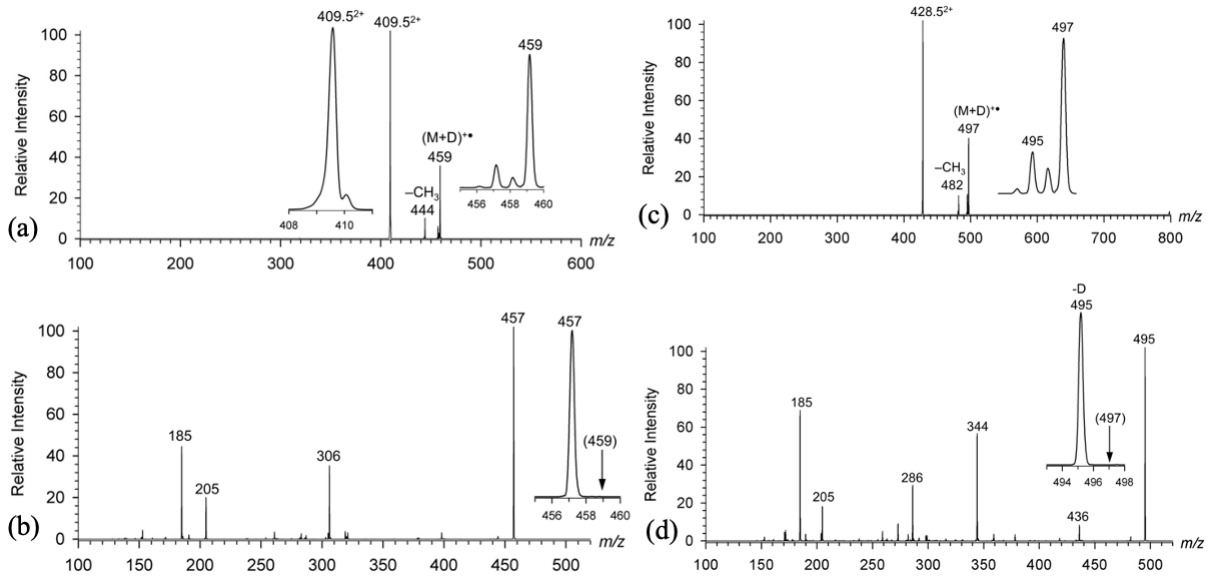

Figure 2.6: (a) ETD-MS^2 spectrum of the (**2**-D_5+D+DBCE)$^{2+}$ complex at m/z 409.5. (b) ETD-CID-MS^3 spectrum of (**2**-D_5+D)$^{+\bullet}$ at m/z 459. (c) ETD-MS^2 spectrum of the (**1**-D_3+D+DBCE)$^{2+}$ complex at m/z 428.5. (d) ETD-CID-MS^3 spectrum of (**1**-D_3+D)$^{+\bullet}$ at m/z 497. Inset shows the loss of D.

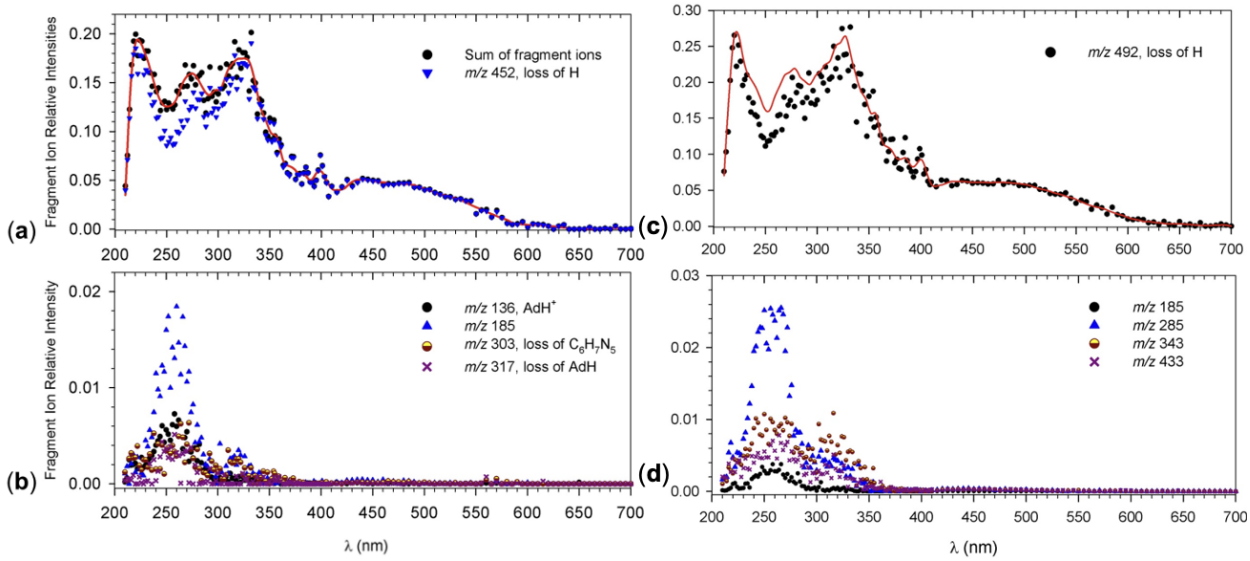

Figure 2.7: UVPD action spectra of (**2**+H)$^{+\bullet}$. (a) The major photodissociation channel by loss of H at m/z 452. (b) Minor photodissociation channels. For fragment ion assignments see Table 2.1. UVPD action spectra of (**1**+H)$^{+\bullet}$. (c) The major photodissociation H-loss channel at m/z 492. (d) Minor photodissociation channels. For fragment ion assignments see Figure 2.3b.

perature of trapped ions in the range of 295–350 K.[36–39] The knowledge of the spontaneous dissociation kinetics allowed us to make background corrections in the UVPD spectra that were obtained on a 100 ms time scale.

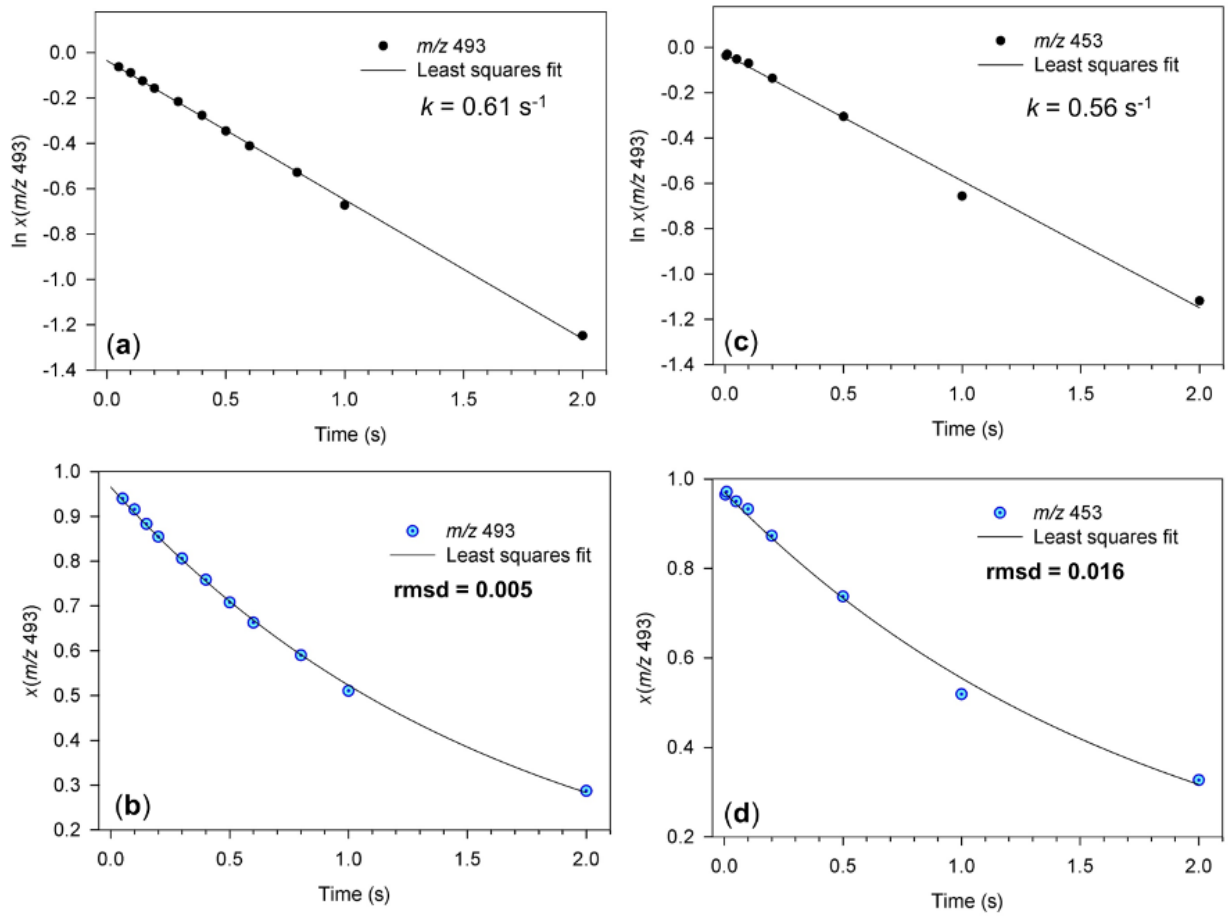

Figure 2.8: Time-dependent spontaneous dissociation by H loss from (a) and (b) $(\mathbf{1}+H)^{+\bullet}$, and (c) and (d) $(\mathbf{2}+H)^{+\bullet}$.

The UVPD action spectra of $(\mathbf{1}+H)^{+\bullet}$ (Figure 2.7c,d) and $(\mathbf{2}+H)^{+\bullet}$ were similar, consisting of four absorption bands. These are illustrated with the spectrum of $(\mathbf{2}+H)^{+\bullet}$ that displayed maxima at 220, 275, and 325 nm and a broad band stretching from 410 to 600 nm (Figure 2.7 a). Minor channels, chiefly due to secondary dissociations of the m/z 492 primary fragment ion, formed the bands peaking at 260 and 320 nm (Figure 2.7b). The

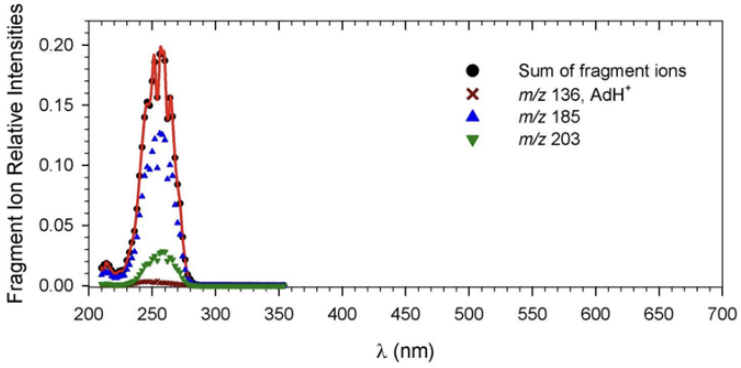

Figure 2.9: UVPD action spectrum of ion $\mathbf{1}^+$.

action spectra of the radicals were quite different from the spectrum of the closed-shell ion $\mathbf{1}^+$ (Figure 2.9). The action spectrum of $(\mathbf{2}{+}\mathrm{H})^{+\bullet}$ was analogous to the transient absorption spectra of adenine derivatives reported by Candeias and Steenken[6] that were taken after irradiation in solution. In particular, the absorption spectrum taken 2 μs after irradiation, that was assigned to an N-protonated adenine radical, showed bands at 315 and 550 nm that were analogous to the 325 and 500 nm bands in the action spectrum. The solution spectrum was found to change with time to develop new bands at 355 and 460 nm that were assigned to a C-8 hydrogen atom adduct.6 In contrast, a strong 355-nm band was not observed in the action spectra of gas-phase $(\mathbf{1}{+}\mathrm{H})^{+\bullet}$ and $(\mathbf{2}{+}\mathrm{H})^{+\bullet}$.

2.3.3 Adenine Conjugate Radicals and UVPD Spectra Interpretation

To interpret the UVPD spectra and assign structures, we undertook an extensive computational study of adenosine radicals, cation-radical conjugates and their dication precursors. Theoretical absorption spectra were obtained by time-dependent density functional theory (TD-DFT) M06-2X/6-31+G(d,p) calculations for the lowest 45 excited states. For 25 excited states, we calculated vibronic transitions from 300 vibrational states populated at 310 K. This covered the wavelength region down to 201–251 nm. Previous benchmark studies established M06-2X/6-31+G(d,p) TD-DFT calculations as giving an excellent match be-

tween the calculated and experimental UV/Vis spectra of nucleobase and nucleoside cation radicals.[31]

Low-energy conformers of protomeric adenosine radical conjugates corresponding to H-atom adducts to N-1 ($2\,a^{+\bullet}$), C-2 ($2\,b^{+\bullet}$), N-3 ($2\,c^{+\bullet}$), N-7 ($2\,d^{+\bullet}$) and C-8 ($2\,e^{+\bullet}$) positions in adenine were obtained by a combination of Born–Oppenheimer molecular dynamics for conformational analysis, DFT geometry optimization, and frequency analysis (Figure 2.10). Computational details are given in subsection 2.2.3. The relative energies were calculated at several levels of DFT and ab initio theory (Table 2.3); the M06-2X/6-311++G(2d,p) energies are discussed in text. The calculations identified the C-8-H adduct $2\,e^{+\bullet}$ as the global energy minimum, in agreement with previous calculations of H-atom adducts to adenine.[9, 40, 41] However, as indicated by the above-described deuterium-labeling experiments, neither $2\,e^{+\bullet}$ nor the second lowest energy C-2-H adduct ($2\,b^{+\bullet}$) were formed in the gas phase. Among the N-H adducts, the N-1-H ($2\,a^{+\bullet}$), N-3-H ($2\,c^{+\bullet}$), and N-7-H ($2\,d^{+\bullet}$) isomers showed very similar relative free energies (Table 2.3), indicating no particular thermodynamic preference for either form. We note that the use of M06-2X relative energies was corroborated by a parallel study of H-atom adducts to adenosine for which we obtained benchmark CCSD(T) energies extrapolated to the complete basis set (Table 2.3). The adenosine radical data pointed to an excellent match between the M06-2X/6-311++G(2d,p) and CCSD(T)/CBS relative energies with the root-mean-square and maximum deviations of 3.3 and 6.0 kJ mol^{-1}, respectively.

The calculated vibronic spectra of $2\,a^{+\bullet}$, $2b^{+\bullet}$, $2\,c^{+\bullet}$, $2\,d^{+\bullet}$ and $2e^{+\bullet}$ are shown in Figure 2.11. The N-1-H adduct $2\,a^{+\bullet}$ showed a broad featureless band resulting from multiple excitations in the 244–692 nm range. In addition, the spectrum showed a strong transition at 204 nm that was outside the range for vibronic analysis but was expected to give rise to a strong narrow band at ca. 210 nm. The N-3-H adduct $2\,c^{+\bullet}$ showed two major bands with maxima at 300 and 400 nm along with broad bands at 440 and 500 nm. The N-7-H adduct $2\,d^{+\bullet}$ showed two major bands with maxima at 240 and 310 nm along with a broad band peaking at 480 nm and extending to above 600 nm . The C-2-H adduct $2\,b^{+\bullet}$ displayed a

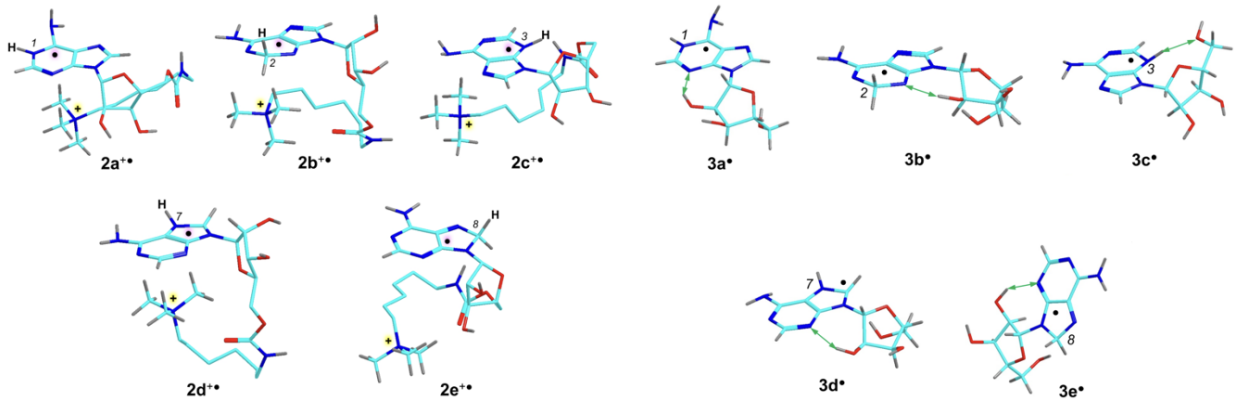

Figure 2.10: M06-2X/6-31+G(d,p) optimized geometries of cation radical conjugates $2a^{+\bullet}$-$2e^{+\bullet}$ and adenosine radicals $3a^{\bullet}$-$3e^{\bullet}$. Atom color coding is as follows: cyan = C, blue = N, red = O, gray = H. The ribose and side-chain C-H hydrogens are not shown for $2a^{+\bullet}$-$2e^{+\bullet}$. Green arrows indicate hydrogen bonds.

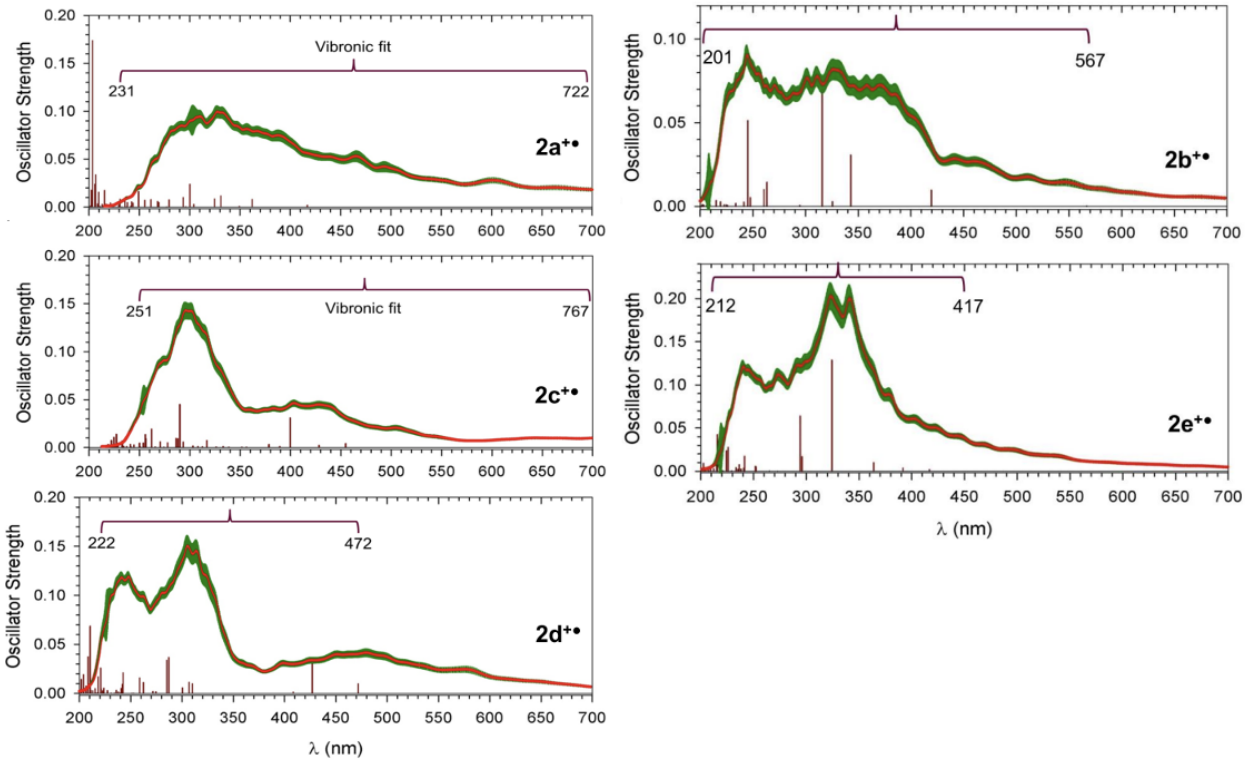

Figure 2.11: M06-2X/6-31+G(d,p) TD-DFT vibronic spectra of $2a^{+\bullet}$, $2b^{+\bullet}$, $2c^{+\bullet}$, $2d^{+\bullet}$ and $2e^{+\bullet}$ plotted to match the experimental wavelength range. The green bars represent the oscillator strength error in vibronic transitions. The brackets show the wavelength range of TD-DFT excitations (red vertical bars) used for vibronic calculations

Table 2.3: Relative energies of adenosine cation-radical conjugates.

Species/reaction	Relative energy[a,b]		
	M06-2X[c] 6-311++G(2d,p)	ωB97X-D 6-31+G(d,p)	PMP2[d] 6-311++G(2d,p)
$2a^{+\bullet}$	11 (5.5)	12	–0.3
$2b^{+\bullet}$	–21 (–20)	–24	–22
$2c^{+\bullet}$	–7.7 (–3.7)	–9.6	–11
$2d^{+\bullet}$	0 (0)	0	0
$2e^{+\bullet}$	–47 (–48)	–52	–47
$2d^{+\bullet} \rightarrow \mathbf{2}^{+} + H^{\bullet}$	67 (42)	81	27
$2a^{+\bullet} \rightarrow$ syn-TS2a	81	100	82
$2a^{+\bullet} \rightarrow$ anti-TS2a	98	109	85
$2b^{+\bullet} \rightarrow$ syn-TS2b	120	138	101
$2b^{+\bullet} \rightarrow$ anti-TS2b	120	137	95
$2c^{+\bullet} \rightarrow$ syn-TS2c	120	138	125
$2c^{+\bullet} \rightarrow$ anti-TS2c	121	142	107
$2d^{+\bullet} \rightarrow$ syn-TS2d	95	109	88
$2d^{+\bullet} \rightarrow$ anti-TS2d	106	117	90
$2e^{+\bullet} \rightarrow$ syn-TS2e	141	161	125
$2e^{+\bullet} \rightarrow$ anti-TS2e	142	161	120

[a] In $kJ\,mol^{-1}$. [b] Including B3LYP/6-31+G(d,p) zero-point energies scaled by 0.975 and referring to 0 K unless stated otherwise. [c] Relative free energies at 310 K in parentheses. [d] From spin-projected MP2/6-311++G(2d,p) calculations

spectrum consisting of a band composed of vibronically broadened transitions in the 201–567 nm range that was substantially different from the spectrum of the C-8-H adduct $2\,e^{+\bullet}$, which showed prominent bands with maxima at 240, 320, and 340 nm. The calculated spectra of $2\,b^{+\bullet}$, $2\,d^{+\bullet}$, and $2\,e^{+\bullet}$ displayed bands that were apparent in the action spectrum of $(\mathbf{2}{+}H)^{+\bullet}$ (Figure 2.7a), with the closest match for $2\,d^{+\bullet}$. In addition, the sharp band at 220 nm in the action spectrum (Figure 2.7a) was represented by the intense transitions at 208 and 210 nm in the TD-DFT spectrum of $2\,d^{+\bullet}$. Considering that $2\,b^{+\bullet}$ and $2\,e^{+\bullet}$ were excluded on the basis of deuterium labeling, the action spectrum can be unambiguously assigned to the

N-7-H adduct 2 $d^{+\bullet}$ as the dominant component. Because the absorption bands of thermal ions are broad, we cannot exclude the presence of very minor amounts of the 2 $a^{+\bullet}$ and 2 $c^{+\bullet}$ whose bands, if present, would be obscured by those from the dominant isomer 2 $d^{+\bullet}$.

2.3.4 Comparison with Natural Adenosine Radicals

The adenosine cation-radical conjugates under study had a fixed-charge group that is absent in natural adenosine radicals, and so we investigated the effect of the fixed charge on the radical equilibrium geometries, electronic structure, and excited states. Cation radicals $2a^{+\bullet}$, $2b^{+\bullet}$, $2c^{+\bullet}$, and $2d^{+\bullet}$ favored conformations in which the charged trimethylammonium group was stacked underneath the purine ring (Figure 2.10). The proximate methyl and methylene hydrogen atoms were within their combined van der Waals radii distance from the adenine ring C and N atoms, e.g., N-3 and C-6 in 2 $a^{+\bullet}$, N-1 and C-2 in 2 $b^{+\bullet}$, NH2 in 2 $c^{+\bullet}$, and C-2 and N-7 in 2 $d^{+\bullet}$ (Figure 2.10). This attractive intramolecular interaction replaced hydrogen bonding of the 2' and 5'-hydroxyls to the purine nitrogen atoms that was prominent in low-energy conformers of adenosine radicals 3 $a^{\bullet}$ –3 $e^{\bullet}$ (Figure 2.10). However, the different conformations of 2 $a^{+\bullet}$ –2 $e^{+\bullet}$ and 3 $a^{\bullet}$ –3 $e^{\bullet}$ had only a minor effect on the electronic structure and excited states. The ground electronic states in all these radicals and cation radicals had the unpaired electron in the singly-occupied molecular orbitals (SOMO) of the π_z type that were delocalized over the purine ring, as illustrated with 2 $d^{+\bullet}$ and 3 $d^{\bullet}$ (Figure 2.12) in which the SOMO π_z orbitals showed the same nodality. The first excited states (A) in both 2 $d^{+\bullet}$ (ΔE_{exc}=2.63 eV) and 3 $d^{\bullet}$ (ΔE_{exc}=2.74 eV) involved electron promotion to a combination of virtual π_z^* orbitals of very similar nodality. A minor difference in the ordering of excited states concerned the weak transition to the C state in 2 $d^{+\bullet}$ (ΔE_{exc}=3.03 eV) that appeared as the B state in 3 $d^{\bullet}$ (ΔE_{exc}=2.83 eV. In each case, these states contained substantial components of Rydberg orbitals (Figure 2.12). The intense transitions at ΔE_{exc}=2.90 eV (B state in 2 $d^{+\bullet}$) and ΔE_{exc}=2.96 eV (C state in 3 $d^{\bullet}$) (Figure 2.13g,h) as well as the G (2 $d^{+\bullet}$) and F (3 $d^{\bullet}$) states involved virtual π_z^* orbitals of very similar nodality for the cation radical and adenosine radical. Very similar assignment of excited states was made for 2 $a^{+\bullet}$ and 3 $a^{\bullet}$

(Figure 2.131,b), $2\,b^{+\bullet}$ and $3\,b^{\bullet}$ (Figure 2.13c,d), and $2\,e^{+\bullet}$ and $3\,e^{\bullet}$ (Figure 2.13i,j). The N-3-H adducts $2\,c^{+\bullet}$ and $3\,c^{\bullet}$ were exceptional in that the spectrum of the latter showed transitions to Rydberg states at 2.19, 2.44, and 2.61 eV that had no equivalents in the spectrum of $2\,c^{+\bullet}$ (Figure 2.13e,f).

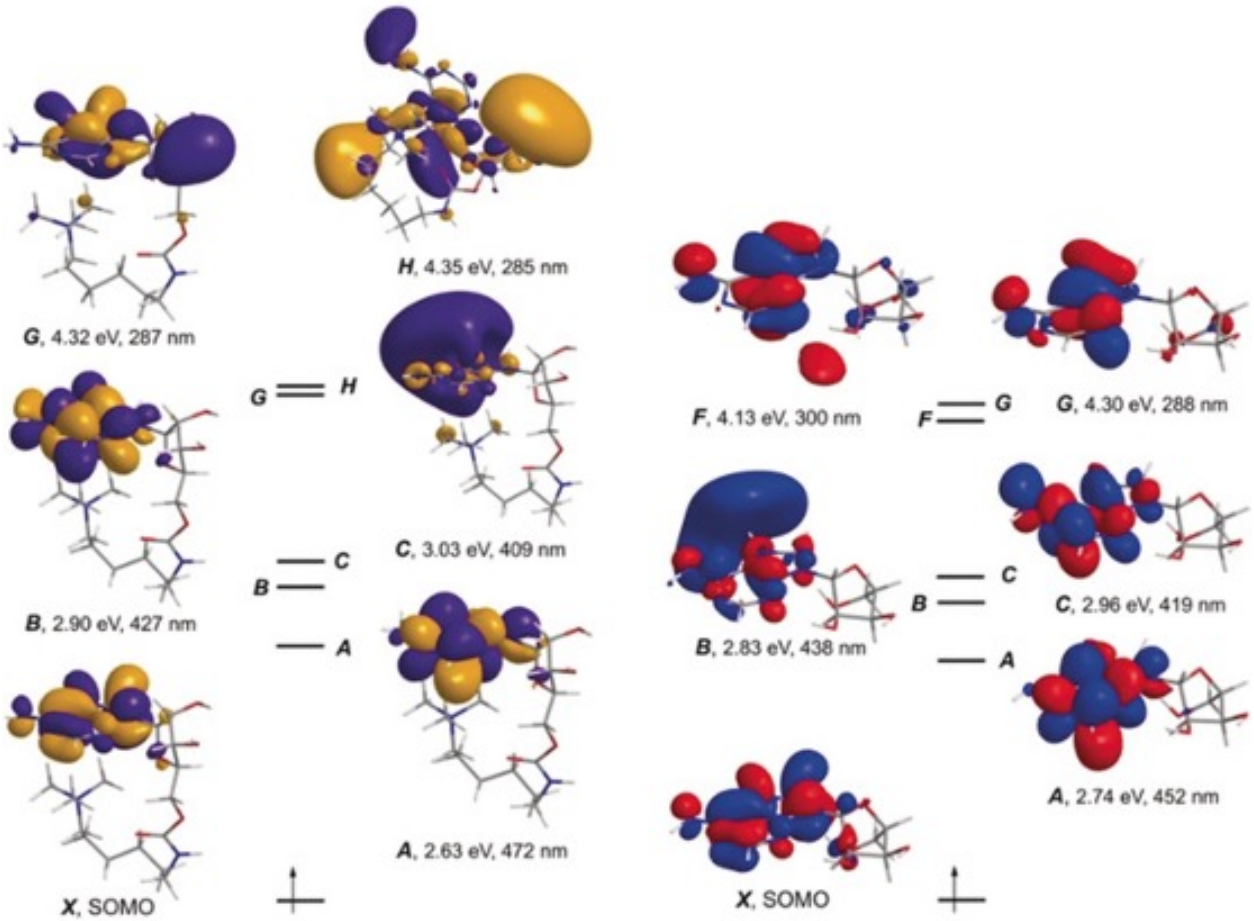

Figure 2.12: Molecular orbital representation of low excited electronic states in adenosine conjugate $2d^{+\bullet}$ (left panel) and adenosine radical $3d^{\bullet}$ (right panel).

2.3.5 Dissociation Energetics and Kinetics

The facile loss of H from $(\mathbf{1}{+}H)^{+\bullet}$ and $(\mathbf{2}{+}H)^{+\bullet}$ was further investigated by obtaining transition state (TS) geometries and energies for adenine C-H and N-H bond dissociations in

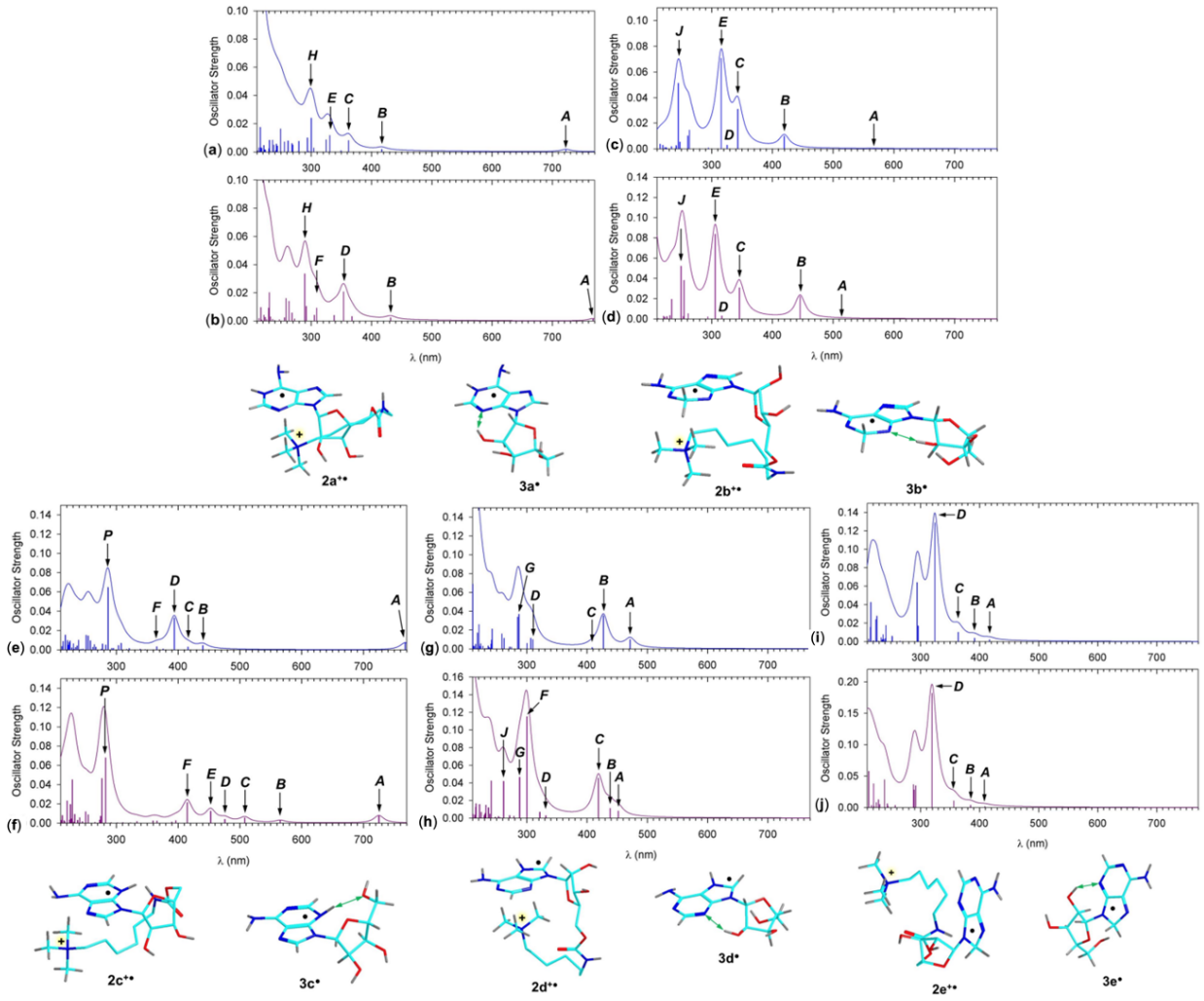

Figure 2.13: M06-2X/6-31+G(d,p) calculated TD-DFT absorption spectra of (a) N-1–H cation-radical conjugate $2a^{+\bullet}$, (b) N-1–H adenosine radical $3a^{\bullet}$, (c) C-2–H cation-radical conjugate $2b^{+\bullet}$, (d) C-2–H adenosine radical $3b^{\bullet}$, (e) N-3–H cation-radical conjugate $2c^{+\bullet}$, (f) N-3–H adenosine radical $3c^{\bullet}$, (g) N-7–H cation-radical conjugate $2d^{+\bullet}$, (h) N-7–H adenosine radical $3d^{\bullet}$, (i) C-8–H cation-radical conjugate $2e^{+\bullet}$, and (j) C-8–H adenosine radical $3e^{\bullet}$ Vertical bars denote the calculated transitions. The band envelopes are from artificial broadening by convolution with Lorentzian functions at 10 nm full width at half maximum.

$2\,a^{+\bullet}$, $2\,b^{+\bullet}$, $2\,c^{+\bullet}$, $2\,d^{+\bullet}$, and $2\,e^{+\bullet}$ (Figure 2.14) and for analogous dissociations in adenosine radicals $3\,a^{\bullet}$ $3\,c^{\bullet}$, and $3\,d^{\bullet}$ (Figure 2.15, Table 2.3 and Table 2.4). The benchmark TS energies for the cleavage of the N-1-H, N-3-H, and N-7-H bonds in $3\,a^{\bullet}$, $3\,c^{\bullet}$, and $3\,d^{\bullet}$ were low, ranging between 95–100 kJ mol$_{-1}$, and showing the weak trend E[TS(N-1-H)] $\leq$

E[TS(N-3-H)] ≤ E[TS(N-7-H)]. Again, the M06-2X-calculated TS energies closely followed the CCSD(T)/CBS benchmarks (Table 2.4).

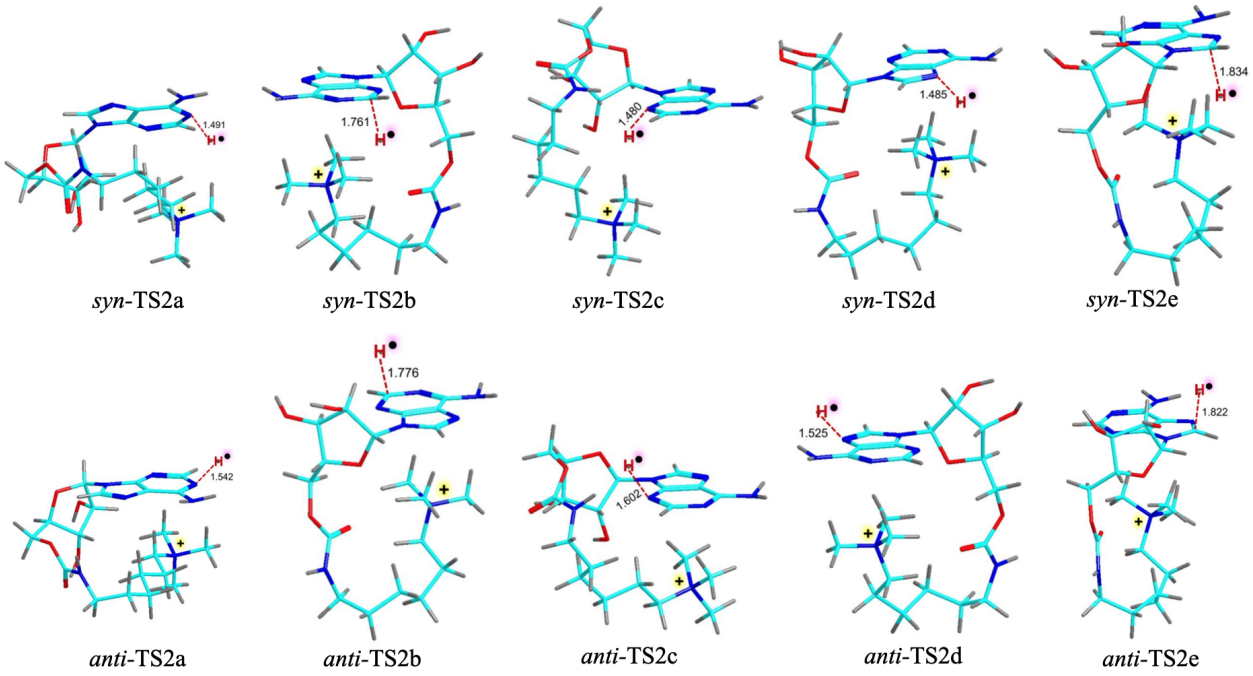

Figure 2.14: M06-2X/6-31+G(d,p) calculated transition state geometries for loss of H from $2a^{+\bullet}$, $2^{+\bullet}$, $2c^{+\bullet}$, $2d^{+\bullet}$ and $2e^{+\bullet}$. The dissociating bonds are shown by broken lines with distances in Ångstrøms.

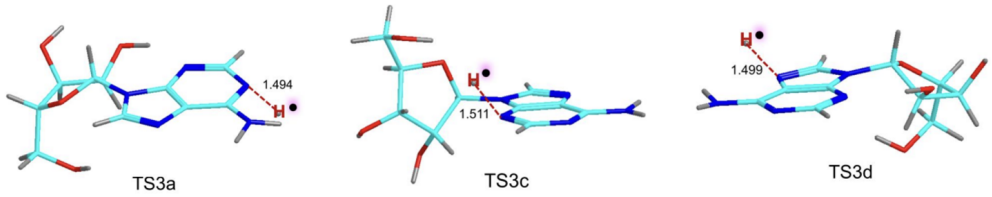

Figure 2.15: M06-2X/6-31+G(d,p) calculated transition state geometries for loss of H from $3a^{\bullet}$, $3c^{\bullet}$, and $3d^{\bullet}$. The dissociating bonds are shown by broken lines with distances in Ångstrøms.

The stacked side chains in the cation radicals made the X-H bond dissociations in $2a^{+\bullet}$-$2e^{+\bullet}$ diastereotopic, leading to *syn* and *anti*-facial transition states of distinct geometries and energies. This effect was most pronounced for the *syn* and *anti*-facial N-H bond dissociations

in $2a^{+\bullet}$, $2c^{+\bullet}$, and $2d^{+\bullet}$ (Figure 2.14). In contrast, the calculated TS energies for the *syn* and *anti*-facial C-H bond dissociations in $2b^{+\bullet}$ and $2e^{+\bullet}$ were nearly identical (Table 2.3). Regarding the N-7-H bond dissociations in the experimentally observed isomer $2d^{+\bullet}$, the *syn*-facial TS (*syn*-TS2d) was found at a shorter N-7-H distance (1.485 Å) and lower energy than the *anti*-facial TS (*anti*-TS2d, Table 2.3), which was at d(N-7$\cdots$H)=1.525 Å. This effect could not be attributed to different electron distributions in the TS, which were nearly identical for the *syn* and *anti*-facial TS. However, *syn*-TS2d showed a larger displacement of the departing H atom from the ring plane than did *anti*-TS2d, allowing a more efficient atomic orbital overlap in the adenine ring HOMO as it was developing in the course of dissociation.

Table 2.4: Relative energies of adenosine radicals.

Species/reaction	Relative energy[a,b]			
	M06-2X[c] 6-311++G(2d,p)	PMP2[c,d]	CCSD(T)[c,e] aug-cc-pVTZ	CCSD(T)[c,f,g] CBS
$3a^{\bullet}$	7.2	–1	5.5	5.2 (0.1)
$3b^{\bullet}$	–18	–21	–23	–20 (–23)
$3c^{\bullet}$	20	17	21	22 (18)
$3d^{\bullet}$	0	0	0	0 (0)[f]
$3e^{\bullet}$	–53	–51	–54	–52 (–55)
$3d^{\bullet} \rightarrow 5 + H^{\bullet}$	66	28	64	64 (36)
$3a^{\bullet} \rightarrow$ TS3a	92	81	92	95
$3c^{\bullet} \rightarrow$ TS3c	95	86	97	97
$3d^{\bullet} \rightarrow$ TS3d	101	85	99	100

[a] In kJ mol^{-1}. [b] Including zero-point energies and referring to 0 K unless stated otherwise. [c] Single-point energy calculations on M06-2X/6-31+G(d,p) optimized geometries. [d] From spin-projected MP2/6-311++G(2d,p) calculations. [e] From basis set expansion: E[CCSD(T)/aug-cc-pVTZ]≈E[CCSD(T)/aug-cc-pVDZ]+ E[PMP2/aug-cc-pVTZ]-E[PMP2/aug-cc-pVDZ]. [f] Extrapolated to the complete basis set. [g] Relative free energies at 310 K in parentheses.

The calculated TS energies were used for transition-state theory (TST) calculations of unimolecular rate constants for the H-atom loss to be compared with the experimental value of k=0.56 s^{-1}. The TST rate constants calculated for the *syn* and *anti* N-3-H dissociations were too low (<10^{-4} s^{-1} at 360 K) to be compatible with the experimental value. The rate constants for the *syn*- and *anti*-N-1-H dissociations, which had low calculated TS energies (Table 2.3), were affected by negative activation entropies, $\Delta S^{\neq}$=-16.4 and -29.7 J mol^{-1} K^{-1}, respectively, at 360 K. These rate constants are shown in Figure S19 a. The rate constant calculated for the *syn*-TS2d energy (95 kJ mol^{-1}, Table 2.3) matched the experimental value for an effective ion temperature of 351 K (Figure 2.16). Considering the estimated ±3 kJ mol^{-1} accuracy of the calculated TS energy, the range of ion effective temperatures giving matching TST rate constants can be expanded to 340–362 K. This fits within or is close to previous estimates of the effective temperature of ions stored in radiofrequency ion traps.[36–39] Thus, the calculated dissociation kinetics of the N-7-H adduct 2 $d^{+\bullet}$ was compatible with the experimental result.

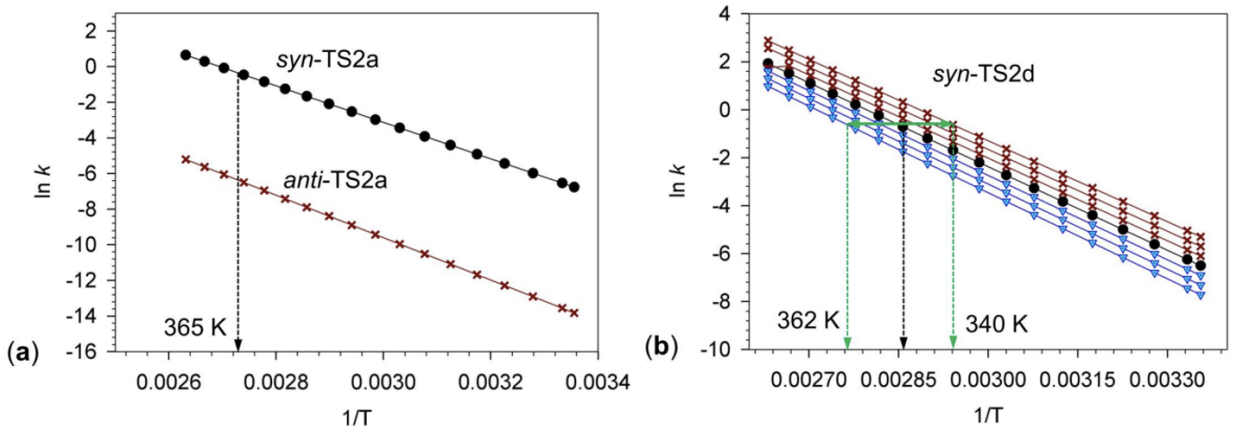

Figure 2.16: Arrhenius plots of calculated TST rate constants for (a) syn-N-1–H and anti-N1–H dissociations in $2a^{+\bullet}$. (b) syn-N-7-H dissociation in $2d^{+\bullet}$. The double-headed green arrow shows the logarithm of the experimental rate constant (k = 0.56 s^{-1}, ln k = –0.5798). The black full circles are for the M06-2X calculated E(TS) = 94.6 kJ mol^{-1}, matching the experimental k at 351 K (black dashed-line arrow). The red crosses are for E(TS) adjusted by –1, –2 and –3 kJ mol^{-1}, matching the experimental k at T ≥ 340 K (right green dashed-line arrow). The blue triangles are for E(TS) adjusted by +1, +2 and +3 kJ mol^{-1}, matching the experimental k at T ≤ 362 K (left green dashed-line arrow).

2.4 Conclusions

In summary, a new method for the generation of charge-tagged nucleoside radicals has been developed that was combined with photodissociation action spectroscopy of well-defined transient molecular species in the gas phase. As illustrated with adenine riboside, the charge-tagged radicals are electronically equivalent to natural nucleoside radicals, and derivatization of the 2' and 3'-OH groups in $(\mathbf{1}{+}\mathrm{H})^{+\bullet}$ by a non-polar group has a negligible effect on the electronic properties of the radicals. Thus, the method has the potential of being applied to the other nucleosides relevant to electron transfer in DNA and RNA to provide electronic structure of reactive intermediates pertinent to the early stages of ionization damage.

2.5 Bibliography

[1] DE Holmes, RB Ingalls, and LS Myers. Esr spectra of free radicals induced in nucleic acid purine and pyrimidine bases and selected analogues by exposure to hydrogen atoms. *International Journal of Radiation Biology and Related Studies in Physics, Chemistry and Medicine*, 13(3):225–234, 1968.

[2] PN Moorthy and E Hayon. Free-radical intermediates produced from the one-electron reduction of purine, adenine, and guanine derivatives in water. *Journal of the American Chemical Society*, 97(12):3345–3350, 1975.

[3] Alfred Hissung, Clemens Von Sonntag, Dieter Veltwisch, and Klaus-Dieter Asmus. The reactions of the 2'-deoxyadenosine electron adduct in aqueous solution. the effects of the radiosensitizer p-nitroacetophenone. a pulse spectroscopic and pulse conductometric study. *International Journal of Radiation Biology and Related Studies in Physics, Chemistry and Medicine*, 39(1):63–71, 1981.

[4] KJ Visscher, MP De Haas, H Loman, B Vojnovic, and JM Warman. Fast protonation of adenosine and of its radical anion formed by hydrated electron attack; a nanosecond

optical and dc-conductivity pulse radiolysis study. *International Journal of Radiation Biology and Related Studies in Physics, Chemistry and Medicine*, 52(5):745–753, 1987.

[5] MD Sevilla, R Failor, C Clark, RA Holroyd, and M Pettei. Electron transfer in dinucleoside phosphate anions. *The Journal of Physical Chemistry*, 80(4):353–358, 1976.

[6] LP Candeias and S Steenken. Electron adducts of adenine nucleosides and nucleotides in aqueous solution: protonation at two carbon sites (c2 and c8) and intra-and intermolecular catalysis by phosphate. *The Journal of Physical Chemistry*, 96(2):937–944, 1992.

[7] J Barnes and William A Bernhard. The protonation state of one-electron reduced cytosine and adenine. 1. initial protonation sites at low temperatures in glassy solids. *The Journal of Physical Chemistry*, 97(13):3401–3408, 1993.

[8] Jeff Barnes and William A Bernhard. Irreversible protonation sites of one-electron-reduced adenine: Comparisons between the c5 and the c2 or c8 protonation sites. *The Journal of Physical Chemistry*, 98(42):10969–10977, 1994.

[9] Xiaohong Chen, Erik A Syrstad, Minh Tho Nguyen, Pascal Gerbaux, and František Tureček. Adenine radicals in the gas phase: An experimental and computational study of hydrogen atom adducts to adenine. *The Journal of Physical Chemistry A*, 109(36):8121–8132, 2005.

[10] Chunxiang Yao, Maria L Cuadrado-Peinado, Miroslav Polášek, and František Tureček. Specific generation of 1-methylcytosine radicals in the gas phase. *Angewandte Chemie International Edition*, 44(41):6708–6711, 2005.

[11] Joseph A Korn, Jan Urban, Andy Dang, Huong TH Nguyen, and František Tureček. Uv–vis action spectroscopy reveals a conformational collapse in hydrogen-rich dinucleotide cation radicals. *The Journal of Physical Chemistry Letters*, 8(17):4100–4107, 2017.

[12] Rodolphe Antoine and Philippe Dugourd. Uv-visible activation of biomolecular ions. In *Laser photodissociation and spectroscopy of mass-Separated biomolecular ions*, pages 93–116. Springer, 2013.

[13] Andy Dang, Joseph A Korn, James Gladden, Brandon Mozzone, and František Tureček. Uv–vis photodissociation action spectroscopy on thermo ltq-xl etd and bruker amazon ion trap mass spectrometers: a practical guide. *Journal of The American Society for Mass Spectrometry*, 30(9):1558–1564, 2019.

[14] Yang Liu and František Tureček. Photodissociative cross-linking of diazirine-tagged peptides with dna dinucleotides in the gas phase. *Journal of The American Society for Mass Spectrometry*, 30(10):1992–2006, 2019.

[15] Herman JC Berendsen, JPM van Postma, Wilfred F Van Gunsteren, ARHJ DiNola, and Jan R Haak. Molecular dynamics with coupling to an external bath. *The Journal of chemical physics*, 81(8):3684–3690, 1984.

[16] Jan Řezáč, Jindřich Fanfrlík, Dennis Salahub, and Pavel Hobza. Semiempirical quantum chemical pm6 method augmented by dispersion and h-bonding correction terms reliably describes various types of noncovalent complexes. *Journal of Chemical Theory and Computation*, 5(7):1749–1760, 2009.

[17] James JP Stewart. Mopac: a semiempirical molecular orbital program. *Journal of computer-aided molecular design*, 4(1):1–103, 1990.

[18] Jan Řezáč. Cuby: An integrative framework for computational chemistry, 2016.

[19] Axel D Becke. Density-functional exchange-energy approximation with correct asymptotic behavior. *Physical review A*, 38(6):3098, 1988.

[20] Jeng-Da Chai and Martin Head-Gordon. Long-range corrected hybrid density functionals with damped atom–atom dispersion corrections. *Physical Chemistry Chemical Physics*, 10(44):6615–6620, 2008.

[21] Yan Zhao and Donald G Truhlar. The m06 suite of density functionals for main group thermochemistry, thermochemical kinetics, noncovalent interactions, excited states, and transition elements: two new functionals and systematic testing of four m06-class functionals and 12 other functionals. *Theoretical chemistry accounts*, 120(1):215–241, 2008.

[22] M. J. Frisch, G. W. Trucks, H. B. Schlegel, G. E. Scuseria, M. A. Robb, J. R. Cheeseman, G. Scalmani, V. Barone, G. A. Petersson, H. Nakatsuji, X. Li, M. Caricato, A. V. Marenich, J. Bloino, B. G. Janesko, R. Gomperts, B. Mennucci, H. P. Hratchian, J. V. Ortiz, A. F. Izmaylov, J. L. Sonnenberg, D. Williams-Young, F. Ding, F. Lipparini, F. Egidi, J. Goings, B. Peng, A. Petrone, T. Henderson, D. Ranasinghe, V. G. Zakrzewski, J. Gao, N. Rega, G. Zheng, W. Liang, M. Hada, M. Ehara, K. Toyota, R. Fukuda, J. Hasegawa, M. Ishida, T. Nakajima, Y. Honda, O. Kitao, H. Nakai, T. Vreven, K. Throssell, J. A. Montgomery, Jr., J. E. Peralta, F. Ogliaro, M. J. Bearpark, J. J. Heyd, E. N. Brothers, K. N. Kudin, V. N. Staroverov, T. A. Keith, R. Kobayashi, J. Normand, K. Raghavachari, A. P. Rendell, J. C. Burant, S. S. Iyengar, J. Tomasi, M. Cossi, J. M. Millam, M. Klene, C. Adamo, R. Cammi, J. W. Ochterski, R. L. Martin, K. Morokuma, O. Farkas, J. B. Foresman, and D. J. Fox. Gaussian˜16 Revision A.01, 2016. Gaussian Inc. Wallingford CT.

[23] Nick Polfer, Boris G Sartakov, and Jos Oomens. The infrared spectrum of the adamantyl cation. *Chemical physics letters*, 400(1-3):201–205, 2004.

[24] Chr Møller and Milton S Plesset. Note on an approximation treatment for many-electron systems. *Physical review*, 46(7):618, 1934.

[25] Jiří Čížek. On the use of the cluster expansion and the technique of diagrams in calculations of correlation effects in atoms and molecules. *Advances in chemical physics*, pages 35–89, 1969.

[26] George D Purvis III and Rodney J Bartlett. A full coupled-cluster singles and dou-

bles model: The inclusion of disconnected triples. *The Journal of Chemical Physics*, 76(4):1910–1918, 1982.

[27] Thom H Dunning Jr. Gaussian basis sets for use in correlated molecular calculations. i. the atoms boron through neon and hydrogen. *The Journal of chemical physics*, 90(2):1007–1023, 1989.

[28] Asger Halkier, Trygve Helgaker, Poul Jørgensen, Wim Klopper, Henrik Koch, Jeppe Olsen, and Angela K Wilson. Basis-set convergence in correlated calculations on ne, n2, and h2o. *Chemical Physics Letters*, 286(3-4):243–252, 1998.

[29] H Bernhard Schlegel. Potential energy curves using unrestricted mo/ller–plesset perturbation theory with spin annihilation. *The Journal of chemical physics*, 84(8):4530–4534, 1986.

[30] I Mayer. Spin-projected ehf method. iv. comparison of potential curves given by different one-electron methods. *International Journal of Quantum Chemistry*, 14(1):29–38, 1978.

[31] Andy Dang, Yue Liu, and František Tureček. Uv–vis action spectroscopy of guanine, 9-methylguanine, and guanosine cation radicals in the gas phase. *The Journal of Physical Chemistry A*, 123(15):3272–3284, 2019.

[32] Mario Barbatti, Matthias Ruckenbauer, Felix Plasser, Jiri Pittner, Giovanni Granucci, Maurizio Persico, and Hans Lischka. Newton-x: a surface-hopping program for nonadiabatic molecular dynamics. *Wiley Interdisciplinary Reviews: Computational Molecular Science*, 4(1):26–33, 2014.

[33] Kenichi Fukui. The path of chemical reactions-the irc approach. *Accounts of chemical research*, 14(12):363–368, 1981.

[34] John EP Syka, Joshua J Coon, Melanie J Schroeder, Jeffrey Shabanowitz, and Donald F Hunt. Peptide and protein sequence analysis by electron transfer dissociation mass

spectrometry. *Proceedings of the National Academy of Sciences*, 101(26):9528–9533, 2004.

[35] Scott A Shaffer and František Tureček. Hydrogentrimethylammonium: A marginally stable hypervalent radical. *Journal of the American Chemical Society*, 116(19):8647–8653, 1994.

[36] Douglas E Goeringer and Scott A McLuckey. Evolution of ion internal energy during collisional excitation in the paul ion trap: A stochastic approach. *The Journal of chemical physics*, 104(6):2214–2221, 1996.

[37] Scott Gronert. Estimation of effective ion temperatures in a quadrupole ion trap. *Journal of the American Society for Mass Spectrometry*, 9(8):845–848, 1998.

[38] Edward R Lovejoy and Robert R Wilson. Kinetic studies of negative ion reactions in a quadrupole ion trap: Absolute rate coefficients and ion energies. *The Journal of Physical Chemistry A*, 102(13):2309–2315, 1998.

[39] William A Donald, George N Khairallah, and Richard AJ O'Hair. The effective temperature of ions stored in a linear quadrupole ion trap mass spectrometer. *Journal of The American Society for Mass Spectrometry*, 24(6):811–815, 2013.

[40] Jóhannes Reynisson and Steen Steenken. One-electron reduction of 2-aminopurine in the aqueous phase. a dft and pulse radiolysis study. *Physical Chemistry Chemical Physics*, 7(4):659–665, 2005.

[41] Stacey D Wetmore, Russell J Boyd, and Leif A Eriksson. Theoretical investigation of adenine radicals generated in irradiated dna components. *The Journal of Physical Chemistry B*, 102(51):10602–10614, 1998.

Chapter 3

CHARGE-TAGGED GUANOSINE RADICALS

Reproduced in part with permission from Yue Liu, Congcong Ma, Calvin JA Leonen, Champak Chatterjee, Gabriela Novakova, Ales Marek, and František Tureček. Tackling a curious case: Generation of charge- tagged guanosine radicals by gas-phase electron transfer and their characterization by uv–vis photodissociation action spectroscopy and theory. *Journal of the American Society for Mass Spectrometry*, 32(3):772-785, 2021.

Abstract *We report the generation of gas-phase riboguanosine radicals that were tagged at ribose with a fixed-charge 6-(trimethylammonium)hexane-1-aminocarbonyl group. The radical generation relied on electron transfer from fluoranthene anion to noncovalent dibenzocrown-ether dication complexes which formed nucleoside cation radicals upon one-electron reduction and crown-ether ligand loss. The cation radicals were characterized by collision-induced dissociation (CID), photodissociation (UVPD), and UV–vis action spectroscopy. Identification of charge-tagged guanosine radicals was challenging because of spontaneous dissociations by loss of a hydrogen atom and guanine that occurred upon storing the ions in the ion trap without further excitation. The loss of H proceeded from an exchangeable position on N-7 in guanine that was established by deuterium labeling and was the lowest energy dissociation of the guanosine radicals according to transition-state energy calculations. Rate constant measurements revealed an inverse isotope effect on the loss of either hydrogen or deuterium with rate constants k_H = 0.25–0.26 s^{-1} and k_D = 0.39–0.54 s^{-1}. We used time-dependent density functional theory calculations, including thermal vibronic effects, to predict the absorption spectra of several protomeric radical isomers. The calculated spectra of low-energy N-7-H guanine-radical tautomers closely matched the action spectra. Transition-state-theory calcu-*

lations of the rate constants for the loss of H-7 and guanine agreed with the experimental rate constants for a narrow range of ion effective temperatures. Our calculations suggest that the observed inverse isotope effect does not arise from the isotope-dependent differences in the transition-state energies. Instead, it may be caused by the dynamics of post-transition-state complexes preceding the product separation.

3.1 Introduction

Guanine (G) is the most readily oxidized nucleobase of a low ionization energy (7.85 eV)[1] and standard oxidation potential (0.81–1.58 V).[2–4] As a result, guanine is readily ionized to a cation radical by electron transfer to another nucleobase cation radical formed by random DNA ionization.[5, 6] In contrast to oxidation, guanine has the largest negative reduction potential among the nucleobases (-2.76 eV),[3] which makes the guanine anion radical extremely reactive toward electron loss and protonation. Regarding electron attachment, the 9-methylguanine-1-methylcytosine anion radical pair has been studied experimentally in the gas phase,[7] and the calculated electron density indicated that the ionizing electron resided in the cytosine ring. The thermodynamics of proton transfer in the guanine-cytosine (C) anion radical pair has been studied by density functional theory (DFT) calculations[8] that pointed out the role of solvation. Protonation of transient nucleobase anion radicals proceeds rapidly in solution,[4] producing reactive neutral hydrogen atom adducts, such as $(G+H)^{\bullet}$, which can undergo further reactions. Our previous computational investigations have indicated that $(G+H)^{\bullet}$ and its 9-methyl derivative are extremely strong bases (pKa $\approx$ 20) that are expected to undergo fast and complete protonation by solvent or another proton donor.[9] Consistent with this analysis, $(G+H)^{\bullet}$ that was transiently produced in a $(GG+2H)^{+\bullet}$ dinucleotide by electron transfer in the gas phase underwent fast exothermic intramolecular protonation forming a stable dihydroguanine cation radical.[9] The high reactivity of $(G+H)^{\bullet}$ has so far thwarted attempts to generate it as a stable species for spectroscopic studies. In particular, a UV–vis absorption spectrum of $(G+H)^{\bullet}$ is needed to characterize the radical's electronic states for transient monitoring by fast spectroscopy.

We now report that guanosine radicals of the $(G+H)^{\bullet}$ type can be generated as isolated species in the gas phase from conjugates $\mathbf{1}^+$ and $\mathbf{2}^+$ that are tagged with a nonreactive fixed-charge group. This approach is illustrated in Figure 3.1 where the fixed-charged tag is a 6-(trimethylammonium)hexane-1-amine group attached via a carbamate linker to O-5' of the ribose moiety. The conjugates are protonated by electrospray ionization (ESI) to form the respective doubly charged ions, $(\mathbf{1}+H)^{2+}$ and $(\mathbf{2}+H)^{2+}$, that are stored in an ion trap and partially discharged by an ion–ion reaction with fluoranthene anion radical.[10]

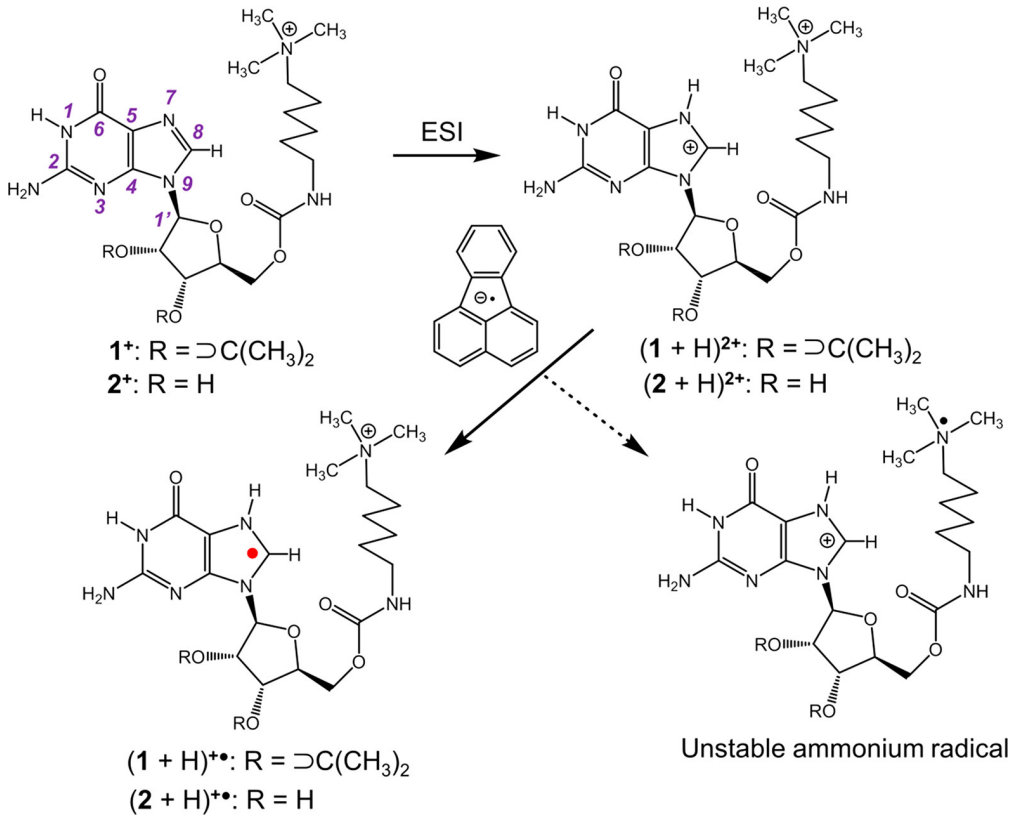

Figure 3.1: Reaction sequence for the generation of charge-tagged guanosine radicals.

Although the electron transfer direction is not specifically controlled in the ion–ion reaction and can result in discharging either positively charged group, reduction of the trimethylammonium group would produce a highly unstable hypervalent ammonium radical of submicrosecond lifetime,[11, 12] which is likely to completely dissociate on the experimental time

scale of several milliseconds. In contrast, cation radicals of the $(G+H)^{\bullet}$ type, such as $(\mathbf{1}+H)^{+\bullet}$ and $(\mathbf{2}+H)^{+\bullet}$ resulting from electron transfer to the guanidine moiety, are amenable to isolation by mass and further interrogation by tandem mass spectrometry and action spectroscopy.

3.2 Experimental Section

3.2.1 Materials and Methods

Solvents (methanol, water, acetic acid) of HPLC quality were purchased from Fisher Scientific (Pittsburgh, PA), distilled to remove dissolved sodium, and stored in Pyrex vessels. Deuterated solvents (>99% D content) were purchased from Cambridge Isotope Laboratories (Tewksbury, MA). 2,3:11,12-Dibenzo-18-crown-6-ether (DBCE) was purchased from Sigma-Aldrich (St. Louis, MO) and used as received. Guanosine conjugate $\mathbf{1}^{+}$ was synthesized from riboguanosine (Figure 3.2), purified by preparative HPLC, and characterized by electrospray and collision-induced dissociation (CID-MS^2) mass spectra (Figure 3.3). Conjugate $\mathbf{2}^{+}$ was prepared in situ by deprotection of the 2',3'-O-isopropylidene group with 60/40 trifluoroacetic acid/water for 10 min at room temperature. After evaporation of solvent to dryness, the product was redissolved in 50/50/1 methanol–water–acetic acid and characterized by high-resolution mass spectrometry (Table 3.1). Mass spectra were measured on a Bruker amaZon Speed 3D ion trap mass spectrometer that was modified for action spectroscopy measurements, as described previously.[13] Collision-induced dissociation (CID) spectra were measured at 0.20 (low excitation amplitude) and 0.40 (high excitation amplitude) instrument power settings. Action spectra were monitored in three wavelength sections, 210–354, 355–409, and 410–700 nm, using two laser pulses, and the laser pulse energies were measured at each experimental wavelength. The photofragment ion intensities were normalized to the number of photons per pulse. The reported spectra were averaged over two runs measured at different days. H/D exchange in $(\mathbf{1}+DBCE+H)^{2+}$ and $(\mathbf{2}+DBCE+H)^{2+}$ was achieved in a $D_2O/CD_3OD/CH_3COOD$ solution, and the D content in the gas-phase ions was sustained

by introducing D_2O vapor in the enclosed electrospray volume.

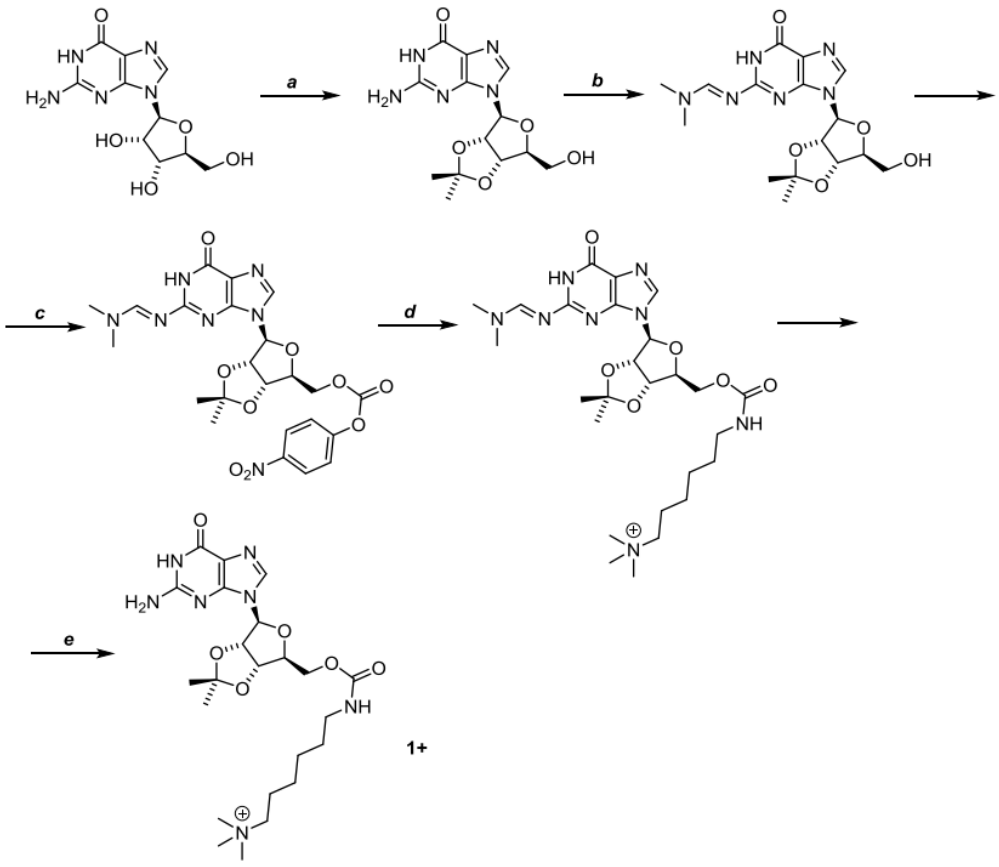

Figure 3.2: Preparation of guanosine conjugate. **a**: 2,2-dimethoxypropane, phosphomolybdic acid, acetone; **b**: N,N-dimethylformamide dimethylacetal, MeOH; **c**: p-nitrophenylchloroformate, diisopropylethylamine (DIPEA), MeCN; **d**: 6-aminohexyl trimethylamonium trifluoroacetate, DIPEA, MeCN; **e**: NH_4OH/EtOH (1/2, v/v)

3.2.2 Calculations

Born–Oppenheimer Molecular Dynamics (BOMD) calculations were performed as described previously.[14, 15] Briefly, multiple trajectories were run with the valence-electron PM6-D3H4 calculations[16] for 20 ps with 1 fs steps using the Berendsen thermostat[17] at 410–610 K and under the Cuby4 platform.[18] The PM6-D3H4 calculations were run with MOPAC 16.[19] Two hundred snapshots were extracted at regular intervals from 20000 steps in each trajectory,

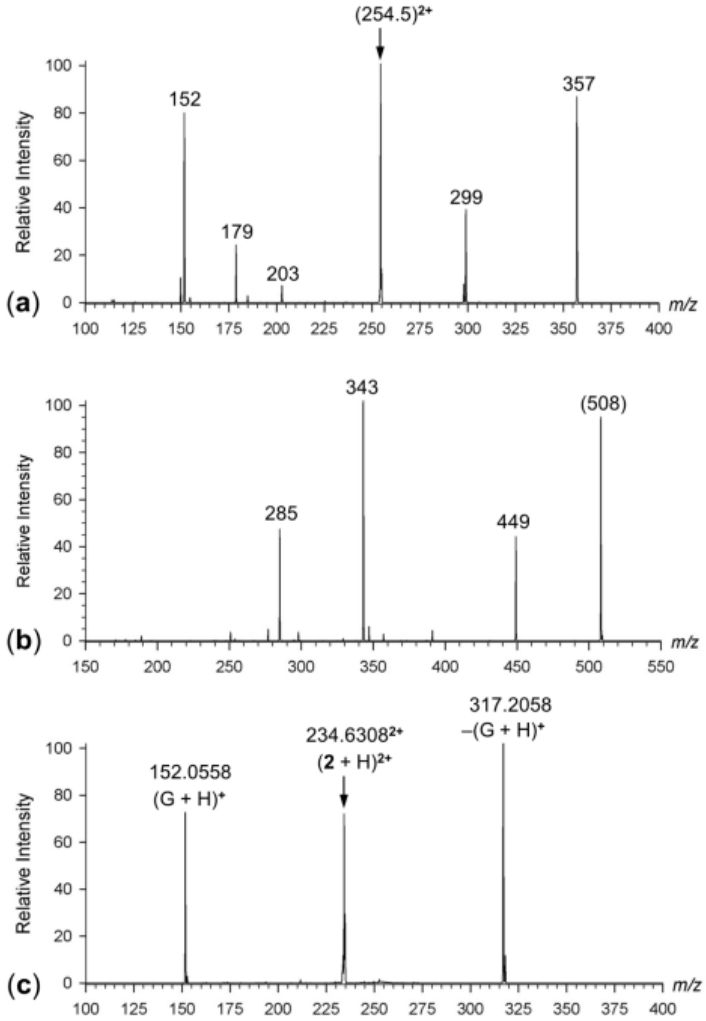

Figure 3.3: Collision-induced dissociation (CID) spectra of (a) $(\mathbf{1}+\mathrm{H})^{2+}$ (b) $\mathbf{1}^{+}$, and (c) $(\mathbf{2}+\mathrm{H})^{2+}$.

reoptimized with PM6-D3H4, and the list of structures was compacted by sorting out duplicates. Selected low-energy conformers were reoptimized with B3LYP/6-31+G(d,p)[20] to provide harmonic frequencies. These were used to calculate enthalpies and entropies at 310 K corresponding to the experimental temperature. Hindered rotors were identified by the procedure included in Gaussian 16[21, 22] and used to correct the calculated entropies. Another set of optimized structures were obtained by M06-2X/6-31+G(d,p)[23] geometry optimizations, followed by M06-2X/6-311++G(2d,p) calculations of single-point energies. Transition states

Table 3.1: Accurate mass measurements for guanosine conjugates.

m/z	formula	error(mmu)	assignment
234.6309	$C_{20}H_{35}N_7O_6(2+)$	−2.1	$(\mathbf{2}+H)^{2+}$
317.2059	$C_{15}H_{29}N_2O_5$	−1.2	$-(GH)^+$ ($C_5H_6N_5O$)
152.0559	$C_5H_5N_5O$	−0.8	$(G+H)^+$
468.2543	$C_{20}H_{34}N_7O_6$	−2.2	$\mathbf{2}^+$
409.1812	$C_{17}H_{25}N_6O_6$	−1.8	$-N(CH_3)_3$
303.1903	$C_{14}H_{27}N_2O_5$	−1.9	$-C_6H_7N_5O$

were located by a stepwise procedure. First, the potential energy surface along the reaction coordinate was mapped by a stepwise bond lengthening in low-energy reactant conformers, and the TS was gradient-optimized to the first-order saddle point with one imaginary frequency. Several thus-obtained transition states were then treated by BOMD at 610 K using the Cuby4 platform in which the bond lengths in the reaction center were fixed at their original TS values while the other internal coordinates were dynamically free. Snapshots from these runs were sorted out by DFT while keeping the TS coordinates fixed, and the resulting conformers were sorted out by energy. Finally, a search was performed for low-energy geometries to arrive at the final, conformationally optimized, TS structures which were confirmed by harmonic frequency analysis. Isotopologue frequencies were calculated using the B3LYP harmonic force constants. Excited-state calculations were performed with time-dependent DFT[24] (TD-DFT) with M06-2X/6-31+G(d,p) for 50 excited states. The choice of this functional and basis set for TD-DFT was based on our previous benchmarking[25, 26] against equation-of-motion coupled cluster calculations[27] for other nucleobase radicals. Vibronic transitions were calculated for 12–24 excited states from Wigner configurations[28, 29] that were generated from 198 harmonic vibrational modes of $(\mathbf{2}+H)^{+\bullet}$ using the NewtonX 16 program.[30] Typically, 300 lowest energy configurations were selected by their Boltzmann factors for TD-DFT calculations.

3.3 Results and Discussion

3.3.1 Cation-Radical Formation, Characterization, and Dissociation Kinetics

Electrospray ionization of $\mathbf{1}^+$ and $\mathbf{2}^+$ yielded doubly charged ions, $(\mathbf{1}+H)^{2+}$ and $(\mathbf{2}+H)^{2+}$, respectively, that were characterized by accurate mass measurements and collision-induced dissociation (CID) spectra (Figure 3.3a,c). The CID spectrum of $(\mathbf{2}+H)^{2+}$ (m/z 234.6) was very simple, displaying the complementary $(G+H)^+$ and $C_{15}H_{29}N_2O_5{}^+$ fragment ions formed by cleavage of the glycosidic C-1'–N-9 bond (Figure 3.3c). The CID spectrum of $(\mathbf{1}+H)^{2+}$ (m/z 254.5) displayed additional fragment ions from the dioxolan ring cleavage (m/z 299, Figure 3.3a). The CID spectrum of $\mathbf{1}^+$ (m/z 508) was also measured for reference (Figure 3.3b). However, electron transfer to $(\mathbf{1}+H)^{2+}$ and $(\mathbf{2}+H)^{2+}$ resulted in a complete dissociation, forming the $\mathbf{1}^+$ and $\mathbf{2}^+$ ions and fragments by loss of NMe_3, while the desired $(\mathbf{1}+H)^{+\bullet}$ and $(\mathbf{2}+H)^{+\bullet}$ cation radicals were absent (Figure 3.4a,b). This result was not completely unexpected, in view of the substantial exoergicity of electron transfer to the dications and the fragility of nucleoside radicals.[31, 32] To facilitate the formation of stable $(\mathbf{1}+H)^{+\bullet}$ and $(\mathbf{2}+H)^{+\bullet}$ we generated by electrospray ionization doubly charged noncovalent complexes of $(\mathbf{1}+H)^{2+}$ and $(\mathbf{2}+H)^{2+}$ with 2,3:11,12-dibenzo-18-crown-6-ether (DBCE) (m/z 414.5 and 434.5, respectively) and used these for ion–ion electron-transfer reactions with the fluoranthene anion.[10] The resulting spectra indicated the formation of stable cation-radicals at m/z 509 and 469 for $(\mathbf{1}+H)^{+\bullet}$ and $(\mathbf{2}+H)^{+\bullet}$, respectively (Figure 3.5a,b). We also generated the $(D_4\text{-}\mathbf{1}+D)^{+\bullet}$ and $(D6\text{-}\mathbf{2}+D)^{+\bullet}$ radicals in which all the exchangeable N–H and O–H were replaced by deuterium (m/z 514 and 476, Figure 3.5c,d). The ETD spectra of the DBCE complexes still showed that, regardless of the protecting groups on ribose, the guanosine cation radicals underwent substantial dissociation, and the main dissociations were loss of H, CH_3, and guanine (Figure 3.5).

The loss of H or D was the most facile dissociation that occurred even upon storing the cation radicals in the ion trap without any activation. In addition, a spontaneous loss of guanine was also observed as a minor dissociation. The peaks of the mass-selected $(\mathbf{1}+H)^{+\bullet}$,

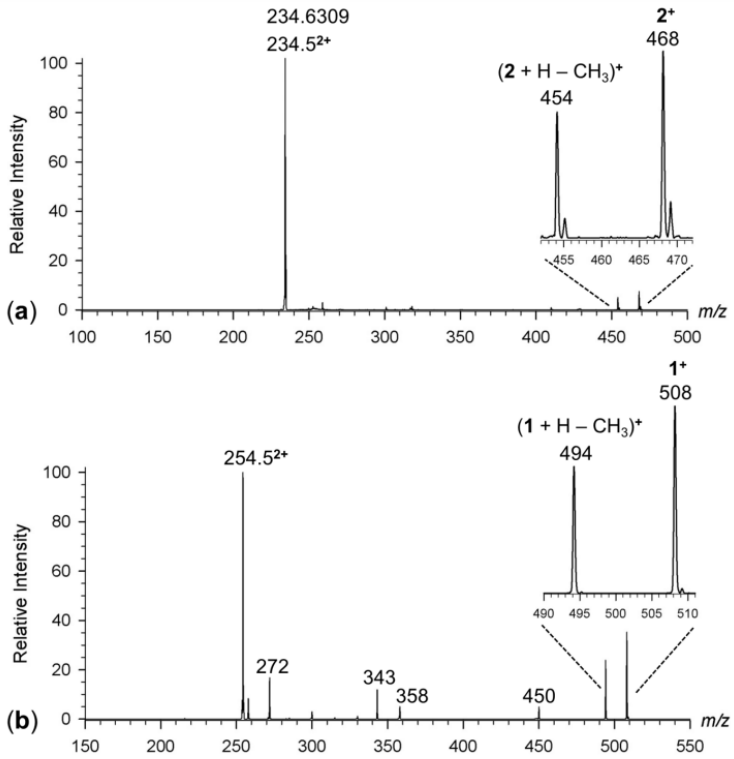

Figure 3.4: Electron transfer dissociation (ETD) spectra of (a) $(\mathbf{2}+H)^{2+}$ and (b) $(\mathbf{1}+H)^{2+}$.

$(D_4\text{-}\mathbf{1}+D)^{+\bullet}$, $(\mathbf{2}+H)^{+\bullet}$, and $(D_6\text{-}\mathbf{1}+D)^{+\bullet}$ ions showed tails on the low m/z sides that were indicative of metastable species that dissociated prior to resonant ejection from the ion trap (Figure 3.6a,b).[33–35] These tails were particularly prominent at short storage times and gradually diminished as the ions were kept longer in the ion trap (Figure 3.6d,e). We utilized these spontaneous dissociations of mass-selected ions at m/z 509, m/z 514, m/z 469, and m/z 476 for $(\mathbf{1}+H)^{+\bullet}$, $(D_4\text{-}\mathbf{1}+D)^{+\bullet}$, $(\mathbf{2}+H)^{+\bullet}$, and $(D_6\text{-}\mathbf{2}+D)^{+\bullet}$, respectively, to monitor the reaction kinetics and determine the apparent unimolecular dissociation rate constants. The logarithmic plot for the $(D_4\text{-}\mathbf{1}+D)^{+\bullet}$ relative intensity was linear, giving the rate constant, $k_D(\mathbf{1}) = 0.58\ s^{-1}$ ($r^2 = 0.999$) (Figure 3.6c), for the overall dissociation which was composed of the rate constants for the competitive loss of D, $k_D(\text{D-loss})(\mathbf{1}) = 0.54\ s^{-1}$ and loss of guanine, $k_D(\text{G-loss})(1) = 0.03 \pm 0.006\ s^{-1}$. The plot for $(\mathbf{1}+H)^{+\bullet}$ was less tight ($r^2 = 0.978$), giving the overall rate constant $k_H(\mathbf{1}) = 0.28\ s^{-1}$ that was composed of $k_H(\text{H-loss})(\mathbf{1}) = 0.26$

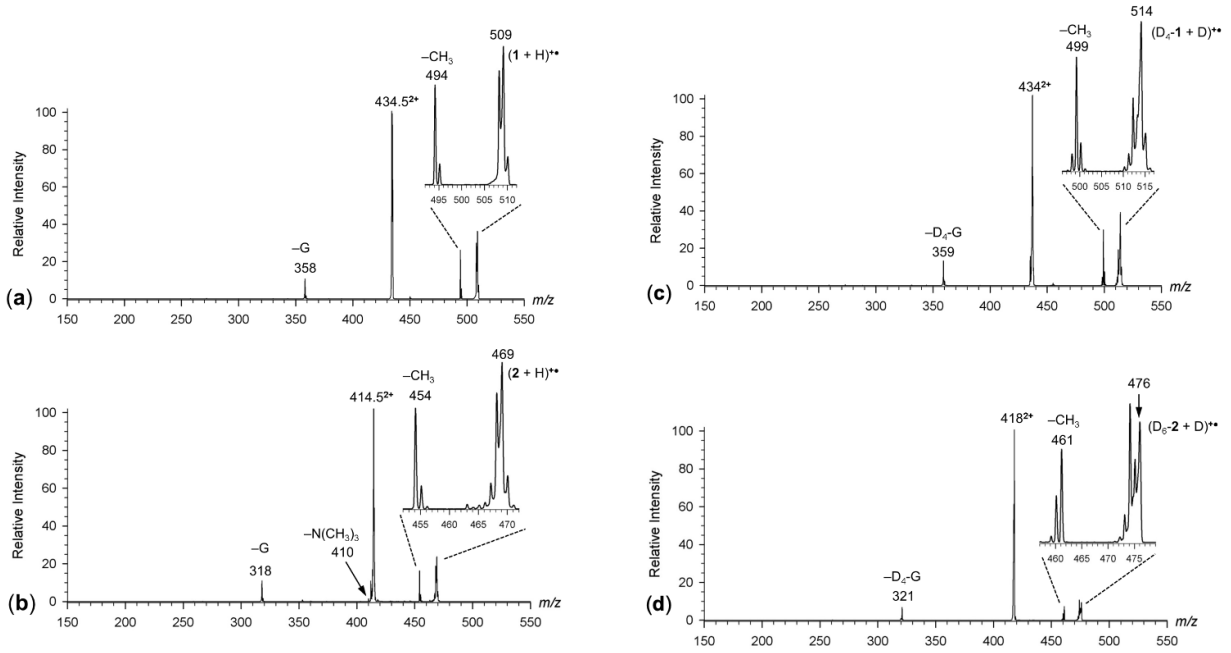

Figure 3.5: ETD spectra of complexes (a) (**1**+DBCE+H)$^{2+}$ at m/z 434.5, (b) (**2**+DBCE+H)$^{2+}$ at m/z 414.5, (c) (D$_4$-**1**+DBCE +D)$^{2+}$ and (d) (D6-**2**+DBCE +D)$^{2+}$ complexes. DBCE stands for 2,3:11,12-dibenzo-18-crown-6-ether.

s^{-1} and k$_H$(G-loss)(**1**) = 0.02 ± 0.005 s^{-1}. Thus, the loss of hydrogen exhibited an inverse isotope effect of k$_H$(H-loss)(**1**)/k$_D$(D-loss)(**1**) = 0.48.

The kinetic plot for the (**2**+H)$^{+\bullet}$ relative intensity (ln x(H), Figure 3.6f) showed a linear part after ca. 400 ms that was least-squares fitted giving the combined rate constant for both dissociation channels as k_H(**2**) = k$_H$(H-loss)(**2**) + k$_H$(G-loss)(**2**) = 0.28 s^{-1} with the correlation coefficient of r^2 = 0.99. From the combined rate constant and the product ion intensity ratios we obtained k$_H$(H-loss)(**2**) and k$_H$(G-loss)(**2**) as 0.26 and 0.02 ± 0.005 s^{-1}, respectively. At earlier ion residence times, the plot showed a steeper descent with an apparent k$_H$(**2**) = 0.62 and a poorer fit r^2 = 0.95. The plot for (D$_6$-**2**+D)$^{+\bullet}$ (x(D), Figure 3.6f) showed an overall linear function with k$_D$(**2**) = k$_D$(D-loss)(**2**) + k$_D$(G-loss)(**2**) = 0.45 s^{-1} and r^2 = 0.99, although the first few points up to 100 ms also indicated a faster dissociation. The faster-dissociating (**2**+H)$^{+\bullet}$ and (D$_6$-**2**+D)$^{+\bullet}$ ions were likely to belong to

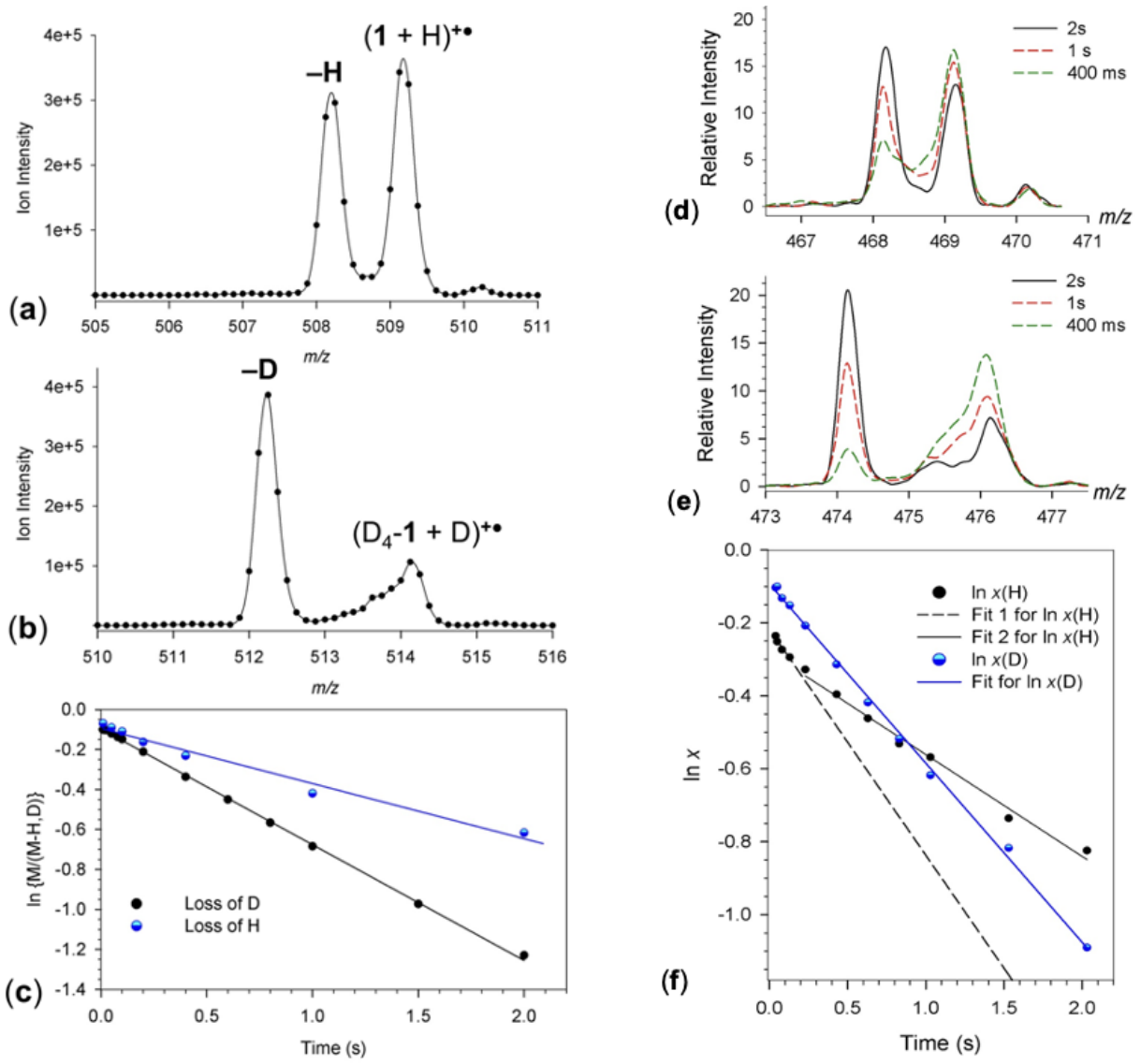

Figure 3.6: Peak profiles for (a) (**1**+H)$^{+\bullet}$ and (b) (D_4-**1**+D)$^{+\bullet}$ ions that were isolated by mass and stored without excitation in the ion trap for 2 s. (c) Logarithmic kinetic plots of precursor ion relative intensities for (**1**+H)$^{+\bullet}$ and (D_4-**1**+D)$^{+\bullet}$, (d) (**2**+H)$^{+\bullet}$ and (e) (D_6-**2**+D)$^{+\bullet}$ ions that were stored without excitation in the ion trap at the indicated times. (f) Logarithmic kinetic plots of precursor ion mole fractions, x(H) and x(D) for (**2**+H)$^{+\bullet}$ (D_6-**2**+D)$^{+\bullet}$, respectively, with lines of least-squares fits.

fractions that were nonresonantly excited upon ion isolation and underwent CID. In contrast, the longer-lived ions were likely to be thermalized to undergo spontaneous dissociations. From the k_D(**2**) we obtained the rate constants k_D(D-loss)(**2**) and k_D(G-loss)(**2**) as 0.39 and

0.06 ± 0.02 s^{-1}, respectively. The kinetic data indicated that the dissociation of the long-lived ions $(\mathbf{2}+H)^{+\bullet}$ also displayed an inverse isotope effect of $k_H(\text{H-loss}(\mathbf{2})/k_D(\text{D-loss})(\mathbf{2}) = 0.65$ that was of a similar magnitude as that measured for $(\mathbf{1}+H)^{+\bullet}$.

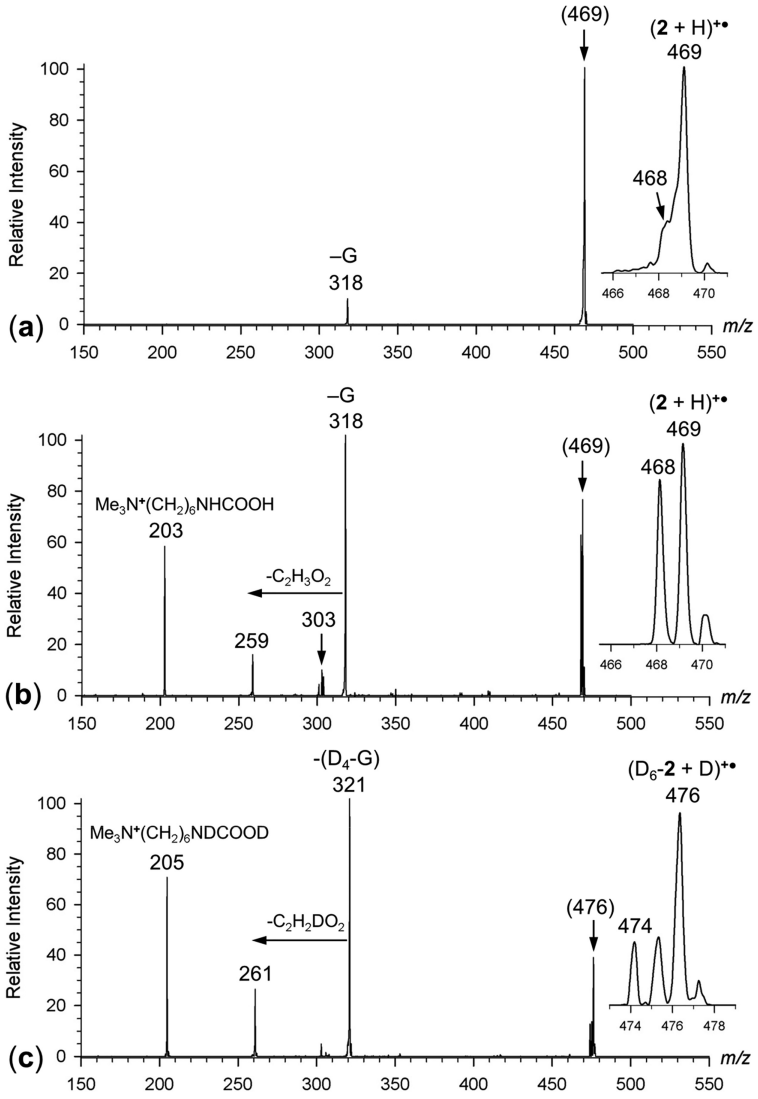

Figure 3.7: CID-MS^3 spectra of (a) $(\mathbf{2}+H)^{+\bullet}$ at a low excitation amplitude; (b) $(\mathbf{2}+H)^{+\bullet}$ at a high excitation amplitude; (c) $(D_6\text{-}\mathbf{2}+D)^{+\bullet}$ at a high excitation amplitude. Insets show the precursor ion and H/D-loss peak profiles.

The $(\mathbf{1}+H)^{+\bullet}$ and $(\mathbf{2}+H)^{+\bullet}$ ions, as well as their deuterated analogues, were further investigated by CID-MS^3. Upon low-energy excitation, the $(\mathbf{2}+H)^{+\bullet}$ ion chiefly lost an H

atom and guanine (m/z 318). Note that the m/z 468 peak due to loss of H was in part obscured by the metastable tail of the m/z 469 precursor (Figure 3.7a). At higher excitation amplitudes, (**2**+H)$^{+\bullet}$ underwent further dissociations by a combined elimination of guanine and $C_2H_3O_2$ from the ribose ring (m/z 259), and a carbamate elimination forming the m/z 203 fragment ion (Figure 3.7b). CID-MS^3 at high excitation amplitudes of (D_6-**2**+D)$^{+\bullet}$ displayed an equal loss of H and D (Figure 3.7c), which contrasted with the spontaneous dissociation leading to a predominant loss of D (Figure 3.6b). The clean elimination of D_4-G (m/z 321) from (D_6-**2**+D)$^{+\bullet}$, as well as the isotope mass shifts in the other fragment ions (m/z 259 → m/z 261, and m/z 203 → m/z 205), clearly indicated that there was no exchange between the guanine deuterium atoms and hydrogen atoms in other parts of the ion.

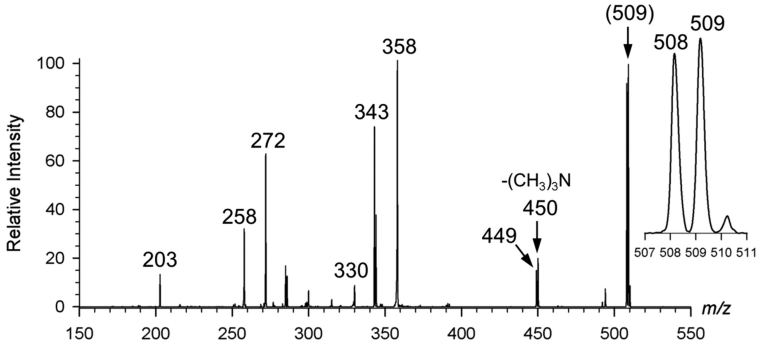

Figure 3.8: CID-MS^3 spectrum of (**1**+H)$^{+\bullet}$. Inset shows the precursor ion and H-loss peak profiles.

The CID spectrum of (**1**+H)$^{+\bullet}$ (Figure 3.8) showed additional fragment ions besides those by loss of H (m/z 508) and guanine (m/z 358). Loss of trimethylamine (m/z 450) in combination with loss of H (m/z 449) was substantially more abundant than for (**2**+H)$^{+\bullet}$. The CID spectrum of (**1**+H)$^{+\bullet}$ newly displayed fragment ions at m/z 344, 343, and 272. The m/z 344 and 343 ions were formed by elimination of $C_6H_7N_5O$, the latter following a hydrogen atom loss. Note that the m/z 343 fragment ion is prominent in the CID spectrum of **1**$^+$ (Figure 3.3), indicating a methyl transfer to the guanine ring. A similar dissociation was seen in the UVPD spectrum of **2**$^+$ (m/z 303, Figure 3.11b) and also for adenosine conjugate cation radicals, as has been reported recently.[32] This reaction is facilitated by an interaction

of the trimethylammonium group in the conjugate with the guanine ring which functions as a nucleophile in singly charged ions. Note that methyl transfer is absent in CID of doubly charged ions (Figure 3.3a,c) where the charged trimethylammonium and protonated guanine ring are kept apart by Coulomb repulsion. The m/z 272 and 258 ions are probably formed by cleavages within the ribose ring following the loss of guanine and methylguanine.

3.3.2 Action Spectra

The fragment ions identified by CID-MS^3 were selected for monitoring the photodissociation of $(\mathbf{1}+H)^{+\bullet}$ and $(\mathbf{2}+H)^{+\bullet}$. The action spectrum of $(\mathbf{1}+H)^{+\bullet}$ was composed of the abundant m/z 508, 358, 343, and 272 photofragment ions. The combined m/z 358, 343, and 272 photofragment ion intensities are plotted in Figure 3.9a. This showed composite bands with maxima at 260 and 330 nm and a broad band at 600 nm. The loss of guanine (m/z 358) channel was the main contributor to the 600 nm band, whereas the 260 and 330 nm bands had contributions from all major channels (Figure 3.9b). The m/z 508 channel (loss of H) displayed another band at 210 nm and a broad featureless band between 400 and 580 nm. However, the m/z 508 peak was partly obscured by the low-mass shoulder of the m/z 509 precursor because of its metastable dissociation that was most pronounced in regions of low photodissociation conversion. This made the intensity measurements at m/z 508 difficult, and it may have affected the action spectrum based on this ion channel.

The action spectrum of $(\mathbf{2}+H)^{+\bullet}$ was monitored at m/z 468, 318, 259, and 203. The combined spectrum is shown in Figure 3.10a, and the individual fragment ion channels are plotted in Figure 3.10b. The action spectrum displayed absorption bands at 270 and 330 nm and a broad band at 580 nm. Similar to $(\mathbf{1}+H)^{+\bullet}$, the 580 nm band was mainly due to the m/z 318, loss of guanine, channel which likely represented a low-energy dissociation, dominating at low photon energies. The 330 nm band was split in the m/z 318, 259, and 203 channels that showed small wavelength shifts from 330 nm for the m/z 203 channel to 340 and 350 nm for the m/z 318 and m/z 259 channels, respectively. These shifts were probably caused by energy-dependent competitive kinetics of these dissociations, whereby the low-

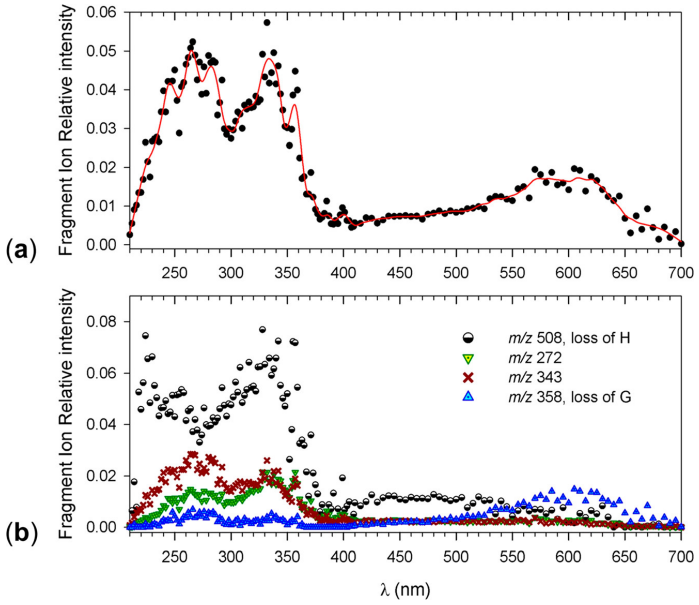

Figure 3.9: UV-Vis action spectra of $(\mathbf{1}{+}\mathrm{H})^{+\bullet}$. (a) Sum of photofragment ion relative intensities. (b) Individual photofragment channels.

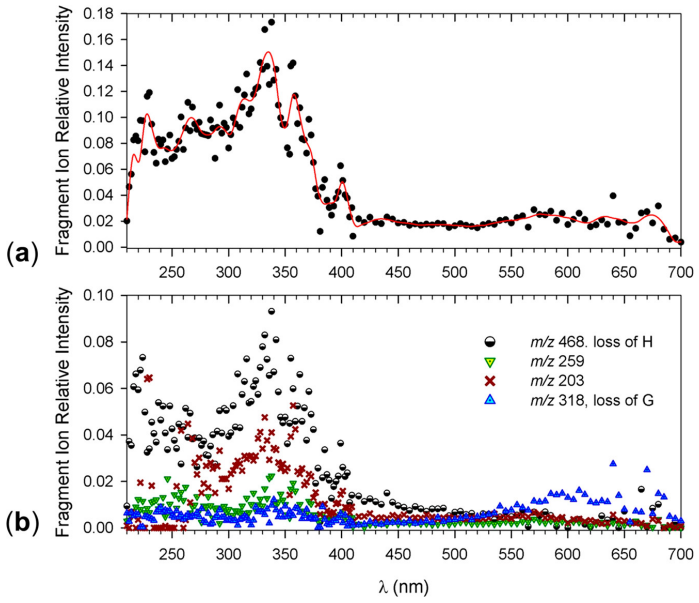

Figure 3.10: UV-Vis action spectra of $(\mathbf{2}{+}\mathrm{H})^{+\bullet}$. (a) Sum of photofragment ion relative intensities. (b) Individual photofragment channels.

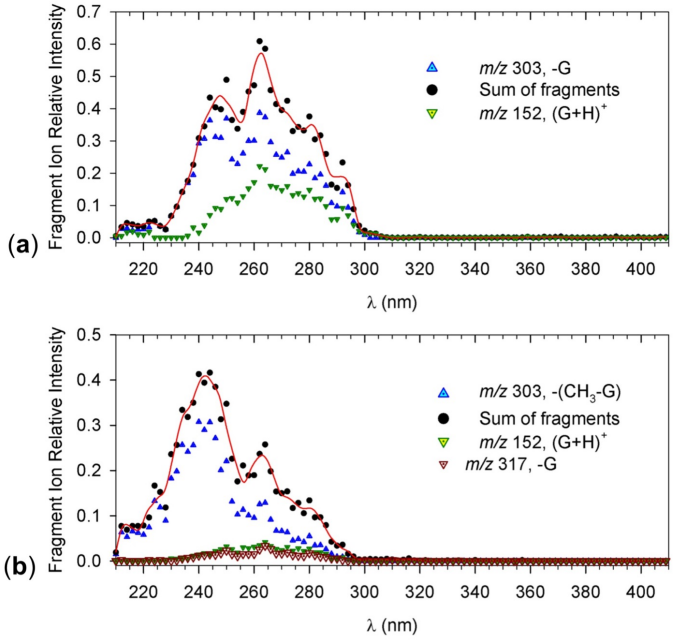

Figure 3.11: UV-Vis action spectra of (a) $(\mathbf{2}{+}\mathrm{H})^{2+}$ and (b) $\mathbf{2}^{+}$. No absorption was observed above 320 nm.

energy m/z 318 channel showed the longest wavelength band onset and maximum. The intensity of the m/z 468 (loss of H) ion was again affected by an overlap with the metastable shoulder of the m/z 469 precursor ion, especially in wavelength regions of low absorbance. We attempted to mitigate this interference by fitting the m/z 469 and m/z 468 with Gaussian profiles and integrating those while ignoring the metastable tail. Nevertheless, this procedure was imperfect, and the remaining interference may explain the featureless bands at 400–500 nm and above 600 nm in the m/z 468 channel (Figure 3.10b).

The action spectrum of $(\mathbf{2}{+}\mathrm{H})^{+\bullet}$ is to be matched against the action spectra of the closed-shell dication $(\mathbf{2}{+}\mathrm{H})^{2+}$ having a protonated guanine ring (Figure 3.11a) and cation $\mathbf{2}^{+}$ with a neutral guanine moiety (Figure 3.11b). The spectrum of $(\mathbf{2}{+}\mathrm{H})^{2+}$ displayed three bands with maxima at 245, 260, and 285 nm that were traced by both major photofragment ions which were $(\mathrm{G}{+}\mathrm{H})^{+}$ at m/z 152 and its complementary ion formed by loss of guanine (m/z 317). The spectrum of $\mathbf{2}^{+}$ also showed three bands with a major absorption at 240 nm that was carried by the rearrangement ion at m/z 303. The other bands at 265 and

280 nm had contributions also from the other photofragment ions at m/z 152 and m/z 317. The spectrum of $(\mathbf{2}+\mathrm{H})^{2+}$ indicated a 10 nm red shift for all three bands compared to the spectrum of $\mathbf{2}^{+}$ that can be attributed to the guanine ring protonation. Note that the guanine π-electron system is the only chromophore absorbing in this wavelength region. More significantly, the spectra of the closed-shell ions did not display any absorption above ca. 300 nm. Thus, the characteristic bands in the action spectrum of $(\mathbf{2}+\mathrm{H})^{+\bullet}$ (340 and 580 nm) can be unequivocally assigned to electron excitations in the guanine radical.

3.3.3 Ion Structures and Action Spectra Assignment

We carried out extensive calculations of cation–radical structures pertinent to $(\mathbf{1}+\mathrm{H})^{+\bullet}$ and $(\mathbf{2}+\mathrm{H})^{+\bullet}$, as well as their ion precursors, dissociation products, and transition states leading to major dissociations. The primary goal of these calculations was to assign the action spectra, with a secondary goal of establishing the relative energies of guanine ion and radical protomers and their conformers. Starting with $(\mathbf{1}+\mathrm{H})^{+\bullet}$, we used Born–Oppenheimer Molecular Dynamics (BOMD) calculations to map the conformational space of guanine, ribose, and the carbamate side chain and then applied DFT for full gradient optimization of low-energy structures identified by BOMD. The relative energies of $(\mathbf{1}+\mathrm{H})^{+\bullet}$ protomers with hydrogen attachment sites at guanine positions N-3, O-6, N-7, and NH_2 (N-10) are summarized in Table 3.2. The DFT calculations indicated very close relative free energies of protomers protonated at N-7 ($1a^{+\bullet}$ and $1b^{+\bullet}$), N-3 ($1c^{+\bullet}$ and $1d^{+\bullet}$), and O-6 ($1e^{+\bullet}$) (Figure 3.12) where the differences were within the usual accuracy limits of the DFT methods employed. Thus, no preference for either structure could be inferred from the energy calculations. The low-energy $(\mathbf{1}+\mathrm{H})^{+\bullet}$ ions displayed some interesting structural features that are briefly discussed here. In contrast to the cation radicals, energy analysis of the $(\mathbf{1}+\mathrm{H})^{2+}$ dications gave N-7-protonated tautomers as the lowest free-energy structures (Figure 3.13). This result was consistent with the preferred protonation at N-7 in gas-phase guanine[36, 37] and guanosine.[38]

The low-energy N-7-H cation–radical tautomers ($1a^{+\bullet}$ and $1b^{+\bullet}$) were pyramidized at C-

Table 3.2: Relative energies of cation radicals $(\mathbf{1}+H)^{+\bullet}$

ion	relative energy[a,b] M06-2X[c]/6-31+G(d,p)	M06-2X[c,d]/6-311++G(2d,p)
$1a^{+\bullet}$	0 (0)	0 (0)
$1b^{+\bullet}$	9.5 (5.7)	9.0 (5.2)
$1c^{+\bullet}$	3.1 (0.2)	4.9 (2.0)
$1d^{+\bullet}$	6.4 (2.7)	6.6 (2.9)
$1e^{+\bullet}$	12 (8.1)	14 (10)
$1f^{+\bullet}$	24 (22)	24 (23)
$1g^{+\bullet}$	56 (62)	61 (67)

[a] In kJ mol^{-1}. [b] Including scaled B3LYP/6-31+G(d,p) zero-point energies and referring to 0 K unless stated otherwise. [c] Relative free energies at 310 K in parentheses. [d] Single-point energies on M06-2X/6-31+G(d,p) optimized geometries.

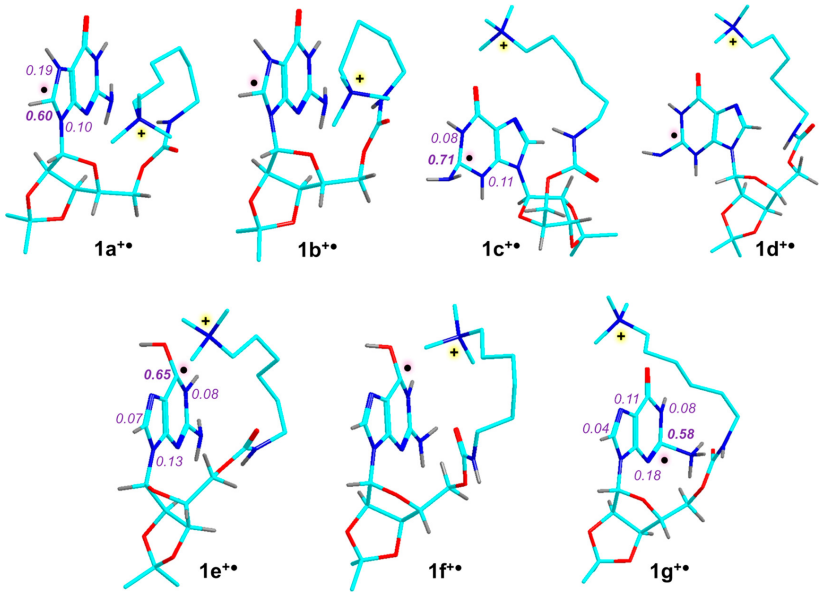

Figure 3.12: M06-2X optimized structures of low-energy $(\mathbf{1}+H)^{+\bullet}$ isomers. Atom color coding is as follows: cyan = C, blue = N, red = O, gray = H. The side-chain aliphatic hydrogens were hidden to avoid clutter. Major atomic spin densities are shown as purple italics.

8, displaying a high atomic spin density at this position (Figure 3.12). The charge-carrying side chain was folded toward the guanine ring such that the proximate trimethylammonium

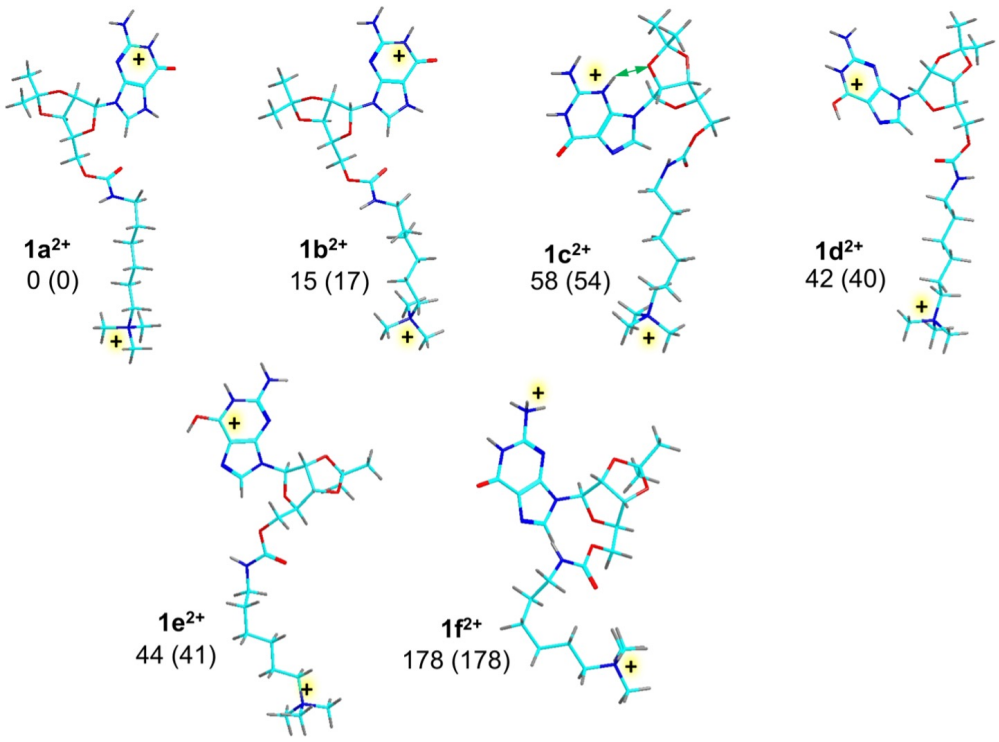

Figure 3.13: M06-2X/6-31+G(d,p) optimized structures of $(\mathbf{1}+\mathrm{H})^{2+}$ dications. Atom color coding is as follows: cyan = C, blue = N, red = O, gray = H. Relative energies in kJ mol^{-1} include scaled B3LYP/6-31+G(d,p) zero-point energies and refer to 0 K. Values in parentheses are relative free energies at 310 K.

hydrogens were within 2.7 Å of the radical carrying C-8. The N-3-H tautomers ($1c^{+\bullet}$ and $1d^{+\bullet}$) showed a high spin density at C-2 which was pyramidized. The side chain in these tautomers was folded to become sandwiched with the guanine ring, but the closest approach of the trimethylammonium hydrogens was toward O-6, not the C-2 radical center. The O-2-H tautomers ($1e^{+\bullet}$ and $1f^{+\bullet}$) carried most of the spin density at C-6. The side chain was folded with the proximate trimethylammonium hydrogens approaching N-7 within 2.4 Å. Finally, the less stable ion $1g^{+\bullet}$ had a substantial spin density at C-2, and the side chain was tightly folded toward the guanine ring with O6$\cdots$H distances within 2.3 Å. The side chain folding was chiefly due to charge-dipole interactions between the trimethylammonium group and the ring N or O atoms of high electron density. Hydrogen bonding involving the carbamate linker was less important, as judged from the CO–N-H$\cdots$ring N distances which

were 2.41, 2.90, and 2.76 Å in $1a^{+\bullet}$, $1c^{+\bullet}$, and $1e^{+\bullet}$, respectively. Ion $1g^{+\bullet}$ was different as it developed a strong hydrogen bond between the NH_3 group and the carbamate carbonyl at 1.75 Å.

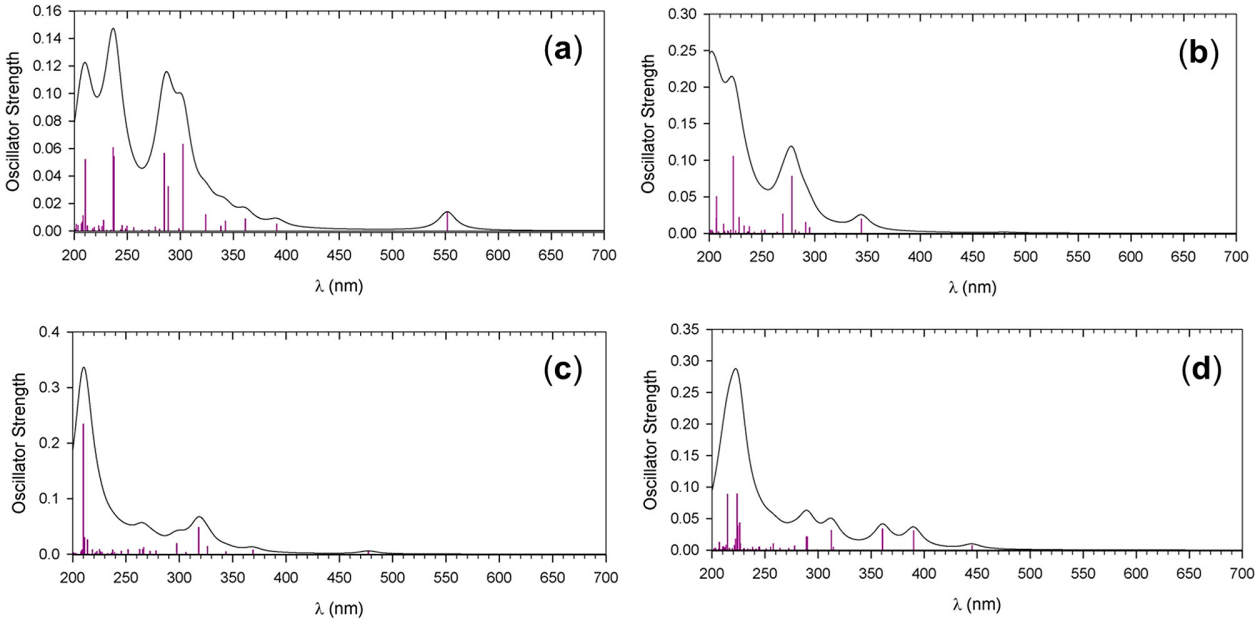

Figure 3.14: M06-2X/6-31+G(d,p) TD-DFT absorption spectra of (a) $1a^{+\bullet}$, (b) $1c^{+\bullet}$, (c) $1e^{+\bullet}$, and (d) $1g^{+\bullet}$. The band profiles are from artificial broadening of the transition lines by convolution with Lorentzian functions at 10 nm full width at half maximum (fwhm).

We used TD-DFT to calculate electronic excitations in $1a^{+\bullet}$-$1g^{+\bullet}$ that were plotted in Figure 3.14 and Figure 3.15 for the lowest energy conformers. Comparison of the calculated spectra with the action spectrum of $(\mathbf{1}+H)^{+\bullet}$ revealed a match of the long-wavelength band (λ_{max} = 550 nm) of $1a^{+\bullet}$ (Figure 3.14a) with the band of $(\mathbf{1}+H)^{+\bullet}$ in same region (Figure 3.9a). Similarly, the calculated bands of $1a^{+\bullet}$ at 240 and 290 nm found a match with the action spectrum bands at 260 and 340 nm, considering a vibronic red shift and band broadening. A similar match was observed for the other N-7-protonated low-energy conformer $1b^{+\bullet}$ (Figure 3.15a). In contrast, the other guanine protomers, $1c^{+\bullet}$, $1e^{+\bullet}$, and $1g^{+\bullet}$ and their conformers displayed various degrees of mismatch with the action spectrum in the characteristic 500–600 and 300–400 nm regions (Figure 3.14b–d). Thus, the action spectrum

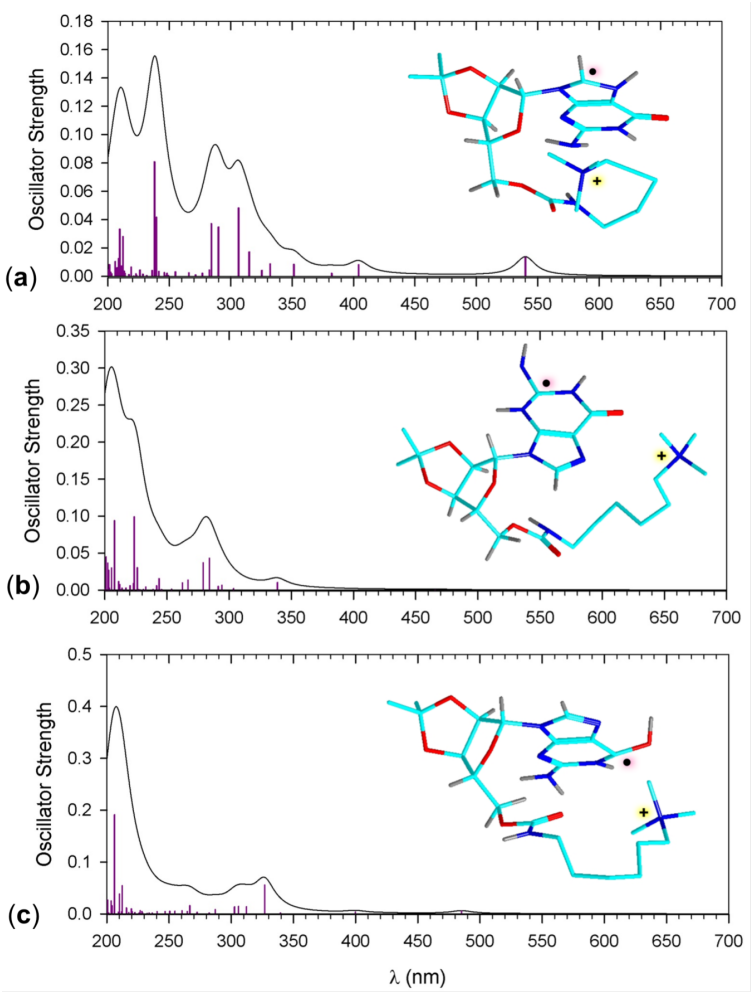

Figure 3.15: M06-2X/6-31+G(d,p) TD-DFT absorption spectra of higher-energy $(1 + H)^{+\bullet}$ conformers (a) $1b^{+\bullet}$, (b) $1d^{+\bullet}$, and (c)$1f^{+\bullet}$. The band profiles are from artificial broadening of the transition lines by convolution with Lorentzian functions at 10 nm full width at half maximum (fwhm).

of $(\mathbf{1}+H)^{+\bullet}$ pointed to the N-7 protonated tautomer $1a^{+\bullet}$ or its low-energy conformer $1b^{+\bullet}$.

We further addressed the structures, energies, and absorption spectra of isomers pertaining to $(\mathbf{2}+H)^{+\bullet}$. The optimized geometries of the lowest energy conformations of tautomers $2a^{+\bullet}$-$2f^{+\bullet}$, originating from ions protonated at the basic N-1, N-3, N-7, and O-6 sites, are shown in Figure 3.16, for relative energies see Table 3.3. The N-7-protonated isomers $2a^{+\bullet}$ and $2b^{+\bullet}$ were the lowest free energy ions that differed in the exo and endo configuration at the pyramidal N-7 atom. These two forms were calculated to be freely convertible by

inversion at N-7. The transition-state energy for the inversion, when corrected for zero-point vibrational energy, was below those of $2a^{+\bullet}$ and $2b^{+\bullet}$. Another isomer ($2c^{+\bullet}$), having an inverted configuration at C-8, was slightly higher in energy. In addition to $2a^{+\bullet}$ –$2c^{+\bullet}$, we found the N-3-H tautomer ($2d^{+\bullet}$) and the O-6-enol form ($2f^{+\bullet}$) to be within 10 kJ mol^{-1} of $2a^{+\bullet}$. Thus, according to the optimized structures and energies, there was no particular preference for either guanosine radical tautomer. It may be noted that the ordering of free energies for $2a^{+\bullet}$ –$2f^{+\bullet}$ was affected by the ion entropies. Because of the side-chain flexibility, the low frequency modes were treated as hindered rotors according to McClurg et al.,[22] resulting in upward entropy corrections.

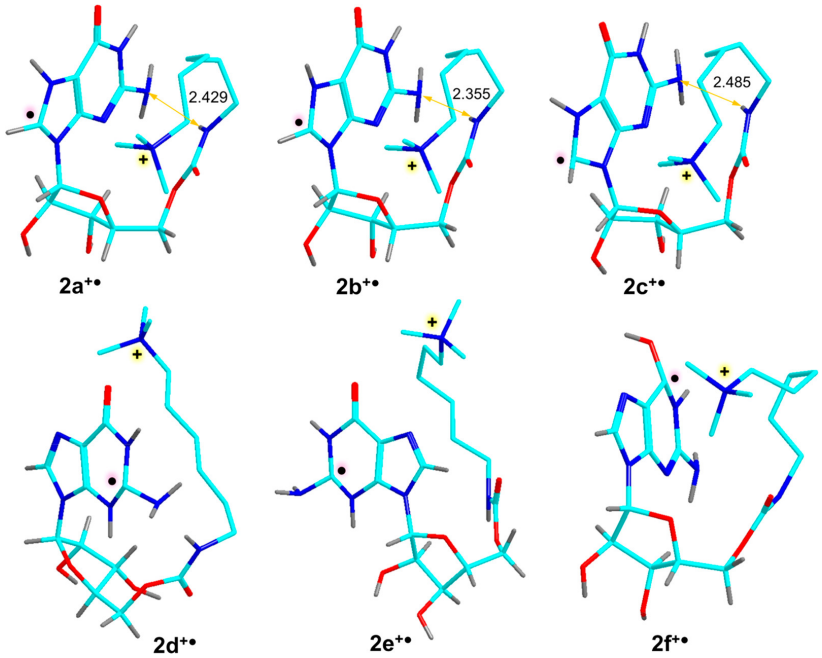

Figure 3.16: M06-2X optimized structures of low-energy (**2**+H)$^{+\bullet}$ isomers. Atom color coding is as follows: cyan = C, blue = N, red = O, gray = H. The side-chain aliphatic hydrogens were hidden to avoid clutter.

The optimized structures of $2a^{+\bullet}$ –$2f^{+\bullet}$ displayed close similarities with those of $1a^{+\bullet}$ –$1g^{+\bullet}$, as far as the interactions between the charged side chain and the radical-carrying guanine ring were concerned. For example, the N-7-H tautomers $2a^{+\bullet}$ –$2c^{+\bullet}$ showed folded conformations in which the trimethylammonium group was in the vicinity of the radical-

Table 3.3: Relative energies of cation radicals (**2**+H)$^{+\bullet}$

ion	relative energy[a,b] M06-2X[c]/6-31+G(d,p)	M06-2X[c,d]/6-311++G(2d,p)
2a$^{+\bullet}$	0 (0)	0 (0)
2b$^{+\bullet}$	3 (–3.4)	4.2 (–2.1)
2c$^{+\bullet}$	5.9 (7.8)	6.3 (8.2)
2d$^{+\bullet}$	–8.6 (1.4)	–3.7 (6.4)
2e$^{+\bullet}$	6.2 (11)	9.3 (14)
2f$^{+\bullet}$	7.9 (4.0)	8.3 (4.3)
2g$^{+\bullet}$	–66 (–65)	–65 (–64)
2h$^{+\bullet}$	–14 (–15)	–14 (–14)
2i$^{+\bullet}$	8.0 (7.0)	8.1 (7.2)
2j$^{+\bullet}$	57 (56)	59 (59)
2k$^{+\bullet}$	74 (66)	75 (67)
2l$^{+\bullet}$	. 11 (0.6)	–13 (–1.6)
3^{+} + H$^{\bullet}$	62 (35)	59 (32)
4$^{+\bullet}$ + Guanine	52 (–6.9)	46 (–13)
TS1	92	94
D_7-TS1	103[e]	105[e]
TS2	92	104
TS3	106	106
TS4	101	104
D_7-TS4	107[e]	110[e]
TS5	95	97

[a] In kJ mol^{-1}. [b] Including scaled B3LYP/6-31+G(d,p) zero-point energies and referring to 0 K unless stated otherwise. [c] Relative free energies at 310 K in parentheses. [d] Single-point energies on M06-2X/6-31+G(d,p) optimized geometries. [e] Relative to D_7-2a$^{+\bullet}$.

carrying imidazole ring, a situation also encountered with 1a$^{+\bullet}$ and 1b$^{+\bullet}$. The absence of the rigid 1,3-dioxolan ring in 2a$^{+\bullet}$-2f$^{+\bullet}$ affected the ribose ring conformation. For example, the O-2–C-2'–C-3'–O-3 dihedral angle in 2a$^{+\bullet}$ (31.0°) was larger than in 1a$^{+\bullet}$ (-3.5°). However, the side-chain conformation allowing the ion-dipole interactions was established to a similar manner in 2a$^{+\bullet}$ and 1a$^{+\bullet}$, as set up by the similar O-5–C-5'–C-4'–C-3' dihedral angles (54.7° and 43.7°, respectively). Thus, the presence of the dioxolan ring in 1a$^{+\bullet}$ –1g$^{+\bullet}$ had only a

minor effect on the ion conformations and tautomer relative free energies.

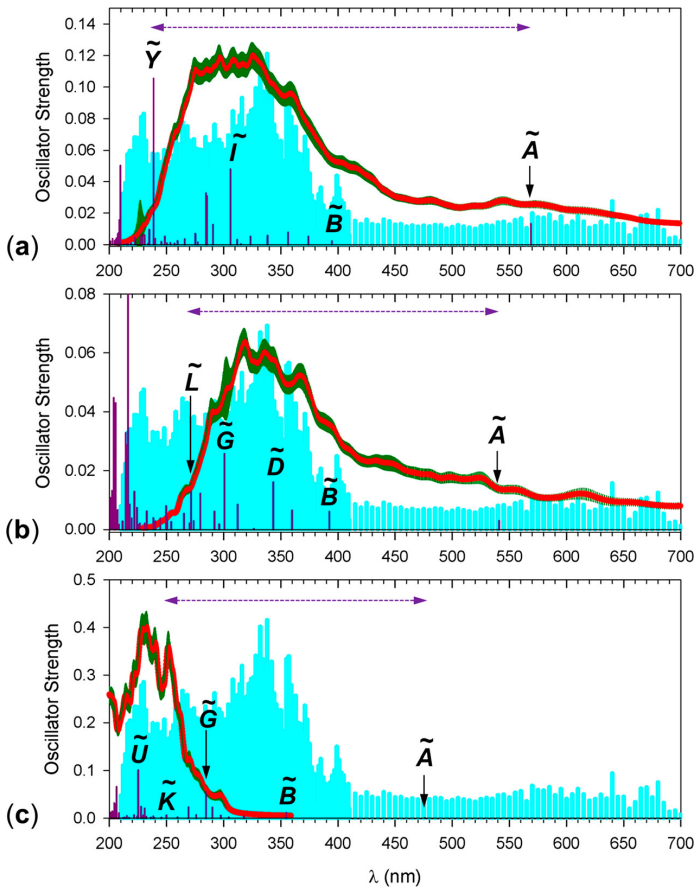

Figure 3.17: M06-2X/6-31+G(d,p) calculated vibronic absorption spectra of (a) $2a^{+\bullet}$, (b) $2f^{+\bullet}$, (c) $2d^{+\bullet}$ tautomers of $(2 + H)^{+\bullet}$. The scaled action spectrum is shown as cyan background. The double arrows indicate the range of excited-state wavelengths used in the vibronic calculations.

For the optimized structures of $2a^{+\bullet}$, $2d^{+\bullet}$, and $2f^{+\bullet}$ we calculated TD-DFT electronic excitations that were expanded to 300 configurations at 310 K to provide vibronic spectra. Because of the size of these ions and the large number of low-oscillator strength excited states in open-shell systems, we limited the number of excited states included in the vibronic calculations to 12–24 states to cover the wavelength range in the visible and near-UV regions. The calculated vibronic spectra along with the excited state assignments are shown in Figure 3.17. The spectrum of $2a^{+\bullet}$ (Figure 3.17a) displayed a broad band at 569 nm due to an

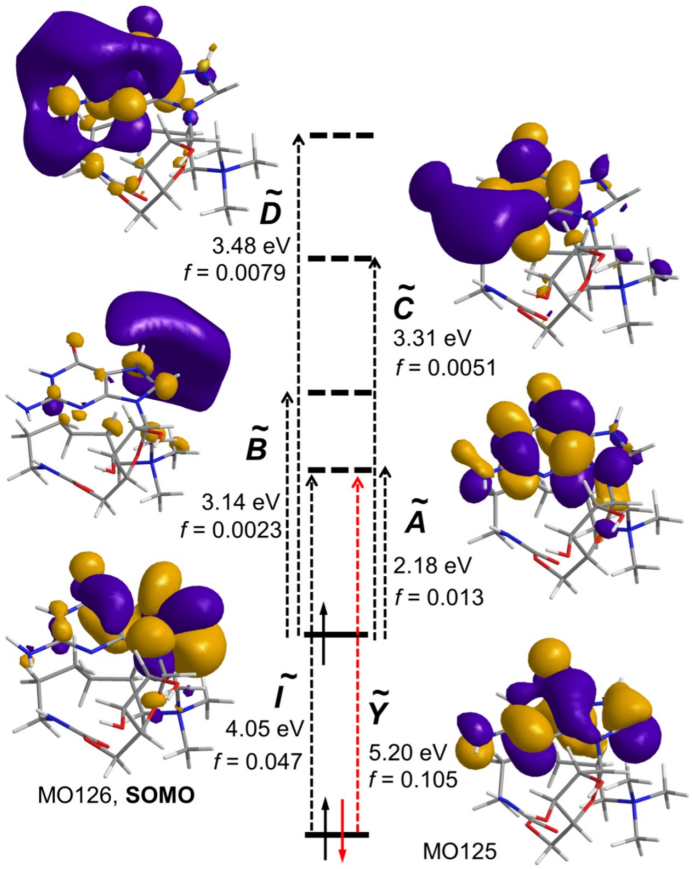

Figure 3.18: Molecular orbital representation of excited states and transitions in $2a^{+\bullet}$. Wave function phases are distinguished by purple and gold color.

excitation to the first (A) excited state. This calculated band, including its vibronic broadening, was in a close agreement with the 580 nm band in the action spectrum (Figure 3.10a). The transition to the A state was identified as a dipole-allowed $\pi_z \rightarrow \pi_z^*$ excitation from the singly occupied molecular orbital (SOMO, MO126) to the virtual orbital space (Figure 3.18). The next three transitions for $2a^{+\bullet}$ (B, C, and D excited states at 395, 374, and 357 nm, respectively), with the pertinent vibronic broadening, gave rise to the broad composite band at 350–450 nm. These excitations occurred from the SOMO to molecular orbitals of the Rydberg (B state) and mixed π_z^*-Rydberg (C and D states) type (Figure 3.18). The intense transition to the I state (306 nm) was due to a $\pi_z \rightarrow \pi_z^*$ type excitation from the doubly

occupied MO125, occurring within the α-MO manifold. Finally, another intense transition to the Y state (239 nm) was also of the $\pi_z \rightarrow \pi_z^*$ type occurring from the doubly occupied MO125, but within the β-MO manifold. In contrast, the absorption spectrum of the N-3-H tautomer ($2d^{+\bullet}$) displayed only very weak transitions in the visible and near-UV regions, as exemplified by the A and B states at 476 and 355 nm (Figure 3.17c). The major bands at 225–230 nm in the calculated vibronic spectrum of $2d^{+\bullet}$ were not prominently represented in the action spectrum. These combined features eliminated $2d^{+\bullet}$ as a plausible structure candidate. The absorption spectrum of the O-6-H tautomer ($2f^{+\bullet}$) did show some similarities with the action spectrum due to excitation to the B-L states in the 270–400 nm region (Figure 3.17b). However, the band pertaining to the transition to the A state (541 nm) was spread over a broad range of wavelengths upon vibronic broadening and did not represent a recognizable feature. Similarly, the most intense transition in $2f^{+\bullet}$ at 216 nm (Figure 3.17b) was not realized as an intense band in the action spectrum. On the basis of this comparison, and considering the match of the closely related $1a^{+\bullet}$ absorption spectrum with the action spectrum of $(\mathbf{1}+H)^{+\bullet}$ (Figure 3.9a), we conclude that both these gas-phase ions were N-7-H tautomers.

3.3.4 Ion Dissociations and Isotope Effects

The spontaneous loss of H and guanine from thermal $(\mathbf{1}+H)^{+\bullet}$ and $(\mathbf{2}+H)^{+\bullet}$ suggested that these dissociations had low activation energies, similar to those previously reported for adenosine conjugates.[32] The spontaneous loss of H chiefly (>95%) involved the exchangeable hydrogens in $(\mathbf{1}+H)^{+\bullet}$ and $(\mathbf{2}+H)^{+\bullet}$, as evidenced by the spectra of the D-labeled analogues. Upon collisional activation of $(D_6\text{-}\mathbf{2}+D)^{+\bullet}$, there was a 50/50 loss of H and D from the guanine moiety (Figure 3.7c, inset). Loss of H can proceed in $1a^{+\bullet}$ –$1g^{+\bullet}$ and $2a^{+\bullet}$ –$2f^{+\bullet}$ to convergently form the lowest energy guanine N-1-H tautomer, such as 3^+ (Figure 3.19). We used BOMD and DFT calculations to determine the transition states (TS) for the dissociation of the N-7–H bond in $2a^{+\bullet}$ and $2b^{+\bullet}$. The loss of H from $2a^{+\bullet}$ had a low threshold energy of $\Delta H_{0,rxn} = 59$ kJ mol^{-1} (Table 3.3). Transition states for N-7–H bond dissociations, TS1–TS4,

were found at 94–106 kJ mol^{-1} relative to 2a$^{+\bullet}$ (Table 3.3). The dissociating bonds showed a moderate N-7$\cdots$H separation in TS1 and TS2, 1.492 and 1.477 Å, respectively (Figure 3.19), and similarly for TS3 and TS4 (Figure 3.20). The conformationally optimized structures of TS1–TS4 revealed substantial changes in the side chain folding compared to those in 2a$^{+\bullet}$ and 2b$^{+\bullet}$. In general, reaching the TS was associated with a side-chain unfolding away from the imidazole ring, regardless of the syn- or anti-facial position of the departing hydrogen atom. The N-7–H bond dissociation led to the formation of a weak complex of the H atom with the guanosine conjugate, as represented by 2j$^{+\bullet}$ and 2k$^{+\bullet}$ (Figure 3.19). The conformational diversity of TS1–TS4, as well as their similar energies, indicated that there may be multiple transition states for the N-7-H loss, converging to conformers of the reaction product 3^{+}.

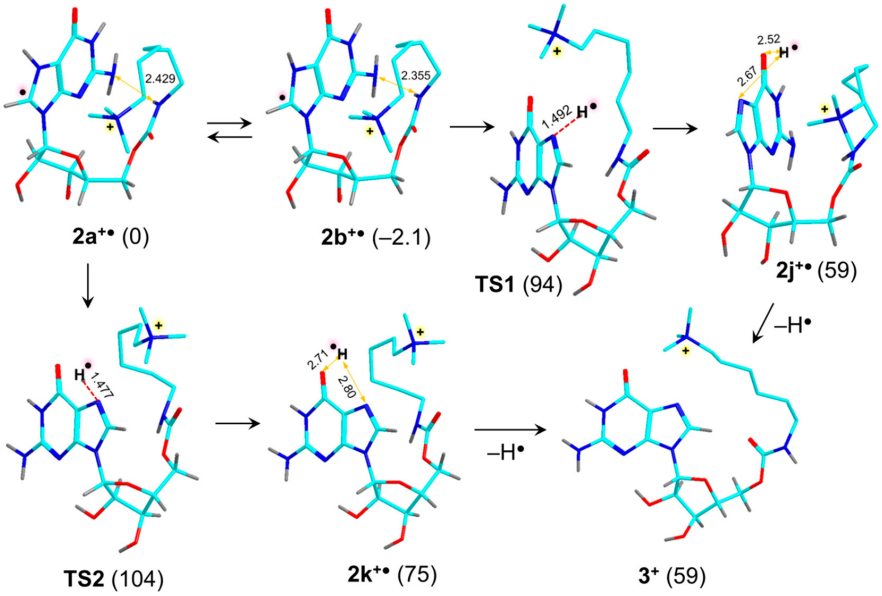

Figure 3.19: M06-2X/6-31+G(d,p) optimized transition states, intermediate complexes and dissociation products. Relative 0 K energies in kJ mol^{-1} in parentheses.

The dissociation by loss of guanine (Figure 3.21) was calculated to produce ion 4$^{+\bullet}$ and the N-7-H tautomer of neutral guanine at a very low threshold energy (46 kJ mol^{-1}, Table 3.3), which was further reduced for the calculated free energy change because of the gain of rotational and translational entropy of the products, resulting in an exoergic dissociation

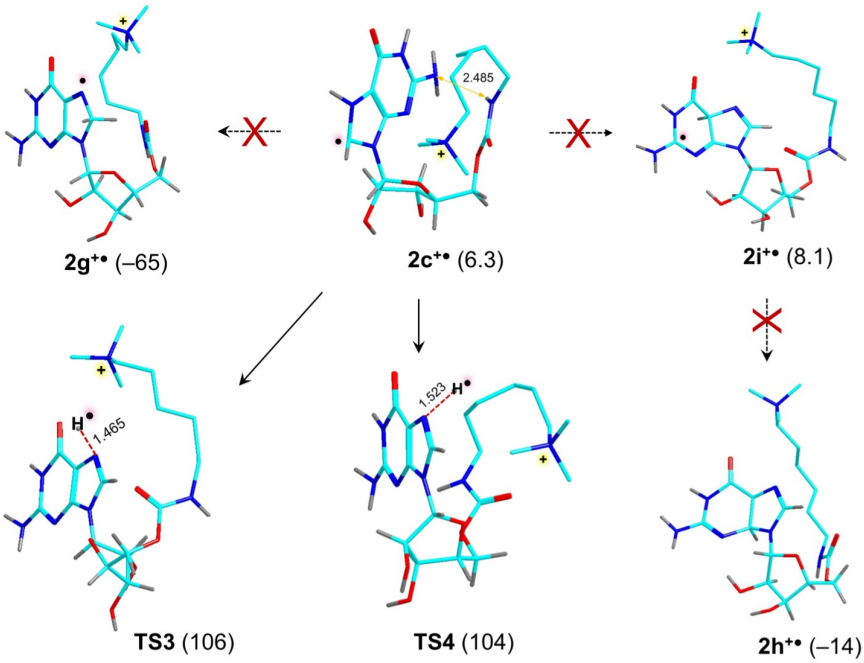

Figure 3.20: M06-2X/6-31+G(d,p) optimized structures and M06-2X/6-311++G(2d,p) relative energies (0 K, kJ mol^{-1}) of guanosine radical isomers and transition states.

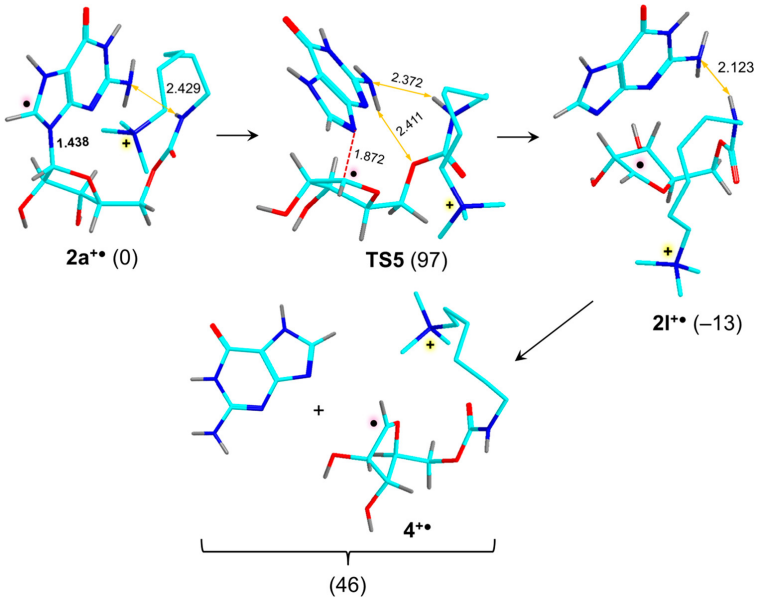

Figure 3.21: Loss of Guanine from Conjugate 2a$^{+\bullet}$ [a]. [a]: Relative 0 K energies in kJ mol^{-1} in parentheses.

($\Delta G_{rxn,310}$ = -13 kJ mol^{-1}) overall. Because of the protonation pattern in 2a$^{+\bullet}$ the neutral guanine molecule was formed as the most stable N-7-H tautomer.[39–41] Investigation of the dissociation pathway for the loss of guanine revealed multiple transition states differing in the side-chain conformation. The lowest energy TS5 was 97 kJ mol^{-1} relative to 2a$^{+\bullet}$ (Table 3.3) and was stabilized by hydrogen bonding between the side-chain carbamate and guanine NH2 groups (Figure 3.21). The separation of N-9 and C-1' in TS5 was remarkably small (1.872 Å, Figure 3.21), indicating a bond elongation of only 0.43 Å(30%) in an early transition state. Accordingly, the N-9–C-1' bond dissociation was exoergic, forming an ion–molecule complex (2l$^{+\bullet}$), which was at -13 kJ mol^{-1} relative to 2a$^{+\bullet}$ at 0 K.

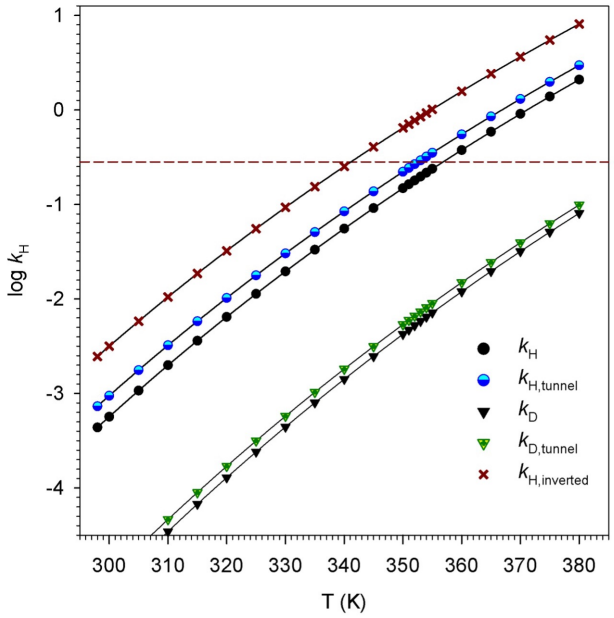

Figure 3.22: TST-calculated rate constants for H and D loss from 2a$^{+\bullet}$ and D_7-2a$^{+\bullet}$. Rate constants k_H,tunnel and k_D,tunnel include corrections for tunneling through parabolic energy barriers with curvatures estimated from the imaginary frequencies, |ΔN–H|= 835 cm-1 and |ΔN–D|= 615 cm^{-1} for TS1 and D_7-TS1, respectively. Rate constant k_H,inverted was calculated for dissociation of 2b$^{+\bullet}$.

We used the lowest energy TS1 for transition-state-theory calculations of the thermal rate constant for the loss of H from 2a$^{+\bullet}$ and 2b$^{+\bullet}$ (k_H). The calculated k_H, as well as the rate constant for the guanine loss (k_{guan}), bracketed the experimental rate constants in the same

narrow interval of temperatures of 340–355 K (Figure 3.22), which were consistent with the typical effective temperatures of ions stored in ion traps.[42–45] The calculated rate constant ratio in this temperature interval, k_{guan}/k_H = 0.079–0.099, was close to the experimental ratio (0.077–0.096). However, TST calculations yielded lower rate constants for the loss of D from D_7-$2a^{+\bullet}$, thus indicating a substantial regular isotope effect (Figure 3.22). This computational result chiefly followed from the standard zero-point energy effect of D substitution that increased the energy of D_7-TS1 relative to D_7-$2a^{+\bullet}$ from 94 to 105 kJ mol^{-1} (Table 3.3). We note that the calculated ratios of partition functions for the TS1 and reactants at 350 K were $Q^{\neq}/Q$ = 2.28 and 2.76 for TS1/$2a^{+\bullet}$ and D_7-TS1/D_7-$2a^{+\bullet}$, respectively, favoring D_7-TS1 by about 20%. However, this small enhancement was insufficient to overcome the much larger effect of increased activation energy.

Inverse isotope effects are usually explained by an isotope-dependent coupled equilibrium that prefers the labeled form (equilibrium isotope effect).[46–49] We examined a possible equilibration of $2a^{+\bullet}$ involving a H-7 or D-7 transfer to an adjacent position. A 1,2-migration of H-7 to C-8 would form ion $2g^{+\bullet}$ (Figure 3.20) which was substantially more stable than $2a^{+\bullet}$ (Table 3.3). However, formation of $2g^{+\bullet}$ as an intermediate would have increased the barrier for H loss to 124 kJ mol^{-1}, which was inconsistent with the rapid kinetics of H/D ejection. Moreover, loss of both D and H should be expected had $2g^{+\bullet}$ been an intermediate, in stark contrast with the experimental results for the spontaneous dissociation. 1,2-Hydrogen atom migration to C-5 would form isomer $2i^{+\bullet}$ of comparable energy as $2a^{+\bullet}$. However, attempts to locate the TS for the 1,2-H migration resulted in dissociation, making $2i^{+\bullet}$ and another low-energy isomer ($2h^{+\bullet}$) kinetically inaccessible from $2a^{+\bullet}$. A tentative explanation of the isotope-effect discrepancy between experiment and TST theory can be invoked from the properties of the potential energy surface post-TS1. The departing hydrogen atom can be temporarily retained in a complex ($2k^{+\bullet}$ or $2j^{+\bullet}$, Figure 3.19), which was calculated to be a potential energy minimum in equilibrium with $2a^{+\bullet}$ or $2b^{+\bullet}$. Complex $2j^{+\bullet}$ was isoenergetic with the products (both at 59 kJ mol^{-1} relative to $2a^{+\bullet}$, Table 3.3), which was due to a stabilizing refolding of the side chain in 3^+ which must have involved a free- energy barrier

(Figure 3.19). Similarly, complex $2k^{+\bullet}$, which was a local energy minimum but above the lowest energy products, owed its existence to a side-chain conformation change on the route to 3^+ that was associated with a free-energy barrier. Unfortunately, calculating these energy barriers turned out to be very demanding and we did not pursue it. Importantly, the reverse H$\cdots$N-7 recombination in $2k^{+\bullet}$ was calculated to be 5.7 fold faster at 350 K than the D$\cdots$N-7 recombination in D_7-$2k^{+\bullet}$. Thus, if the overall dynamics of the loss of H and D from complexes $2j^{+\bullet}$ or $2k^{+\bullet}$ and their D_7-isotopologues preferred the departure of the heavier isotope, the inverse isotope effect could be attributed to an isotope-dependent coupled equilibrium involving H-atom complexes with the conformers of product ion 3^+. This could be investigated by all-electron molecular dynamics starting from the transition state and including vibrationally excited H-atom complexes. However, because of the open-shell nature of the system and relatively small variations of the potential energy surface, such calculations would require an ab initio Hamiltonian and a basis set of good quality to capture the dissociation kinetics, which is beyond the scope of the present work.

3.4 Conclusions

Elusive guanosine radicals representing hydrogen atom adducts to guanine, $(G+H)^\bullet$, were generated for the first time in the gas phase in the form of conjugates carrying a fixed-charge trialkylammonium group. The successful generation necessitated an indirect approach, consisting of electron transfer dissociation of a noncovalent crown-ether complexes of the doubly charged conjugates. This technique appears to be generally applicable to forming fragile biomolecular radicals in the gas phase. The charged tag was transparent in the 210–700 nm range, and its absorption did not interfere with that of the nucleoside radical that can be studied by ion action spectroscopy. Charge-tagged guanosine radicals represent a case of transient intermediates that are susceptible to spontaneous dissociation that makes them a challenging target for experimental studies. At the same time, the conformational flexibility of the charged tag requires Born–Oppenheimer molecular dynamics to adequately treat the ion thermodynamics and obtain conformationally optimized transition states. Despite these

difficulties, we were able to spectroscopically characterize the ions as being guanosine N-7-H radical tautomers. The absorption bands in the visible and near-UV regions of the spectrum were found to be characteristic of guanosine radicals of this position-specific $(G+H)^{\bullet}$ type while distinguishing them from other radical protomers. This UV–vis absorption characteristic can be used to identify guanine radicals in more complex guanine-containing oligonucleotide and DNA radicals of relevance for DNA damage. The guanine radical dissociations were found to display a large inverse isotope effect on the spontaneous loss of H. Accurate treatment of this effect using ab initio molecular dynamics appears to be necessary to explain this interesting observation.

3.5 Bibliography

[1] D Dougherty, ES Younathan, R Voll, S Abdulnur, and SP McGlynn. Photoelectron spectroscopy of some biological molecules. *Journal of Electron Spectroscopy and Related Phenomena*, 13(3):379–393, 1978.

[2] Hong Xie, Daiwen Yang, Adam Heller, and Zhiqiang Gao. Electrocatalytic oxidation of guanine, guanosine, and guanosine monophosphate. *Biophysical journal*, 92(8):L70–L72, 2007.

[3] Claus AM Seidel, Andreas Schulz, and Markus HM Sauer. Nucleobase-specific quenching of fluorescent dyes. 1. nucleobase one-electron redox potentials and their correlation with static and dynamic quenching efficiencies. *The Journal of Physical Chemistry*, 100(13):5541–5553, 1996.

[4] Steen Steenken and Slobodan V Jovanovic. How easily oxidizable is dna? one-electron reduction potentials of adenosine and guanosine radicals in aqueous solution. *Journal of the american chemical society*, 119(3):617–618, 1997.

[5] Sriram Kanvah, Joshy Joseph, Gary B Schuster, Robert N Barnett, Charles L Cleveland,

and UZI Landman. Oxidation of dna: damage to nucleobases. *Accounts of chemical research*, 43(2):280–287, 2010.

[6] Katsuhito Kino, Masayo Hirao-Suzuki, Masayuki Morikawa, Akane Sakaga, and Hiroshi Miyazawa. Generation, repair and replication of guanine oxidation products. *Genes and Environment*, 39(1):1–8, 2017.

[7] Anna Szyperska, Janusz Rak, Jerzy Leszczynski, Xiang Li, Yeon Jae Ko, Haopeng Wang, and Kit H Bowen. Valence anions of 9-methylguanine- 1-methylcytosine complexes. computational and photoelectron spectroscopy studies. *Journal of the American Chemical Society*, 131(7):2663–2669, 2009.

[8] Hsing-Yin Chen, Chai-Lin Kao, and Sodio CN Hsu. Proton transfer in guanine- cytosine radical anion embedded in b-form dna. *Journal of the American Chemical Society*, 131(43):15930–15938, 2009.

[9] Yang Liu, Joseph A Korn, Andy Dang, and František Tureček. Hydrogen-rich cation radicals of dna dinucleotides: Generation and structure elucidation by uv–vis action spectroscopy. *The Journal of Physical Chemistry B*, 122(42):9665–9680, 2018.

[10] Joshua J Coon, Beatrix Ueberheide, John EP Syka, Deanna D Dryhurst, Juan Ausio, Jeffrey Shabanowitz, and Donald F Hunt. Protein identification using sequential ion/ion reactions and tandem mass spectrometry. *Proceedings of the National Academy of Sciences*, 102(27):9463–9468, 2005.

[11] Scott A Shaffer and František Tureček. Hydrogentrimethylammonium: A marginally stable hypervalent radical. *Journal of the American Chemical Society*, 116(19):8647–8653, 1994.

[12] Lars Frøsig and František Tureček. Hypervalent pyrrolidinium radicals by neutralization—reionization mass spectrometry: Metastability and radical leaving group abilities. *Journal of the American Society for Mass Spectrometry*, 9(3):242–254, 1998.

[13] Andy Dang, Joseph A Korn, James Gladden, Brandon Mozzone, and František Tureček. Uv–vis photodissociation action spectroscopy on thermo ltq-xl etd and bruker amazon ion trap mass spectrometers: a practical guide. *Journal of The American Society for Mass Spectrometry*, 30(9):1558–1564, 2019.

[14] Christopher J Shaffer, Prokopis C Andrikopoulos, Jan Řezáč, Lubomír Rulíšek, and František Tureček. Efficient covalent bond formation in gas-phase peptide–peptide ion complexes with the photoleucine stapler. *Journal of the American Society for Mass Spectrometry*, 27(4):633–645, 2016.

[15] Huong TH Nguyen, Prokopis C Andrikopoulos, Daniel Bím, Lubomír Rulíšek, Andy Dang, and František Tureček. Radical reactions affecting polar groups in threonine peptide ions. *The Journal of Physical Chemistry B*, 121(27):6557–6569, 2017.

[16] Jan Řezáč, Jindřich Fanfrlík, Dennis Salahub, and Pavel Hobza. Semiempirical quantum chemical pm6 method augmented by dispersion and h-bonding correction terms reliably describes various types of noncovalent complexes. *Journal of Chemical Theory and Computation*, 5(7):1749–1760, 2009.

[17] Herman JC Berendsen, JPM van Postma, Wilfred F Van Gunsteren, ARHJ DiNola, and Jan R Haak. Molecular dynamics with coupling to an external bath. *The Journal of chemical physics*, 81(8):3684–3690, 1984.

[18] Jan Řezáč. Cuby: An integrative framework for computational chemistry, 2016.

[19] James JP Stewart. Stewart computational chemistry. *http://openmopac. net/*, 2007.

[20] Axel D Becke. Density-functional exchange-energy approximation with correct asymptotic behavior. *Physical review A*, 38(6):3098, 1988.

[21] M. J. Frisch, G. W. Trucks, H. B. Schlegel, G. E. Scuseria, M. A. Robb, J. R. Cheeseman, G. Scalmani, V. Barone, G. A. Petersson, H. Nakatsuji, X. Li, M. Caricato,

A. V. Marenich, J. Bloino, B. G. Janesko, R. Gomperts, B. Mennucci, H. P. Hratchian, J. V. Ortiz, A. F. Izmaylov, J. L. Sonnenberg, D. Williams-Young, F. Ding, F. Lipparini, F. Egidi, J. Goings, B. Peng, A. Petrone, T. Henderson, D. Ranasinghe, V. G. Zakrzewski, J. Gao, N. Rega, G. Zheng, W. Liang, M. Hada, M. Ehara, K. Toyota, R. Fukuda, J. Hasegawa, M. Ishida, T. Nakajima, Y. Honda, O. Kitao, H. Nakai, T. Vreven, K. Throssell, J. A. Montgomery, Jr., J. E. Peralta, F. Ogliaro, M. J. Bearpark, J. J. Heyd, E. N. Brothers, K. N. Kudin, V. N. Staroverov, T. A. Keith, R. Kobayashi, J. Normand, K. Raghavachari, A. P. Rendell, J. C. Burant, S. S. Iyengar, J. Tomasi, M. Cossi, J. M. Millam, M. Klene, C. Adamo, R. Cammi, J. W. Ochterski, R. L. Martin, K. Morokuma, O. Farkas, J. B. Foresman, and D. J. Fox. Gaussian˜16 Revision A.01, 2016. Gaussian Inc. Wallingford CT.

[22] Richard B McClurg, Richard C Flagan, and William A Goddard III. The hindered rotor density-of-states interpolation function. *The Journal of chemical physics*, 106(16):6675–6680, 1997.

[23] Yan Zhao and Donald G Truhlar. The m06 suite of density functionals for main group thermochemistry, thermochemical kinetics, noncovalent interactions, excited states, and transition elements: two new functionals and systematic testing of four m06-class functionals and 12 other functionals. *Theoretical chemistry accounts*, 120(1):215–241, 2008.

[24] Filipp Furche and Reinhart Ahlrichs. Adiabatic time-dependent density functional methods for excited state properties. *The Journal of chemical physics*, 117(16):7433–7447, 2002.

[25] Shu R Huang and František Tureček. Cation radicals of hachimoji nucleobases. canonical purine and noncanonical pyrimidine forms generated in the gas phase and characterized by uv–vis photodissociation action spectroscopy. *The Journal of Physical Chemistry A*, 124(35):7101–7112, 2020.

[26] Shu R Huang, Andy Dang, and František Tureček. Ground and excited states of gas-

phase dna nucleobase cation-radicals. a uv–vis photodisociation action spectroscopy and computational study of adenine and 9-methyladenine. *Journal of the American Society for Mass Spectrometry*, 31(6):1271–1281, 2020.

[27] Donald C Comeau and Rodney J Bartlett. The equation-of-motion coupled-cluster method. applications to open-and closed-shell reference states. *Chemical Physics Letters*, 207(4-6):414–423, 1993.

[28] E. Wigner. On the quantum correction for thermodynamic equilibrium. *Phys. Rev.*, 40:749–759, Jun 1932.

[29] Vlasta Bonačić-Koutecký and Roland Mitrić. Theoretical exploration of ultrafast dynamics in atomic clusters: Analysis and control. *Chemical reviews*, 105(1):11–66, 2005.

[30] Mario Barbatti, Matthias Ruckenbauer, Felix Plasser, Jiri Pittner, Giovanni Granucci, Maurizio Persico, and Hans Lischka. Newton-x: a surface-hopping program for nonadiabatic molecular dynamics. *Wiley Interdisciplinary Reviews: Computational Molecular Science*, 4(1):26–33, 2014.

[31] Joseph A Korn, Jan Urban, Andy Dang, Huong TH Nguyen, and František Tureček. Uv–vis action spectroscopy reveals a conformational collapse in hydrogen-rich dinucleotide cation radicals. *The Journal of Physical Chemistry Letters*, 8(17):4100–4107, 2017.

[32] Yue Liu, Andy Dang, Jan Urban, and František Tureček. Charge-tagged dna radicals in the gas phase characterized by uv/vis photodissociation action spectroscopy. *Angewandte Chemie International Edition*, 132(20):7846–7851, 2020.

[33] Joseph E McClellan, James P Murphy, Joseph J Mulholland, and Richard A Yost. Effects of fragile ions on mass resolution and on isolation for tandem mass spectrometry in the quadrupole ion trap mass spectrometer. *Analytical chemistry*, 74(2):402–412, 2002.

[34] Danielle L Swaney, Graeme C McAlister, Matthew Wirtala, Jae C Schwartz, John EP Syka, and Joshua J Coon. Supplemental activation method for high-efficiency electron-transfer dissociation of doubly protonated peptide precursors. *Analytical chemistry*, 79(2):477–485, 2007.

[35] Robert Pepin, Erik D Layton, Yang Liu, Carlos Afonso, and František Tureček. Where does the electron go? stable and metastable peptide cation radicals formed by electron transfer. *Journal of The American Society for Mass Spectrometry*, 28(1):164–181, 2016.

[36] Carles Colominas, Francisco J Luque, and Modesto Orozco. Tautomerism and protonation of guanine and cytosine. implications in the formation of hydrogen-bonded complexes. *Journal of the American Chemical Society*, 118(29):6811–6821, 1996.

[37] Antarip Halder, Sohini Bhattacharya, Ayan Datta, Dhananjay Bhattacharyya, and Abhijit Mitra. The role of n7 protonation of guanine in determining the structure, stability and function of rna base pairs. *Physical Chemistry Chemical Physics*, 17(39):26249–26263, 2015.

[38] RR Wu, Bo Yang, G Berden, J Oomens, and MT Rodgers. Gas-phase conformations and energetics of protonated 2'-deoxyguanosine and guanosine: Irmpd action spectroscopy and theoretical studies. *The Journal of Physical Chemistry B*, 118(51):14774–14784, 2014.

[39] Amir Karton. Thermochemistry of guanine tautomers re-examined by means of high-level ccsd (t) composite ab initio methods. *Australian Journal of Chemistry*, 72(8):607–613, 2019.

[40] Michal Hanus, Filip Ryjácek, Martin Kabelác, Tomáš Kubař, Tetyana V Bogdan, Semen A Trygubenko, and Pavel Hobza. Correlated ab initio study of nucleic acid bases and their tautomers in the gas phase, in a microhydrated environment and in aqueous

solution. guanine: surprising stabilization of rare tautomers in aqueous solution. *Journal of the American Chemical Society*, 125(25):7678–7688, 2003.

[41] Jiří Šponer and Pavel Hobza. Molecular interactions of nucleic acid bases. a review of quantum-chemical studies. *Collection of Czechoslovak chemical communications*, 68(12):2231–2282, 2003.

[42] Douglas E Goeringer and Scott A McLuckey. Evolution of ion internal energy during collisional excitation in the paul ion trap: A stochastic approach. *The Journal of chemical physics*, 104(6):2214–2221, 1996.

[43] Scott Gronert. Estimation of effective ion temperatures in a quadrupole ion trap. *Journal of the American Society for Mass Spectrometry*, 9(8):845–848, 1998.

[44] Edward R Lovejoy and Robert R Wilson. Kinetic studies of negative ion reactions in a quadrupole ion trap: Absolute rate coefficients and ion energies. *The Journal of Physical Chemistry A*, 102(13):2309–2315, 1998.

[45] William A Donald, George N Khairallah, and Richard AJ O'Hair. The effective temperature of ions stored in a linear quadrupole ion trap mass spectrometer. *Journal of The American Society for Mass Spectrometry*, 24(6):811–815, 2013.

[46] Gerard Parkin. Temperature-dependent transitions between normal and inverse isotope effects pertaining to the interaction of h- h and c- h bonds with transition metal centers. *Accounts of chemical research*, 42(2):315–325, 2009.

[47] Tan-Yun Cheng and R Morris Bullock. Isotope effects on hydride transfer reactions from transition metal hydrides to trityl cation. an inverse isotope effect for a hydride transfer. *Journal of the American Chemical Society*, 121(13):3150–3155, 1999.

[48] William D Jones. Isotope effects in c- h bond activation reactions by transition metals. *Accounts of chemical research*, 36(2):140–146, 2003.

[49] LS Petralia, A Tsikritea, J Loreau, TP Softley, and BR Heazlewood. Strong inverse kinetic isotope effect observed in ammonia charge exchange reactions. *Nature communications*, 11(1):1–7, 2020.

Chapter 4

CHARGE-TAGGED CYTIDINE RADICALS

Reproduced in part with permission from Yue Liu, Congcong Ma, Gabriela Novakova, Ales Marek, and František Tureček. Charge-tagged nucleosides in the gas phase: Uv–vis action spectroscopy and structures of cytidine cations, dications, and cation radicals. *The Journal of Physical Chemistry A*, 125(28):6096-6108, 2021.

Abstract *Cytidine ribonucleosides were furnished at O5' with fixed-charge 6-trimethylammoniumhexan-1-aminecarbonyl tags and studied by UV–vis photodissociation action spectroscopy in the gas phase to probe isolated nucleobase chromophores in their neutral, protonated, and hydrogen-adduct radical forms. The action spectrum of the doubly charged cytidine conjugate showed bands at 310 and 270 nm that were assigned to the N3- and O2-protonated cytosine tautomers formed by electrospray, respectively. In contrast, cytidine conjugates coordinated to dibenzo-18-crown-6-ether (DBCE) in a noncovalent complex were found to strongly favor protonation at N3, forming a single-ion tautomer. This allowed us to form cytidine N3–H radicals by electron transfer dissociation of the complex and study their action spectra. Cytidine radicals showed only very weak absorption in the visible region of the spectrum for dipole-disallowed transitions to the low (A and B) excited states. The main bands were observed at 360, 300, and 250 nm that were assigned with the help of theoretical vibronic spectra obtained by time-dependent density functional theory calculations of multiple (>300) radical vibrational configurations. Collision-induced dissociations of cytidine radicals proceeded by major cleavage of the N1–C1' glycosidic bond leading to loss of cytosine and competitive loss of N3-hydrogen atom. These dissociations were characterized by calculations of transition-state structures and energies using combined Born–Oppenheimer molecular dynamics and*

DFT calculations. Overall, cytidine radicals were found to be kinetically and thermodynamically more stable than previously reported analogous adenosine and guanosine radicals.

4.1 Introduction

Capture of a slow secondary electron by a nucleobase forms a transient anion radical, triggering one of the principal pathways for radiative DNA damage.[1, 2] Nucleobase anion radicals are highly reactive, undergoing fast protonation by solvent or other proton sources, producing neutral radicals in the form of hydrogen atom adducts. In particular, radiation damage to cytosine has been the subject of numerous early studies that used pulse radiolysis in solution or solid state to generate cytosine radicals and study them by electron paramagnetic resonance (EPR) spectroscopy. Radicals produced by hydrogen atom addition to cytosine C5, C6, N3, and N7 positions have been reported,[3–9] even though their identity has been a matter of discussion,[10] and their kinetic and thermodynamic stability has not been addressed experimentally. Fast UV–vis spectroscopy is another method that has been used to monitor the formation of transient species related to radiative damage.[11–16] To assign the transient spectra, it is necessary to structurally characterize the absorbing chromophore, which is difficult in mixtures produced by pulse radiolysis and in the absence of well-defined standards. Nucleobase radicals have been shown to be moderate to strong bases in aqueous solution to undergo further protonation.[11–15] For example, the radical hydrogen adduct to cytosine, $(C + H)^{\bullet}$, has been calculated to have a pKa very similar to that of cytosine (pKa 4.6), representing a weak base in water.[17] We have been pursuing an alternative approach to nucleobase radicals that relies on a specific protonation of the nucleobase in the gas phase to generate a stable ion precursor. The ion is isolated by mass and discharged by a single-electron transfer to form the radical to be analyzed by tandem mass spectrometry. Previous research of nucleobase radicals has relied on femtosecond collisional electron transfer to fast (keV kinetic energy) ions and investigation of the kinetics of radical unimolecular dissociations.[18–20] However, limitations due to low number densities of fast neutrals and the microsecond observation time have made spectroscopic studies difficult.[21, 22] Recently, we

have introduced a new method that relies on one-electron reduction in the gas phase of doubly charged conjugates of ribonucleosides.[23, 24] One charge, which is fixed in a remote functional group, serves as a tag to allow mass spectrometric analysis after reduction. The fixed-charge group is designed so as to be transparent in the 210–700 nm wavelength region used to study light absorption by the nucleoside radicals. The other charge is introduced by protonating the nucleobase by electrospray ionization, and its reduction creates the nucleobase radical. Concurrent reduction of the fixed-charge trialkylammonium group is readily distinguished because the incipient hypervalent ammonium radical has a submicrosecond lifetime[25, 26] and dissociates before mass isolation. The reduction step is carried out by an ion–ion reaction of mass-selected ions in an ion trap mass spectrometer that also provides the means for ion manipulations and laser photodissociation (Figure 4.1). We have developed multistage tandem mass spectrometry coupled to UV–vis action spectroscopy[27] in the valence-electron excitation region of 210–700 nm to study nucleoside radicals. Action spectroscopy utilizes wavelength-dependent photodissociation with photofragment ion detection to map the absorption profile of the ion and thus detect its absorption bands.[28–31] This approach has been applied to the generation and UV–vis spectroscopy of charge-tagged adenosine and guanosine radicals that provided reference spectra and helped identify radical structures.[23, 24] Because the charge tags are transparent in the wavelength region of interest, the conjugates can be used to study light absorption of nucleosides carrying neutral, protonated, and radical nucleobases of different electronic structure. We now apply the charge-tagging method for the first specific generation of cytidine radicals in the gas phase and combine it with UV–vis action spectroscopy to study cytidine radical chromophores. Also presented here is an application of the charge-tagging method to obtain UV–vis action spectra of cytidine derivatives carrying the protonated and neutral nucleobase. An important component of these studies has been the application of Born–Oppenheimer molecular dynamics, ab initio, and density functional theory (DFT) calculations to obtain relative energies of conformers and tautomers, transition-state energies for dissociations, as well as time-dependent DFT calculations of vibronic absorption spectra. These are reported here for cytidine radicals.

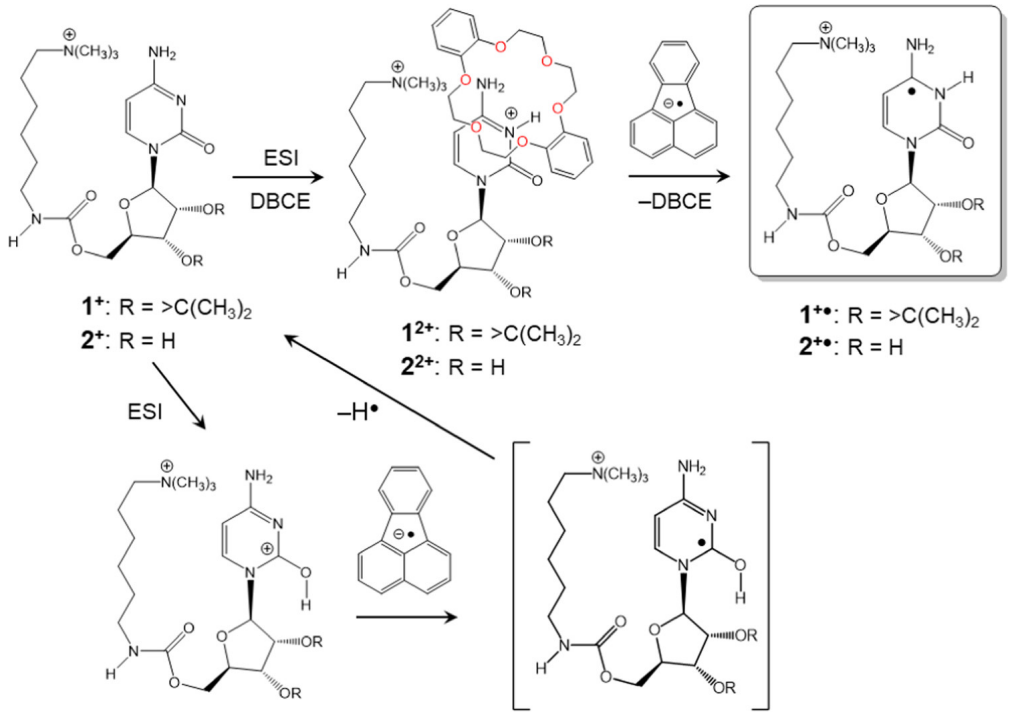

Figure 4.1: Formation of charge-tagged cytidine radicals. DBCE stands for dibenzocrown ether.

4.2 Experimental Section

4.2.1 Materials and Methods

Solvents (methanol, water, acetic acid, HPLC quality) were purchased from Fisher Scientific (Pittsburgh, PA) and distilled to remove dissolved sodium. 2,3:11,12-Dibenzo-18-crown-6-ether (DBCE) was purchased from Sigma-Aldrich (St. Louis, MO). Deuterated solvents (>99% D content) were from Cambridge Isotope Laboratories (Tewksbury, MA). Cytidine conjugate $\mathbf{1}^+$ was prepared as a trifluoroacetate salt as described in Figure 4.2, purified by HPLC chromatography,[24] and characterized by ^{1}H-NMR spectroscopy and high-resolution mass spectrometry. Conjugate $\mathbf{2}^+$ was prepared in situ by deprotection of the 2,3-O'-isopropylidene group in $\mathbf{1}^+$ by treatment with 60% aqueous trifluoroacetic acid for 15 min at room temperature. The solvents were evaporated with a stream of nitrogen and the residue was dissolved in the electrospray solvent, water–methanol–acetic acid, 50:50:1. Mass spectra

and photodissociation action spectra were measured on a modified Bruker amaZon Speed 3D quadrupole ion trap instrument furnished with an auxiliary chemical ionization source for the generation of fluoranthene anions to be used in ion–ion reactions. The mass spectrometer was coupled to an EKSPLA NL301G Nd-YAG laser (Altos Photonics, Bozeman, MT) equipped with a PG142C optical parametric oscillator, as described previously.[27] Photodissociation action spectra were recorded in three wavelength regions, 210–354, 355–409, and 410–700 nm, using 2–3 laser pulses for the cation radicals and 6–10 laser pulses for cations and dications. The laser pulse energies were measured at each experimental wavelength and the photofragment ion intensities were normalized to the number of photons per pulse.

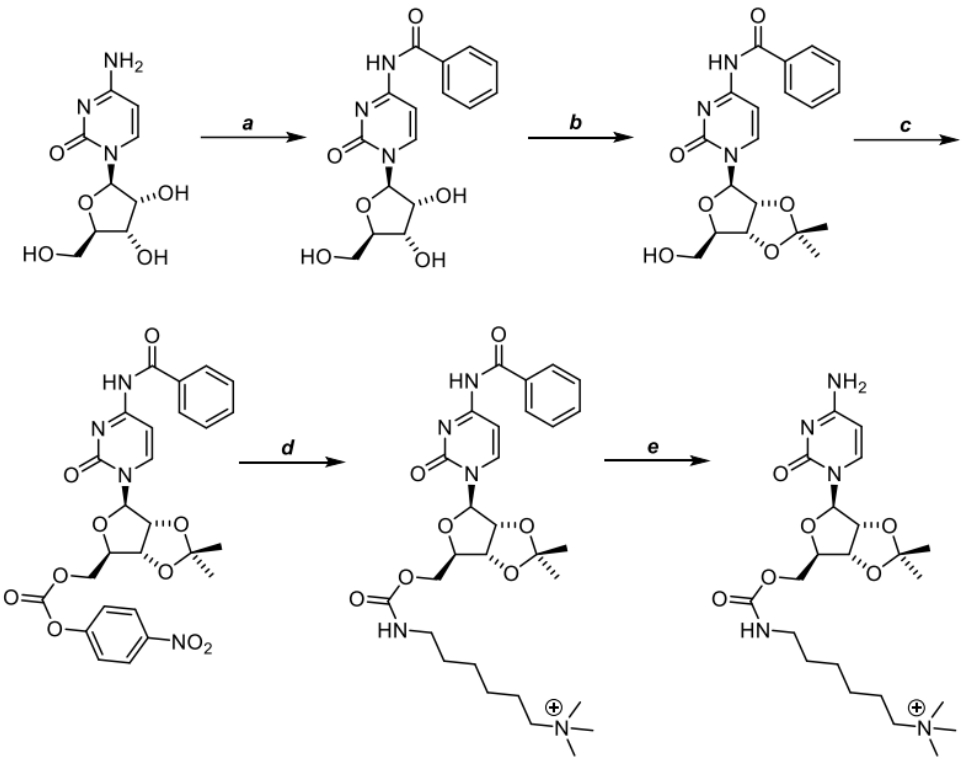

Figure 4.2: Preparation of cytidine conjugate. a:benzoic anhydride, EtOH; b: 2,2-dimethoxypropane, p-TSA.H2O, acetone; c: p-nitrophenylchloroformate, DIPEA, MeCN; d: 6-aminohexyltrimethylamonium trifluoroacetate, DIPEA, MeCN; e: NH4OH/EtOH 1/2

4.2.2 Calculations

Cation, dication, and cation-radical structures were obtained at several levels of theory, starting with conformer analysis and followed by full gradient geometry optimization, transition-state search, and single-point energy calculations. Conformers were generated by Born–Oppenheimer molecular dynamics (BOMD) calculations using the semiempirical, all-valence-electron, PM6 method[32] supplemented with dispersion and hydrogen-bonding corrections, PM6-D3H4,[33] and run by MOPAC[34] under the high-level Cuby4 platform,[35] as described previously.[24] Selected low-energy conformers from the BOMD runs were reoptimized by density functional theory (DFT) calculations using the B3LYP[36] and M06-2X[37] hybrid functionals with the 6-31+G(d,p) basis set. The structures were confirmed as local energy minima by harmonic frequency analysis. Energy ranking was based on single-point energy calculations with M06-2X using the 6-311++G(2d,p) basis set. Calculations of cation radicals were performed for doublet spin states within the spin unrestricted formalism. Transition states (TS) were located by a step-wise procedure including full conformational analysis, as described previously.[24] Briefly, after locating and characterizing the TS by DFT calculations in a few low-energy conformers, the obtained TS were treated by BOMD at 610 K using the Cuby4 platform, in which the bond lengths in the reaction center were fixed at their original TS values, while the other internal coordinates were dynamically free. The resulting conformers were sorted out by energy, and a new search was performed by DFT for low-energy geometries to arrive at the final, conformationally optimized, TS structures which were confirmed by harmonic frequency analysis. Excitation energies and oscillator strengths were obtained for multiple excited states by time-dependent DFT calculations[38] with M06-2X/6-31+G(d,p), according to previous benchmarking studies.[39] Vibronically broadened absorption spectra were obtained by multiple TD-DFT calculations of 24–36 excited states over >300 Wigner vibrational configurations generated by Newton-X software[40] (version 2.0, www.newtonx.org) and weighted according to their Boltzmann factors at 310 K. All of the electronic structure calculations were performed with the Gaussian 16 (Revision A03) suite of

programs.[41] Rice–Ramsperger–Kassel–Marcus (RRKM) calculations[42] of unimolecular rate constants were performed using the QCPE program[43] that was recompiled for Windows.[44] The RRKM calculations were run with direct count of quantum states, and molecular rotations were treated adiabatically. The k(E, J, K) rate constants were Boltzmann-averaged over the rotational state distribution at 300 K.

4.3 Results and Discussion

4.3.1 Cytidine Ion Generation and Action Spectra

Electrospray of cytidine conjugate $\mathbf{1}^+$ produced singly and doubly charged ions, $\mathbf{1}^+$ and $\mathbf{1}^{2+}$, m/z 468 and 234.5, respectively, that were characterized by CID-MS^2 spectra (Figure 4.3a,b) including accurate mass measurements (Table 4.1). Ion $\mathbf{1}^+$ showed dissociations by loss of trimethylamine (m/z 409) and methylcytosine (m/z 343) followed by elimination of a C_3H_6O neutral (m/z 285), presumably originating from the dioxolan ring. The loss of methylcytosine indicated a methyl transfer to the nucleobase which was similar to analogous dissociations of singly charged adenine and guanine conjugates.[23, 24] This unusual methyl-transfer dissociation was absent in the CID spectrum of $\mathbf{1}^{2+}$ which showed the complementary singly charged fragments from the ribose and side chain (m/z 357) and cytosine (m/z 112, Figure 4.3b). The m/z 299 fragment ion in the Figure 4.3b spectrum was assigned to a loss of C3H6O from the dioxolan ring in the m/z 357 primary fragment ion. The absence of methyl transfer upon CID of $\mathbf{1}^{2+}$ can be attributed to Coulomb repulsion keeping the charged groups apart and preventing cytosine interaction with the trimethylammonium group. CID of $\mathbf{2}^{2+}$ gave rise to a very simple spectrum consisting of the complementary fragment ions at m/z 112 and 317 for $CytH^+$ and ($\mathbf{2}^{2+}$ –$CytH^+$), respectively (Figure 4.4a).

The formation of closely related monocations and dications provided us with an opportunity to record action spectra of gas-phase neutral and protonated cytosine chromophores and compare them with previous data reported for neutral[45–50] and protonated cytosine.[51, 52] Note that the other groups in these ions do not absorb light in the 210–700 nm wavelength re-

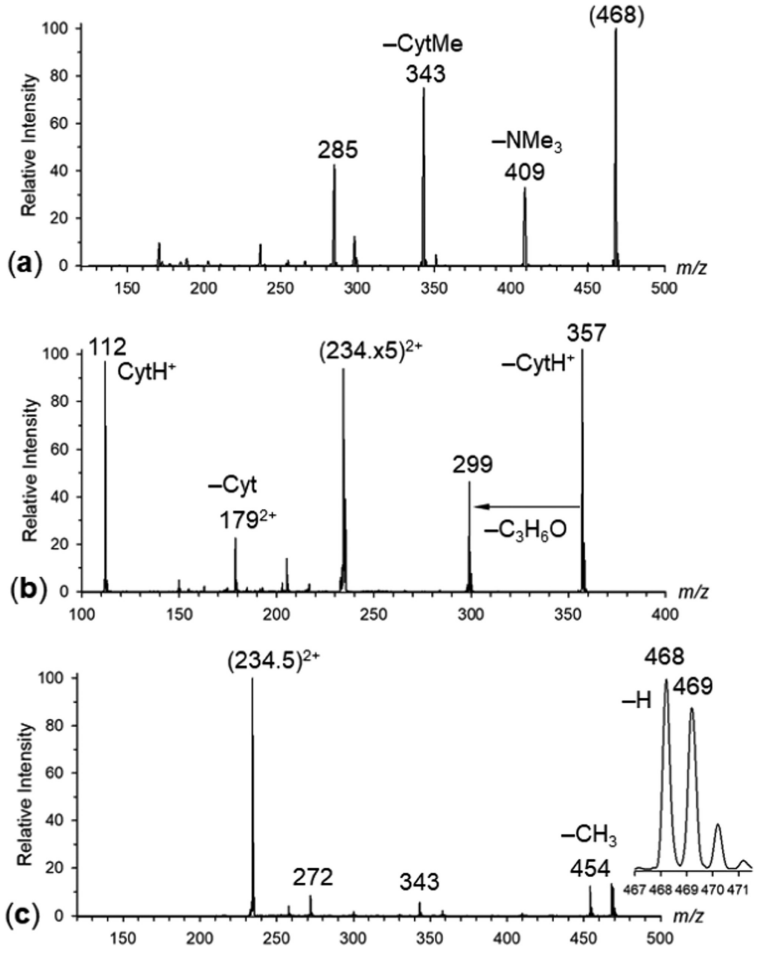

Figure 4.3: CID-MS^2 spectra of (a) $\mathbf{1}^+$ at m/z 468 and (b) $\mathbf{1}^{2+}$ at m/z 234.5. (c) ETD spectrum of $\mathbf{1}^{2+}$.

gion and thus do not interfere with cytosine absorption. The action spectrum of $\mathbf{1}^{2+}$ showed overlapping bands with maxima at 310, 295, 272, 250, and 222 nm that were proportionately carried by all major photodissociation channels at m/z 357, 299, 179, and 112 (Figure 4.5a). The action spectrum of $\mathbf{1}^+$ (Figure 4.5b) showed overlapping bands with maxima at 278, 242, 234, 224, and 214 nm. In this case, the individual photofragment channels showed different wavelength profiles. The m/z 185 ion was the major contributor to the 278 and 242 nm bands, whereas the 216–234 nm bands arose from photodissociations forming the m/z 343 ions. To interpret the spectra, we carried out calculations aimed at establishing structures of low-energy isomers and we used those for determining electronic transitions by

Table 4.1: Accurate ion mass measurements in CID-MS^2 spectra.

Ion	m/z	Composition	Error (millimass)	Assignment
$\mathbf{1}^+$				
	468.2757	$C_{22}H_{38}N_5O_6$	-6.0	M
	409.2030	$C_{19}H_{29}N_4O_6$	-5.2	$-NMe_3$
	343.2186	$C_{17}H_{31}N_2O_5$	-4.1	-(Cyt+CH_3)
	298.1614	$C_{15}H_{24}NO_5$	-3.5	343 – C_2H_7N
	285.1775	$C_{14}H_{25}N_2O_4$	-3.4	343 – C_3H_6O
	237.1318	$C_{11}H_{17}N_4O_2$	-2.8	
	171.1470	$C_9H_{19}N_2O$	-2.2	343 – $C_8H_{12}O_4$
$\mathbf{1}^{2+}$				
	234.6415	$C_22H_{39}N_5O_6{}^{2+}$	-5.9	
	357.2340	$C_18H_{33}N_2O_5$	-4.4	
	299.1929	$C_15H_{27}N_2O_4$	-3.6	357 – C_3H_6O
	205.6208	$C_19H_{33}N_5O_5{}^{2+}$	-5.2	
	150.0997	$C_8H_{12}N_3$	-2.9	
	112.0488	$C_4H_6N_3O$	-1.7	$CytH^+$

time-dependent DFT.

4.3.2 Cytidine Cation Structures and Energetics

The formation of both singly and doubly charged ions from $\mathbf{1}^+$ and $\mathbf{2}^+$ indicated that these species were stable in the gas phase even in the environment of the ion-transfer region where they underwent multiple collisions with much more abundant methanol and water solvent molecules. According to our calculations, low-Gibbs-energy monocations $\mathbf{1}^+$ showed coiled structures, indicating charge–dipole interactions between the side chain and the nucleobase. The lowest-Gibbs-energy cation ($1a^+$) showed a side-chain C5-hydrogen at a 2.6 and 2.4 Å distance to the cytosine O2 and N3, respectively, and another interaction was observed between O2 and a methyl hydrogen at 2.4 Å (Figure 4.6).

Protonation of the cytosine ring in $1a^+$ can occur at O2 or N3,[53] giving rise to O2-protonated dication $1b^{2+}$ or the N3-protonated tautomer $1c^{2+}$, which were the lowest-energy

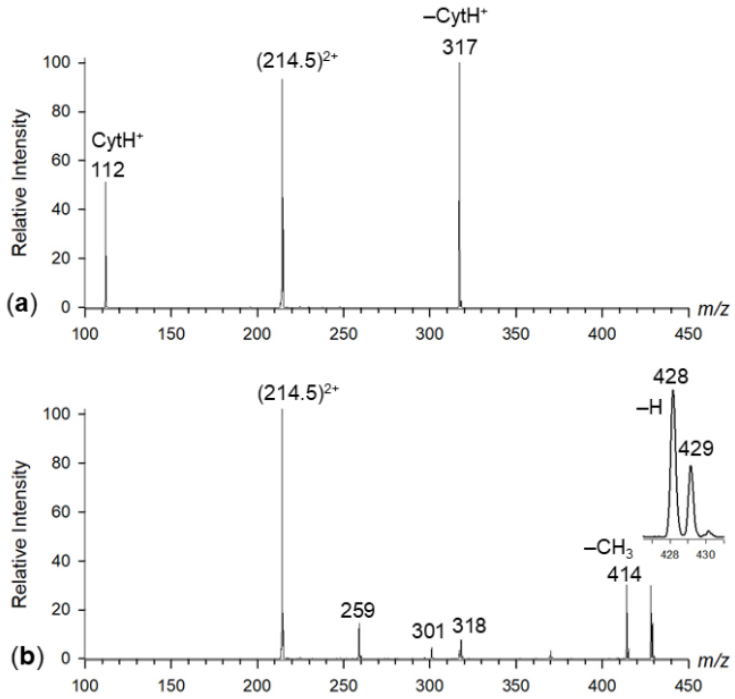

Figure 4.4: (a) CID-MS^2 and (b) ETD-MS^2 of $\mathbf{2}^{2+}$ at m/z 214.5.

conformers in each group (Figure 4.6). Cytosine protonation resulted in a side-chain unfolding in the low-Gibbs-energy dications, which had extended structures to minimize Coulomb repulsion between the charges. The calculated gas-phase basicities (GB) of $1a^+$ slightly preferred protonation at O2 (GB = 750 kJ mol^{-1} for $1b^{2+}$) against N3 of GB = 740 kJ mol^{-1} for $1c^{2+}$. It is noteworthy that the relative Gibbs energies of the N3–H and O2–H dication tautomers were reversed in water-solvated ions where the lowest-energy N3–H tautomer $1c^{2+}$ was 22 kJ mol^{-1} more stable than the O2–H tautomer $1b^{2+}$. This stability reversal may affect the formation of dication tautomers in electrospray.

The deprotected ribocytidine ions ($\mathbf{2}^+$) also showed coiled structures with the cytosine O2 in proximity with the methyl hydrogens. The global Gibbs-energy minimum in this group ($2a^+$) had O2 engaged in a hydrogen bonding with the ribose 2'-OH at 1.85 Å (Figure 4.7). Protonation of $2a^+$ was calculated to be entirely analogous to that of $1a^+$, giving the O2- and N3-protonated tautomers $2b^{2+}$ and $2c^{2+}$ with GB = 750 and 741 kJ mol^{-1}, respectively.

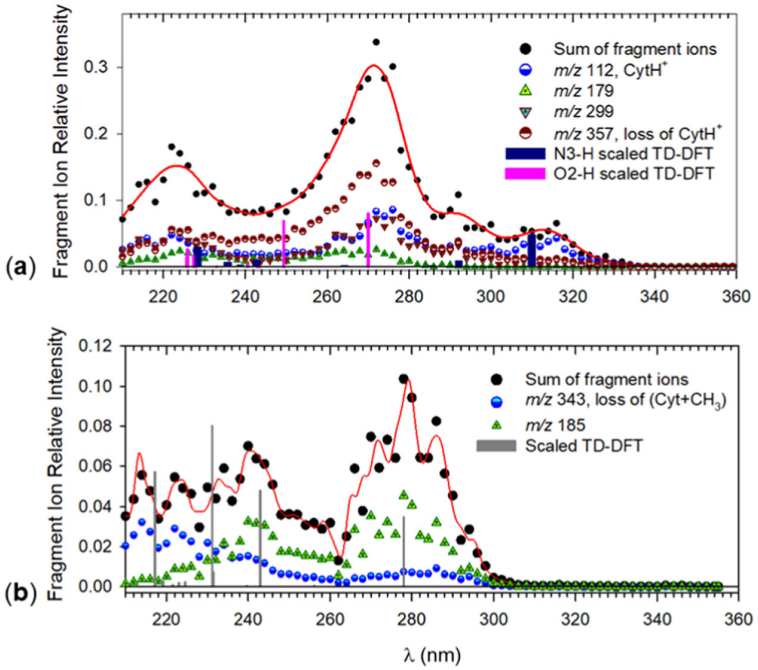

Figure 4.5: UV photodissociation action spectra of (a) $\mathbf{1}^{2+}$ at m/z 234.5 and (b) $\mathbf{1}^{+}$ at m/z 468. No absorption was detected above 350 nm.

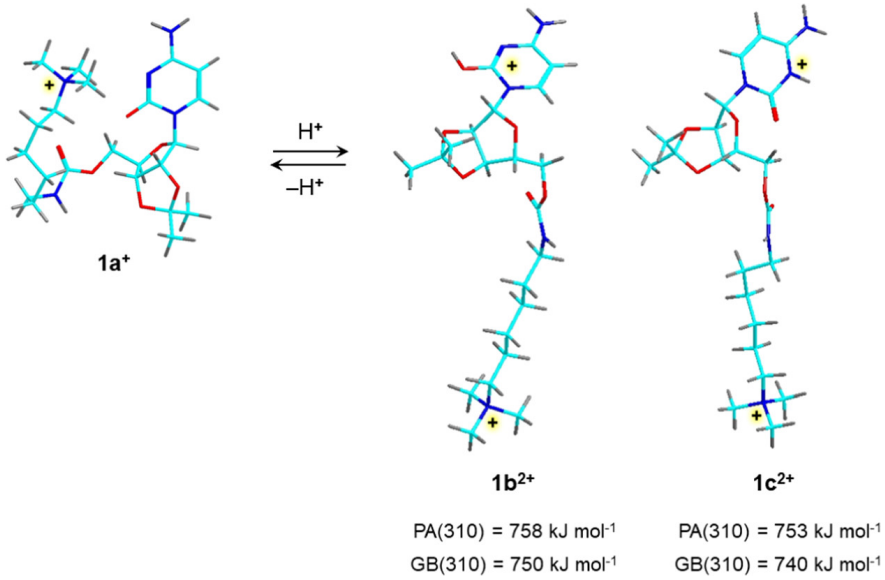

Figure 4.6: Protonation Energetics of Charge-Tagged Cytidine Conjugate $1a^{+}$. Atom color coding is as follows: cyan = C, blue = N, red = O, gray = H.

The relative enthalpies and Gibbs energies, favoring the O2-protonated tautomer $2b^{2+}$, can be compared to those of singly charged cytidine and 2'-deoxycytidine ions that have been calculated to have very similar relative energies slightly favoring N3–H protomers.[53] Both forms have been found to coexist in the gas phase.[54–56] Protonation of $2a^+$ resulted in an unfolding of the side chain, as illustrated by the lowest-Gibbs-energy structures $2b^{2+}$ and $2c^{2+}$ (Figure 4.7). Overall, the calculated protonation energetics of $1a^+$ and $2a^+$ pointed to substantially lower basicity of these cations compared to neutral cytosine (PA = 950 kJ mol^{-1}, GB = 918 kJ mol^{-1})[57] or ribocytidine. For the latter, an approximate experimental PA = 982 kJ mol^{-1} ([58]) and a calculated value (1001 kJ mol^{-1})[56] indicated an up to 51 kJ mol^{-1} decrease of proton affinity in $2a^+$ due to the remote charge effect. Importantly, however, the gas-phase basicity of $1a^+$ and $2a^+$ was higher than those of electrospray solvents water (GB = 660 kJ mol^{-1}), and methanol (GB = 725 kJ mol^{-1}),[57] disfavoring endoergic deprotonation of the dications by gas-phase solvent molecules.

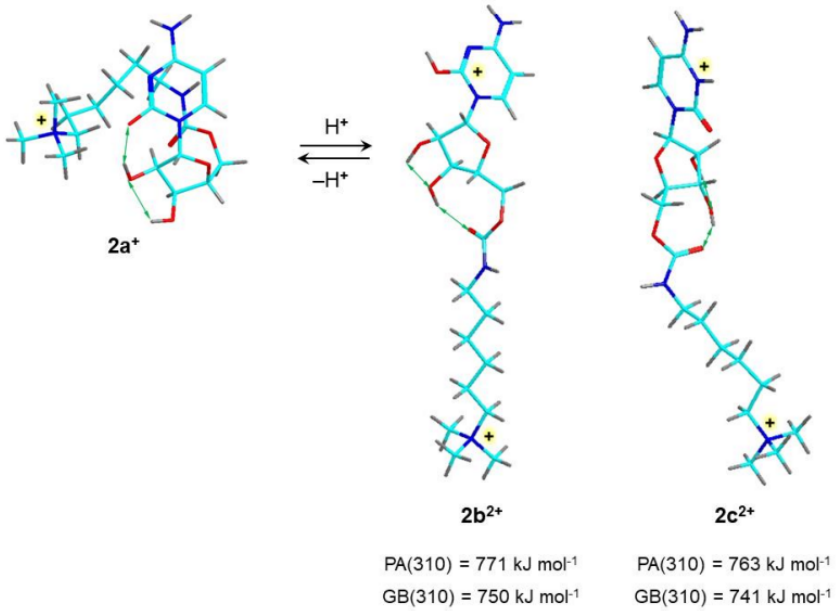

Figure 4.7: Protonation Energetics of Charge-Tagged Cytidine Conjugate $2a^+$. Atom color coding is as follows: cyan = C, blue = N, red = O, gray = H.

In contrast to $1b^{2+}$, $1c^{2+}$, $2b^{2+}$, and $2c^{2+}$, the complexes with DBCE of doubly protonated cytidine ions unequivocally preferred N3-protonated tautomers (Figure 4.8). This substantial reversal of ion-relative Gibbs energies from +10 kJ mol^{-1} for $1b^{2+}$ and $1c^{2+}$ to -56 kJ mol^{-1} in favor of N3 protonation in $(1c{+}DBCE)^{2+}$ can be ascribed to hydrogen bonding to the crown ether. In the N3-protonated ions such as $(1c{+}DBCE)^{2+}$, the cytosine ring developed three stabilizing N–H···O hydrogen bonds to the crown ether, in contrast to the O2-protonated tautomers $(1b{+}DBCE)^{2+}$ that can form only two hydrogen bonds (Figure 4.8).

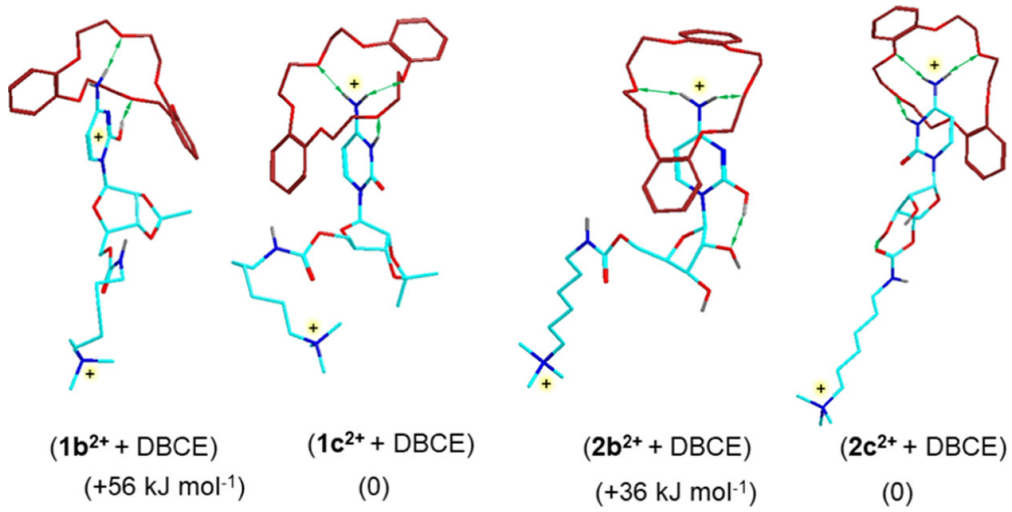

Figure 4.8: M06-2X/6-31+G(d,p) optimized structures of low-energy dication complexes $(\mathbf{1}{+}DBCE)^{2+}$ and $(\mathbf{2}{+}DBCE)^{2+}$. Atom color coding is as follows: cyan = C in the conjugate, brown = C in DBCE, red = O, blue = N, gray = H. Only exchangeable (N–H, O–H) hydrogens are shown to avoid clutter. Hydrogen bonds are shown as double-headed green arrows. The relative Gibbs energies refer to the lowest-energy tautomer/conformer in each group.

The situation was somewhat more intricate for the $(\mathbf{2}{+}DBCE)^{2+}$ complexes (Figure 4.8). The lowest-energy N3-protonated tautomer $(2c{+}DBCE)^{2+}$ again formed three N–H···O hydrogen bonds to DBCE. In the lowest-energy O2-protonated tautomer $(2b{+}DBCE)^{2+}$, at +36 kJ mol^{-1} relative to $(2c{+}DBCE)^{2+}$, the NH_2 group formed only two H bonds to the crown ether while the cytosine 2-OH was H-bonded to ribose 2'-OH (Figure 4.8). Evidently, this stabilizing interaction was less energetically favorable than H-bonding to the crown ether, possibly also because it disrupted H bonding of ribose 3'-OH to the carbamate, which is a

stabilizing factor in $(2c+DBCE)^{2+}$ (Figure 4.8). It is worth noting that solvation in water dielectric further increased the free energy difference between the N3- and O2-protonated complexes in favor of the former. These data strongly indicated that the formation of cytosine N3–H tautomers was favored in gas-phase DBCE complexes.

4.3.3 Cytidine Cation Electronic Spectra

To assign the bands in the action spectra of $\mathbf{1}^{+}$ and $\mathbf{1}^{2+}$, we carried out M06-2X/6-31+G(d,p) TD-DFT calculations of electronic transitions and the pertinent molecular orbitals (MO) in the low-energy monocation $1a^{+}$ and dications $1b^{2+}$ and $1c^{2+}$. The calculated spectra are depicted as vertical lines in Figure 4.5a,b. Since the calculated vertical transitions referred to 0 K and did not capture vibronic redshifts pertinent to the experimental temperature, we only sought in Figure 4.5a,b to distinguish the line patterns by aligning the calculated lines for the first excited states with the experimental maxima of the longest-wavelength bands. The calculated lines for $1c^{2+}$ showed a pattern overlapping with the 310, 295, and 222 nm bands in the action spectrum (Figure 4.5a). The 310 nm band was characteristic of the N3–H tautomer of protonated cytosine which had an onset at 304 nm in the cold-ion spectrum.[51] The 270 nm band in the action spectrum of $\mathbf{1}^{2+}$ was analogous to the band assigned to the O2–H tautomer of protonated cytosine with an onset at 268 nm.[51] The unresolved band at 250 nm, which is best recognizable in the m/z 357 channel (Figure 4.5a), belonged to the O2–H tautomer. The broad 222 nm band had contributions from both N3–H and O2–H tautomers. The composition of the gas-phase ions $\mathbf{1}^{2+}$, as judged from the characteristic UV-band intensities in Figure 4.5a, indicated a slight preference for the O2–H tautomers, perhaps as a result of balancing their opposite Gibbs-energy ranking in the gas-phase and aqueous solution (vide supra).

The nature of the electronic transitions in $\mathbf{1}^{2+}$ was visualized by MO diagrams (Figure 4.9). The highest occupied orbitals in $1b^{2+}$ had most of electron density in the carbamate group π-electronic system (HOMO126) and dioxolan oxygen n-orbitals (MO125) which were away from the cytosine ring. However, electrons in these orbitals did not significantly

participate in transitions to the A and C excited states which represented the two most intense bands in the spectrum. Excitations to the A and C states were by $\pi_z \rightarrow \pi_z^*$ transitions involving the lower-lying cytosine-centered MO124 and virtual orbitals MO127 and MO128 (Figure 4.9). Similarly to $1b^{2+}$, the HOMO in the N3–H tautomer $1c^{2+}$ (MO126) was a π_z orbital localized in the carbamate group (Figure 4.9). Excitation to the A state, representing the 310 nm band in the action spectrum, was due to $\pi_z \rightarrow \pi_z^*$ transitions chiefly involving MO123 and MO121, but also included n-orbitals on the dioxolan ring oxygens.

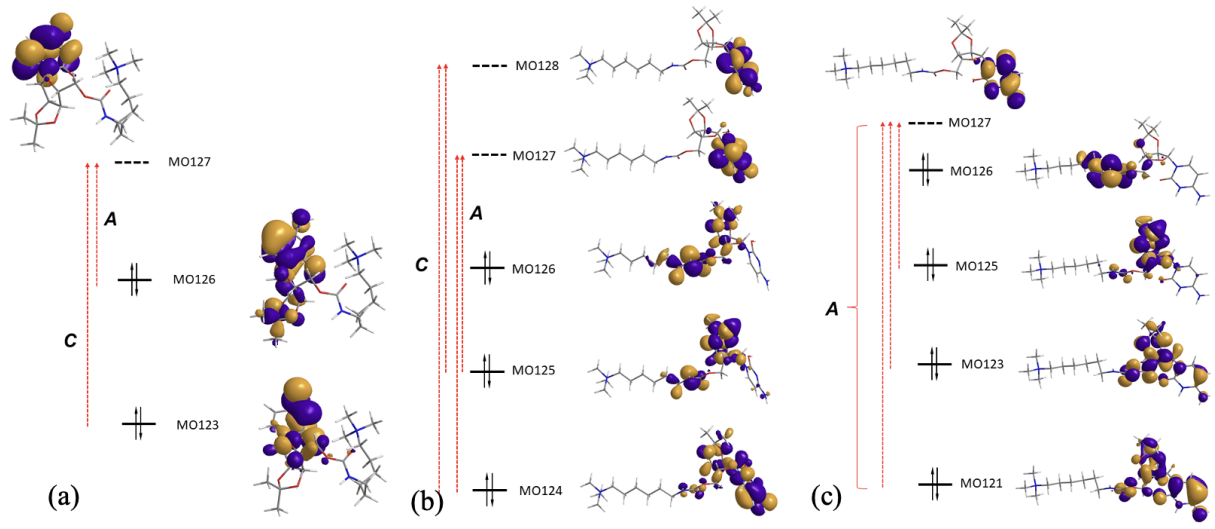

Figure 4.9: Molecular-orbitals for electronic excitations in (a) $1a^{2+}$, (b) $1b^{2+}$, and (c) $1c^{2+}$.

The frontier molecular orbitals and excitations in $1a^+$ were notably different from those in the doubly charged ions. The HOMO (MO126) was a cytosine π_z orbital participating as a major component in the electron transition to MO127 leading to the A state (Figure 4.9). Another intense transition was from MO123 to MO127 leading to the C state. These represented the major bands in the action spectrum of $\mathbf{1}^+$ at 278 and 242 nm (Figure 4.5b). The 278 nm band in the action spectrum was analogous to the 260–270 nm broad absorption band of cytosine in aqueous solution[48] which has been shown by ab initio calculations to also be representative of gas-phase cytosine.[46, 59] The 220–243 nm bands for $1a^+$ were anal-

ogous to the broad band at 205–231 nm in the cytosine spectrum in solution that has been interpreted as arising from $\pi_z \rightarrow \pi_z^*$ electron excitations to the B state.[59, 60] The differences in the electronic structure of isoelectronic ions $\mathbf{1}^+$, on the one hand, and $1b^{2+}$ and $1c^{2+}$, on the other hand, were probably caused by a significant lowering of electron energies in the cytosine π_z orbitals as a result of protonation at N_3 and O_2.

Because of the folded conformations of low-energy $1a^+$ and $2a^+$ conformers in which the charged trimethylammonium group was close to the neutral cytosine ring, we investigated the effect of the side-chain groups on the absorption spectra. The uncorrected TD-DFT spectrum of $2a^+$ (Figure 4.10a) was compared to the spectra of a neutral cytidine derivative with a truncated carbamate side chain (2aa, Figure 4.10b) and ribocytidine (2ab, Figure 4.10c). All of these showed excitations from the cytosine π_z HOMO that represented the most prominent bands at 243, 260, and 261 nm, respectively. The 0.35 eV difference in the excitation energies can be attributed to the stabilization of the ground electronic state in $2a^+$ by the proximate charged group.

4.3.4 Cation-Radical Generation and Action Spectra

Electron transfer to doubly charged ions $\mathbf{1}^{2+}$ and $\mathbf{2}^{2+}$ resulted in substantial dissociation of the respective cation radicals $\mathbf{1}^{+\bullet}$ and $\mathbf{2}^{+\bullet}$. Figure 4.3c shows a major loss of H, CH_3, and chain cleavage upon formation of $\mathbf{1}^{+\bullet}$ from $\mathbf{1}^{2+}$, and similar dissociations were observed for $\mathbf{2}^{+\bullet}$ (Figure 4.4b). To facilitate the generation of stable cation radicals $\mathbf{1}^{+\bullet}$ and $\mathbf{2}^{+\bullet}$, we resorted to ETD of complexes of $\mathbf{1}^{2+}$ and $\mathbf{2}^{2+}$ with dibenzocrown ether (DBCE).[23, 24] ETD of mass-selected $(\mathbf{1}{+}\text{DBCE})^{2+}$ at m/z 414.5 resulted in charge reduction accompanied by loss of the DBCE ligand, providing cation radicals $\mathbf{1}^{+\bullet}$ (m/z 469) in an excellent yield and free of contamination by dissociation byproducts (Figure 4.11a). Similarly, ETD of $(\mathbf{2}{+}\text{DBCE})^{2+}$ at m/z 394.5 resulted in the formation of cation radical $\mathbf{2}^{+\bullet}$ at m/z 429, although in this case, it was accompanied by $\mathbf{2}^+$ at m/z 428 (Figure 4.11b). Both cation radicals were further characterized by CID-MS^3 (Figure 4.11a,b, insets) to map their dissociations and select fragment ions for action spectroscopy. The CID spectrum of $\mathbf{1}^{+\bullet}$ showed a major

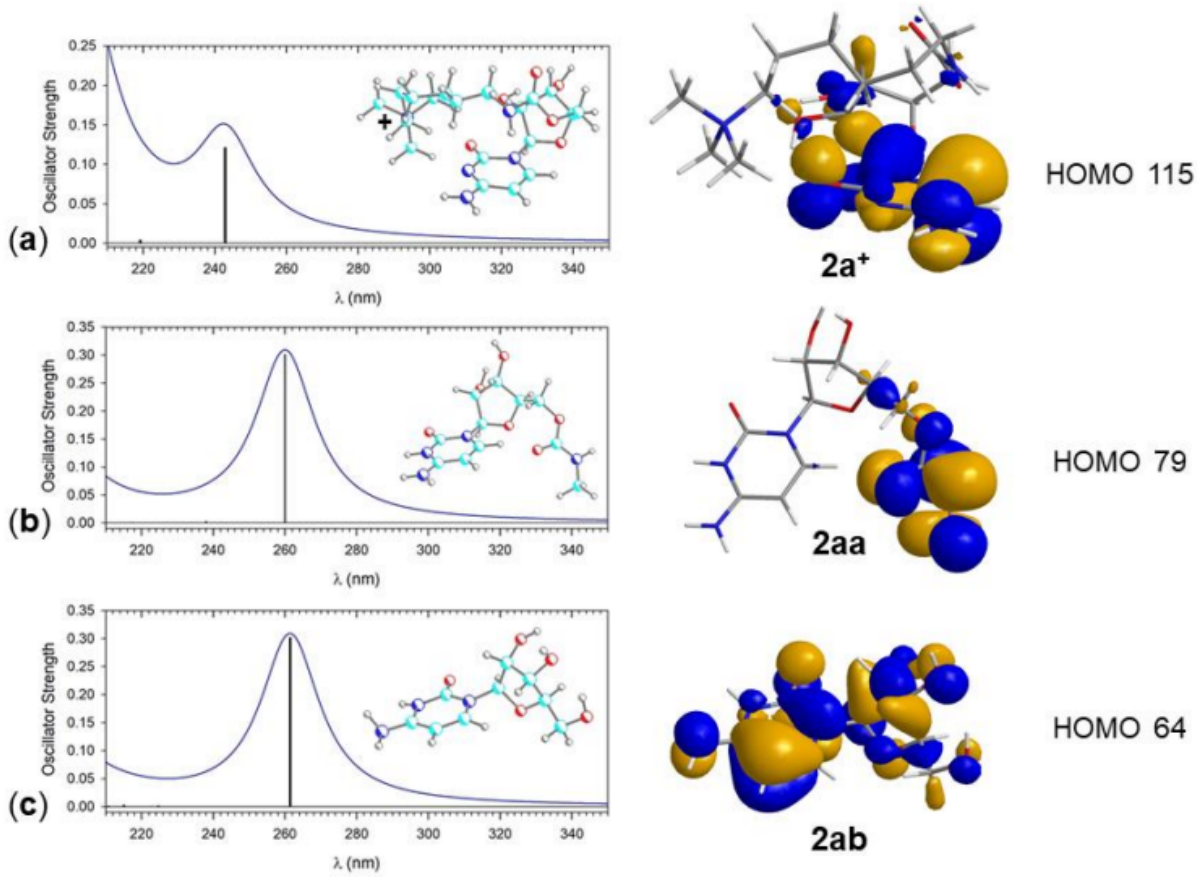

Figure 4.10: TD-DFT absorption spectra of (a) $2a^+$, (b) 2aa and (c) 2ab, and their highest occupied molecular orbitals (HOMO). Calculations with M06-2X/6-31+G(d,p).

loss of cytosine (m/z 358) which was accompanied by loss of methylcytosine (m/z 343) and dissociations of the ribose and dioxolan rings (m/z 330, 272, and 258, Figure 4.11a, inset). The assignments were corroborated by CID-MS^3 of the D4-derivative, $(\mathbf{1}\text{-}D_4)^{+\bullet}$, in which all labile protons were exchanged for deuterium. The spectrum (Figure 4.12a) showed retention of one deuterium in all fragment ions after loss of D_3-cytosine (m/z 359) and D3-methylcytosine (m/z 344). The CID spectrum of $\mathbf{2}^{+\bullet}$ was simpler (Figure 4.11b, inset), showing fragment ions by loss of cytosine (m/z 318), followed by loss of $C_2H_3O_2$ (m/z 259), and the side-chain carbamate ion at m/z 203 which was also seen in the CID spectrum of $\mathbf{1}^{+\bullet}$. The fragment ion assignments were corroborated by the CID-MS^3 of the (OD, ND)-

exchanged derivative, $(\mathbf{2}\text{-}D_6)^{+\bullet}$ (Figure 4.12b). The spectrum showed a consecutive loss of D3-cytosine (m/z 321) and $C_2H_2DO_2$ radical (m/z 261) that indicated cleavage of the C1'–C4' and C2'–C3' bonds of the ribose ring. The side-chain carbamate ion (m/z 205) received a deuterium from one of the ribose hydroxyls. Overall, the dissociations of $\mathbf{1}^{+\bullet}$ and $\mathbf{2}^{+\bullet}$ were readily interpreted and provided suitable fragment ion channels for action spectra measurements.

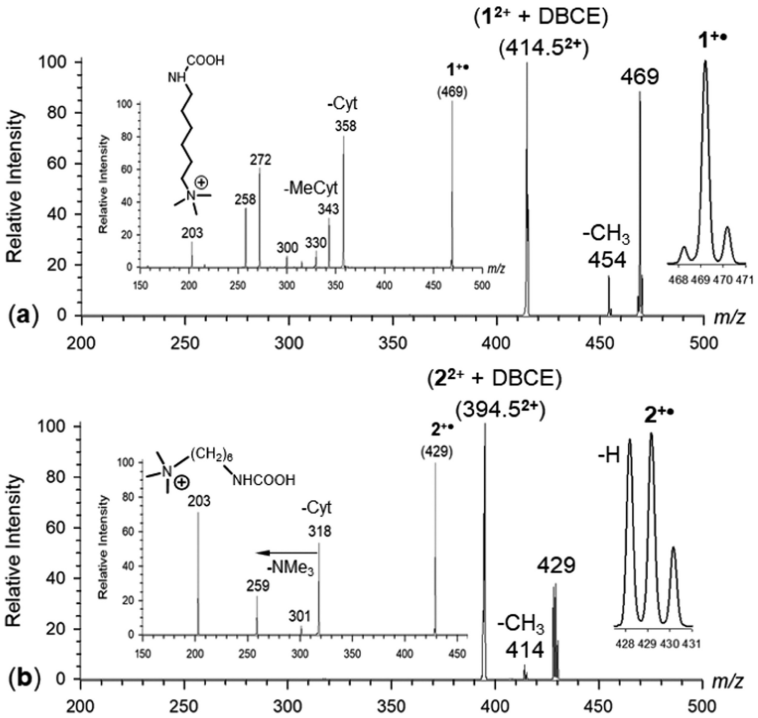

Figure 4.11: (a) ETD-MS^2 spectrum of $(\mathbf{1}{+}DBCE)^{2+}$ at m/z 414.5. The inset shows the CID-MS^3 spectrum of $\mathbf{1}^{+\bullet}$ at m/z 469. (b) ETD-MS^2 spectrum of $(\mathbf{2}{+}DBCE)^{2+}$ at m/z 394.5. The inset shows the CID-MS^3 spectrum of $\mathbf{2}^{+\bullet}$ at m/z 429.

The action spectrum of $\mathbf{1}^{+\bullet}$ (Figure 4.13a) showed several bands in the 210–550 nm wavelength region that were distinguished by monitoring four major photofragment ion channels, m/z 468 (loss of H), m/z 358 (loss of cytosine), m/z 343 (loss of methylcytosine), and m/z 272. The m/z 358 channel showed a weak band with a maximum at 357 nm and another stronger band at 330 nm. These bands were also apparent for m/z 468 which was the major

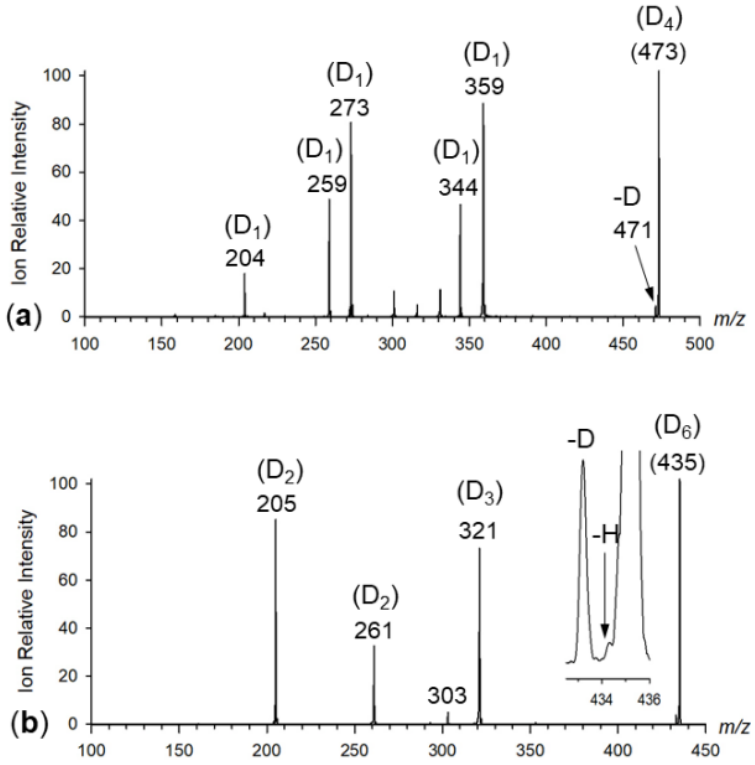

Figure 4.12: CID-MS^3 spectra of (a) (**1**-D$_4$)$^{+\bullet}$ at m/z 473 and (b) (**2**-D$_6$)$^{+\bullet}$ at m/z 435.

photodissociation fragment ion. The strongest absorption was observed as a broad band with a maximum at 250 nm. No photodissociation was observed above 500 nm. The action spectrum of **2**$^{+\bullet}$ (Figure 4.14a,b) was overall very similar to that of **1**$^{+\bullet}$. The m/z 318 (loss of cytosine) channel showed a band with a maximum at 360 nm that extended with a tail up to 500 nm (Figure 4.14b). The main absorption bands were at 300 and 250 nm that were carried by three major fragment ion channels at m/z 428 (loss of H), 259, and 203 (Figure 4.14a). The minor channel at m/z 303 (loss of methylcytosine) showed a red-shifted maximum at 270 nm (Figure 4.14b). It may be noted that analogous absorption bands at 350 and 270 nm have been reported for the action spectrum of the dinucleotide (dCC + 2H)$^{+\bullet}$ cation radical with a (C + H)$^{\bullet}$ radical chromophore.[61]

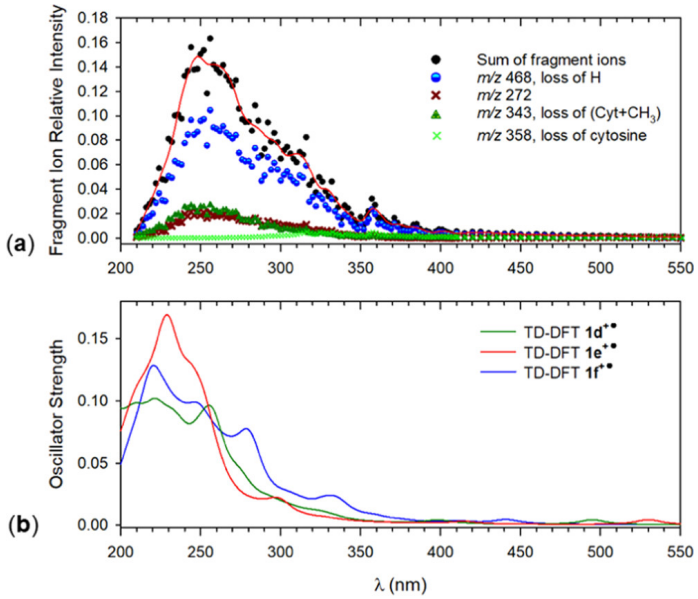

Figure 4.13: (a) UV action spectrum of $\mathbf{1}^{+\bullet}$. (b) M06-2X/6-31+G(d,p) TD-DFT spectra of N3–H tautomers $1d^{+\bullet}$, $1e^{+\bullet}$, and O2–H tautomer $1f^{+\bullet}$. The band profiles are from artificial broadening of the calculated lines by convolution with Lorentzian functions at 10 nm full width at half-maximum. No absorption was observed above 550 nm.

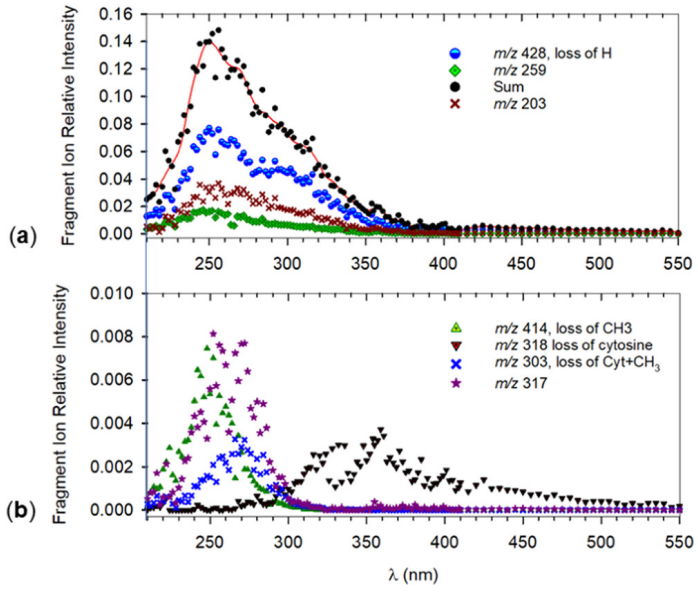

Figure 4.14: UV action spectrum of $\mathbf{2}^{+\bullet}$. (a) Major photofragment ions and (b) minor photofragment ions. No absorption was observed above 550 nm.

4.3.5 Cation-Radical Structures and Electronic Spectra

To interpret the action spectra and assign structures to the charge-tagged cytidine radicals, we carried out extensive DFT geometry optimizations and TD-DFT calculations of excited states. A common feature of $\mathbf{1}^{+\bullet}$ and $\mathbf{2}^{+\bullet}$ was that the N3–H radical tautomers were substantially more stable than the O2–H radicals. This is illustrated in Figure 4.15 for the lowest-energy conformers of both N3–H and O2–H radical types. This finding was consistent with previous energy analysis of gas-phase cytosine[62] and 1-methylcytosine radicals,[63] that identified N3–H tautomers as the lowest-energy isomers in these groups. The atomic spin densities in $1d^{+\bullet}$ –$2g^{+\bullet}$ chiefly were at C4 and C6 of the cytosine ring (Figure 4.15). Another common structural feature was the out-of-plane rotation and pyramidization of the cytosine 4-amino group. Similar to the lowest-energy singly charged ions $1a^{+}$ and $2a^{+}$, the low-energy radicals $1d^{+\bullet}$, $1e^{+\bullet}$, $2d^{+\bullet}$, and $2e^{+\bullet}$ showed structures with coiled side chains indicating ion–dipole interactions between the charged and electron-rich groups. However, the specific side-chain conformations differed among the cations and cation radicals. In $1a^{+}$, the trimethylammonium group was close to the neutral cytosine ring, while in $1d^{+\bullet}$ and $1e^{+\bullet}$, it was coiled towards the dioxolan ring (Figure 4.15). The conformations of $2a^{+}$, $2d^{+\bullet}$, and $2e^{+\bullet}$ differed less in that in both the cation and cation radicals the trimethylammonium group was in the vicinity of the cytosine O2. A differentiating feature was the interaction in $2d^{+\bullet}$ and $2e^{+\bullet}$ of the trimethylammonium group with the carbamate carbonyl oxygen. The lowest-energy O2–H tautomers $1f^{+\bullet}$, $2f^{+\bullet}$, and $2g^{+\bullet}$ displayed hydrogen bonds between the cytosine 2-OH and ribose O4 (Figure 4.15). The energy analysis of cation radicals $1d^{+\bullet}$ –$2g^{+\bullet}$ as well as their dication–DBCE complex precursors indicated that the formation of N3–H tautomers upon ETD should be preferred.

TD-DFT calculations of electronic excitations in $1d^{+\bullet}$ –$1f^{+\bullet}$ (Figure 4.13b) indicated weak transitions above 430 nm for all three isomers that were not apparent in the action spectrum. The 250, 300, and 350 nm regions were represented in the calculated spectra of $1d^{+\bullet}$ –$1f^{+\bullet}$ and, considering vibronic wavelength redshifts and band broadening in the

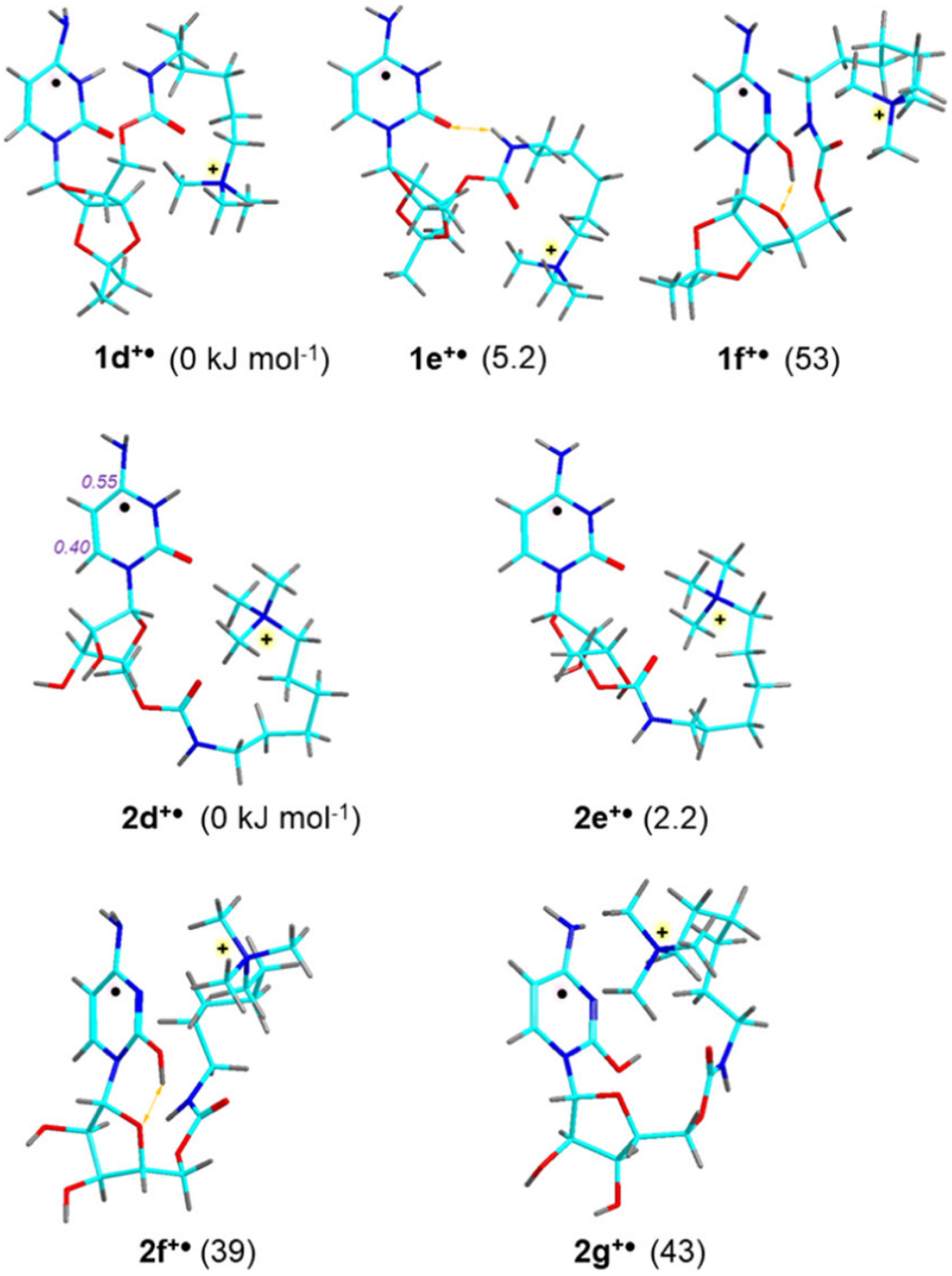

Figure 4.15: M06-2X/6-31+G(d,p) optimized structures of low-energy $\mathbf{1}^{+\bullet}$ and $\mathbf{2}^{+\bullet}$ isomers. Atom color coding as in Figure 4.6. Relative Gibbs energies (kJ mol^{-1} in parentheses) refer to the lowest-energy isomer in each group.

action spectrum, did not provide unambiguous distinction for the tautomers and conformers. Therefore, we focused on the spectra of the deprotected cation radicals $2d^{+\bullet}$ –$2g^{+\bullet}$. The side-chain conformers of the N3–H tautomer $2d^{+\bullet}$ gave similar bands for excitations to the A–G states in the 300–550 nm region of the spectrum (Figure 4.16a–f). Differences due to different conformations appeared in the 200–280 nm region for transitions to higher excited states. These were likely to be rather poorly resolved at the experimental temperature because of thermal band broadening. To compare the theoretical and experimental spectra, we calculated vibronic absorption spectra for the top 36 excited states in $2d^{+\bullet}$ –$2g^{+\bullet}$, which covered the wavelength range down below 200 nm, including all major bands in the action spectrum. The lowest-energy conformers carrying the hydrogen atom at cytosine N3 ($2d^{+\bullet}$ and $2e^{+\bullet}$, Figure 4.17a,b) showed very weak bands for transitions to the A and B excited states. These possibly corresponded to very weak absorption observed in the action spectrum of $\mathbf{2}^{+\bullet}$ as a band at 420 nm and a shoulder extending above 500 nm, as represented by the m/z 318 photofragment channel (Figure 4.14b). The region between 300 and 350 nm in the action spectrum appeared as a shoulder due to vibronic broadening of transitions to the G and H states of $2d^{+\bullet}$ and $2e^{+\bullet}$ at 300 nm. The O2–H tautomers $2f^{+\bullet}$ and $2g^{+\bullet}$ had weak bands for excitations to the A state at 800–810 nm that were outside of the action spectrum wavelength range. The B states gave rise to weak transitions at 428–435 nm (Figure 4.17c,d). Ion $2g^{+\bullet}$ showed absorption in the 300–400 nm region, although it was red-shifted to 350 nm and had an extended tail from the 376 nm (D state) and 435 nm transitions that did not match the action spectrum. The most distinguishing feature of the vibronic spectra was found in the 200–220 nm region. The N3–H tautomers $2d^{+\bullet}$ and $2e^{+\bullet}$ showed a weak shoulder at about 225 nm that had a counterpart in the action spectrum. By contrast, the O2–H tautomers $2f^{+\bullet}$ and $2g^{+\bullet}$ showed strong lines between 210 and 220 nm that appeared as an intense band or shoulder in their vibronic spectra, while not matching the action spectrum of $\mathbf{2}^{+\bullet}$. In a summary of this section, the combined evidence of precursor-ion and cation-radical energetics and action spectra matches pointed to cytidine N3–H tautomers $2d^{+\bullet}$ and $2e^{+\bullet}$ as the most likely structures representing the $\mathbf{2}^{+\bullet}$ ions generated in the gas phase.

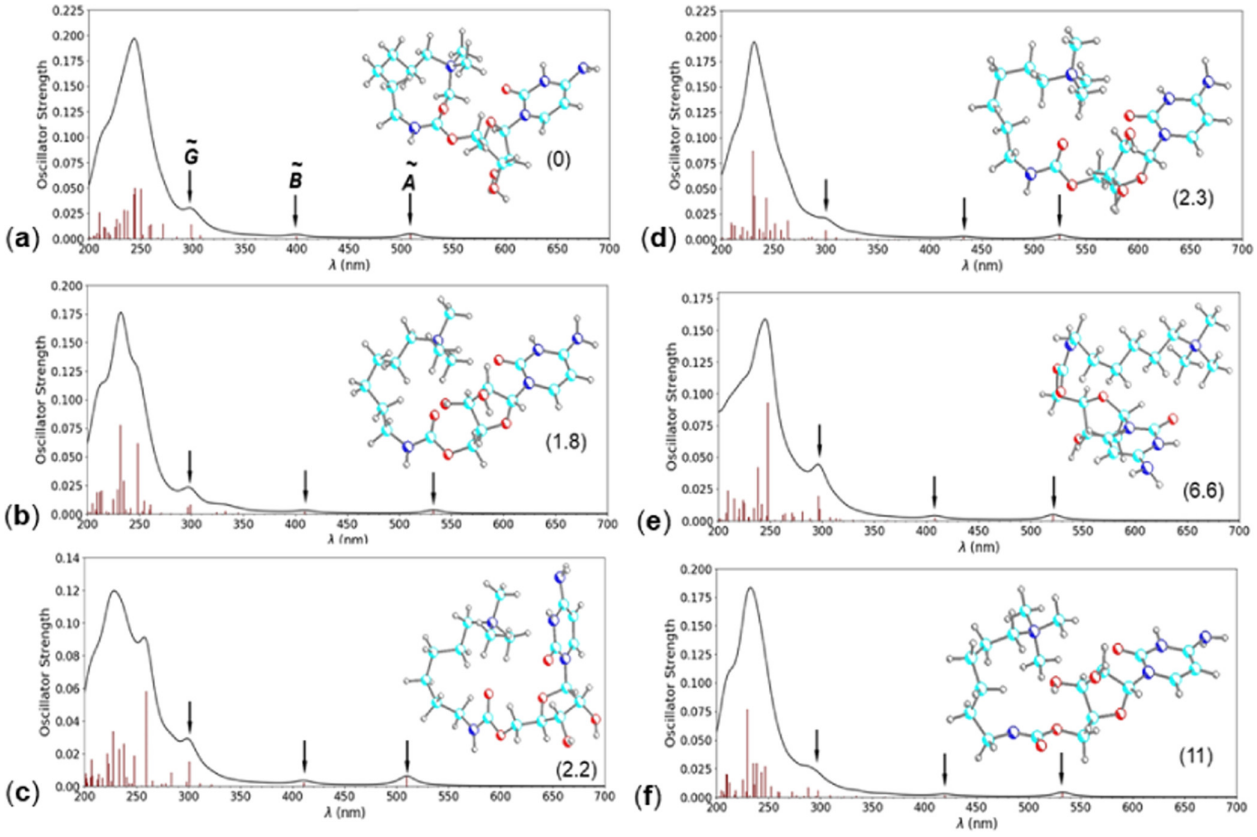

Figure 4.16: M06-2X/6-31+G(d,p) TD-DFT absorption spectra of (a) $2d^{+\bullet}$, (b) $2e^{+\bullet}$, and (c–f) their low-Gibbs-energy conformers. Arrows indicate assignments of the A, B, and G states. The band shapes are from artificial line broadening by convolution with Lorentzian functions at 10 nm full width at half-maximum. The values in parentheses are relative Gibbs energies at 310 K from M06-2X/6-31+G(d,p) calculations.

The effect on the absorption spectra of the charged side-chain group was investigated with TD-DFT spectra of $2d^{+\bullet}$ (Figure 4.18a) and its neutral truncated radical derivatives $2da^{\bullet}$ and $2db^{\bullet}$ (Figure 4.18b,c). In both the cation radical and the neutral radicals, the SOMO was a cytosine ring π_z orbital. The transition to the low-intensity A excited state in $2d^{+\bullet}$ showed a 0.15 eV redshift relative to $2da^{\bullet}$ and $2db^{\bullet}$. The interaction between the charged group and the cytosine ring is attractive and likely to polarize the π-electron system. Note that the polarizability of the cytosine radical is likely higher than that of neutral cytosine, as judged from their respective adiabatic ionization energies (5.17[62] and 8.45 eV[57]). The polarization can lead to a slight increase of the SOMO energy and potentially a lowering of

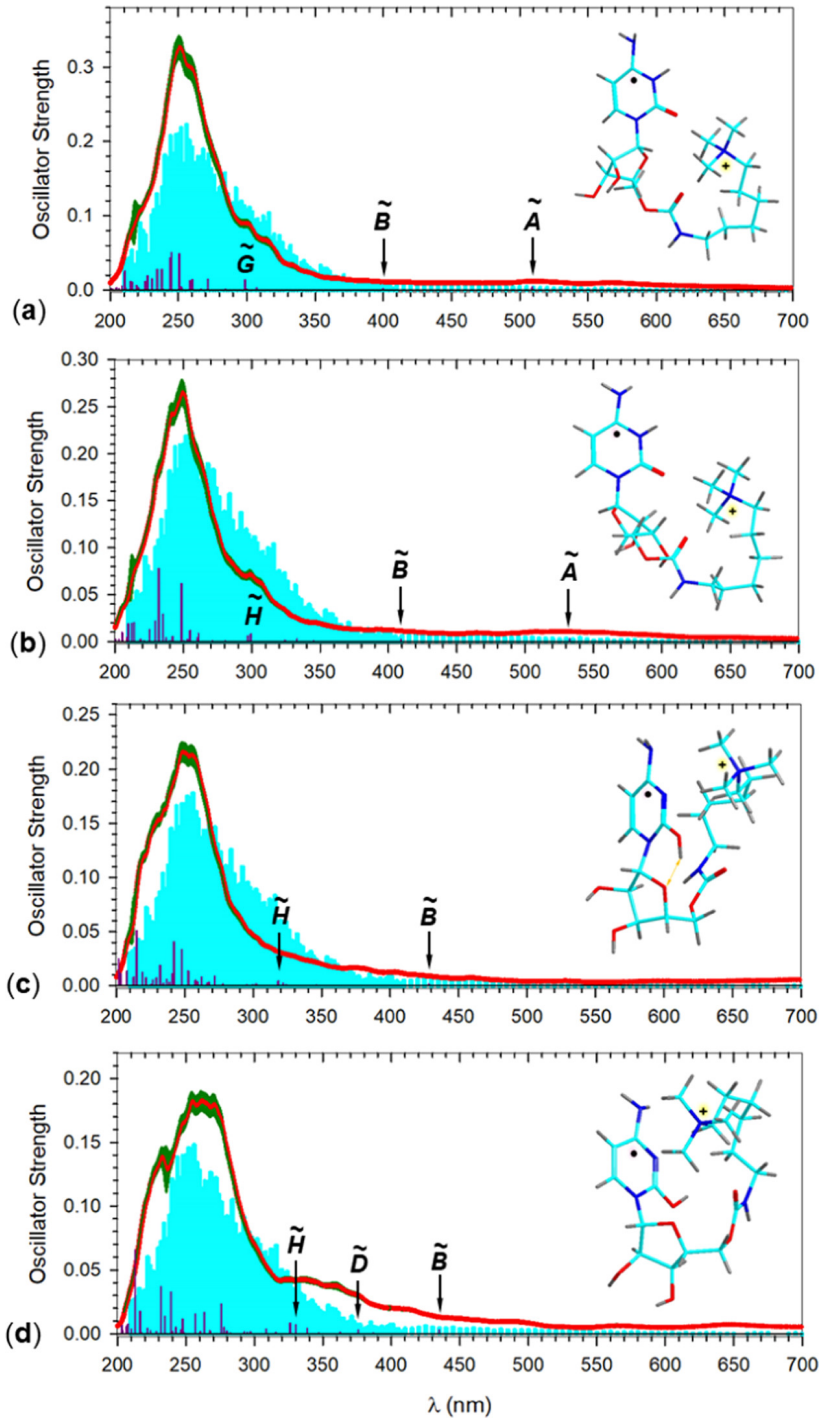

Figure 4.17: Calculated vibronic absorption spectra of (a) $2d^{+\bullet}$, (b) $2e^{+\bullet}$, (c) $2f^{+\bullet}$, and (d) $2g^{+\bullet}$. The action spectrum of $\mathbf{2}^{+\bullet}$ is overlaid as a cyan background and scaled to fit the format.

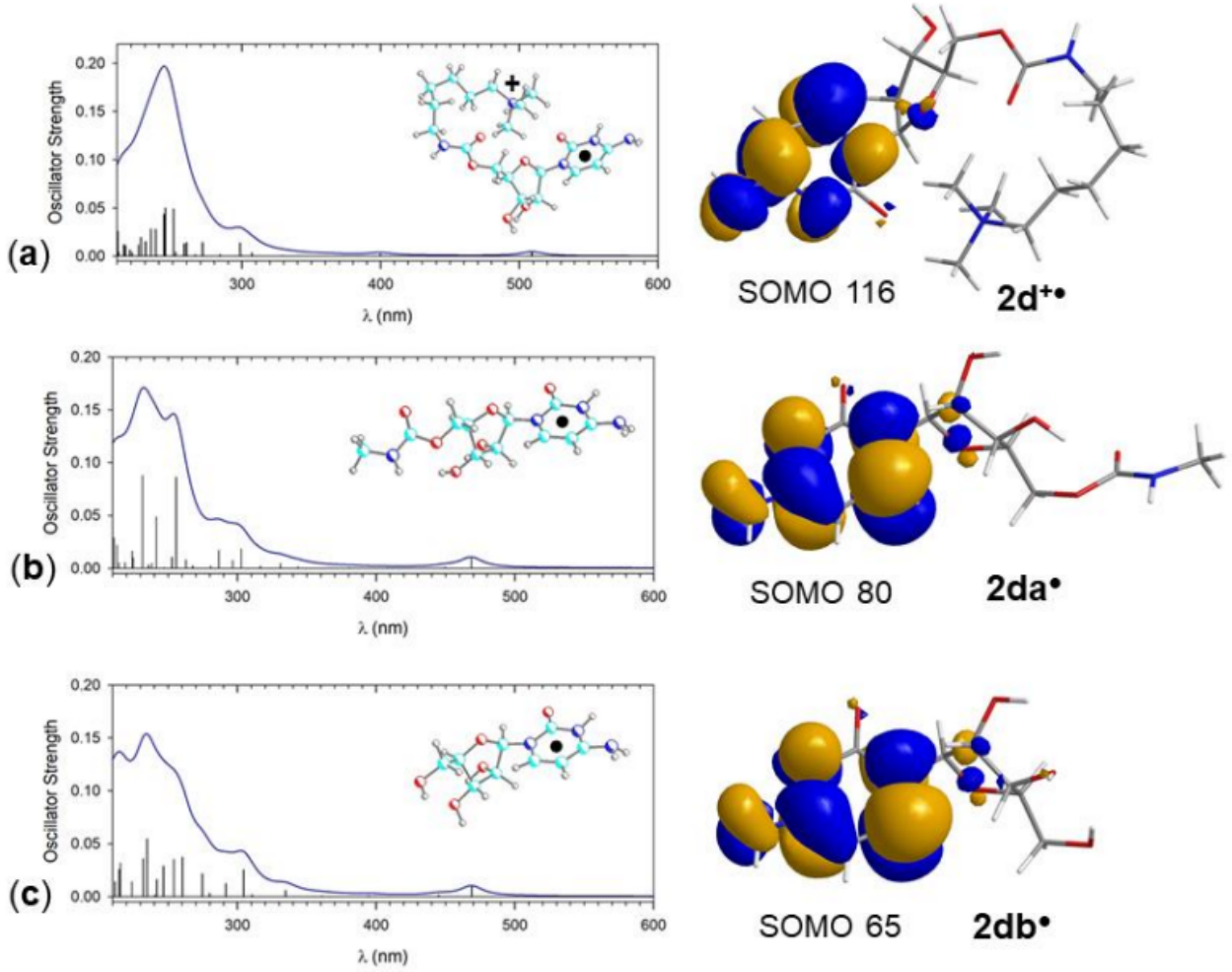

Figure 4.18: TD-DFT absorption spectra of (a) $2d^{+\bullet}$, (b) $2da^{\bullet}$ and (c) $2db^{\bullet}$, and their singly occupied molecular orbitals (SOMO). Calculations with M06-2X/6-31+G(d,p).

the excited state energy, resulting in the observed small redshift for the A state. In contrast, the bands at 300–320 nm, corresponding to excitation to the F and G states in $2d^{+\bullet}$, were essentially unaffected by the presence of the charged side-chain group.

4.3.6 Ion Dissociation Energetics and RRKM Kinetics

The formation of cation radicals $\mathbf{1}^{+\bullet}$ and $\mathbf{2}^{+\bullet}$ from the dication precursors and their further spontaneous or collision-induced dissociations raised important questions about the energet-

ics of these processes that we addressed by M06-2X calculations. Electron attachment to $1b^{2+}$ to form $1f^{+\bullet}$ was calculated to be 620 kJ mol^{-1} exoergic at 310 K, representing the absolute value of the adiabatic recombination energy ($|RE_{adiab}|$) of the dication (Equation 4.1).

$$1b^{2+} + e \rightarrow 1f^{+\bullet} \quad \Delta H^{\circ}_{rxn,g} = -620 kJ mol^{-1} \tag{4.1}$$

$$1b^{2+} + [fluoranthene]^{-\bullet} \rightarrow 1f^{+\bullet} + fluoranthene \quad \Delta H^{\circ}_{rxn,g} = -561 kJ mol^{-1} \tag{4.2}$$

$$2b^{2+} + [fluoranthene]^{-\bullet} \rightarrow 2f^{+\bullet} + fluoranthene \quad \Delta H^{\circ}_{rxn,g} = -547 kJ mol^{-1} \tag{4.3}$$

Electron attachment to the N3–H tautomer $1c^{2+}$ forming $1d^{+\bullet}$ was more exoergic with $|RE_{adiab}|$ = 675 kJ mol^{-1}. When combined with the experimental electron affinity (EA) of fluoranthene (0.61 eV, 59 kJ mol^{-1}),[64] the energy balance for the electron transfer reaction forming $1f^{+\bullet}$ was ΔH_{rxn} = -620 + 59 = -561 kJ mol^{-1} (Equation 4.2). Electron transfer to $1c^{2+}$ forming $1d^{+\bullet}$, including the fluoranthene EA, was more exoergic at ΔH_{rxn} = -616 kJ mol^{-1}. We presumed that the reaction energy was partitioned between the products, $1d^{+\bullet}$ and fluoranthene, according to their heat capacities, which can be roughly estimated from the pertinent numbers of vibrational degrees of freedom.[65] These considerations led to an estimate of the initial vibrational excitation in $1d^{+\bullet}$ and $1f^{+\bullet}$ as Eexc = 460 and 418 kJ mol^{-1}, respectively. Calculations, addressing electron transfer to $2b^{2+}$ and $2c^{2+}$ and forming the pertinent cation radicals $2f^{+\bullet}$ and $2d^{+\bullet}$, gave ΔH_{rxn} = -547 (Equation 4.3) and -590 kJ mol^{-1}, respectively. Considering vibrational energy partitioning between the products, these internal energies, acquired upon electron transfer, indicated a vibrational excitation in $2f^{+\bullet}$ and $2d^{+\bullet}$ as Eexc = 396 and 427 kJ mol^{-1}, respectively. These internal energies can be expected to drive fast dissociation of $\mathbf{1}^{+\bullet}$ and $\mathbf{2}^{+\bullet}$, as indeed observed in the ETD spectra

of the dications.

Electron transfer to (**2**+DBCE)$^{2+}$ was calculated to be less exoergic when based on the dication $|RE_{adiab}|$ = 527 kJ mol^{-1}, which was reduced to ΔH_{rxn} = -468 kJ mol^{-1} by including fluoranthene EA (Equation 4.4), and further to 385 kJ mol^{-1} by excess-energy sharing with fluoranthene according to their rovibrational heat capacities.

$$[2{+}DBCE]^{2+}{+}[fluoranthene]^{-\bullet} \rightarrow [2^{+\bullet}{+}DBCE]{+}fluoranthene \quad \Delta H^{\circ}_{rxn,g} = -468 kJmol^{-1} \tag{4.4}$$

We note that an analogous lowering of $|RE_{adiab}|$ in crown ether–cation complexes compared to naked ions has been reported previously for ammonium, [66] peptide, [67] and dinucleotide ions. [68] Electron transfer to (**2**+DBCE)$^{2+}$ weakened the DBCE complex with 2d$^{+\bullet}$ for which we calculated a 90 kJ mol^{-1} threshold dissociation energy (Equation 4.5).

$$[2^{+\bullet} + DBCE] \rightarrow 2d^{+\bullet} + DBCE \quad \Delta H^{\circ}_{rxn,g} = 90 kJmol^{-1} \tag{4.5}$$

Combining the energy terms and partitioning between the products yielded an estimate of the vibrational excitation in 2d$^{+\bullet}$ acquired by ETD of (**2**+DBCE)$^{2+}$ as Eexc = 168 kJ mol^{-1}.

To describe dissociations of **2**$^{+\bullet}$, we obtained conformationally optimized transition states (TS) and products for the loss of hydrogen from N3 and cleavage of the glycosidic N1–C1' bond in 2d$^{+\bullet}$, leading to loss of isocytosine. The TS for the loss of N3–H (TS1, Figure 4.19) was calculated to be at 136 kJ mol^{-1} above 2d$^{+\bullet}$. TS1 was the lowest-energy conformer that showed the departing hydrogen atom on the exo face of the cytosine ring while developing a hydrogen bond between O2 and 2'-OH. The loss of H was 115 kJ mol^{-1} endoergic forming the lowest-energy product-ion conformer 5^{+}. The N3–H bond dissociation energy in the cytidine radical conjugate 2d$^{+\bullet}$ was substantially higher than those for the N7–H bonds in adenosine and guanosine radicals that were calculated as 67 and 59 kJ mol^{-1}, respectively, at the same

level of theory.[23, 24] The competing loss of isocytosine by cleavage of the N1–C1' bond in $2d^{+\bullet}$ can proceed via the lowest-energy TS2 at 106 kJ mol^{-1} relative to $2d^{+\bullet}$, forming an ion–molecule complex. Structure $6^{+\bullet}$ (Figure 4.19) was the lowest-energy conformer among the complexes at 0.3 kJ mol^{-1} relative to $2d^{+\bullet}$. The energy threshold for the fragments, $8^{+\bullet}$ and isocytosine, was at 119 kJ mol^{-1} relative to $2d^{+\bullet}$, which was only marginally higher than for 5^{+} + $H^{\bullet}$.

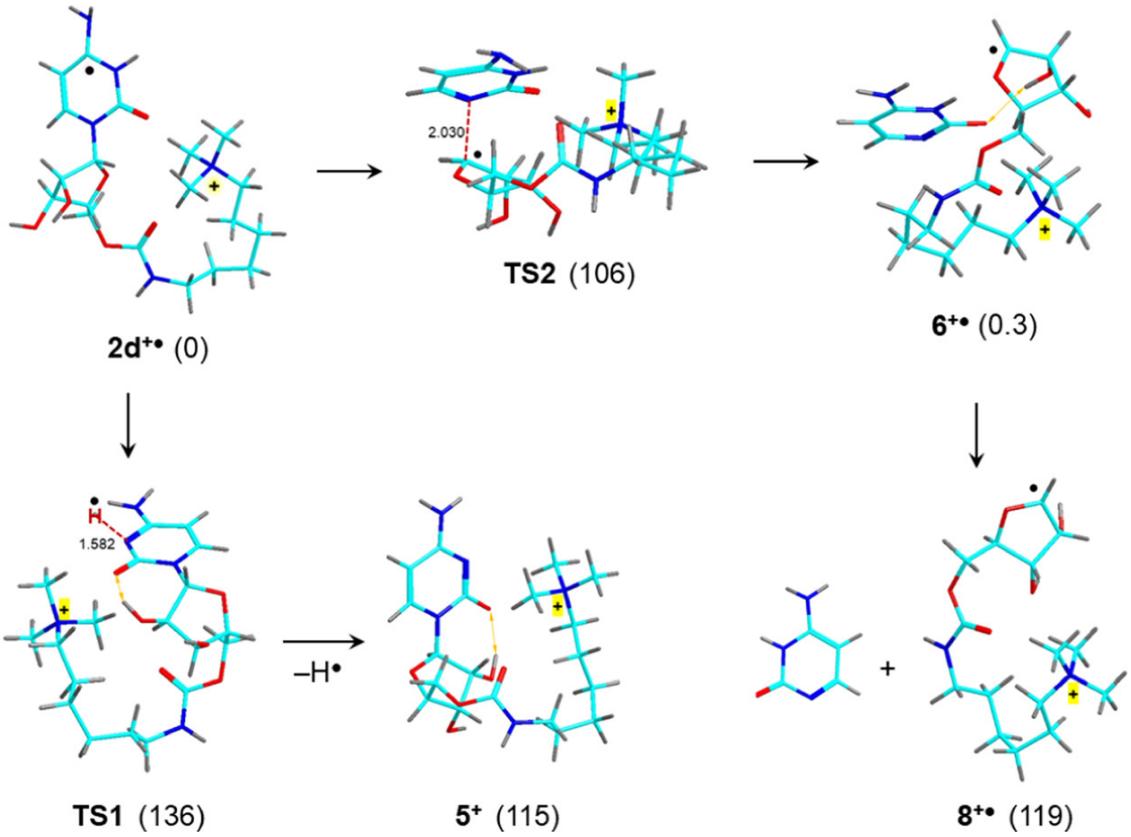

Figure 4.19: Structures and M06-2X/6-311++G(2d,p) + ZPVE energies for dissociations of $2d^{+\bullet}$ referring to 0 K.

The very close relative energies $2d^{+\bullet}$ and $6^{+\bullet}$ raised the question of whether $2d^{+\bullet}$ could isomerize to $6^{+\bullet}$ upon exoergic formation by electron transfer (vide supra). We addressed this question by analyzing the TD-DFT absorption spectrum of $6^{+\bullet}$ (Figure 4.20). The spectrum showed a strong band with a maximum at 202 nm that upon vibronic broadening

and redshift was expected to extend past 210 nm and reach the experimental region in the action spectrum. However, this region in the action spectrum of $\mathbf{2}^{+\bullet}$ did not display salient bands, indicating that $6^{+\bullet}$ was not formed as a major component.

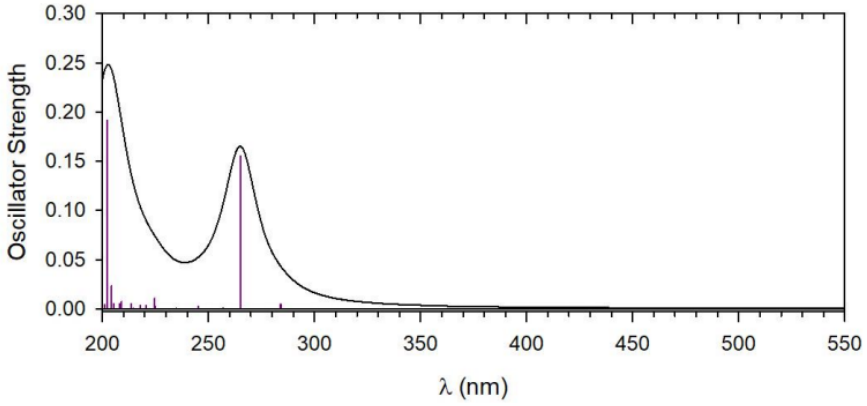

Figure 4.20: TD-DFT M06-2X/6-31+G(d,p) absorption spectrum of complex $6^{+\bullet}$.

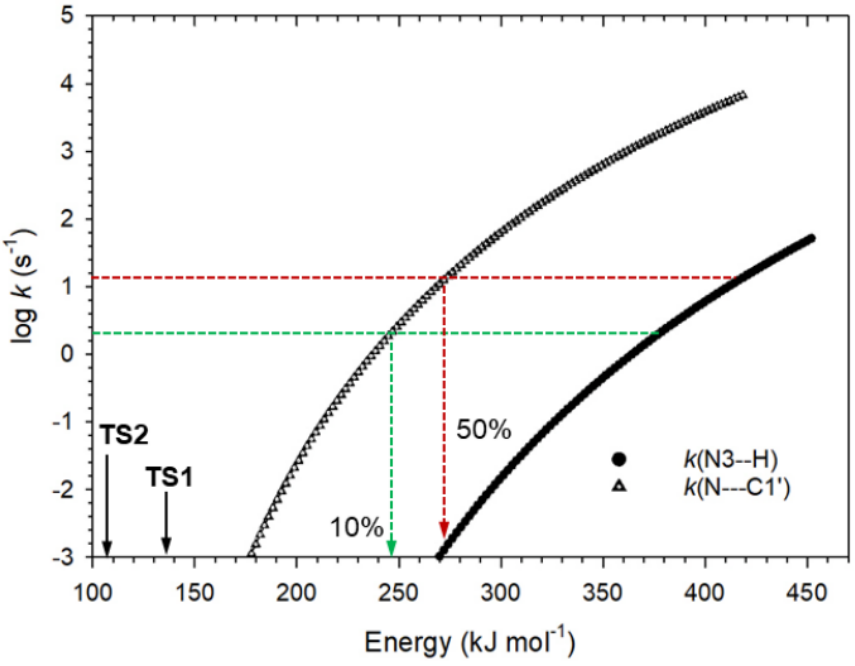

Figure 4.21: RRKM rate constants for the N3—H and N1—C1' dissociations in $2d^{+\bullet}$. Broken lines show the rate constants needed for 10% (greenline) and 50% (red line) conversion on the 0.05 s time scale.

We used RRKM calculations to investigate the kinetics of $2d^{+\bullet}$ dissociations via TS1 and TS2 (Figure 4.21). The N3–C1' bond cleavage showed a slowly rising log k curve and a large kinetic shift.[69] The rate constants indicated that achieving conversion of $2d^{+\bullet}$ to $6^{+\bullet}$ on the experimental time scale of 0.05 s would require high internal energies. For example, a 10% conversion would require >246 kJ mol^{-1}, which was higher than our estimated initial excitation in $2d^{+\bullet}$ due to exoergic electron transfer. Thus, this primarily formed radical was expected to be kinetically stable. Note that longer reaction times potentially leading to higher conversion were prevented by rapid collisional cooling of the ions in the ion trap.[65] The loss of H was calculated to be 3–4 orders of magnitude slower than the N3–C1' bond cleavage (Figure 4.21). This was qualitatively consistent with the CID spectrum of $\mathbf{2}^{+\bullet}$ (Figure 4.11a) that showed a major loss of cytosine but only a very minor loss of H.

4.4 Conclusions

Charge-tagged nucleoside conjugates provide a common molecular platform for acquiring photodissociation action spectra of neutral, protonated, and radical nucleobase chromophores in the gas phase. Combinations of these structural building blocks occur in cation radicals derived from more complex DNA oligonucleotides, and thus the absorption bands obtained from the action spectra of simpler, well-defined, nucleoside conjugates can serve as standards for interpreting action spectra of larger ions. The cytidine radicals reported here did not show strong absorption bands in the visible region of the spectrum, which was consistent with previous studies of deoxycytidine dinucleotide cation radicals.[61] Cytidine radicals were found to be intrinsically stable against spontaneous unimolecular dissociation by loss of cytosine and hydrogen atom. Their stability exceeds that of purine nucleoside radicals where a spontaneous loss of hydrogen atom from the nucleobase has been found to complicate experimental studies. The present results for cytidine, as well as the spectra interpretation supported by theory, will be utilized in upcoming studies of larger DNA cation-radical oligomers, where theoretical analysis by DFT and TD-DFT calculations exceeds the limits of current computer technology.

4.5 Bibliography

[1] Douglas J Crawford-Brown. Physical and chemical mechanisms in molecular radiation biology, 1993.

[2] Clemens von Sonntag. Free-radical-induced dna damage as approached by quantum-mechanical and monte carlo calculations: an overview from the standpoint of an experimentalist. *Advances in quantum chemistry*, 52:5–20, 2007.

[3] E Westhof, W Flossmann, and A Müller. Radical formation in salts of pyrimidines: Ii. cytosine. hcl crystals. *International Journal of Radiation Biology and Related Studies in Physics, Chemistry and Medicine*, 28(5):427–438, 1975.

[4] William A Bernhard and Robert A Farley. Esr of hydrogen addition radicals in single crystals of 1-methylcytosine and 1-methyluracil. *Radiation Research*, 66(2):189–198, 1976.

[5] Jeff Barnes, William A Bernhard, and Kermit R Mercer. Distribution of electron trapping in dna: Protonation of one-electron reduced cytosine. *Radiation research*, 126(1):104–107, 1991.

[6] Einar Sagstuen, Eli O Hole, William H Nelson, and David M Close. Protonation state of radiation-produced cytosine anions and cations in the solid state: Epr/endor of cytosine monohydrate single crystals x-irradiated at 10 k. *The Journal of Physical Chemistry*, 96(21):8269–8276, 1992.

[7] Paul M Cullis, Mark E Malone, Ian D Podmore, and Martyn CR Symons. Site of protonation of one-electron-reduced cytosine and its derivatives in aqueous methanol glasses. *The Journal of Physical Chemistry*, 99(22):9293–9298, 1995.

[8] Eli O Hole, William H Nelson, Einar Sagstuen, and David M Close. Electron paramagnetic resonance and electron nuclear double resonance studies of x-irradiated crystals of

cytosine hydrochloride. part i: Free radical formation at 10 k after high radiation doses. *Radiation research*, 149(2):109–119, 1998.

[9] Michael G Debije, David M Close, and William A Bernhard. Reductive damage in directly ionized dna: saturation of the c5= c6 bond of cytosine in d (cgcg) 2 crystals. *Radiation research*, 157(3):235–242, 2002.

[10] František Tureček. Computational studies of radicals relevant to nucleic acid damage. *Advances in Quantum Chemistry*, 52:89–120, 2007.

[11] Steen Steenken. Purine bases, nucleosides, and nucleotides: aqueous solution redox chemistry and transformation reactions of their radical cations and e-and oh adducts. *Chemical Reviews*, 89(3):503–520, 1989.

[12] LP Candeias and S Steenken. Electron adducts of adenine nucleosides and nucleotides in aqueous solution: protonation at two carbon sites (c2 and c8) and intra-and intermolecular catalysis by phosphate. *The Journal of Physical Chemistry*, 96(2):937–944, 1992.

[13] Luis Pedro Candeias, Petra Wolf, Peter O'Neill, and Steen Steenken. Reaction of hydrated electrons with guanine nucleosides: Fast protonation on carbon of the electron adduct. *The Journal of Physical Chemistry*, 96(25):10302–10307, 1992.

[14] J Barnes and William A Bernhard. The protonation state of one-electron reduced cytosine and adenine. 1. initial protonation sites at low temperatures in glassy solids. *The Journal of Physical Chemistry*, 97(13):3401–3408, 1993.

[15] Jeff P Barnes and William A Bernhard. One-electron-reduced cytosine in acidic glasses: conformational states before and after proton transfer. *The Journal of Physical Chemistry*, 98(3):887–893, 1994.

[16] Steen Steenken and Slobodan V Jovanovic. How easily oxidizable is dna? one-electron reduction potentials of adenosine and guanosine radicals in aqueous solution. *Journal of the american chemical society*, 119(3):617–618, 1997.

[17] Yang Liu, Joseph A Korn, Andy Dang, and František Tureček. Hydrogen-rich cation radicals of dna dinucleotides: Generation and structure elucidation by uv–vis action spectroscopy. *The Journal of Physical Chemistry B*, 122(42):9665–9680, 2018.

[18] Erik A Syrstad, Shetty Vivekananda, and František Tureček. Direct observation of a hydrogen atom adduct to c-5 in uracil. a neutralization-reionization mass spectrometric and ab initio study. *The Journal of Physical Chemistry A*, 105(36):8339–8351, 2001.

[19] Jill K Wolken and František Tureček. Direct observation of a hydrogen atom adduct to o-4 in uracil. energetics and kinetics of uracil radicals. *The Journal of Physical Chemistry A*, 105(36):8352–8360, 2001.

[20] Chunxiang Yao, Maria L Cuadrado-Peinado, Miroslav Polášek, and František Tureček. Specific generation of 1-methylcytosine radicals in the gas phase. *Angewandte Chemie International Edition*, 44(41):6708–6711, 2005.

[21] Martin Sadílek and František Tureček. Probing hypervalent radicals by neutralization-laser photoionization mass spectrometry. *The Journal of Physical Chemistry*, 100(23):9610–9614, 1996.

[22] Martin Sadílek and František Tureček. Laser photolysis of nd4. and trimethylamine formed by collisional neutralization of their cations in the gas phase. *Chemical physics letters*, 263(1-2):203–208, 1996.

[23] Yue Liu, Andy Dang, Jan Urban, and František Tureček. Charge-tagged dna radicals in the gas phase characterized by uv/vis photodissociation action spectroscopy. *Angewandte Chemie International Edition*, 132(20):7846–7851, 2020.

[24] Yue Liu, Congcong Ma, Calvin J. A. Leonen, Champak Chatterjee, Gabriela Nováková, Aleš Marek, and František Tureček. Tackling a curious case: Generation of charge-tagged guanosine radicals by gas-phase electron transfer and their characterization by uv–vis photodissociation action spectroscopy and theory. *Journal of the American Society for Mass Spectrometry*, 32(3):772–785, 2021.

[25] Gregory I Gellene and Richard F Porter. Neutralized ion-beam spectroscopy. *Accounts of Chemical Research*, 16(6):200–207, 1983.

[26] Scott A Shaffer and František Tureček. Hydrogentrimethylammonium: A marginally stable hypervalent radical. *Journal of the American Chemical Society*, 116(19):8647–8653, 1994.

[27] Andy Dang, Joseph A Korn, James Gladden, Brandon Mozzone, and František Tureček. Uv–vis photodissociation action spectroscopy on thermo ltq-xl etd and bruker amazon ion trap mass spectrometers: a practical guide. *Journal of The American Society for Mass Spectrometry*, 30(9):1558–1564, 2019.

[28] John R Eyler. Infrared multiple photon dissociation spectroscopy of ions in penning traps. *Mass spectrometry reviews*, 28(3):448–467, 2009.

[29] Tomas Baer and Robert C Dunbar. Ion spectroscopy: where did it come from; where is it now; and where is it going? *Journal of the American Society for Mass Spectrometry*, 21(5):681–693, 2010.

[30] Nick C Polfer. Infrared multiple photon dissociation spectroscopy of trapped ions. *Chemical Society Reviews*, 40(5):2211–2221, 2011.

[31] Nicolas C Polfer and Philippe Dugourd. *Laser photodissociation and spectroscopy of mass-separated biomolecular ions*, volume 83. Springer, 2013.

[32] James JP Stewart. Optimization of parameters for semiempirical methods v: Modification of nddo approximations and application to 70 elements. *Journal of Molecular modeling*, 13(12):1173–1213, 2007.

[33] Jan Řezáč, Jindřich Fanfrlík, Dennis Salahub, and Pavel Hobza. Semiempirical quantum chemical pm6 method augmented by dispersion and h-bonding correction terms reliably describes various types of noncovalent complexes. *Journal of Chemical Theory and Computation*, 5(7):1749–1760, 2009.

[34] James JP Stewart. Mopac: a semiempirical molecular orbital program. *Journal of computer-aided molecular design*, 4(1):1–103, 1990.

[35] Jan Řezáč. Cuby: An integrative framework for computational chemistry, 2016.

[36] Axel D Becke. Density-functional exchange-energy approximation with correct asymptotic behavior. *Physical review A*, 38(6):3098, 1988.

[37] Yan Zhao and Donald G Truhlar. The m06 suite of density functionals for main group thermochemistry, thermochemical kinetics, noncovalent interactions, excited states, and transition elements: two new functionals and systematic testing of four m06-class functionals and 12 other functionals. *Theoretical chemistry accounts*, 120(1):215–241, 2008.

[38] Filipp Furche and Reinhart Ahlrichs. Adiabatic time-dependent density functional methods for excited state properties. *The Journal of chemical physics*, 117(16):7433–7447, 2002.

[39] Shu R Huang, Andy Dang, and František Tureček. Ground and excited states of gas-phase dna nucleobase cation-radicals. a uv–vis photodisociation action spectroscopy and computational study of adenine and 9-methyladenine. *Journal of the American Society for Mass Spectrometry*, 31(6):1271–1281, 2020.

[40] Mario Barbatti, Matthias Ruckenbauer, Felix Plasser, Jiri Pittner, Giovanni Granucci, Maurizio Persico, and Hans Lischka. Newton-x: a surface-hopping program for nonadiabatic molecular dynamics. *Wiley Interdisciplinary Reviews: Computational Molecular Science*, 4(1):26–33, 2014.

[41] M. J. Frisch, G. W. Trucks, H. B. Schlegel, G. E. Scuseria, M. A. Robb, J. R. Cheeseman, G. Scalmani, V. Barone, G. A. Petersson, H. Nakatsuji, X. Li, M. Caricato, A. V. Marenich, J. Bloino, B. G. Janesko, R. Gomperts, B. Mennucci, H. P. Hratchian, J. V. Ortiz, A. F. Izmaylov, J. L. Sonnenberg, D. Williams-Young, F. Ding, F. Lipparini, F. Egidi, J. Goings, B. Peng, A. Petrone, T. Henderson, D. Ranasinghe, V. G. Zakrzewski, J. Gao, N. Rega, G. Zheng, W. Liang, M. Hada, M. Ehara, K. Toyota, R. Fukuda, J. Hasegawa, M. Ishida, T. Nakajima, Y. Honda, O. Kitao, H. Nakai, T. Vreven, K. Throssell, J. A. Montgomery, Jr., J. E. Peralta, F. Ogliaro, M. J. Bearpark, J. J. Heyd, E. N. Brothers, K. N. Kudin, V. N. Staroverov, T. A. Keith, R. Kobayashi, J. Normand, K. Raghavachari, A. P. Rendell, J. C. Burant, S. S. Iyengar, J. Tomasi, M. Cossi, J. M. Millam, M. Klene, C. Adamo, R. Cammi, J. W. Ochterski, R. L. Martin, K. Morokuma, O. Farkas, J. B. Foresman, and D. J. Fox. Gaussian˜16 Revision A.01, 2016. Gaussian Inc. Wallingford CT.

[42] Robert G Gilbert and Sean C Smith. *Theory of unimolecular and recombination reactions*. Publishers' Business Services [distributor], 1990.

[43] L Zhu and WL Hase. Quantum chemistry program exchange, 1994.

[44] Joshua A Gregersen and František Tureček. Mass-spectrometric and computational study of tryptophan radicals (trp+ h)˙ produced by collisional electron transfer to protonated tryptophan in the gas phase. *Physical Chemistry Chemical Physics*, 12(41):13434–13447, 2010.

[45] Miriam Michael Stimson and Marie Joannes O'Donnell. The infrared and ultraviolet

absorption spectra of cytosine and isocytosine in the solid state1, 2. *Journal of the American chemical Society*, 74(7):1805–1808, 1952.

[46] Leigh B Clark, Gary G Peschel, and Ignacio Tinoco Jr. Vapor spectra and heats of vaporization of some purine and pyrimidine bases1. *The Journal of Physical Chemistry*, 69(10):3615–3618, 1965.

[47] Leigh B Clark and Ignacio Tinoco Jr. Correlations in the ultraviolet spectra of the purine and pyrimidine bases1. *Journal of the American Chemical Society*, 87(1):11–15, 1965.

[48] László Láng and József Szőke. *Absorption spectra in the ultraviolet and visible region: a theoretical and technical introduction.* Publishing House of the Hungarian Academy of Sciences, 1961.

[49] Patrik R Callis and William Simpson. Polarization of electronic transitions in cytosine. *Journal of the American Chemical Society*, 92(12):3593–3599, 1970.

[50] Alex Domingo, Antonio Rodríguez-Fortea, and Coen de Graaf. The absorption spectrum of cytosine tautomers: Beyond the static approach. *Journal of Chemical Theory and Computation*, 8(1):235–244, 2012.

[51] Matias Berdakin, Géraldine Féraud, Claude Dedonder-Lardeux, Christophe Jouvet, and Gustavo A Pino. Excited states of protonated dna/rna bases. *Physical Chemistry Chemical Physics*, 16(22):10643–10650, 2014.

[52] Géraldine Féraud, Matias Berdakin, Claude Dedonder-Lardeux, Christophe Jouvet, and Gustavo A Pino. Excited states of proton-bound dna/rna base homodimers: pyrimidines. *The Journal of Physical Chemistry B*, 119(6):2219–2228, 2015.

[53] Y Zhu, LA Hamlow, CC He, HA Roy, NA Cunningham, MU Munshi, G Berden, J Oomens, and MT Rodgers. Conformations and n-glycosidic bond stabilities of sodium

cationized 2'-deoxycytidine and cytidine: solution conformation of [cyd+ na]+ is preserved upon esi. *International Journal of Mass Spectrometry*, 429:18–27, 2018.

[54] RR Wu, Bo Yang, CE Frieler, G Berden, J Oomens, and MT Rodgers. N3 and o2 protonated tautomeric conformations of 2'-deoxycytidine and cytidine coexist in the gas phase. *The Journal of Physical Chemistry B*, 119(18):5773–5784, 2015.

[55] Antonello Filippi, Caterina Fraschetti, Flaminia Rondino, Susanna Piccirillo, Vincent Steinmetz, Leonardo Guidoni, and Maurizio Speranza. Protonated pyrimidine nucleosides probed by irmpd spectroscopy. *International Journal of Mass Spectrometry*, 354:54–61, 2013.

[56] Hou U Ung, Kathy T Huynh, John C Poutsma, Jos Oomens, Giel Berden, and Thomas Hellman Morton. Investigation of proton affinities and gas phase vibrational spectra of protonated nucleosides, deoxynucleosides, and their analogs. *International Journal of Mass Spectrometry*, 378:294–302, 2015.

[57] Edward P Hunter and Sharon G Lias. Proton affinity evaluation. *NIST Chemistry WebBook, NIST Standard Reference Database Number*, 69, 2005.

[58] Angelo Liguori, Anna Napoli, and Giovanni Sindona. Survey of the proton affinities of adenine, cytosine, thymine and uracil dideoxyribonucleosides, deoxyribonucleosides and ribonucleosides. *Journal of mass spectrometry*, 35(2):139–144, 2000.

[59] Mario Barbatti, Adelia JA Aquino, and Hans Lischka. The uv absorption of nucleobases: semi-classical ab initio spectra simulations. *Physical Chemistry Chemical Physics*, 12(19):4959–4967, 2010.

[60] Sara Øvad Pedersen, Camilla Skinnerup Byskov, František Tureček, and Steen Brøndsted Nielsen. Structures of protonated thymine and uracil and their monohydrated gas-phase ions from ultraviolet action spectroscopy and theory. *The Journal of Physical Chemistry A*, 118(24):4256–4265, 2014.

[61] Yang Liu, Joseph A Korn, and František Tureček. Uv-vis action spectroscopy and structures of hydrogen-rich 2'-deoxycytidine dinucleotide cation radicals. a difficult case. *International Journal of Mass Spectrometry*, 443:22–31, 2019.

[62] Chunxiang Yao, František Tureček, Michael J Polce, and Chrys Wesdemiotis. Proton and hydrogen atom adducts to cytosine. an experimental and computational study. *International Journal of Mass Spectrometry*, 265(2-3):106–123, 2007.

[63] František Tureček and Chunxiang Yao. Hydrogen atom addition to cytosine, 1-methylcytosine, and cytosine- water complexes. a computational study of a mechanistic dichotomy. *The Journal of Physical Chemistry A*, 107(43):9221–9231, 2003.

[64] Josef Michl. Electronic structure of non-alternant hydrocarbons: Their analogues and derivatives: Xviii. the electronic spectrum and electron affinity of fluoranthene. *Journal of Molecular Spectroscopy*, 30(1-3):66–76, 1969.

[65] Robert Pepin and František Tureček. Kinetic ion thermometers for electron transfer dissociation. *The Journal of Physical Chemistry B*, 119(7):2818–2826, 2015.

[66] Anne IS Holm, Mikkel K Larsen, Subhasis Panja, Preben Hvelplund, Steen Brøndsted Nielsen, Ryan D Leib, William A Donald, Evan R Williams, Changtong Hao, and František Tureček. Electron capture, femtosecond electron transfer and theory: A study of noncovalent crown ether 1, n-diammonium alkane complexes. *International Journal of Mass Spectrometry*, 276(2-3):116–126, 2008.

[67] Emilie Viglino, Cheuk Kuen Lai, Xiaoyan Mu, Ivan K Chu, and František Tureček. Ground and excited-electronic-state dissociations of hydrogen-rich and hydrogen-deficient tyrosine peptide cation radicals. *Journal of The American Society for Mass Spectrometry*, 27(9):1454–1467, 2016.

[68] Joseph A Korn, Jan Urban, Andy Dang, Huong TH Nguyen, and František Tureček. Uv–

vis action spectroscopy reveals a conformational collapse in hydrogen-rich dinucleotide cation radicals. *The Journal of Physical Chemistry Letters*, 8(17):4100–4107, 2017.

[69] C Lifshitz. Time-resolved appearance energies, breakdown graphs, and mass spectra: The elusive "kinetic shift". *Mass Spectrometry Reviews*, 1(4):309–348, 1982.

Chapter 5

GUANINE-ADENINE INTERACTIONS IN DNA TETRANUCLEOTIDE CATION RADICALS

Reproduced in part with permission from Yue Liu, Shu R. Huang, and František Tureček. Guanine-adenine interactions in DNA tetranucleotide cation radicals revealed by UV/vis photodissociation action spectroscopy and theory. *Physical Chemistry Chemical Physics*, 22(29):16831-16842, 2020.

Abstract *Hydrogen-rich cation radicals (GATT + 2H)$^{+\bullet}$ and (AGTT + 2H)$^{+\bullet}$ represent oligonucleotide models of charged hydrogen atom adducts to DNA. These tetranucleotide cation radicals were generated in the gas phase by one-electron reduction of the respective (GATT + 2H)$^{2+}$ and (AGTT + 2H)$^{2+}$ dications in which the charging protons were placed on the guanine and adenine nucleobases. We used wavelength-dependent UV/Vis photodissociation in the valence-electron excitation region of 210-700 nm to produce action spectra of (GATT + 2H)$^{+\bullet}$ and (AGTT + 2H)$^{+\bullet}$ that showed radical-associated absorption bands in the near-UV (330 nm) and visible (400-440 nm) regions. Born-Oppenheimer molecular dynamics and density-functional theory calculations were used to obtain and rank by energy multiple (GATT + 2H) dication and cation-radical structures. Time-dependent density functional theory (TD-DFT) calculations of excited-state energies and electronic transitions in (GATT + 2H)$^{+\bullet}$ were augmented by vibronic spectra calculations at 310 K for selected low-energy cation radicals to provide a match with the action spectrum. The stable product of one-electron reduction was identified as having a 7,8-dihydroguanine cation radical moiety, formed by intramolecular hydrogen atom migration from adenine N-1-H. The hydrogen migration was calculated to have a transition state with a low activation energy, Ea = 96.5*

kJ mol^{-1}, and positive activation entropy, $\Delta S^{\neq}$ = 75 J mol^{-1} K^{-1}. This allowed for a fast isomerization of the primary reduction products on the ion-trap time scale of 150 ms that was substantially accelerated by highly exothermic electron transfer.

5.1 Introduction

Ionization of DNA by photons or high-energy particles forms cation radicals that undergo fast electron and proton transfer as the two fundamental secondary chemical processes.[1] The electron transfer kinetics in oligonucleotide and DNA intermediates has been elucidated for a number of model systems using down stream analysis of radical products.[2–5] In contrast, proton transfer between the Watson-Crick nucleobase pairs in DNA cation radicals has been studied for a limited number of model systems in solution,[6–8] as well as by density-functional theory calculations.[9–15] The main difficulty with studying DNA cation radicals in the early stages following ionization stems from their high reactivity in the condensed phase. Deprotonation by solvent has been shown to occur on a microsecond time scale, forming mixtures of secondary neutral products even from ionized nucleobases,[16, 17] while experimental data for cation radicals of oligonucleotides have been scarce. Hence, it is advantageous to generate and study transient intermediates, such as DNA cation radicals, in an inert environment of the rarefied gas phase.[18] Following this strategy, O'Hair and coworkers have generated the cation radical of the cytosine-guanine Watson-Crick pair and characterized it by infrared multiphoton dissociation (IRMPD) action spectroscopy.[19] This method relies on generating the pertinent ion in an ion trap, isolating it by the mass-to-charge ratio (m/z), and monitoring its photodissociation over a range of wavelengths.[20–22] The ion trap conditions, which are ultrahigh vacuum for ion-cyclotron resonance mass spectrometry, or low pressure (3 mTorr) of helium in quadrupole ion traps, provide an inert medium that prevents intermolecular reactions that plague condensed phase studies of highly reactive species. In addition, detection of photofragment ions by mass spectrometry provides a highly sensitive means of monitoring ion light absorption even at an extremely low optical thickness of the absorber.

We have combined the multistage capabilities of quadrupole ion traps with UV-Vis pho-

todissociation (UVPD) action spectroscopy to generate and characterize cation radicals of all four DNA nucleobases[23–26] as well as adenosine[27] and guanosine nucleosides.[25] Our strategy for the generation of oligonucleotide cation radicals relies on dication precursors that are formed in the gas phase by electrospray ionization. This guarantees that the charges, in the form of added protons, are localized on separate nucleobases in the dication. The dications are partly discharged by electron transfer from a gaseous donor, typically by an ion-ion reaction with fluoranthene anion radical produced in an auxiliary ion source (Figure 5.1).[28] Stable oligonucleotide cation radicals are selected by mass and studied by methods of tandem mass spectrometry, including UVPD action spectroscopy. The Figure 5.1 reaction sequence, in which one-electron reduction follows protonation, can be viewed as a reversal of a pulse radiolysis sequence where addition of an electron is followed by protonation.[29, 30] We have used one-electron reduction of dications to generate cation radicals from DNA dinucleotides AA,[31] GG, GC, CG,[32] and CC,[33] as well as tetranucleotides GATC and AGTC.[34] The previous studies have revealed that the cations and radicals that were located at different nucleobases in these oligonucleotides can undergo proton transfer between the nucleobases in a manner which depends on the nucleobases, their sequence, and oligonucleotide cation radical conformation. Here, we address the question of nucleobase cation-radical interaction in tetranucleotides GATT and AGTT. Because of the very different gas-phase basicities of G and A on one hand and T on the other,[35] these sequences are suitable for steering protonation towards the G and A nucleotides while preserving the conformational complexity of the dications and their cation-radical analogues. We wish to show that despite their low basicity, the thymine nucleotides engage in extensive hydrogen bonding interactions and thus have an effect on the conformational properties of the tetranucleotide cation radicals that affect proton transfer kinetics.

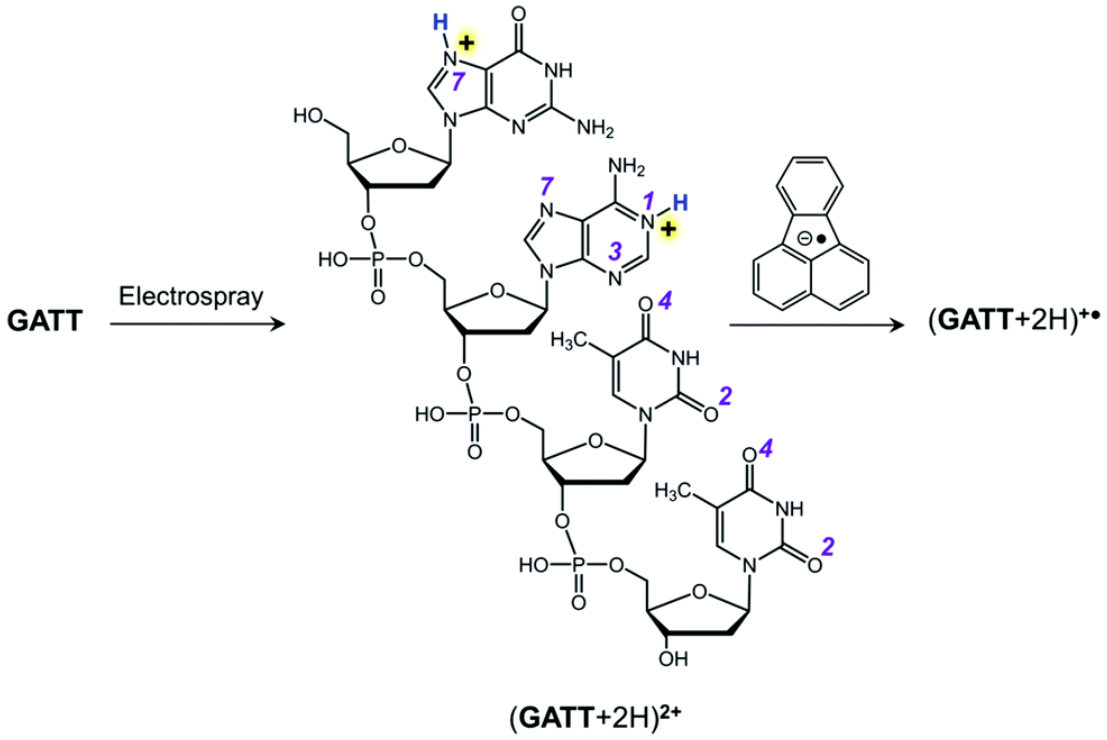

Figure 5.1: Formation of (GATT + 2H)$^{+\bullet}$ ions for UV-Vis action spectroscopy.

5.2 Experimental section

5.2.1 Materials

DNA tetranucleotides GATT and AGTT were purchased from Integrated DNA Technologies (Coralville, IA) and used as received.

5.2.2 Methods

Mass spectra were measured on a modified Bruker amaZon Speed 3D ion trap mass spectrometer (Bruker Daltonik, Bremen, Germany) equipped with an auxiliary ion source for electron transfer dissociation (ETD) and coupled to a laser.[36] The tetranucleotides were dissolved in 50:50:1 acetonitrile-water-acetic acid at 10-20 μM concentrations and electrosprayed into the ion trap. The doubly charged ions were partially reduced by ion-ion reactions with

fluoranthene anion radicals at a 150 ms reaction time. The resulting cation radicals were again selected by mass in the ion trap and probed by laser photodissociation. An EKSPLA NL301G Nd-YAG laser (Altos Photonics, Bozeman, MT, USA) provided a beam at 20 Hz frequency and 3- to 6 ns pulse width. The photon pulses were treated by a PG142C unit (Altos Photonics, Bozeman, MT, USA) to enable wavelength tuning in the range of 210-700 nm, as reported previously.[37–39] The laser pulse energies were measured at each experimental wavelength using an EnergyMax-USB J-10MB energy sensor (Coherent Inc., Santa Clara, CA, USA) and used to normalize the action spectra according to the number of photons per pulse.

5.2.3 Calculations

Precursor $(GATT + 2H)^{2+}$ dication structures were obtained for all 18 theoretical combinations of protomers in which protons were placed in the basic positions on different nucleobases, which were N-7 on G, N-1 or N-3 on A, and O-2 or O-4 on T3 and T4. Born-Oppenheimer molecular dynamics (BOMD) calculations were used to obtain 20 ps trajectories at 410-610 K using the Berendsen thermostat algorithm,[40] with the semiempirical all-valence-electron PM6 method[41] supplemented with corrections for dispersion and hydrogen bonding interactions, PM6-D3H4.[42] These calculations were run by MOPAC[43] under the Cuby4 platform,[44] as described previously.[33] Selected low-energy conformers from the BOMD runs of each protomer were reoptimized by density functional theory (DFT) calculations using the B3LYP[45] and ωB97X-D,[46] hybrid functionals with the 6-31+G(d,p) basis set. The B3LYP calculations provided harmonic frequencies that were used to calculate ion enthalpies and entropies at the ion trap temperature (310 K). The ωB97X-D calculations provided the electronic terms. The electronic, enthalpy, and entropy terms were combined to produce free energies that were used to rank conformers of each protomer. In addition, solvation energies in water were calculated with ωB97X-D/6-31+G(d,p) using the polarizable continuum model.[47] The lowest-free-energy gas-phase ions in each group were used for the selection of protomers in the charge-reduced $(GATT + 2H)^{+\bullet}$ cation radicals. Cation-radical

structures were optimized by B3LYP and M06-2X[48] calculations with the 6-31+G(d,p) basis set that were run within the spin unrestricted formalism. Single-point energies were calculated with M06-2X/6-311++G(2d,p) on the M06-2X/6-31+G(d,p) optimized geometries. Atomic spin densities were calculated using the natural population analysis[49] of the M06-2X/6-31+G(d,p) wave functions.

We selected UM06-2X/6-31+G(d,p) for time-dependent DFT calculations[50] of an extensive set of vertical and vibronic transitions in the cation radicals. This selection was based on our previous TD-DFT calculations that were benchmarked against high-level equation-of-motion coupled clusters (EOM-CCSD) calculations.[25, 26] Vertical excitations were calculated for 90-145 excited states to probe all transitions within the experimentally studied region of 210-700 nm. To calculate vibronic excitations, we used 300 Boltzmann-ranked ground-state configurations that were generated by the Newton X program[51] from the B3LYP/6-31+G(d,p) calculated harmonic normal modes of each cation radical at 310 K and submitted for TD-DFT calculations. Because of the size of the tetranucleotide cation radicals and their open-shell nature we used a limited number of 10 excited electronic states in these vibronic TD-DFT calculations. All the electronic structure calculations were performed with the Gaussian 16 (revision A.03) suite of programs.[52] Rice-Ramsperger-Kassel-Marcus calculations[53] were run with a QCEP program[54] that was recompiled for Windows 7.[55] The calculations were performed in the 167-830 kJ mol^{-1} energy range with 2.092 kJ mol^{-1} (0.5 kcal mol^{-1}) steps and with a direct count of quantum states for the 393 and 392 normal vibrational modes in the reactant and transition state, respectively. Rotations were treated adiabatically, and the microcanonical k(E,J,K) rate constants were Boltzmann-averaged over the population of rotational states at 310 K. Transition state theory calculations used the standard formula with the M06-2X/6-311++G(2d,p) activation energies and partition functions for the reactants and transition states that were based on B3LYP/6-31+G(d,p) normal-mode vibrational analysis and principal moments of inertia.

5.3 Results and Discussion

5.3.1 Ion Formation and Characterization

Electrospray ionization of the GATT and AGTT tetranucleotides produced doubly charged ions, $(GATT + 2H)^{2+}$ and $(AGTT + 2H)^{2+}$, respectively, at m/z 595 (Figure 5.1), that upon ion-ion reaction with fluoranthene anions formed the respective cation radicals, $(GATT + 2H)^{+\bullet}$ and $(AGTT + 2H)^{+\bullet}$, at m/z 1190 (Figure 5.2a and b). One-electron reduction was accompanied by very little dissociation, resulting in a clean and efficient generation of the cation radicals. Likewise, proton transfer to the reagent anion, which is a common side reaction in ETD,[28] was minimal as evidenced by the low relative intensity of the $(GATT + H)^{+}$ and $(AGTT + H)^{+}$ ions at m/z 1189 (Figure 5.2a and b insets).

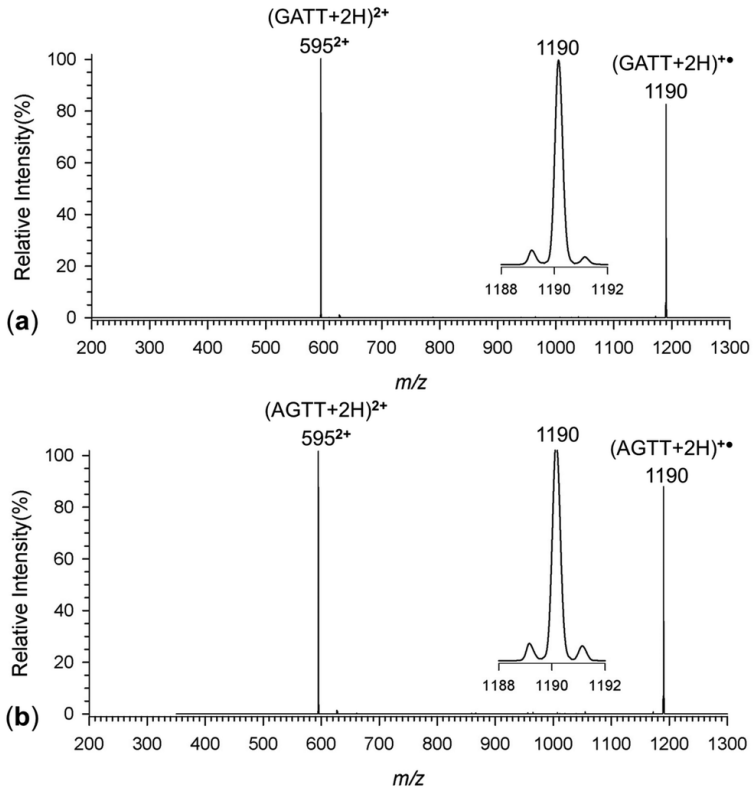

Figure 5.2: Electron-transfer dissociation mass spectra of doubly charged m/z 595 ions (a) $(GATT + 2H)^{2+}$, and (b) $(AGTT + 2H)^{2+}$. Insets show the peak profiles for charge-reduced ions.

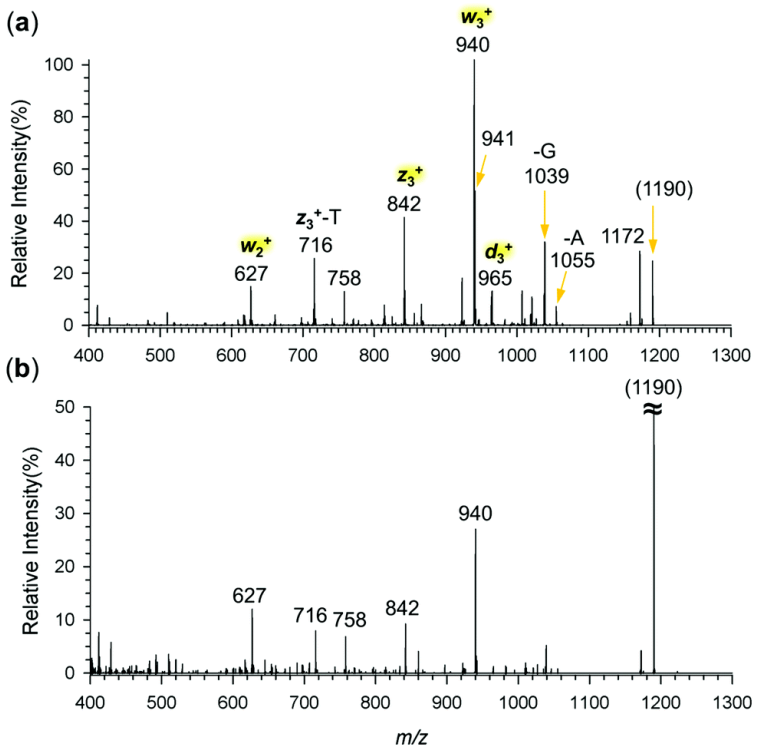

Figure 5.3: Tandem MS^3 spectra of $(GATT + 2H)^{+\bullet}$ at m/z 1190. (a) CID-MS^3, (b) UVPD-MS^3 with 2 laser pulses at 250 nm. Ion relative intensities in both spectra are scaled to that of the most abundant ion as 100%.

The tetranucleotide cation radicals were selected by mass and investigated by collision-induced dissociation (CID-MS^3) to identify the fragment ions that may be suitable as detection channels for action spectroscopy. CID of $(GATT + 2H)^{+\bullet}$ resulted in loss of water, adenine, and guanine nucleobases, forming cation-radical fragment ions at m/z 1172, 1055, and 1039, respectively (Figure 5.3a). The main dissociations were backbone cleavages forming the 3'-terminal fragment ions w_3^+, z_3^+, and w_2^+ at m/z 940, 842, and 627, respectively (Figure 5.3a). These were formed by loss of neutral radical fragments from the 5'-terminus and corresponded to even-electron ions. The backbone dissociations of this tetranucleotide cation radical were analogous to standard DNA ion fragmentations (for the DNA fragment ion nomenclature see ref. [56] and [57]), as also reported for other tetranucleotides.[34] UVPD at 250 nm of $(GATT + 2H)^{+\bullet}$ produced fragment ions that were analogous to those from CID.

The main difference was a diminished loss of guanine (m/z 1039) upon UVPD (Figure 5.3b) compared to CID.

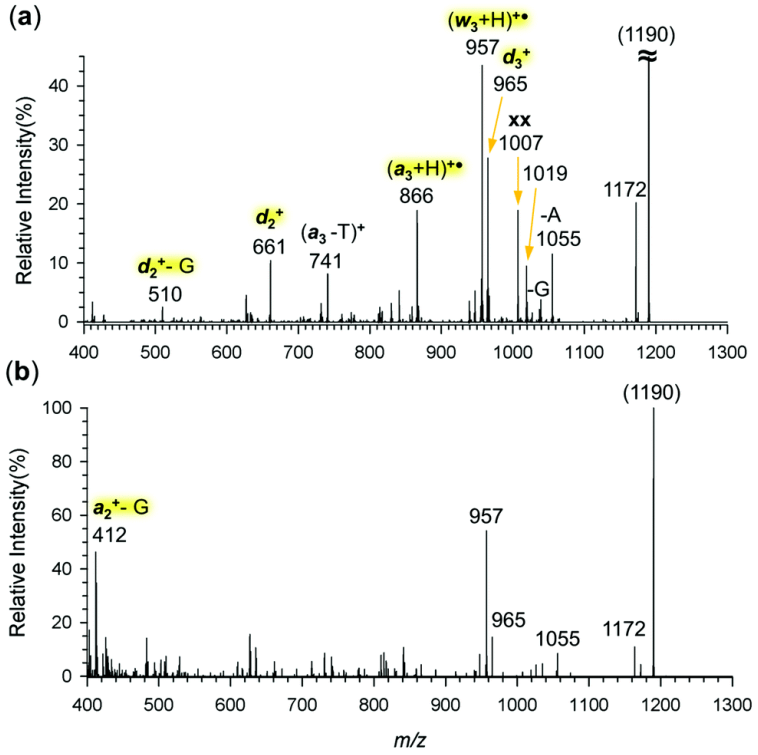

Figure 5.4: Tandem MS^3 spectra of $(AGTT + 2H)^{+\bullet}$ at m/z 1190. (a) CID-MS^3, (b) UVPD-MS^3 with 3 laser pulses at 250 nm. Ion relative intensities in both spectra are scaled to that of the most abundant precursor ion as 100%.

CID-MS^3 of $(AGTT + 2H)^{+\bullet}$ (Figure 5.4a) resulted in dissociations that differed from those of $(GATT + 2H)^{+\bullet}$. Loss of 5'-terminal adenine (m/z 1055) was more abundant than loss of guanine (m/z 1039), pointing to the effect of the nucleobase position in the sequence. The dominant backbone cleavage between A and G led to the 3'-terminal $(w_3 + H)^{+\bullet}$ cation radical at m/z 957 (Figure 5.4) that retained both the charging proton and the reduced hydrogen atom. However, the majority of backbone fragment ions from $(AGTT + 2H)^{+\bullet}$ retained the 5'-terminus, such as the d_3^+ (m/z 965), $(a_3 + H)^{+\bullet}$ (m/z 866), and d_2^+ (m/z 661) ions. In addition, we observed fragment ions at m/z 1007 and 1019 that can be formed by cross-ring dissociations in the T4 nucleotide and elimination of $(T + H_2O + CO)$ for

the former, and (T + C_3H_6O) for the latter fragment ion. These fragment ions are labeled with xx in the Figure 5.4a spectrum. UVPD-MS^3 at 250 nm of $(AGTT + 2H)^{+\bullet}$ showed fragment ions that were similar to those from CID. Noteworthy is the enhanced formation on UVPD of the m/z 412 fragment ion. This can be formed from the d_2^+ ion by consecutive eliminations of guanine (m/z 510) and phosphoric acid, resulting in an ion of the (a_2 - G) type (Figure 5.4b).

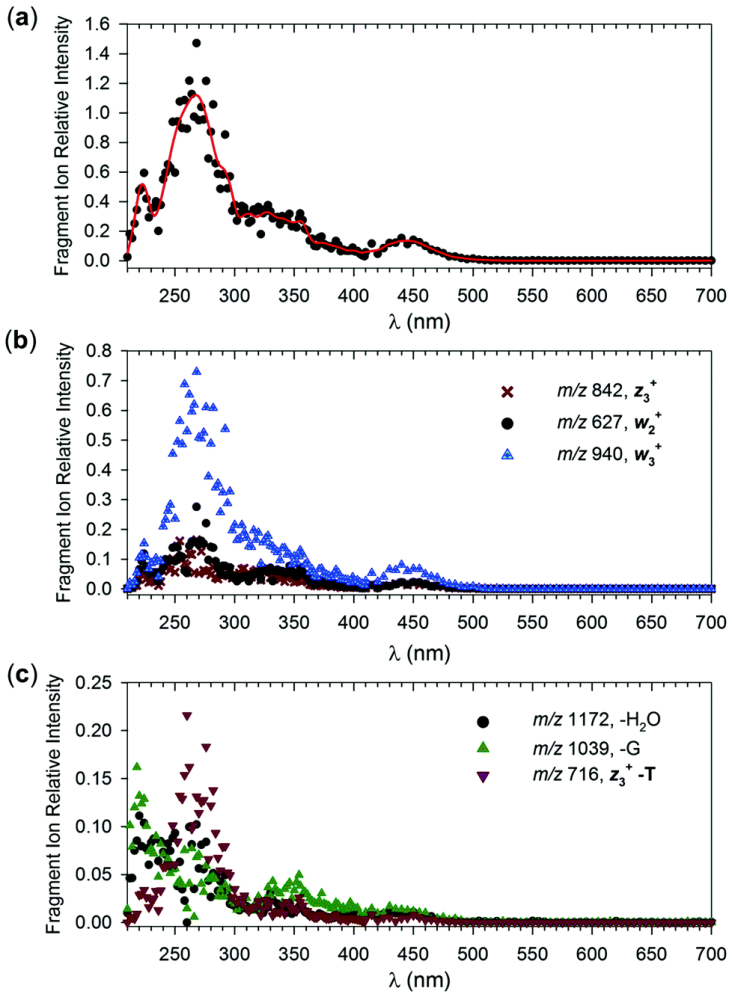

Figure 5.5: Photodissociation action spectra of $(GATT + 2H)^{+\bullet}$ plotted as (a) sum of fragment ion relative intensities, (b) selected major and (c) minor dissociation channels.

5.3.2 Action Spectra

Wavelength-dependent photodissociation of $(GATT + 2H)^{+\bullet}$ was monitored at the main dissociation channels, m/z 1172, 1039, 940, 842, 716, and 627. The overall spectrum profile (Figure 5.5a) is based on the sum of photofragment ion intensities. The action spectrum showed four distinct bands with maxima at 445, 330, 270, and 220 nm. These were all represented in the major mass-resolved photodissociation channels for the w_3^+, w_2^+, and (z_3-T)+ fragment ions (Figure 5.5b and c). The channel for loss of G (m/z 1039) showed a stronger absorption band at 210-230 nm, and a slight shift of the near-UV band maximum from 330 nm to 350 nm (Figure 5.5c). The bands above 300 nm can be assigned to radical chromophores, because neither nucleosides nor nucleoside gas-phase ions with closed electron shells absorb light above 300 nm.[58–60]

The action spectrum of $(AGTT + 2H)^{+\bullet}$ showed bands with maxima at 430, 330, 270, and 220 nm (Figure 5.6a). The apparent split in the 270 nm band in the summed spectrum was caused by the slightly shifted maxima for the major contributing channels at m/z 957 and m/z 627 that appeared at ca. 260 and 275 nm, respectively (Figure 5.6b). The major contributors to the 220 nm band were the m/z 1172, 965, and 866 channels (Figure 5.6c). Overall, the action spectra of the $(AGTT + 2H)^{+\bullet}$ and $(GATT + 2H)^{+\bullet}$ sequence variants showed very similar overall absorption bands, indicating similar chromophores in these cation radicals.

5.3.3 Ion Structures

To interpret the action spectra and assign structures to the cation radicals we carried out a detailed computational analysis of prototropic isomers of $(GATT + 2H)^{2+}$ precursor ions and $(GATT + 2H)^{+\bullet}$ cation radicals. Because of the large number of structures to be considered (vide infra) and the size and open-shell nature of the cation-radicals, we limited our analysis to the GATT set. On the basis of the low gas-phase basicity of thymine,[35] we presumed that double protonation by electrospray would primarily affect the more basic guanine and adenine

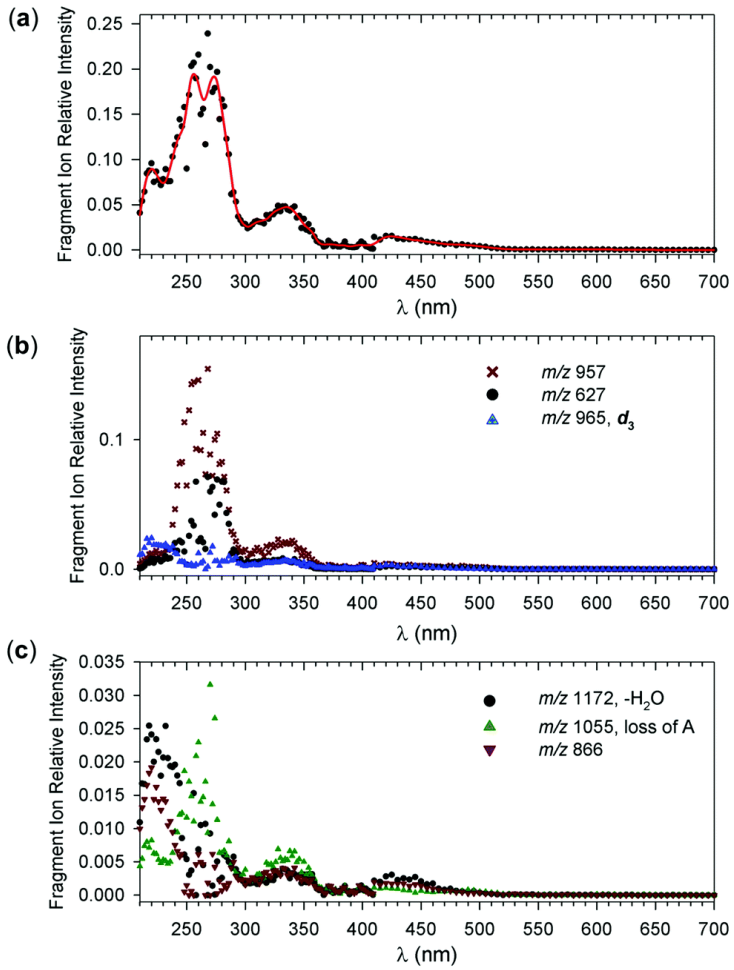

Figure 5.6: Photodissociation action spectra of $(AGTT + 2H)^{+\bullet}$ plotted as (a) sum of fragment ion relative intensities, (b) selected major and (c) minor dissociation channels.

nucleobases. Nevertheless, this assumption need not be satisfied in more complex systems, such as tetranucleotides, where internal hydrogen bonding may result in thymine protonation. Therefore, we carried out an extensive analysis of structures and energies of all 18 dication protomers. Based on the previous studies of topical gas-phase basicities of adenine,[61–63] guanine,[64–68] and thymine[69] we selected the N-1 and N-3 positions in adenine, N-7 in guanine, and O-2 and O-4 positions in thymine residues as the most probable protonation sites. The protomers are labeled according to the protonation sites, e.g.G7A1 for the G-N-7, A-N-1 protomer and likewise for the others. For the nucleobase ring numbering, see

Figure 5.1. Several low-energy conformers of each of the 18 dication protomers were identified by Born-Oppenheimer molecular dynamics followed by full geometry optimization with DFT, as detailed in Section 2.3. Since the dications were produced from electrospray droplets in the presence of solvent, we also obtained relative free energies including solvation energies in water that were approximated using the polarizable continuum model.[47] According to our previous experience,[32] the ranking of relative energies of ions solvated by water and acetonitrile were very similar for both solvents, and so water solvation was deemed sufficient to capture the solvent effects in water-acetonitrile mixtures used in electrospray. The dication relative free energies are summarized in Table 5.1, the optimized structures of selected low-energy isomers are shown in Figure 5.7.

Table 5.1: Relative energies of $(GATT + 2H)^{2+}$ dications

		Relative energy[a,b]		
Ion	Protonation sites	$\Delta H_{0,g}$	$\Delta G^{[c]}_{310,g}$	$\Delta G^{[d]}_{310,aq-}$
G7A1a	G-N7, A-N1	0	0	5
G7A1b	G-N7, A-N1	14	1.7	15
G7A1c	G-N7, A-N1	14	16	0
G7A3a	G-N7, A-N3	39	19	29
G7A3b	G-N7, A-N3	43	28	42
A1T3-4	A-N1, T3-O4	39	33	52
G7T3-2	G-N7, T3-O2	44	16	24
G7T3-4	G-N7, T3-O4	76	64	86

[a] In kJ mol^{-1} for ωB97X-D/6-31+G(d,p) optimized structures.
[b] Including B3LYP/6-31+G(d,p) zero-point vibrational energies scaled by 0.975 and referring to 0 K unless stated otherwise.
[c] Relative free energies at 310 K.
[d] Relative free energies from ωB97X-D/6-31+G(d,p) calculations including PCM solvation energies in the water dielectric.

The Table 5.1 data indicated that conformers of the G-7, A-1-protonated tautomer represented the lowest-energy structures of the $(GATT + 2H)^{2+}$ dications. The lowest ΔH0 conformer (G7A1a) displayed a highly folded globular conformation in which the protonated

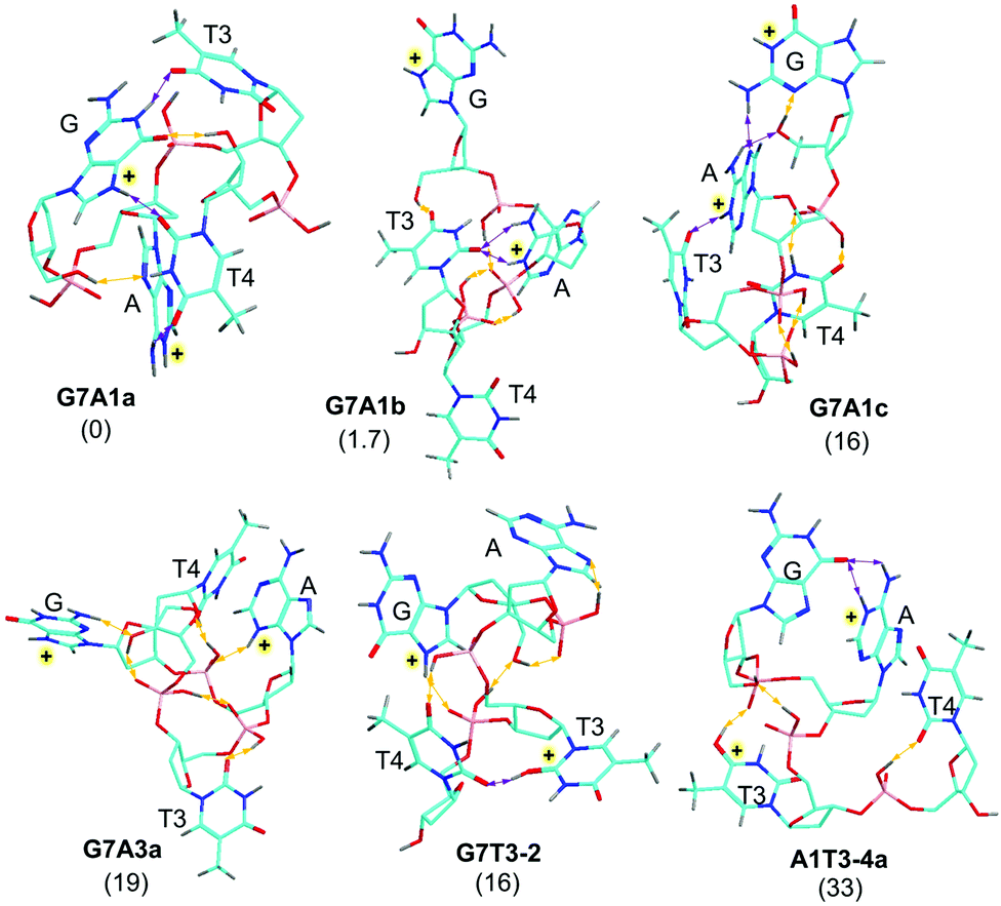

Figure 5.7: ωB97X-D/6-31+G(d,p) optimized structures of low-energy $(GATT + 2H)^{2+}$ dications. Atom color coding is as follows: cyan = C, red = O, blue = N, bronze = P, gray = H. Only exchangeable O–H, N–H and nucleobase hydrogen atoms are shown. Yellow double-headed arrows indicate hydrogen bonds involving backbone oxygens. Purple arrows indicate hydrogen bonds between the nucleobases. Relative free energies in kJ mol^{-1} are for gas-phase ions at 310 K.

guanine was hydrogen-bonded to both neutral thymine nucleobases and the 3'-OH group (Figure 5.7). Despite the extensive H-bonding, the G-7 and A-1 protons in G7A1a were positioned on the opposite faces of the ion at a 11.1 Ådistance to minimize Coulomb repulsion. Two other low-energy conformers with the same protonation sites were represented by G7A1b, and G7A1c. The second lowest-energy conformer (G7A1b) had an extended geometry with the protonated guanine and T-3 on the opposite sides while the protonated adenine and T-4 were tightly hydrogen bonded (Figure 5.7). This conformation allowed for

a higher entropy of G7A1b that decreased its ΔG310 relative to G7A1a to 1.7 kJ mol^{-1} (Table 5.1). The other conformer, G7A1c, showed H-bonding between the protonated guanine and adenine nucleobases, which developed a further H-bond to T-3 (Figure 5.7). This conformation was particularly stabilized by solvation to become the global free energy minimum of (GATT + 2H)$^{2+}$ ions solvated by water. In general, however, the energy differences between these conformers were small and well within the typical accuracy of the DFT calculations (estimated at $\pm$10 kJ mol^{-1}) to allow any of these to be represented among the gas phase dications.

Out of the other tautomers, the G-7, A-3 and G-7, T-2 protonated ions, G7A3a and G7T3-2, respectively, had gas-phase free energies within 20 kJ mol^{-1} of G7A1a, while being disfavored by solvation (Table 5.1). The chief stabilizing structure feature of gas-phase G7A3a was the strong hydrogen bond of N-3-H to the proximate phosphate oxygen at 1.917 Åthat allosterically enhanced H-bonding between the T4 O-2 and the phosphoester O-H at 1.588 Å(Figure 5.7). Noteworthy is the backbone hydrogen bonding of the phosphate groups that formed the core of the G7A3a conformation (Figure 5.7). Likewise, T3 protonation in G7T3-2 was stabilized by a strong H-bond between T3 O-2-H and T4 O-2 at 1.450 Å, and the conformation was further reinforced by several phosphate H-bonds (Figure 5.7). The ranges of conformer gas-phase free energies for all 18 (GATT + 2H)$^{2+}$ tautomers are shown in Figure 5.8. The data indicated that only the G7A1, G7A3, and G7T3-2 tautomers had conformations that were within an energy range allowing their formation by proton-transfer under equilibrium conditions.

Several low-energy precursor dications (Table 5.1) representing different conformers of the G7A1, G7A3, G7T3-2 tautomers were used as initial structures for electron attachment to obtain optimized structures and relative energies of (GATT + 2H)$^{+\bullet}$ cation radicals (Table 5.2). Nucleobase reduction resulted in the formation of an adenine radical (G7rA1) from the G7A1a dication, while the other dication conformers yielded guanine based radicals rG7A1a and rG7A1b of similar relative energies (Table 5.2 and Figure 5.9). Since DFT calculations provide the ground electronic states of the cation-radicals, the site of reduc-

Table 5.2: Relative energies of (GATT + 2H)$^{+\bullet}$ cation radicals

Species/reaction	Radical location	Relative energy[a,b] M06-2X[c] 6-31+G(d,p)	M06-2X[c,d] 6-311++G(2d,p)
G7rA1	A	0 (0)	0 (0)
rG7A1a	G	6.8 (6.4)	2.8 (2.4)
rG7A1b	G	34 (13)	21 (-1.1)
G7rT3	T3	-17 (-33)	-25 (-40)
A1rT3	T3	67 (50)	54 (37)
G7rT4	T4	-1.5 (-13)	-6 (-18)
rG78a	G	-112 (-125)	-120 (-132)
G7rA8	A	-89 (-98)	-94 (-104)
rG78b	G	-73 (-83)	-78 (-88)
rG78c	G	-40 (-49)	-78 (-88)
rA78	A	-45 (-45)	-47 (-46)
G7rA1→ TS1	111	93	
G7rA1→ $w_3^+ + a_1^\bullet$	107 (44)	90 (27)	
G7rT4 → TS2	123	117	

[a] In kJ mol^{-1}.
[b] Including B3LYP/6-31+G(d,p) zero-point vibrational energies scaled by 0.975 and referring to 0 K unless stated otherwise.
[c] Relative free energies at 310 K in parentheses.
[d] Single-point energy calculations on M06-2X/6-31+G(d,p) optimized geometries.

tion reflects the relative ion-electron recombination energies of the protonated nucleobases, whereby the site with the larger recombination energy was reduced to form the ground electronic state of the cation radical. This is illustrated by electron attachment to G7A3a that was accompanied by a phosphate proton migration, producing a thymine radical G7rT3 in which the protonated guanine and adenine ring retained charge, the latter in a zwitterionic pair with a phosphate anion (Figure 5.9). Electron attachment to thymine-protonated dications resulted in the formation of thymine radicals, such as G7rT4 and A1rT3 (Figure 5.9). The Table 5.2 data further indicated that thymine radicals G7rT3 and G7rT4 were thermodynamically more stable than the adenine and guanine radicals of the G7rA1 and rG7A1 type.

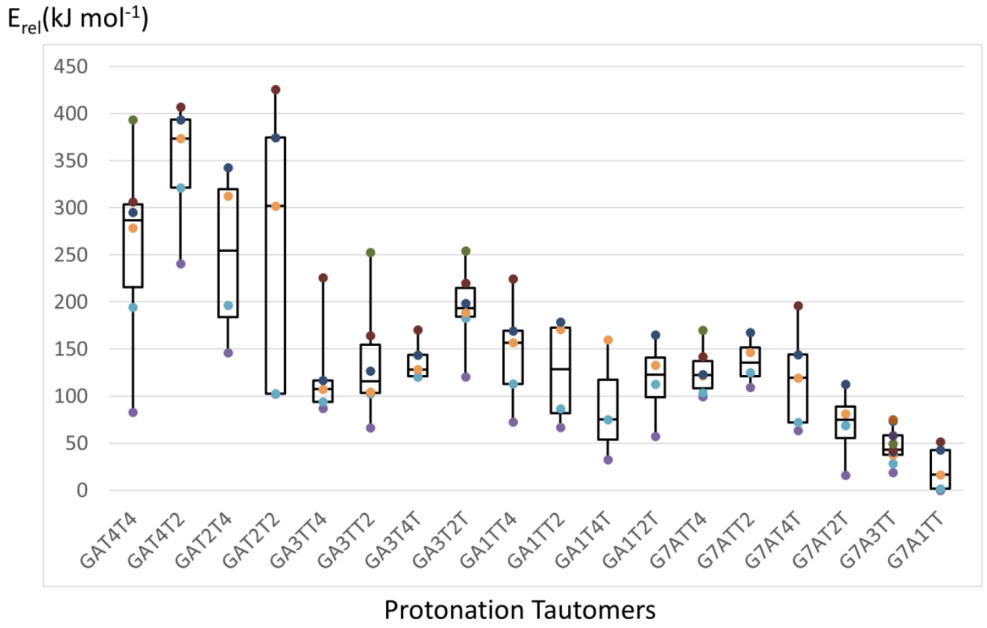

Figure 5.8: Ranges of ωB97X-D/6-31+G(d,p) calculated relative free energies for conformers of 18 $(GATT+2H)^{2+}$ tautomers. The ranges show maxima and minima, the boxes indicate first and third quartiles and medians.

5.3.4 Action Spectra Assignment

We used TD-DFT calculations to investigate excited electronic states in the above-discussed cation radicals with the goal of assigning the experimental action spectrum. However, none of the several cation-radical structures produced by electron attachment gave an absorption spectrum that would match the experiment (Figure 5.10). The low-energy adenine-based (G7rA1, Figure 5.10a) and guanine-based radicals (rG7A1a, rG7A1b, Figure 5.10b, c) were calculated to have absorption bands for transitions to the B-D excited states at 550-600 nm that, however, were absent in the action spectrum. The low-energy thymine-based radicals (G7rT3, G7rT4, Figure 5.10d, e) had only extremely weak bands above 350 nm, which contradicted the action spectrum that showed distinct bands with maxima at 330 and 450 nm. We calculated TD-DFT absorption spectra of several other, higher-energy, radicals, but these revealed no match with the action spectrum either.

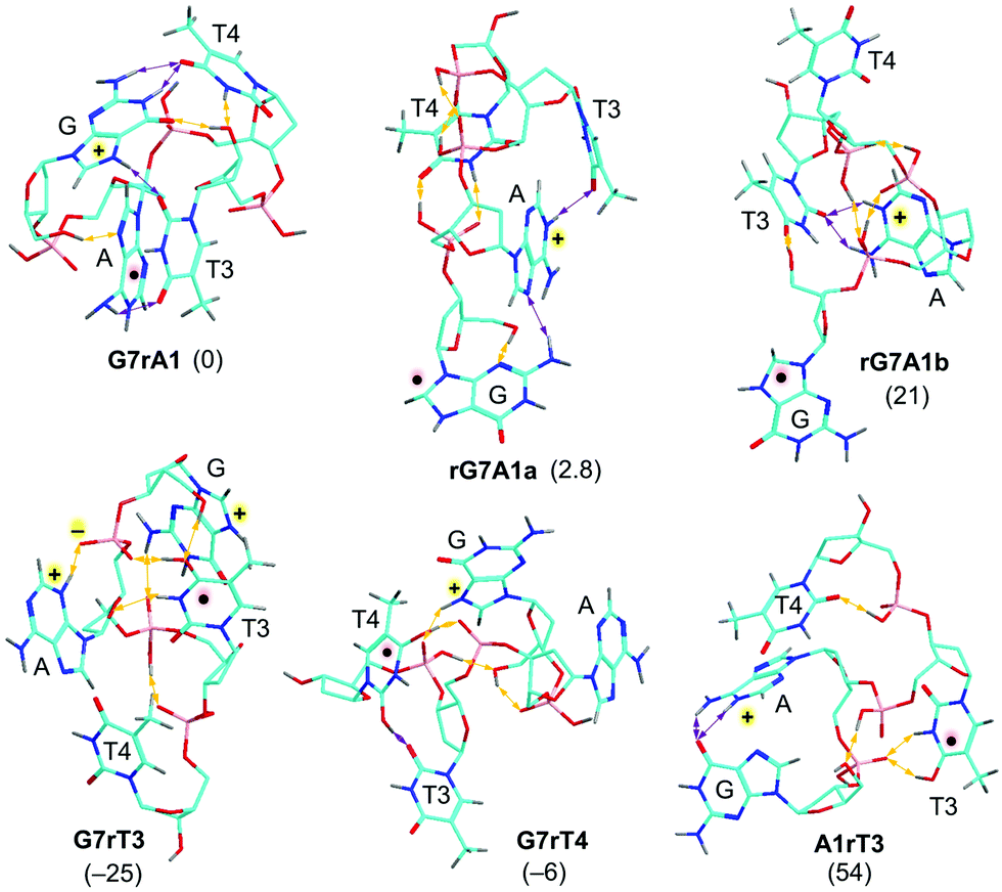

Figure 5.9: M06-2X/6-31+G(d,p) optimized structures of selected primary $(GATT + 2H)^{+\bullet}$ cation radicals by electron attachment to dications. Atom color coding and hydrogen bonds as in Figure 5.7. Relative energies in parentheses (kJ mol^{-1}) are for gas-phase ions at 0 K.

The mismatch of the calculated and action spectra indicated that the species produced by electron transfer did not retain the initially formed nucleobase radical chromophores of hydrogen atom adducts $(A + H)^{\bullet}$, $(G + H)^{\bullet}$, or $(T + H)^{\bullet}$. In particular, the UV-Vis action spectrum of a charge-tagged $(A + H)^{\bullet}$ radical has recently been reported to display a dominant band at 320 nm,[27] which is only weakly represented in the action spectrum of $(GATT + 2H)^{+\bullet}$. According to previous studies of DNA di- and tetranucleotide radicals, the 330 and 450 nm bands in the action spectra could be indicative of 7,8-dihydroguanine[32] or 7,8-dihydroadenine cation radicals[31] produced by intramolecular hydrogen migration.

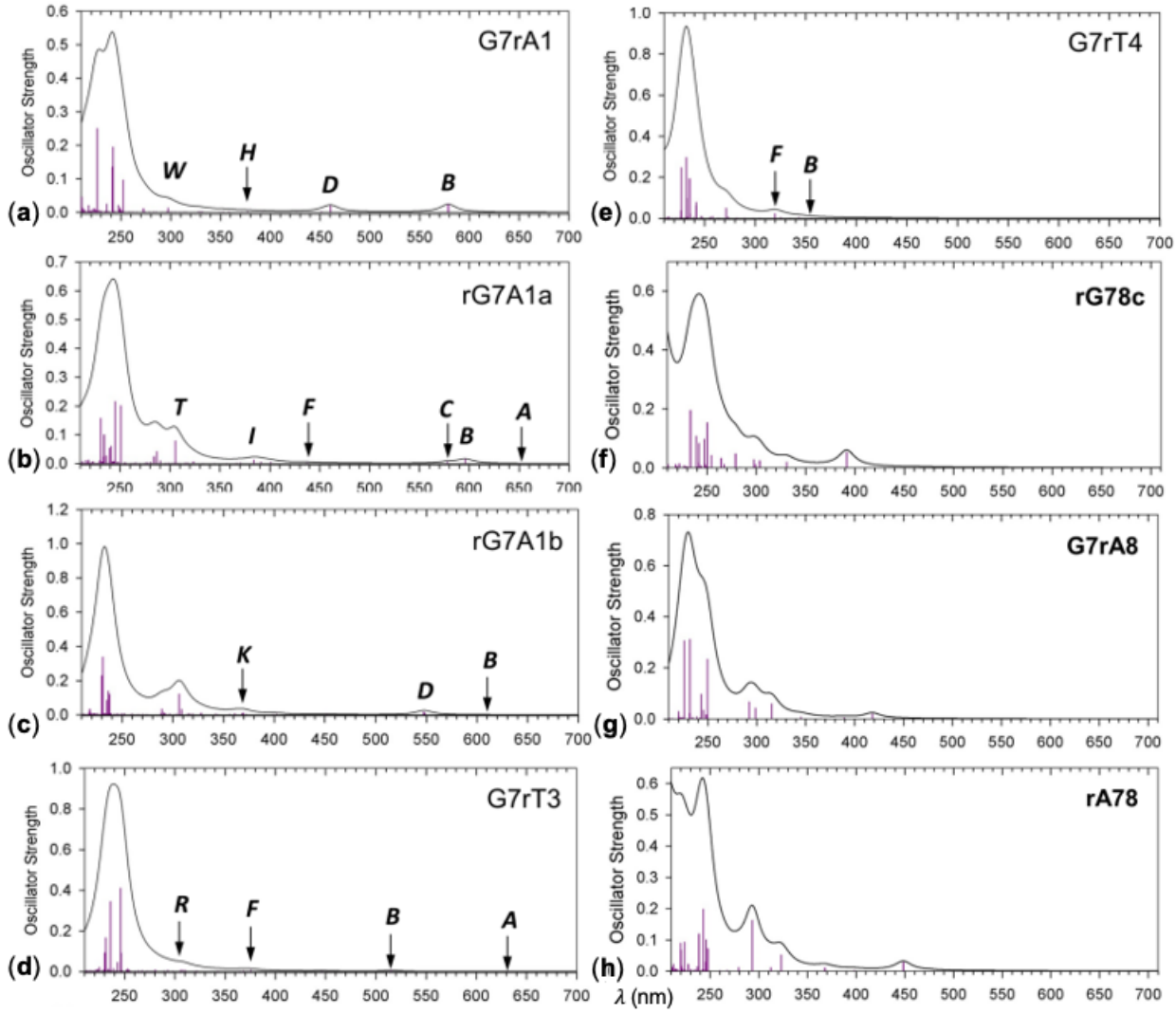

Figure 5.10: M06-2X/6-31+G(d,p) TDDFT absorption spectra of (a) adenine radical G7rA1, (b),(c) guanine radicals rG7A1a and rG7A1b, (d) thymine-3 radical G7rT3, (e) thymine-4 radical G7rT4, (f) adenine radical G7rA8, (g) guanine radical rG78c, (h) adenine radical rA78. The bands are from artificial Lorentzian broadening of the excitation lines with at 10 nm full width at half maximum.

To pursue this line of thought, we generated several cation-radical structures having the 7,8-dihydroguanine and 7,8-dihydroadenine motifs and found them to be substantially more stable than G7rA1 (Table 5.2). The lowest energy isomers were 7,8-dihydroguanine cation radicals rG78a, rG78b, and rG78c, 7,8-dihydroadenine cation radical rA78, and the distonic adenine radical G7rA8, which retained the charging proton at guanine N-7 (Figure 5.11).

The energy data in Table 5.2 indicated that hydrogen atom migration to the C-8 positions in both guanine and adenine was substantially exothermic, providing the driving force for the isomerization. The relevant structures of the reactants, products, and transition state (TS) are shown in Figure 5.12.

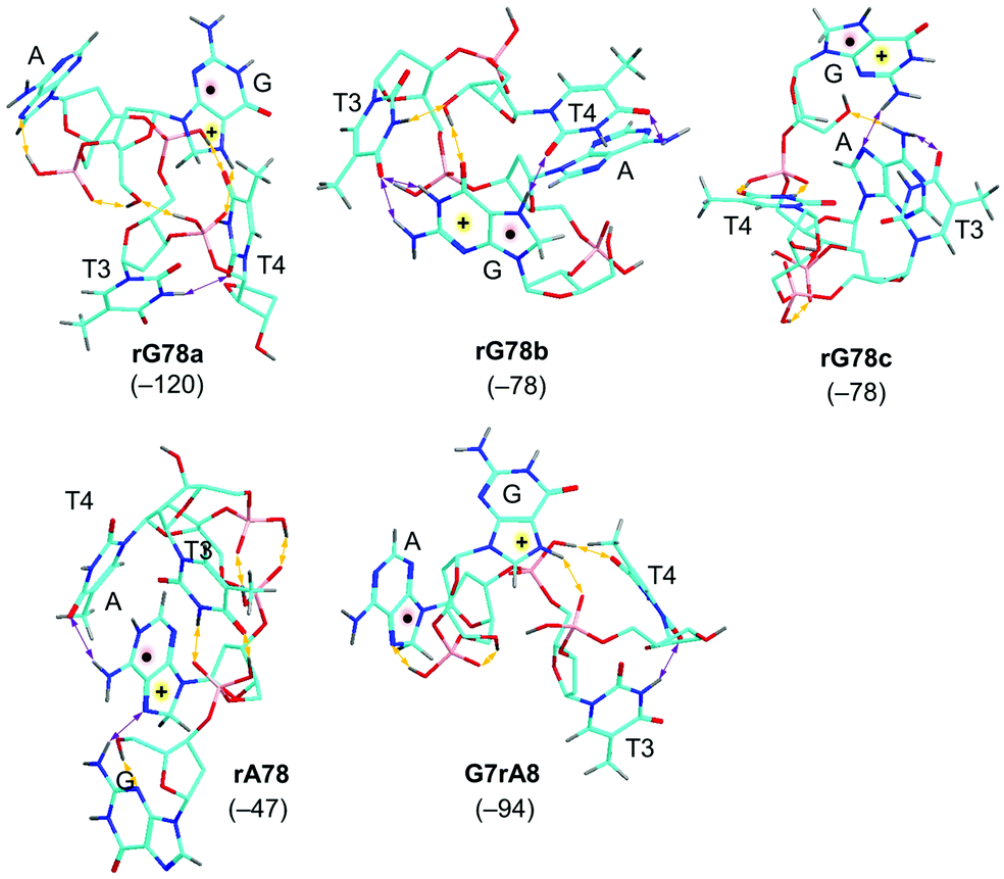

Figure 5.11: M06-2X/6-31+G(d,p) optimized structures of selected $(GATT + 2H)^{+\bullet}$ cation radicals formed by hydrogen migration. Atom color coding and hydrogen bonds as in Figure 5.7. Relative energies in parentheses (kJ mol^{-1}) are for gas-phase ions at 0 K.

The absorption properties of a number of isomers potentially arising from isomerization were examined by TD-DFT spectra. Among these we found two conformational isomers, rG78a and rG78b (Figure 5.13a and b), whose calculated absorption spectra showed approximate match with the action spectrum in the near UV and visible region. In particular, the spectrum of rG78b displayed bands with maxima at 394 and 330 nm due to transitions to

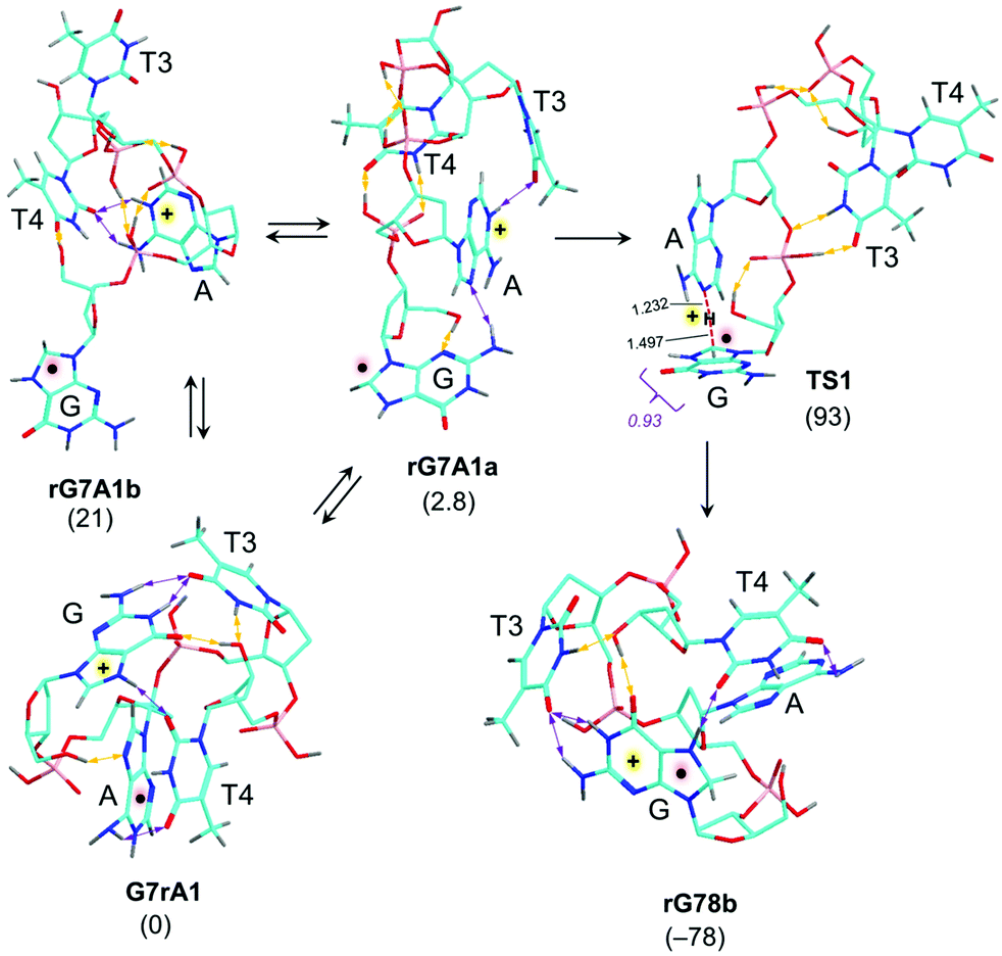

Figure 5.12: Reactant and transition-state structures for hydrogen migration and exothermic isomerization of $(GATT + 2H)^{+\bullet}$. Bond lengths (Å) and spin density in the guanine ring are shown for TS1. Relative energies (ΔH_0, kJ mol^{-1}) in parentheses.

the respective B and D excited states whereas the A and C states were silent. The spectrum of rG78a showed bands at 381 and 335 nm due to transitions to the respective A and C excited states. These two ions were selected for calculations of vibronic spectra of thermal ions at 310 K that included 10 lowest excited states, covering the critical wavelength range above 300 nm to be matched with the action spectrum. Covering a broader range of excited states in 300 vibrational configurations was unfeasible for these large open-shell systems of 1797 basis functions (3003 primitive Gaussians). The 310-500 nm bands in the vibronic

spectrum of rG78b showed an excellent match with the 330 and 445 nm bands in the action spectrum, as shown by the overlaid band profiles (Figure 5.13b). The vibronic spectrum of rG78a (Figure 5.13a) displayed a substantial dispersion and red shift of the 381 nm band due to ground state vibrations that resulted in a decreased match with the bands in the action spectrum. We note that the TD-DFT spectra of the other low-energy isomers (Figure 5.10f, g and h) provided a much less satisfactory match by either showing bands that were absent in the action spectrum, or conversely lacking some action spectrum bands. Based on the vibronic spectra and favorable relative energy, we assign the action spectrum to rG78b as the dominant component of cation radials formed by electron transfer to $(GATT + 2H)^{2+}$ dications. Because of the broad bands in the action spectrum and ensuing limited wavelength resolution, we cannot exclude the presence of minor components that would overlap with rG78b and be compatible with the $(GATT + 2H)^{+\bullet}$ relative energies.

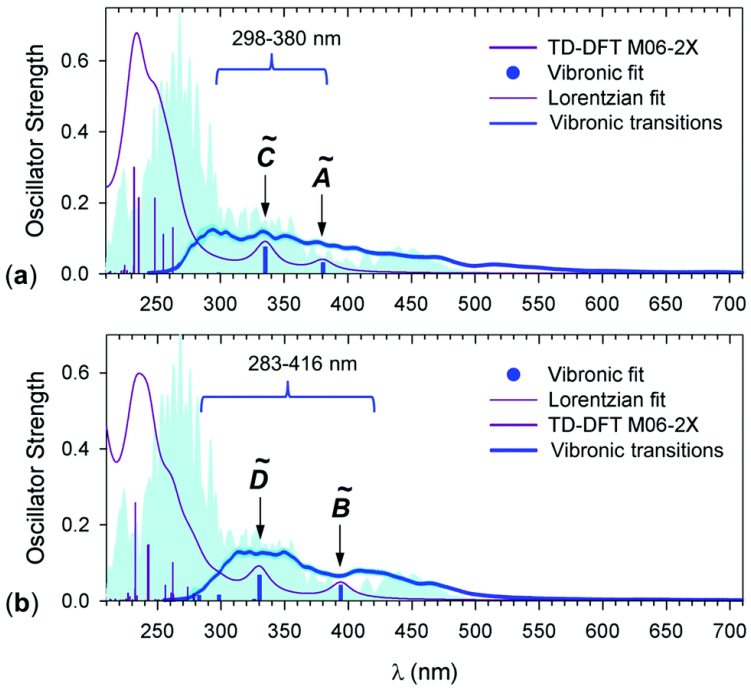

Figure 5.13: M06-2X/6-31+G(d,p) calculated absorption spectra of (a) rG78a and (b) rG78b. Blue lines show vibronic spectra for 10 excited states spanning the wavelength region indicated by the brackets. Blue bands in the background are action spectra scaled to fit the oscillator strength range.

5.3.5 Excited State Molecular Orbital Analysis

The nature of the electronic excitations in rG78b and rG78a was examined by molecular orbital analysis that revealed further differences. The lowest-energy excitation (A state, ΔE = 2.98 eV) in rG78b was dipole disallowed (oscillator strength f = 0.0006) and was not expected to give rise to a band in the spectrum. This pertinent excitation involved an internal electron transition to the semi-occupied molecular orbital SOMO, (MO310β) that displayed substantial components of charge transfer from adenine to guanine. The B state, corresponding to the 392 nm band, also involved excitation within the β-electron manifold of π_z orbitals on guanine (MO304β $\rightarrow$ MO310β, Figure 5.14, left panel). The D state, corresponding to the 330 nm band, was realized by an excitation from the SOMO (MO310α) to the virtual orbital space with a major component of MO312α. Interestingly, this transition involved substantial charge transfer from the adenine ring to the guanine radical (Figure 5.14). In contrast, the lowest-energy transition leading to the A state in rG78a, which was represented by the 381 nm band, was a pure charge transfer from the thymine π-electron system (MO303β) to the SOMO on adenine (MO310β) that did not directly involved the guanine cation-radical. The substantial thermal broadening of the corresponding band (Figure 5.14b, right panel) is understandable, because thermal motion in the ion affects the distance and mutual orientation of the adenine and thymine ring, thus affecting the dipole coupling for the electron transition. The next transition in this wavelength region (335 nm) was to the C state and involved π_z orbitals on guanine (MO310α $\rightarrow$ MO311α, Figure 5.14).

5.3.6 GATT Isomerization, Dissociation Energies and Kinetics

The action spectra and energy analysis indicated that isomerization of G7rA1 proceeded upon electron transfer and was 78 kJ mol^{-1} exothermic (by ΔH_0) when forming the rG78b cation radical (Figure 5.12). The energy associated with the electron transfer reaction, $\Delta H_{rxn} < 0$, was estimated from Equation 5.1, which can be equivalently described by heats of formation

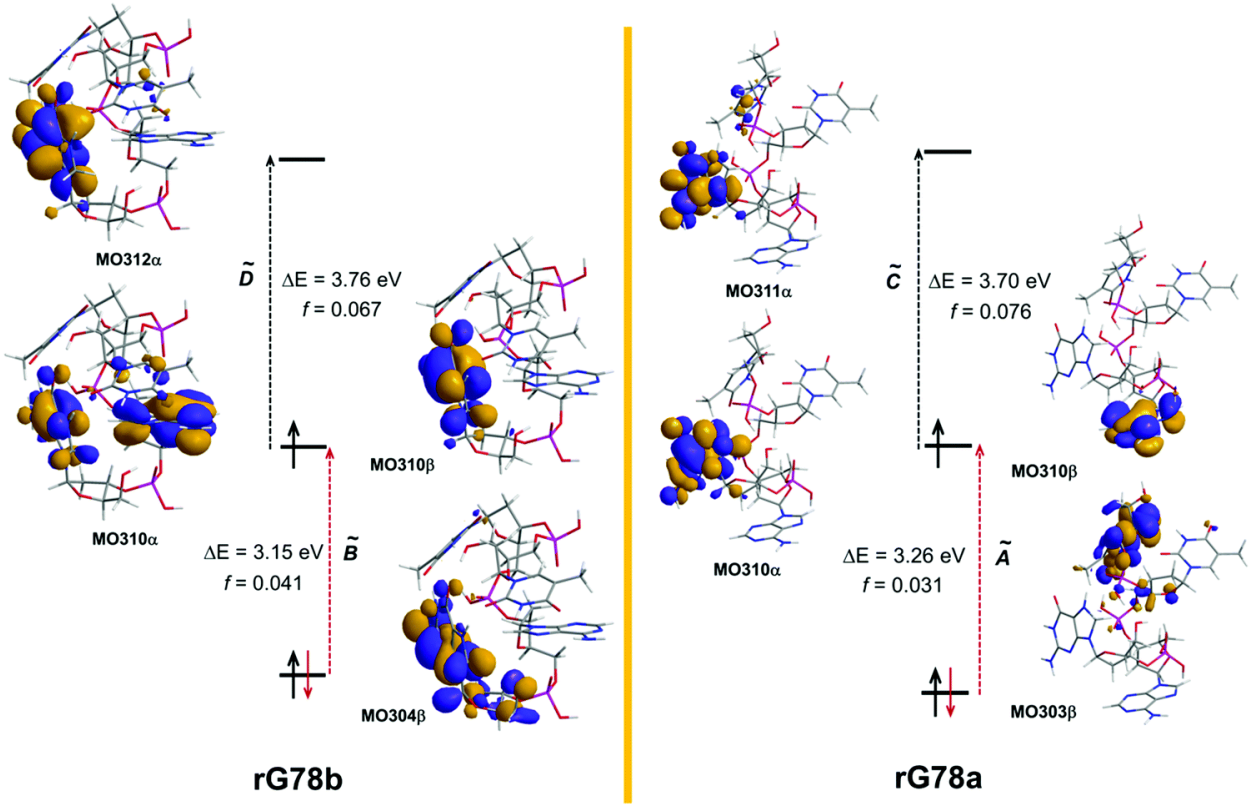

Figure 5.14: Molecular orbitals involved in electron excitation to low excited states in rG78b (left panel) and rG78a (right panel). The wave function phases are distinguished by color. Excitation energies are from M06-2X/6-31+G(d,p) TD-DFT calculations.

($\Delta H_{f,eqn}(2)$) or recombination energies (Equation 5.3), where RE < 0 is the recombination energy of the G7A1a dication, and EA is the electron affinity of fluoranthene. Equation 5.2 and Equation 5.3 in part rely on our previous finding that electron transfer from fluoranthene anion produces the neutral molecule in the ground singlet electronic state.[70]

$$(G7A1a)^{2+} + [fluoranthene]^{-\bullet} \rightarrow (G7rA1)^{+\bullet} + fluoranthene \tag{5.1}$$

$$\Delta H_{rxn} = \Delta H_f(G7rA1)^{+\bullet} - \Delta H_f(fluoranthene)^{-\bullet} \tag{5.2}$$

$$\Delta H_{rxn} = RE(G7A1a)^{2+} + EA(fluoranthene) \tag{5.3}$$

We used the calculated RE for the lowest energy dications, -RE = 586, 589, and 552 kJ mol^{-1} for G7A1a, G7A1b, and G7A1c, respectively, and the EA of fluoranthene (EA = 82 kJ mol^{-1})[34] to estimate the electron transfer energy as 470-507 kJ mol^{-1}. This excess energy was supposed to be partitioned between (GATT + 2H)$^{+\bullet}$ and the fluoranthene molecule in the ratio of their rovibrational heat capacities, giving an initial vibrational excitation in (GATT + 2H)$^{+\bullet}$ as Eexc = 504 × 68.5/(68.5 + 10.7) = 436 kJ mol^{-1}. The internal energy distribution in the cation radical produced by electron transfer, P(E), was expressed as a convolution of the precursor ion thermal energy at 310 K and the Eexc (Figure 5.15a). RRKM rate constants k(E) were calculated using the M06-2X/6-311++G(2d,p) energy for TS1 (93 kJ mol^{-1}, Table 5.2) and convoluted with the P(E) (Figure 5.15b), to estimate the population-weighed rate of isomerization, kisom (Equation 5.4), for the isomerization:G7rA1 → TS1 → rG78b.

$$k_{isom} = \int_{E_{TS}}^{\infty} k(E)P(E)dE \tag{5.4}$$

This result, kisom = 9.6 × 106 s^{-1}, indicated that G7rA1 would have a 72 ns half-life and therefore should isomerize completely on the time scale of the measurement (0.15 s). A complicating factor in these rate estimates was the collisional cooling of the internally hot ions under the conditions of 3 mTorr He in the ion trap. While the collision rate can be estimated from the He pressure and the calculated collision cross section, the collision energy transfer and its dependence on the ion internal energy were unknown. We have previously addressed this problem by expressing collisional cooling by competitive kinetics,[34, 70] to solve Equation 5.5-Equation 5.8 for a range of cooling rate constants kcool. The mole fraction of the rG78b isomerization product (xrG78b) is expressed by Equation 5.9:

$$-\frac{d[G7rA1]_{hot}}{dt} = -(k_{isom} + k_{cool})[G7rA1]_{hot} \tag{5.5}$$

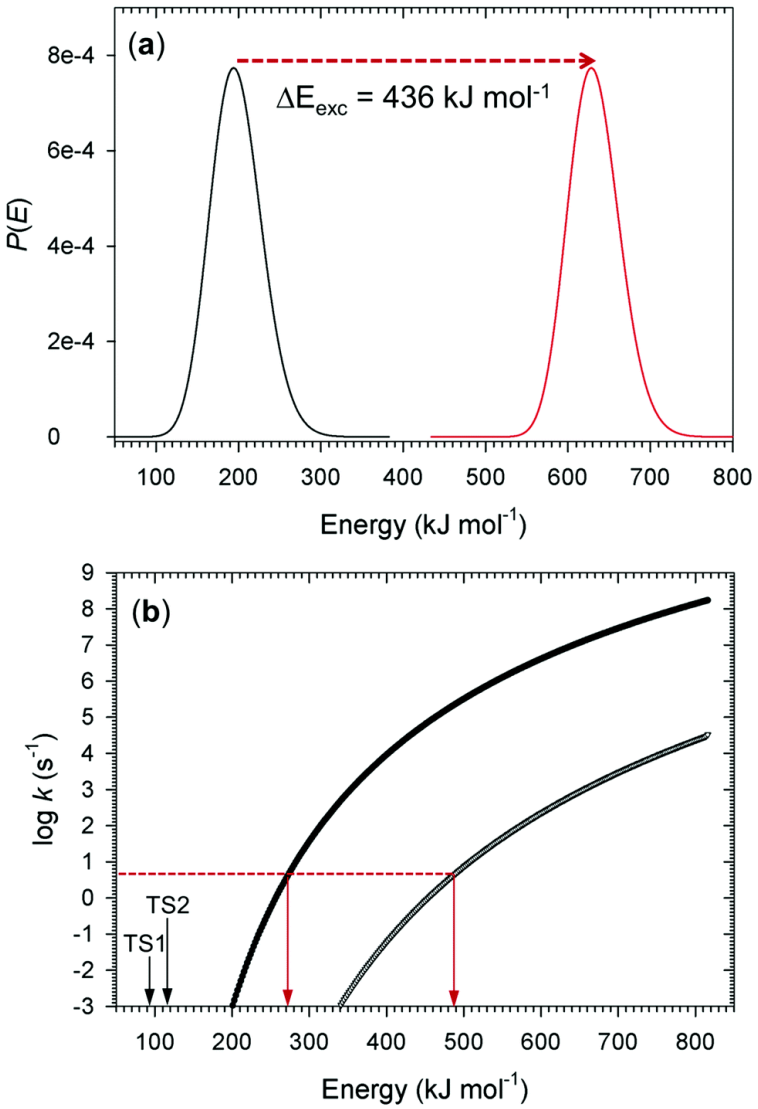

Figure 5.15: (a) Vibrational energy distribution, P(E), in (black) the G7A1a dication precusror at 310 K and (red) G7rA1 cation radical after exothermic electron transfer. (b) RRKM rate constants for the G7rA1 (full circles) and G7rT4 (empty triangles) isomerizations as a function of internal energy. Red arrows indicate the internal energies needed for log k_{isom} = 0.665 to achieve 50% conversion at 150 ms.

$$\frac{d[rG78b]}{dt} = k_{isom}[G7rA1]_{hot} \tag{5.6}$$

$$\frac{d[G7rA1]_{cool}}{dt} = k_{cool}[G7rA1]_{hot} \tag{5.7}$$

$$x_{G7rA1} = [G7rA1]_{hot} + [G7rA1]_{cool} \tag{5.8}$$

$$x_{rG78b} = \int_{E_{TS}}^{\infty} \frac{k_{isom}(E)}{k_{isom}(E) + k_{cool}} \{1 - e^{-(k_{isom}(E)+k_{cool})t}\} P(E)\, dE \tag{5.9}$$

Using the kisom(E) in Equation 5.9 indicated that for kcool < 105 s^{-1} the isomerization would still proceed with 99% efficiency, xrG78b ≥ 0.99, on the 0.15 s time scale. Previous estimates of kcool ranged at <104 s^{-1},70 suggesting that collisional cooling should be insufficient to prevent the isomerization of G7rA1. Efficient isomerization was also predicted by transition-state-theory (TST) kinetics for fully thermalized G7rA1. Figure 5.16 (ESI) indicates that for ion trap temperatures of >320 K the isomerization would be >99% complete. The facile isomerizaiton was promoted by a low Arrhenius activation energy, Ea = 96.5 kI mol^{-1}, and a high frequency factor of logA = 17.42. The latter was due to a positive entropy change for G7rA1 $\rightarrow$ TS1, $\Delta S^{\neq}$ = 74-75 J mol^{-1} K^{-1} for the indicated temperature range. The TS1 structure (Figure 5.12) showed only a partial disruption of the dissociating adenine N-1-H bond at d(N-H) = 1.232 Å, consistent with an early transition state for the highly exothermic reaction. Population analysis indicated that 93% spin density was contained in the guanine ring in TS1 (Figure 5.12). At the same time, the G7rA1 conformation in which T3 and T4 were hydrogen bonded to A and G refolded, resulting in a more open conformation of TS1 and increasing its vibrational entropy.

An alternative pathway can be visualized as starting from the guanine radical rG7A1a, which is nearly isoenergetic with G7rA1 (Table 5.2). Radical rG7A1a can undergo a proton transfer from the adenine N-1 position to the guanine C-8 via the same TS1. TST kinetic analysis under thermal conditions yielded Ea = 75.6 kJ mol^{-1} and log A = 13.51. Hence, this pathway had a lower activation energy but also a lower frequency factor than the one starting from G7rA1, which was consistent with a smaller rise of entropy in TS1 ($\Delta S^{\neq}$ = 22-23 J mol^{-1} K^{-1} for the indicated temperature range). The temperature dependence (Figure 5.16) indicated >95% isomerization at T > 330 K, which is within the range of ion-trap effective

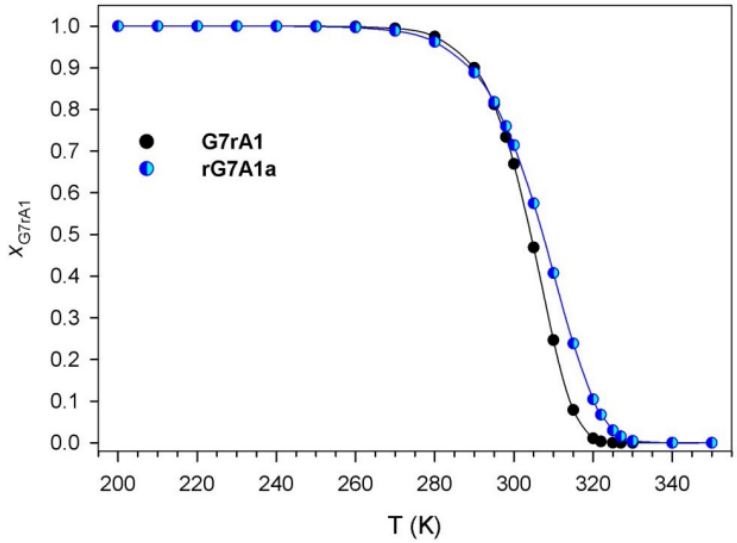

Figure 5.16: Temperature-dependent mole fractions of G7rA1 and rG7A1a isomerizing to rG78b via TS1 within 150 ms.

temperatures.[27, 71–74]

We also considered an isomerization by hydrogen migration from thymine O-2 to guanine C-8 in the low-energy isomers G7rT3 and G7rT4 (Figure 5.9) in which these nucleobases were in proximity. However, analysis of the potential energy surface along the presumed H-transfer trajectory indicated that it was associated with a disruption of strong hydrogen bonds of T4 to T3 and a phosphate (Figure 5.9). For isomerization of G7rT3, this resulted in a substantial increase of potential energy. We located a transition state (TS2) for the isomerization of G7rT4, which was at 117 kJ mol^{-1} relative to G7rT4 (Table 5.2 and Figure 5.17). TST rate constants for the reaction G7rT4 $\rightarrow$ TS2 were below 0.002 s^{-1} at 350 K (Figure 5.18), indicating that this thymine radical would not undergo spontaneous isomerization upon storage in the ion trap. The RRKM rate constants for the G7rT4 isomerization viaTS2 (Figure 5.15b) were >3 orders of magnitude lower than those for G7rT3. Nevertheless, at a high excitation following electron transfer the population-averaged rate constant for G7rT3, k2,isom(E) = 7.4 $\times$ 102 s^{-1}, indicated 0.9 ms lifetime for the radical. Collisional cooling was expected to have a substantial effect on the isomerization of G7rT3. For kcool = 1000

s^{-1}, we calculated only 36% of G7rT3 isomerizing to a guanine C-8 radical. It should be noted that the RRKM kinetics (Figure 5.15b) also indicated a large difference in the kinetic shifts for the isomerizations of G7rA1 and G7rT4. The dissociations of G7rA1 and G7rT4 required 180 and 371 kJ mol^{-1} of excess internal energy above the respective TS in order to reach 50% conversion at 150 ms (Figure 5.15b).

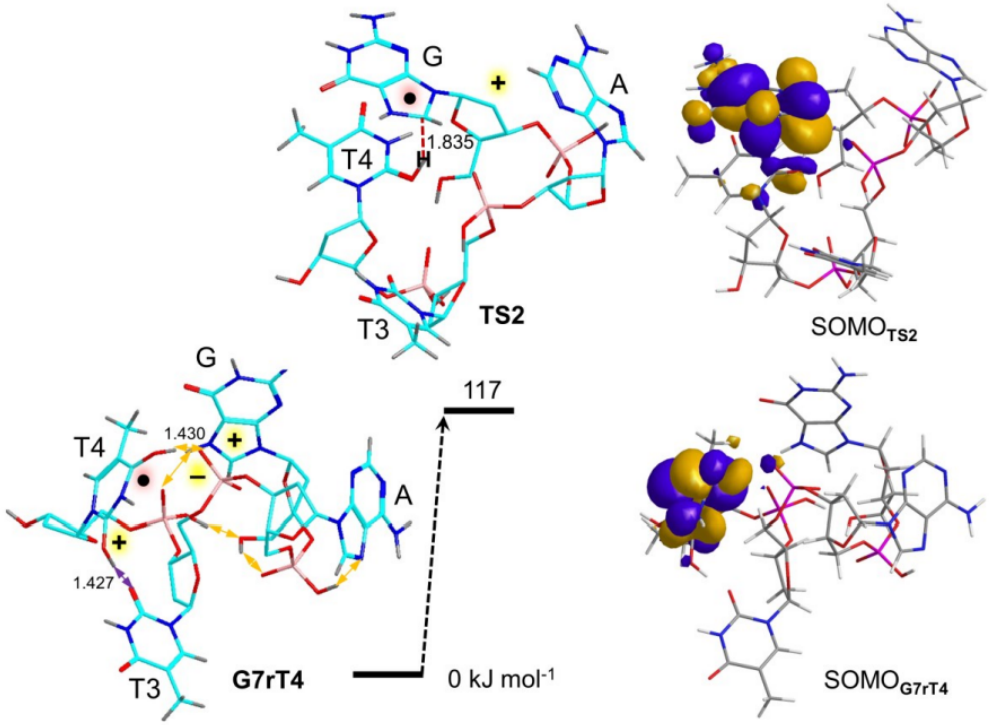

Figure 5.17: Hydrogen atom migration in G7rT4. The right panel shows the singly-occupied molecular orbitals (SOMO) for the G7rT4 reactant and TS2.

Interestingly, the dissociation of $(GATT + 2H)^{+\bullet}$ to w_3^+ and that was observed upon CID and UVPD (Figure 5.3) was calculated to have a relatively low threshold energy of 90 kJ mol^{-1} for G7rA1 (Table 5.2), which was similar to the TS energy for the isomerization. However, the dissociation did not proceed spontaneously upon the exothermic electron transfer (Figure 5.2a), despite the substantial vibrational excitation in the $(GATT + 2H)^{+\bullet}$ formed (436 kJ mol^{-1}, vide supra). This may indicate that the phosphate elimination in-

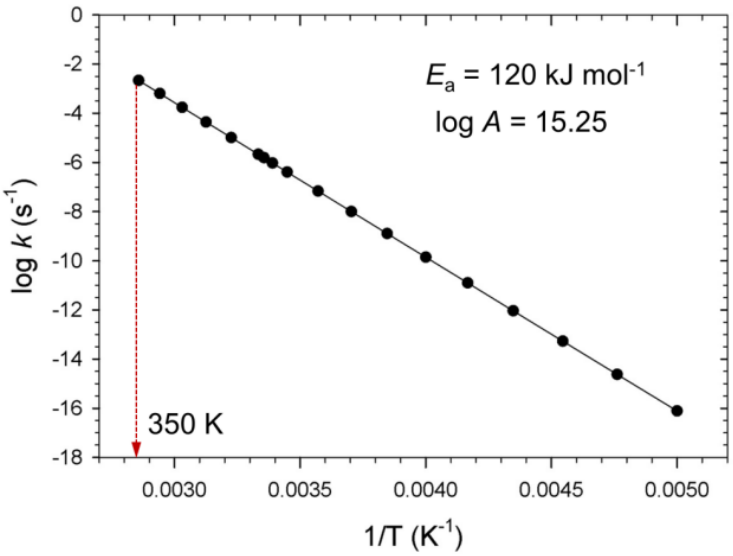

Figure 5.18: Arrhenius plot of calculated TST rate constants for G7rT4 isomerizing via TS2.

volved in the formation of the w_3^+ ion had a substantial activation energy. Because of the fast isomerization of hot G7rA1 or rG7A1 to rG78, the more stable radical product was facing a substantially higher dissociation threshold (167 kJ mol^{-1}), resulting in a slow dissociation that was further limited by collisional cooling. Thus, fast isomerization of the primary G7rA1 or rG7A1 cation radicals, as predicted by RRKM calculations, was consistent with the observed stability of the (GATT + 2H)$^{+\bullet}$ ions produced by highly exothermic electron transfer.

5.3.7 Comparison of Tetranucleotide Cation Radicals

It was interesting to compare the structures and reactivity of (GATT + 2H)$^{+\bullet}$ cation radicals vis-a-vis those of the related (GATC + 2H)$^{+\bullet}$ tetranucleotide system.[34] In both systems, the primary cation radicals underwent exothermic isomerization by hydrogen migration to guanine C-8. However, in (GATC + 2H)$^{+\bullet}$ the source of the hydrogen atom was the reduced 3'-cytosine radical whereas with (GATT + 2H)$^{+\bullet}$ the H-atom originated from reduced adenine. The differences in the reduction sites in (GATC + 2H)$^{+\bullet}$ and (GATT + 2H)$^{+\bullet}$ can

Table 5.3: Calculated total and recombination energies of protonated DNA nucleobases.

	Energy[a]				
Species	B3LYP 6-31+G(d,p)	ZPVE[b]	M06-2X 6-31+G(d,p)	M06-2X[c] 6-31++G(2d,p)	CCSD(T)[c,d] CBS
Adenine-N-1-H^+	-467.724170	329.8	-467.534187	-467.652321	-467.131484
Adenine-N-1-$H^\bullet$	-467.888374	318.7	-467.696672	-467.815835	-467.294236
Guanine-N-7-H^+	-542.968650	341.3	-542.751844	-542.894554	-542.315853
Guanine-N-7-$H^\bullet$	-543.134895	331.3	-542.913537	-543.058757	-542.478326
Cytosine-N-3-H^+	-395.339050	295.2	-395.168685	-395.274671	-394.858909
Cytosine-N-3-$H^\bullet$	-395.528648	283.1	-395.356707	-395.464292	-395.047311
Thymine-O-4-H^+	-454.510897	334.6	-454.317138	-454.442311	-453.973843
Thymine-O-4-$H^\bullet$	-454.710370	320.2	-454.515429	-454.641156	-454.171437
	Recombination Energy[e]				
RE(adenine-N-1-H)$^+$	-4.58		-4.53	-4.56	-4.54
RE(guanine-N-7-H)$^+$	-4.62		-4.50	-4.57	-4.52
RE(cytosine-N-3-H)$^+$	-5.28		-5.24	-5.28	-5.25
RE(thymine-O-4-H)$^+$	-5.57		-5.54	-5.56	-5.52

[a] Total energies in hartrees, 1 hartree = 2625.5 kJ mol^{-1}.
[b] Unscaled zero point energies in kJ mol^{-1} from B3LYP/6-31+G(d,p) harmonic vibrational analysis.
[c] Single-point calculations on M06-2X/6-31+G(d,p) optimized geometries.
[d] Effective single-point energies from basis set expansion to the complete basis set via spin-projected PMP2 energies: E[CCSD(T)/CBS] $\cong$ ΔE[ROHF/augcc-pVQZ)] + ΔEcorr[PMP2/CBS] + E[CCSD(T)/aug-cc-pVDZ)] – E[PMP2/aug-cc-pVDZ)].
[e] Adiabatic recombination energies at 0 K in electron volts.

be seen as reflecting the different adiabatic recombination energies (REadiab) of the protonated nucleobases. These were calculated as -REadiab = 4.54, 4.52, 5.25, and 5.52 eV for protonated N-1-H adenine, N-7-H guanine, N-3-H cytosine and O-4-H thymine cations, respectively (Table 5.3). These figures are consistent with electron attachment to protonated cytosine in low-energy (GATC + 2H)$^{2+}$ conformers where it led to a ground electronic state of the primary cytosine radical intermediate. In contrast, protonated thymine tautomers were energetically prohibitive in (GATT + 2H)$^{2+}$ as indicated by the relative energies of

A1T3-4, G7T3-2, and G7T3-4 (Table 5.1) and thus were unlikely to be present as radical precursors. Electron attachment to a thymine ion tautomer would produce low-energy radicals G7rT3, and G7rT4 (Table 5.2) which, however, were excluded by action spectra analysis. Electron attachment to protonated adenine or guanine nucleobases can be expected to be non-specific, judged by the very similar REadiab of the nucleobase ions (vide supra). The differences in the reduction sites in G7rA1 on the one hand and rG7A1a and rG7A1b on the other, indicated a modulation of the nucleobase ion recombination energies depending on the charge and dipolar interactions created by the ion conformation. Similar effects have been reported for charge and dipole-guided electron attachment to peptide dications,[75–77] and ribonucleotide chimeras.[31] We note that effects on ionization energy of guanine stacking have been studied computationally, and the guanine ionization energies have been shown to decrease in artificially stacked dimers and trimers.[78] In contrast, effects on ionization or recombination energies of the DNA strand conformation have not been previously explored.

5.4 Conclusions

This combined experimental and computational study pointed to a spontaneous isomerization of $(GATT + 2H)^{+\bullet}$ cation radicals when produced by one-electron reduction of $(GATT + 2H)^{2+}$ dications in the gas phase. The primary reduction site, A or G, was determined by the protonation sites in the precursor dications that favored the basic adenine and guanine nucleobases. On the basis of action spectra, we concluded that the dominant final reduction product was a 7,8-dihydroguanine cation radical. Kinetic analysis of the reactants and transition states was interpreted as favoring a migration of adenine N-1-H to guanine C-8 that can proceed spontaneously at 320 K on the 0.15 s scale of ion storage and was substantially accelerated by internal excitation provided by highly exothermic electron transfer. Comparison of related tetranucleotide cation radicals, $(GATT + 2H)^{+\bullet}$ and $(GATC + 2H)^{+\bullet}$, both containing the 7,8-dihydroguanine cation-radical moiety, revealed differences in the reaction mechanisms for hydrogen atom migrations that were affected by the protonation sites as well as by the network of intramolecular hydrogen bonds in the reactants and transition states.

5.5 Bibliography

[1] Hans-Achim Wagenknecht. Principles and mechanisms of photoinduced charge injection, transport, and trapping in dna. *Charge Transfer in DNA: From Mechanism to Application*, pages 1–26, 2005.

[2] Melanie A O'Neill and Jacqueline K Barton. Sequence-dependent dna dynamics: The regulator of dna-mediated charge transport. *Charge Transfer in DNA: From Mechanism to Application*, pages 27–75, 2005.

[3] CJ Murphy, MR Arkin, Yl Jenkins, ND Ghatlia, SH Bossmann, NJ Turro, and JK Barton. Long-range photoinduced electron transfer through a dna helix. *Science*, 262(5136):1025–1029, 1993.

[4] Bernd Giese. Long-distance charge transport in dna: the hopping mechanism. *Accounts of chemical research*, 33(9):631–636, 2000.

[5] Bernd Giese, Jérôme Amaudrut, Anne-Kathrin Köhler, Martin Spormann, and Stephan Wessely. Direct observation of hole transfer through dna by hopping between adenine bases and by tunnelling. *Nature*, 412(6844):318–320, 2001.

[6] Avik K Ghosh and Gary B Schuster. Role of the guanine n1 imino proton in the migration and reaction of radical cations in dna oligomers. *Journal of the American Chemical Society*, 128(13):4172–4173, 2006.

[7] Jungkweon Choi, Sachiko Tojo, Doo-Sik Ahn, Mamoru Fujitsuka, Shunichi Miyamoto, Kazuo Kobayashi, Hyotcherl Ihee, and Tetsuro Majima. Proton transfer accompanied by the oxidation of adenosine. *Chemistry–A European Journal*, 25(32):7711–7718, 2019.

[8] Jungkweon Choi, Dae Won Cho, Sachiko Tojo, Mamoru Fujitsuka, and Tetsuro Majima. Structural study of various substituted biphenyls and their radical anions based on time-resolved resonance raman spectroscopy combined with pulse radiolysis. *The Journal of Physical Chemistry A*, 119(5):851–856, 2015.

[9] Anil Kumar and Michael D Sevilla. Influence of hydration on proton transfer in the guanine- cytosine radical cation (g•+- c) base pair: A density functional theory study. *The Journal of Physical Chemistry B*, 113(33):11359–11361, 2009.

[10] L Rodriguez-Santiago, M Noguera, J Bertan, and M Sodupe. Hydrogen bonding and proton transfer in ionized dna base pairs. *Amino Acids and Peptides. In Quantum Biochemistry*, pages 219–242.

[11] Juan Bertran, Antonio Oliva, Luis Rodríguez-Santiago, and Mariona Sodupe. Single versus double proton-transfer reactions in watson- crick base pair radical cations. a theoretical study. *Journal of the American Chemical Society*, 120(32):8159–8167, 1998.

[12] Anny Odile Colson, Brent Besler, and Michael D Sevilla. Ab initio molecular orbital calculations on dna base pair radical ions: Effect of base pairing on proton-transfer energies, electron affinities, and ionization potentials. *The Journal of Physical Chemistry*, 96(24):9787–9794, 1992.

[13] Michael Hutter and Timothy Clark. On the enhanced stability of the guanine- cytosine base-pair radical cation. *Journal of the American Chemical Society*, 118(32):7574–7577, 1996.

[14] Xifeng Li, Zhongli Cai, and Michael D Sevilla. Investigation of proton transfer within dna base pair anion and cation radicals by density functional theory (dft). *The Journal of Physical Chemistry B*, 105(41):10115–10123, 2001.

[15] Xifeng Li, Zhongli Cai, and MD Sevilla. Energetics of the radical ions of the at and au base pairs: A density functional theory (dft) study. *The Journal of Physical Chemistry A*, 106(40):9345–9351, 2002.

[16] Steen Steenken. Purine bases, nucleosides, and nucleotides: aqueous solution redox chemistry and transformation reactions of their radical cations and e-and oh adducts. *Chemical Reviews*, 89(3):503–520, 1989.

[17] Steen Steenken and Slobodan V Jovanovic. How easily oxidizable is dna? one-electron reduction potentials of adenosine and guanosine radicals in aqueous solution. *Journal of the american chemical society*, 119(3):617–618, 1997.

[18] František Tureček. Transient intermediates of chemical reactions by neutralization-reionization mass spectrometry. *Modern Mass Spectrometry*, pages 77–129, 2003.

[19] Linda Feketeova, Bun Chan, George N Khairallah, Vincent Steinmetz, Philippe Maitre, Leo Radom, and Richard AJ O'Hair. Watson–crick base pair radical cation as a model for oxidative damage in dna. *The Journal of Physical Chemistry Letters*, 8(13):3159–3165, 2017.

[20] Robert C Dunbar. Photodissociation of trapped ions. *International Journal of Mass Spectrometry*, 200(1-3):571–589, 2000.

[21] Rodolphe Antoine and Philippe Dugourd. Uv-visible activation of biomolecular ions. In *Laser photodissociation and spectroscopy of mass-Separated biomolecular ions*, pages 93–116. Springer, 2013.

[22] Nicolas C Polfer and Philippe Dugourd. *Laser photodissociation and spectroscopy of mass-separated biomolecular ions*, volume 83. Springer, 2013.

[23] Michael Lesslie, John T Lawler, Andy Dang, Joseph A Korn, Daniel Bím, Vincent Steinmetz, Philippe Maître, František Tureček, and Victor Ryzhov. Cytosine radical cations: A gas-phase study combining irmpd spectroscopy, uvpd spectroscopy, ion–molecule reactions, and theoretical calculations. *ChemPhysChem*, 18(10):1293–1301, 2017.

[24] Andy Dang, Huong TH Nguyen, Heather Ruiz, Elettra Piacentino, Victor Ryzhov, and František Tureček. Experimental evidence for noncanonical thymine cation radicals in the gas phase. *The Journal of Physical Chemistry B*, 122(1):86–97, 2018.

[25] Andy Dang, Yue Liu, and František Tureček. Uv–vis action spectroscopy of guanine, 9-methylguanine, and guanosine cation radicals in the gas phase. *The Journal of Physical Chemistry A*, 123(15):3272–3284, 2019.

[26] Shu R Huang, Andy Dang, and František Tureček. Ground and excited states of gas-phase dna nucleobase cation-radicals. a uv–vis photodisociation action spectroscopy and computational study of adenine and 9-methyladenine. *Journal of the American Society for Mass Spectrometry*, 31(6):1271–1281, 2020.

[27] Yue Liu, Andy Dang, Jan Urban, and František Tureček. Charge-tagged dna radicals in the gas phase characterized by uv/vis photodissociation action spectroscopy. *Angewandte Chemie International Edition*, 132(20):7846–7851, 2020.

[28] John EP Syka, Joshua J Coon, Melanie J Schroeder, Jeffrey Shabanowitz, and Donald F Hunt. Peptide and protein sequence analysis by electron transfer dissociation mass spectrometry. *Proceedings of the National Academy of Sciences*, 101(26):9528–9533, 2004.

[29] Kazuo Kobayashi and Seiichi Tagawa. Direct observation of guanine radical cation deprotonation in duplex dna using pulse radiolysis. *Journal of the American Chemical Society*, 125(34):10213–10218, 2003.

[30] Kazuo Kobayashi, Ryuhei Yamagami, and Seiichi Tagawa. Effect of base sequence and deprotonation of guanine cation radical in dna. *The Journal of Physical Chemistry B*, 112(34):10752–10757, 2008.

[31] Joseph A Korn, Jan Urban, Andy Dang, Huong TH Nguyen, and František Tureček. Uv–vis action spectroscopy reveals a conformational collapse in hydrogen-rich dinucleotide cation radicals. *The Journal of Physical Chemistry Letters*, 8(17):4100–4107, 2017.

[32] Yang Liu, Joseph A Korn, Andy Dang, and František Tureček. Hydrogen-rich cation

radicals of dna dinucleotides: Generation and structure elucidation by uv–vis action spectroscopy. *The Journal of Physical Chemistry B*, 122(42):9665–9680, 2018.

[33] Yang Liu, Joseph A Korn, and František Tureček. Uv-vis action spectroscopy and structures of hydrogen-rich 2'-deoxycytidine dinucleotide cation radicals. a difficult case. *International Journal of Mass Spectrometry*, 443:22–31, 2019.

[34] Shu R Huang, Yue Liu, and František Tureček. Uv–vis photodissociation action spectroscopy reveals cytosine–guanine hydrogen transfer in dna tetranucleotide cation radicals upon one-electron reduction. *The Journal of Physical Chemistry B*, 124(17):3505–3517, 2020.

[35] Sharon G. Lias and John E. Bartmess. Nist chemistry webbook, srd 69.

[36] Andy Dang, Joseph A Korn, James Gladden, Brandon Mozzone, and František Tureček. Uv–vis photodissociation action spectroscopy on thermo ltq-xl etd and bruker amazon ion trap mass spectrometers: a practical guide. *Journal of The American Society for Mass Spectrometry*, 30(9):1558–1564, 2019.

[37] Christopher J Shaffer, Robert Pepin, and František Tureček. Combining uv photodissociation action spectroscopy with electron transfer dissociation for structure analysis of gas-phase peptide cation-radicals. *Journal of Mass Spectrometry*, 50(12):1438–1442, 2015.

[38] Huong TH Nguyen, Christopher J Shaffer, Robert Pepin, and František Tureček. Uv action spectroscopy of gas-phase peptide radicals. *The Journal of Physical Chemistry Letters*, 6(23):4722–4727, 2015.

[39] Emilie Viglino, Christopher J Shaffer, and František Tureček. Uv/vis action spectroscopy and structures of tyrosine peptide cation radicals in the gas phase. *Angewandte Chemie International Edition*, 55(26):7469–7473, 2016.

[40] Herman JC Berendsen, JPM van Postma, Wilfred F Van Gunsteren, ARHJ DiNola, and Jan R Haak. Molecular dynamics with coupling to an external bath. *The Journal of chemical physics*, 81(8):3684–3690, 1984.

[41] James JP Stewart. Optimization of parameters for semiempirical methods v: Modification of nddo approximations and application to 70 elements. *Journal of Molecular modeling*, 13(12):1173–1213, 2007.

[42] Jan Řezáč, Jindřich Fanfrlík, Dennis Salahub, and Pavel Hobza. Semiempirical quantum chemical pm6 method augmented by dispersion and h-bonding correction terms reliably describes various types of noncovalent complexes. *Journal of Chemical Theory and Computation*, 5(7):1749–1760, 2009.

[43] James JP Stewart. Stewart computational chemistry. *http://openmopac. net/*, 2007.

[44] Jan Řezáč. Cuby: An integrative framework for computational chemistry, 2016.

[45] Axel D Becke. Density-functional exchange-energy approximation with correct asymptotic behavior. *Physical review A*, 38(6):3098, 1988.

[46] Jeng-Da Chai and Martin Head-Gordon. Long-range corrected hybrid density functionals with damped atom–atom dispersion corrections. *Physical Chemistry Chemical Physics*, 10(44):6615–6620, 2008.

[47] Jacopo Tomasi, Benedetta Mennucci, and Roberto Cammi. Quantum mechanical continuum solvation models. *Chemical reviews*, 105(8):2999–3094, 2005.

[48] Yan Zhao and Donald G Truhlar. The m06 suite of density functionals for main group thermochemistry, thermochemical kinetics, noncovalent interactions, excited states, and transition elements: two new functionals and systematic testing of four m06-class functionals and 12 other functionals. *Theoretical chemistry accounts*, 120(1):215–241, 2008.

[49] Alan E Reed, Robert B Weinstock, and Frank Weinhold. Natural population analysis. *The Journal of Chemical Physics*, 83(2):735–746, 1985.

[50] Filipp Furche and Reinhart Ahlrichs. Adiabatic time-dependent density functional methods for excited state properties. *The Journal of chemical physics*, 117(16):7433–7447, 2002.

[51] Mario Barbatti, Matthias Ruckenbauer, Felix Plasser, Jiri Pittner, Giovanni Granucci, Maurizio Persico, and Hans Lischka. Newton-x: a surface-hopping program for nonadiabatic molecular dynamics. *Wiley Interdisciplinary Reviews: Computational Molecular Science*, 4(1):26–33, 2014.

[52] M. J. Frisch, G. W. Trucks, H. B. Schlegel, G. E. Scuseria, M. A. Robb, J. R. Cheeseman, G. Scalmani, V. Barone, G. A. Petersson, H. Nakatsuji, X. Li, M. Caricato, A. V. Marenich, J. Bloino, B. G. Janesko, R. Gomperts, B. Mennucci, H. P. Hratchian, J. V. Ortiz, A. F. Izmaylov, J. L. Sonnenberg, D. Williams-Young, F. Ding, F. Lipparini, F. Egidi, J. Goings, B. Peng, A. Petrone, T. Henderson, D. Ranasinghe, V. G. Zakrzewski, J. Gao, N. Rega, G. Zheng, W. Liang, M. Hada, M. Ehara, K. Toyota, R. Fukuda, J. Hasegawa, M. Ishida, T. Nakajima, Y. Honda, O. Kitao, H. Nakai, T. Vreven, K. Throssell, J. A. Montgomery, Jr., J. E. Peralta, F. Ogliaro, M. J. Bearpark, J. J. Heyd, E. N. Brothers, K. N. Kudin, V. N. Staroverov, T. A. Keith, R. Kobayashi, J. Normand, K. Raghavachari, A. P. Rendell, J. C. Burant, S. S. Iyengar, J. Tomasi, M. Cossi, J. M. Millam, M. Klene, C. Adamo, R. Cammi, J. W. Ochterski, R. L. Martin, K. Morokuma, O. Farkas, J. B. Foresman, and D. J. Fox. Gaussian˜16 Revision A.01, 2016. Gaussian Inc. Wallingford CT.

[53] Robert G Gilbert and Sean C Smith. *Theory of unimolecular and recombination reactions*. Publishers' Business Services [distributor], 1990.

[54] L Zhu and WL Hase. Quantum chemistry program exchange, 1994.

[55] Joshua A Gregersen and František Tureček. Mass-spectrometric and computational study of tryptophan radicals (trp+ h)˙ produced by collisional electron transfer to protonated tryptophan in the gas phase. *Physical Chemistry Chemical Physics*, 12(41):13434–13447, 2010.

[56] Kermit K Murray. Dna sequencing by mass spectrometry. *Journal of Mass Spectrometry*, 31(11):1203–1215, 1996.

[57] Scott A McLuckey, Gary J Van Berkel, and Gary L Glish. Tandem mass spectrometry of small, multiply charged oligonucleotides. *Journal of the American Society for Mass Spectrometry*, 3(1):60–70, 1992.

[58] Marin Sapunar, Wolfgang Domcke, and Nađa Došlić. Uv absorption spectra of dna bases in the 350–190 nm range: Assignment and state specific analysis of solvation effects. *Physical Chemistry Chemical Physics*, 21(41):22782–22793, 2019.

[59] Andrey V Tataurov, Yong You, and Richard Owczarzy. Predicting ultraviolet spectrum of single stranded and double stranded deoxyribonucleic acids. *Biophysical chemistry*, 133(1-3):66–70, 2008.

[60] Leigh B Clark, Gary G Peschel, and Ignacio Tinoco Jr. Vapor spectra and heats of vaporization of some purine and pyrimidine bases1. *The Journal of Physical Chemistry*, 69(10):3615–3618, 1965.

[61] Christel Marian, Dirk Nolting, and Rainer Weinkauf. The electronic spectrum of protonated adenine: Theory and experiment. *Physical Chemistry Chemical Physics*, 7(18):3306–3316, 2005.

[62] Yevgeniy Podolyan, Leonid Gorb, and Jerzy Leszczynski. Protonation of nucleic acid bases. a comprehensive post-hartree- fock study of the energetics and proton affinities. *The Journal of Physical Chemistry A*, 104(31):7346–7352, 2000.

[63] František Turecček and Xiaohong Chen. Protonated adenine: Tautomers, solvated clusters, and dissociation mechanisms. *Journal of the American Society for Mass Spectrometry*, 16(10):1713–1726, 2005.

[64] Carles Colominas, Francisco J Luque, and Modesto Orozco. Tautomerism and protonation of guanine and cytosine. implications in the formation of hydrogen-bonded complexes. *Journal of the American Chemical Society*, 118(29):6811–6821, 1996.

[65] Nicholas V Hud and Thomas Hellman Morton. Dft energy surfaces for aminopurine homodimers and their conjugate acid ions. *The Journal of Physical Chemistry A*, 111(17):3369–3377, 2007.

[66] Antarip Halder, Sohini Bhattacharya, Ayan Datta, Dhananjay Bhattacharyya, and Abhijit Mitra. The role of n7 protonation of guanine in determining the structure, stability and function of rna base pairs. *Physical Chemistry Chemical Physics*, 17(39):26249–26263, 2015.

[67] RR Wu, Bo Yang, G Berden, J Oomens, and MT Rodgers. Gas-phase conformations and energetics of protonated 2'-deoxyguanosine and guanosine: Irmpd action spectroscopy and theoretical studies. *The Journal of Physical Chemistry B*, 118(51):14774–14784, 2014.

[68] Antonello Filippi, Caterina Fraschetti, Flaminia Rondino, Susanna Piccirillo, Vincent Steinmetz, Leonardo Guidoni, and Maurizio Speranza. Protonated pyrimidine nucleosides probed by irmpd spectroscopy. *International Journal of Mass Spectrometry*, 354:54–61, 2013.

[69] Jean-Yves Salpin, Sébastien Guillaumont, Jeanine Tortajada, Luke MacAleese, Joël Lemaire, and Philippe Maitre. Infrared spectra of protonated uracil, thymine and cytosine. *ChemPhysChem*, 8(15):2235–2244, 2007.

[70] Robert Pepin and František Tureček. Kinetic ion thermometers for electron transfer dissociation. *The Journal of Physical Chemistry B*, 119(7):2818–2826, 2015.

[71] Douglas E Goeringer and Scott A McLuckey. Evolution of ion internal energy during collisional excitation in the paul ion trap: A stochastic approach. *The Journal of chemical physics*, 104(6):2214–2221, 1996.

[72] Scott Gronert. Estimation of effective ion temperatures in a quadrupole ion trap. *Journal of the American Society for Mass Spectrometry*, 9(8):845–848, 1998.

[73] Edward R Lovejoy and Robert R Wilson. Kinetic studies of negative ion reactions in a quadrupole ion trap: Absolute rate coefficients and ion energies. *The Journal of Physical Chemistry A*, 102(13):2309–2315, 1998.

[74] William A Donald, George N Khairallah, and Richard AJ O'Hair. The effective temperature of ions stored in a linear quadrupole ion trap mass spectrometer. *Journal of The American Society for Mass Spectrometry*, 24(6):811–815, 2013.

[75] František Tureček and Ryan R Julian. Peptide radicals and cation radicals in the gas phase. *Chemical reviews*, 113(8):6691–6733, 2013.

[76] Christopher L Moss, Thomas W Chung, Jean A Wyer, Steen Brøndsted Nielsen, Preben Hvelplund, and František Tureček. Dipole-guided electron capture causes abnormal dissociations of phosphorylated pentapeptides. *Journal of the American Society for Mass Spectrometry*, 22(4):731–751, 2011.

[77] Iwona Anusiewicz, Piotr Skurski, and Jack Simons. Refinements to the utah–washington mechanism of electron capture dissociation. *The Journal of Physical Chemistry B*, 118(28):7892–7901, 2014.

[78] Emilie Cauët and Jacques Liévin. Radical cations of the nucleic bases and radiation damage to dna: Ab initio study. *Advances in Quantum Chemistry*, 52:121–147, 2007.